Cooperative Non-Equilibrium Dynamics in a Thermal Rydberg Ensemble

CHRISTOPHER CARR

Cooperative Non-Equilibrium Dynamics in a Thermal Rydberg Ensemble

Christopher Carr

Abstract

This thesis reports the investigation of cooperative non-equilibrium dynamics in a thermal Rydberg ensemble. Cooperative behaviour arises due to resonant dipole-dipole interactions between highly excited Rydberg atoms. In order to transfer atomic population from the ground state to the Rydberg state in a caesium vapour, a three-photon excitation scheme is developed. This scheme has a number of benefits over traditional two-photon Rydberg excitation as each transition utilises inexpensive high-power diode lasers. The process of developing the excitation scheme produces a number of important results, including an excited-state polarisation spectroscopy technique and the observation of coherent three-photon electromagnetically induced transparency.

The optical response and atomic dynamics of the interacting ensemble can be separated into two distinct phases. When the Rydberg number density is low and the interactions are negligible, the system can be described by the behaviour of a single atom. However, when the Rydberg number density is high, resonant dipole-dipole interactions result in a significant modification of the ensemble properties. This cooperative many-body phase cannot be described by the behaviour of a single atom. In the frequency domain, the interactions produce an excitation-dependent cooperative energy shift that is observed using probe transmission spectroscopy. In the time domain, the interactions result in a cooperative enhancement of the atomic decay rate that is analysed using fluorescence spectroscopy.

At the transition between the single-body and many-body phase, a first-order non-equilibrium phase transition occurs. This is observed spatially along the length of the excitation region as a sharp switch in the emitted fluorescence. The first-order phase transition is also observed in the temporal response of the ensemble through critical slowing down. The divergence of the switching time to steady state follows a universal scaling law for phase transitions and the determined critical exponent is in excellent agreement with previous work on non-equilibrium phase transitions.

Cooperative Non-Equilibrium Dynamics in a Thermal Rydberg Ensemble

Christopher Carr

A thesis submitted in partial fulfilment
of the requirements for the degree of
Doctor of Philosophy

Department of Physics
Durham University

3rd June 2013

Contents

List of Figures

List of Tables

Declaration

I confirm that no part of the material offered has previously been submitted by myself for a degree in this or any other university. Where material has been generated through joint work, the work of others has been indicated.

Christopher Carr
Durham, 3rd June 2013

Acknowledgements

First and foremost I would like to thank my supervisor Charles Adams. After working together during my Master's project, I was inspired by his passion for Atomic Physics and decided to complete a PhD in Atmol. His continued guidance and support has allowed me to achieve more than I thought possible. Thanks must also go to Kevin Weatherill who I have had the opportunity to work with over the last three years.

I am grateful to Simon Gardiner, Ifan Hughes and Matt Jones for the tea room discussions and invaluable advice they have provided. During my time in Atmol, I have had the pleasure of working with a number of dedicated individuals including Richard Abel, Monsit Tanassitokosol, Armen Sargysan and Christopher Wade. Further thanks must go to Alban Urvoy, David Sarkisyan, Robert Löw and Tilman Pfau for the opportunity to collaborate.

Although he was only in Durham for six months, Ralf Ritter made a significant impact upon the work that is presented in this thesis. The combination of heavy metal music and ciao ciao sandwiches certainly made for an unexpectedly productive day! Life in the lab would not have been the same without trying to decipher James Keaveney. Four years later and I'm still struggling! Jokes aside, I am immensely grateful for James' support and wisdom.

Particular thanks must go to Lee Weller, Ray Sharples and Bart Lomanowski for the loan of equipment and Christoph Vaillant and Jon Pritchard for offering theoretical support. I would also like to thank the whole of the Atmol group for providing a stimulating and supportive environment. A special thanks must go to Lynne in the tea room for the years of Dairy Milk caramel and for keeping my dentist in business!

I am indebted to Ulrich Krohn both in and out of Physics for making PhD life much more enjoyable. His constant desire to be travelling around the North East and visiting new places is truly infectious. His help, support and many hours of proof reading will always be remembered.

Finally, I would like to thank my parents and my sister for their endless support and encouragement. Without them I wouldn't be where I am today. And of course, these acknowledgements wouldn't be complete without thanking my long-suffering girlfriend Melanie for reminding me that there is life outside of my PhD.

Dedicated to my parents,
to whom I owe everything.

In memory of David Wood,
for his love, support and encouragement.

1. Introduction

The work presented in this thesis is motivated by the desire to study strongly-interacting systems which are driven far from equilibrium. Non-equilibrium systems can be found throughout nature and society, for example in ecosystems, financial markets and climate [1]. These open systems are in constant interaction with the external environment through driving and dissipation processes. As a result, the steady state of a non-equilibrium system is a dynamical equilibrium between the energy that enters and leaves the system. Whilst the description of equilibrium thermodynamics has existed for more than a century, the understanding of non-equilibrium systems is still in its infancy. Non-equilibrium systems exhibit a rich array of dynamics [2] and dissipation-induced correlation was recently observed in a cold molecular gas [3]. Dynamical phase transitions in non-equilibrium systems are particularly interesting as they occur due to long-range correlation in a system with cooperative interactions [4]. Theoretical work in this area has provided much insight [2, 5, 6, 7] including analysis of dynamical phase transitions in spin systems [8, 9, 10].

In the absence of inter-particle interactions, a many-body system can be described by decomposing it into constituent particles. The response of the many-body system can be obtained from the response of a single particle which is multiplied by the total particle number. In the presence of interactions, this description is no longer valid as the response of an individual particle is dependent upon its interaction with nearby particles. This results in a cooperative non-linearity [11] as the response of the system scales non-linearly with the total particle number.

Cooperative interactions between the particles in a non-equilibrium system can result in the formation of macroscopic temporal or spatial structures [12]. An excellent example of this is the laser, a non-equilibrium medium which is pumped by an external source. When the medium is weakly pumped, the photons are emitted with a random phase and the system exists in a state of disorder. However, when the strength of the pump field is above a critical value, the medium suddenly switches to an ordered state. Now the photons are emitted with a well-defined phase and the medium becomes a coherent source of radiation. This phase transition between order and disorder arises due to cooperative interactions and results in a self organisation [12] of atoms in the gain medium.

The desire to understand cooperative non-equilibrium systems led to the foun-

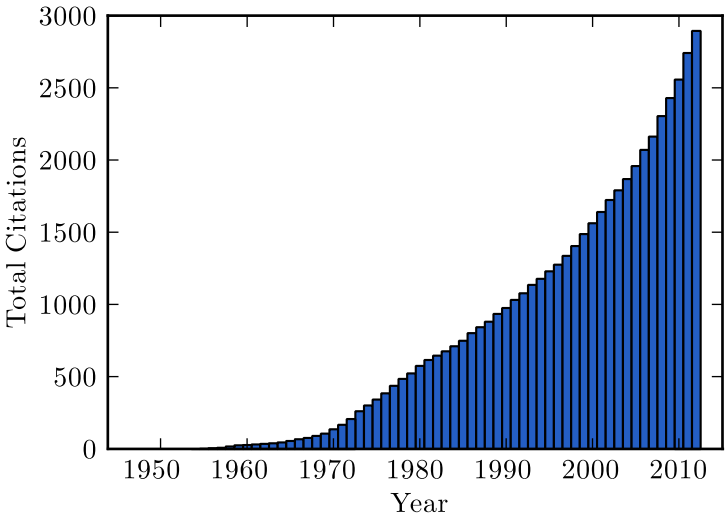

Figure 1.1.: The total number of citations to Dicke's seminal paper, *Coherence in spontaneous radiation processes*, published in Physical Review **93** 99 (1954). Data obtained from Thomson Reuters Web of Knowledge database.

dation of Synergetics by Hermann Haken in 1980 [1]. The aim of synergetics is to provide a unified understanding of the appearance of macroscopic structures in systems with cooperative interactions. Ultimately, this research has identified that cooperative behaviour can be found in almost every discipline including neurology (visual perception), anatomy (movement coordination), ecology (population dynamics) and politics (formation of public opinion).

In atomic physics, cooperative phenomena arise due to resonant dipole-dipole interactions. In the theory proposed by Dicke in his seminal paper [13], the system can be described by a quantum mechanical many-body wavefunction. This proposal has received great interest, particularly in the last ten years, as can be seen in Fig. 1.1 by the number of citations that the paper receives each year. Through microscopic dipole-dipole interactions, a macroscopic phase can arise between the dipoles. Consider, for example, an isotropic medium of N two-level atoms which are all in the excited state. When the inter-particle separation is large and interactions can be neglected, each atom evolves independently. However, when the inter-particle separation is small, the spontaneous decay of a single atom results in a phasing of the ensemble. This can also be understood as the system entering a many-body state where there are $(N-1)$ shared excitations. This many-body state results in a dramatic change in the evolution of the system. In the time domain, the decay rate of the excited state is modified and can be cooperatively enhanced resulting in superradiance or subradiance [13, 14, 15, 16]. In the case of superradiance, an intense burst of radiation is emitted as the medium rapidly decays on timescales much shorter than the natural lifetime of the excited state. Recent pioneering experiments

have observed subradiant and superradiant states in the interaction between two trapped ions [17] and two fluorescent molecules [18]. These experiments represent an important confirmation of Dicke's theory in its most elementary form.

In the frequency domain, resonant dipole-dipole interactions result in a cooperative excitation-dependent shift of the excited-state energy [16, 19, 20]. Intrinsic optical bistability is perhaps the most striking consequence of the cooperative frequency shift induced by resonant dipole-dipole interactions [21]. The phenomena of bistability arises due to presence of feedback in a non-linear system [22, 23]. Optical bistability was first observed by placing a medium with a non-linear response in a Fabry-Perot cavity where the cavity mirrors provide feedback upon the atoms [24]. However, in intrinsic optical bistability, the feedback arises instead due to strong interactions between the atoms and the dipolar field [25, 26, 27].

At this point, it is important to recognise the complementary work that has taken place in cavity quantum electrodynamics (QED) [28]. First proposed theoretically as the self-coupling of an atom with a mirror [29], the cavity-enhanced interaction between an atom and its radiated field results in a resonant dipole-dipole interaction. This interaction induces an energy shift and modified decay rate of the atomic state [30]. Furthermore, cavity QED has been utilised to create a single-atom maser [31] and a single-photon source [32].

In an atomic ensemble without external feedback, the level of cooperativity can be determined by the number density of interacting atoms $\mathcal{N}$ and the extent of the interaction, characterised by the interaction wavelength λ. These two components are combined to form the cooperativity parameter $C = \frac{\mathcal{N}\lambda^3}{4\pi^2}$. In the case of optically-driven ground-state transitions, cooperative effects can only be observed in dense media where $\mathcal{N} > 10^{15}$ cm^{-3}. As a result, intrinsic optical bistability has only been previously observed in an up-conversion process in a solid state crystal [21]. The difficulty in observing cooperative effects can be overcome in dilute media by using highly-excited Rydberg states [33, 34] where the interaction wavelength is on millimetre length scales.

The remarkable properties of Rydberg atoms make them ideal candidates for studying quantum many-body physics [35]. Through the choice of Rydberg state or atomic separation it is possible to tune the strength, sign and spatial dependence of the dipole-dipole interactions [36]. The long-range coupling of the resonant dipole-dipole interaction can be used to perform non-local energy transfer between Rydberg atoms. The spatial dependence of the interaction has been measured experimentally [37] and radio frequencies used to drive interactions between spatially separated volumes [38]. Furthermore, recent experimental work has identified the emergence of spatial structures in a Rydberg gas [39].

When the shift of the Rydberg state is greater than the linewidth of the excitation laser, only single Rydberg excitations can exist within a "blockade" sphere [40]. The

Rydberg blockade effect has received much interest for its potential application in quantum information processing [41, 42, 43] and the creation of a source of single-atoms [44], single-photons [44] and single-ions [45].

The small energy separation between neighbouring Rydberg states allows for microwave dressing [46] to be performed. Furthermore, the large polarisability of Rydberg atoms in response to external electric fields has been used to measure DC electric fields with high sensitivity [47, 48, 49]. This sensitivity has also been used to perform electrometry near a dielectric surface [50]. The long radiative lifetime of Rydberg atoms allows coherent Rabi oscillations to be observed [51]. In analogy to the Dicke model, this is a many-body oscillation of N atoms between the ground and Rydberg state with a cooperative enhancement of the Rabi frequency by a factor $\sqrt{N}$.

The main drawback that has to be overcome when working with Rydberg atoms is the small excitation probability due to the weak coupling between the ground state and the Rydberg state. As a result, direct optical excitation of Rydberg states is very inefficient. Consequently, a number of alternative methods for conducting Rydberg state spectroscopy have been developed. A destructive, yet highly efficient technique, involves applying a large electric field to ionise the Rydberg atom [34]. The constituent ion and electron can then be detected using a highly sensitive micro-channel plate. Non-destructive techniques where the Rydberg state remains unperturbed during detection are particularly desirable, for example in quantum information processing applications [41, 52]. Coherent electromagnetically induced transparency is a multi-photon non-destructive technique that transfers the weak Rydberg transition onto a strong optical transition [53, 54, 55, 56]. This technique has been extensively used to study dipole-dipole interactions between Rydberg atoms [11, 57, 58]. Electron shelving is an incoherent non-destructive technique that utilises a strong probe beam to excite atomic population into the long-lived Rydberg state. As the lifetime of the Rydberg state is orders of magnitude longer than low-lying excited states, the absorption of the probe beam is significantly modified [59].

Thermal vapours offer a simple and inexpensive system for studying dipole-dipole interactions between Rydberg atoms. Research in this area began with the observation of spectral line broadening in a gas [60]. More recently, the van der Waals interaction has been observed between Rydberg atoms [61]. Thermal vapours have been proposed as a scalable system for quantum information processing applications [62]. Particular benefit arises from vapour cells which can be fabricated for their intended purpose, for example electrical read-out of Rydberg population with metal coatings on the vapour cell windows [63]. Furthermore, vapour cells have been micro-fabricated for use as chip-scale atomic clocks [64] or to perform sub-picotesla atomic magnetometry [65].

In this thesis, a three-photon excitation scheme to Rydberg states in a thermal

caesium vapour is developed. Utilising high-power semiconductor diode lasers at convenient wavelengths, atomic population can be efficiently transferred from the ground state into the Rydberg state. During the development process, each transition in the excitation scheme is fully characterised in order to gain a thorough understanding of the underlying processes. This excitation scheme is then used to observe strong cooperative interactions and a non-equilibrium phase transition in the Rydberg ensemble. Furthermore, the millimetre transition wavelength for the dipole-dipole interaction enables a first-order non-equilibrium phase transition to be observed on macroscopic optically-resolvable length scales.

Thesis Outline

The structure of the thesis is summarised below:

- Chapter 2 introduces the theoretical subjects which form the foundation of the thesis; the atom-light interaction, coherent and incoherent processes in the excitation of atoms, Rydberg atoms and thermal vapours.

- Chapter 3 considers the theoretical description of the resonant interaction between optically-induced atomic dipoles. Firstly, the Liénard-Wiechert potential is presented and applied to the pairwise interaction between two dipoles. This is then extended to a many-body system where the resonant dipole-dipole interaction energy shift can be decomposed into the Lorentz-Lorentz local field, the cooperative Lamb shift and the collisional shift.

- Chapter 4 presents ground-state spectroscopy of atoms in a thermal vapour. Using a strong pump and weak probe it is possible to reduce the Doppler shift and obtain Doppler-free resonances. Polarisation spectroscopy is then used to obtain narrow dispersive atomic resonances which can be used for laser frequency stabilisation.

- Chapter 5 demonstrates excited-state spectroscopy in a thermal vapour. The excited-state transition linewidth is analysed theoretically and found to be sub-natural when the lower state is coherently prepared. This result is then confirmed experimentally using a simple three-level system. Following this, a novel excited-state polarisation spectroscopy technique is presented which can be used for frequency stabilisation of lasers coupling excited-state transitions.

- Chapter 6 considers an inverted-wavelength system where the wavelength of the probe laser is shorter than the wavelength of the coupling laser. In the weak probe regime, it is shown that electromagnetically-induced transparency is significantly suppressed in a thermal vapour. In the strong probe regime,

two-photon population transfer processes are observed experimentally. The observation of transmissive and absorptive features is investigated and it is shown that they depend on the interaction time between the thermal atom and the laser.

- Chapter 7 examines coherent and incoherent spectroscopy of the Rydberg state. In the former case, three-photon electromagnetically induced transparency is observed experimentally and a theoretical model is devised which shows excellent quantitative agreement with the data. In the latter case, electron shelving is utilised to transfer a large fraction of the ground-state population into the Rydberg state. This serves as a starting point for the next Chapter.

- Chapter 8 presents the observations of cooperative Rydberg interactions in a thermal vapour. The cooperative frequency shift is examined by conducting probe transmission spectroscopy of the ensemble. The cooperative decay rate is investigated by performing high precision fluorescence spectroscopy in the single and many-body phases. Finally, a temporal and spatial first-order non-equilibrium phase transition is observed in the atomic dynamics. Through the divergence in the atomic time dynamics at the phase transition, the critical exponent is determined.

- Chapter 9 summarises the important results and draws conclusions from the work that has been carried out. An outlook and suggestions for further work is then discussed.

Publications

Work related to this thesis

[66] C. Carr, C. S. Adams and K. J. Weatherill, *Polarization spectroscopy of an excited state transition*, Optics Letters **37**, 118 (2012).

[67] M. Tanasittikosol, C. Carr, C. S. Adams and K. J. Weatherill, *Subnatural linewidths in two-photon excited-state spectroscopy*, Physical Review A **85**, 033830 (2012).

[68] C. Carr, M. Tanasittikosol, A. Sargsyan, D. Sarkisyan, C. S. Adams and K. J. Weatherill, *Three-photon electromagnetically induced transparency using Rydberg states*, Optics Letters **37**, 3858 (2012).

[69] A. Urvoy, C. Carr, R. Ritter, C. Veit, C.S. Adams, K. J. Weatherill and R. Löw, *Optical coherences and wavelength mismatch in ladder systems*, in preparation (2013).

[70] C. Carr, R. Ritter, C. G. Wade, C. S. Adams and K. J. Weatherill, *Nonequilibrium phase transition in a dilute Rydberg ensemble*, Physical Review Letters **111**, 113901 (2013).

Other work

[50] R. P. Abel, C. Carr, U. Krohn and C. S. Adams, *Electrometry near a dielectric surface using Rydberg electromagnetically induced transparency*, Physical Review A **84**, 023408 (2011).

2. Theoretical Foundation

2.1. Introduction

This Chapter introduces a broad range of theoretical subjects which form the foundation of the thesis. The description of the interaction between atoms and light is first considered in a two-level atom. This is then extended to a three-level atom, where coherent electromagnetically-induced phenomena are analysed. The discussion closes with a consideration of multi-level atoms where incoherent population transfer processes can emerge. The Chapter proceeds to analyse the transition dipole moment and relevant information for caesium is presented. This is followed by a discussion of the unusual properties of Rydberg atoms. Finally, the chapter concludes with a consideration of the benefits of thermal vapours and the common methods of confining the atoms for experimental analysis.

2.2. Two-Level Atom-Light Interaction

Coherent excitation occurs when an atom interacts with a monochromatic radiation field whose frequency is close to an atomic eigenfrequency [71, 72]. The temporal evolution of an atomic system under coherent excitation can be described theoretically and is presented in this section for the case of a two-level atom. Consider an atomic system with two non-degenerate levels which are coupled by a near-resonant electromagnetic field. The ground state $|1\rangle$ with energy $\hbar\omega_1$ is coupled to the excited state $|2\rangle$ with energy $\hbar\omega_2$ by an electromagnetic field produced by a laser with frequency ω_{L}. The laser is detuned from resonance by $\Delta = \omega_{\mathrm{L}} - \omega_0$, where the transition frequency $\omega_0 = \omega_2 - \omega_1$. The excited state $|2\rangle$ is unstable and the atom decays by spontaneous emission back to the ground state $|1\rangle$ with rate Γ.

2.2.1. Semi-Classical and Dipole Approximation

A number of approximations can be implemented to reduce the complexity of the problem. In the semi-classical approximation, a quantised atomic system is considered to be interacting with a classical electromagnetic field. Furthermore, only the interaction between the applied field and the electric dipole moment of the atom is considered [73]. This approximation neglects higher-order multipole terms in the coupling. Finally, under the electric dipole approximation, the spatial variation

of the electric field is ignored as the wavelength is much greater than the atomic dimensions [74]. The total Hamiltonian $\hat{\mathcal{H}}_{\text{tot}}$ for the atomic system is given by

$$\hat{\mathcal{H}}_{\text{tot}} = \hat{\mathcal{H}}_{\text{atom}} + \hat{\mathcal{H}}_{\text{int}}, \tag{2.1}$$

where $\hat{\mathcal{H}}_{\text{atom}}$ is the Hamiltonian for the bare atom and $\hat{\mathcal{H}}_{\text{int}}$ is the Hamiltonian for the atom-light interaction. Within the electric dipole approximation, the interaction Hamiltonian is given by $\hat{\mathcal{H}}_{\text{int}} = -\boldsymbol{d} \cdot \boldsymbol{\mathcal{E}}$ where $\boldsymbol{d}$ is the electric dipole moment and $\boldsymbol{\mathcal{E}} = \boldsymbol{\mathcal{E}}_0 \cos \omega_L t$ is the classical electromagnetic field. The temporal evolution of the atomic system, described by the atomic wavefunction $|\psi\rangle$, can be obtained using the time-dependent Schrödinger equation

$$i\hbar \frac{\partial}{\partial t} |\psi\rangle = \hat{\mathcal{H}}_{\text{tot}} |\psi\rangle . \tag{2.2}$$

2.2.2. Density Matrix Formalism

The orthonormal basis states $\{|i\rangle\}$ of the bare atomic Hamiltonian $\hat{\mathcal{H}}_{\text{atom}}$ form a complete set. Therefore a general quantum state of the atom $|\psi\rangle$ can be written as a superposition of basis states

$$|\psi\rangle = \sum_i c_i |i\rangle , \tag{2.3}$$

where the complex coefficient c_i is the probability amplitude to be in the basis state $|i\rangle$. Using the definition of the density operator $\rho = |\psi\rangle \langle\psi|$, the density matrix for a two-level atom can be written as

$$\hat{\rho} = \begin{pmatrix} c_1 \\ c_2 \end{pmatrix} \begin{pmatrix} c_1^* & c_2^* \end{pmatrix} = \begin{pmatrix} |c_1|^2 & c_1 c_2^* \\ c_1^* c_2 & |c_2|^2 \end{pmatrix} = \begin{pmatrix} \rho_{11} & \rho_{12} \\ \rho_{21} & \rho_{22} \end{pmatrix}, \tag{2.4}$$

where the diagonal matrix elements ρ_{ii} represent the population of each level and the off-diagonal matrix elements ρ_{ij} represent the coherence between the levels. In this representation, the bare atomic Hamiltonian $\mathcal{H}_{\text{atom}}$ is given by

$$\hat{\mathcal{H}}_{\text{atom}} = \begin{pmatrix} \hbar\omega_1 & 0 \\ 0 & \hbar\omega_2 \end{pmatrix} \equiv \begin{pmatrix} 0 & 0 \\ 0 & \hbar\omega_0 \end{pmatrix}. \tag{2.5}$$

The electric dipole moment $\boldsymbol{d}$ is purely non-diagonal in the basis $\{|i\rangle\}$ as it describes a coupling between atomic levels For a two-level system, the dipole moment is given by

$$\boldsymbol{d} = d_{21}(|2\rangle \langle 1| + |1\rangle \langle 2|), \tag{2.6}$$

where $|2\rangle\langle 1|$ is the raising operator from state $|1\rangle$ to state $|2\rangle$ and $|1\rangle\langle 2|$ is the lowering operator from state $|2\rangle$ to state $|1\rangle$. Using this description, the atom-light interaction Hamiltonian $\hat{\mathcal{H}}_{\text{int}}$ can be written as [73]

$$\hat{\mathcal{H}}_{\text{int}} = -\boldsymbol{d}\cdot\boldsymbol{\mathcal{E}} \tag{2.7a}$$

$$= \frac{d_{21}\mathcal{E}_0}{2}\left(|2\rangle\langle 1| + |1\rangle\langle 2|\right)\left(e^{i\omega_L t} + e^{-i\omega_L t}\right), \tag{2.7b}$$

where the electric field $\boldsymbol{\mathcal{E}}$ has been written in exponential form. The term $e^{i\omega_L t}$ can be identified with photon emission whilst the term $e^{-i\omega_L t}$ can be identified with photon absorption. Under the Rotating Wave Approximation (RWA), the terms corresponding to the emission of a photon which promotes the atom to state $|2\rangle$ and the absorption of a photon which relaxes the atom to state $|1\rangle$ in Eq. (2.7b) are neglected. These anti-resonant terms average to zero in a rotating frame [74]. Defining the angular Rabi frequency $\Omega = (d_{21}\mathcal{E}_0)/\hbar$, the interaction Hamiltonian can be written as

$$\hat{\mathcal{H}}_{\text{int}} = \frac{\hbar}{2}\begin{pmatrix} 0 & \Omega e^{i\omega_{\text{L}} t} \\ \Omega e^{-i\omega_{\text{L}} t} & 0 \end{pmatrix}. \tag{2.8}$$

The total Hamiltonian $\hat{\mathcal{H}}_{\text{tot}}$ can then be written using Eq. (2.5) and Eq. (2.8) as

$$\hat{\mathcal{H}}_{\text{tot}} = \hbar\begin{pmatrix} 0 & \Omega/2 e^{i\omega_L t} \\ \Omega/2 e^{-i\omega_L t} & \omega_0 \end{pmatrix}. \tag{2.9}$$

The Liouville-von Neumann equation is the equivalent of the Schrödinger equation for the time evolution of the density matrix and is given by

$$i\hbar\frac{d\hat{\rho}}{dt} = \left[\hat{\mathcal{H}}_{\text{tot}}, \hat{\rho}\right], \tag{2.10}$$

where the term $[\hat{\mathcal{H}}_{\text{tot}}, \hat{\rho}]$ represents the commutator between the total Hamiltonian and the density matrix. In order to account for spontaneous emission in the semi-classical description, a phenomenological decay term $\hat{\mathcal{L}}$ must be added to Liouville-von Neumann equation. This produces what is known as the Lindblad master equation for the time evolution of the atomic system

$$\frac{d\hat{\rho}}{dt} = -\frac{i}{\hbar}\left[\hat{\mathcal{H}}_{\text{tot}}, \hat{\rho}\right] + \hat{\mathcal{L}}. \tag{2.11}$$

The diagonal elements of the decay matrix $\mathcal{L}_{ii}$ represent the transfer of population between the atomic levels and must be entered manually. The off-diagonal elements which represent the decay of the coherences between the levels are given by $\mathcal{L}_{ij} =$

$-(\Gamma_i + \Gamma_j)\tilde{\rho}_{ij}/2$. For a two-level atom, the decay matrix can be written as

$$\hat{\mathcal{L}} = \frac{1}{2}\begin{pmatrix} 2\Gamma\rho_{22} & -\Gamma\tilde{\rho}_{12} \\ -\Gamma\tilde{\rho}_{21} & -2\Gamma\rho_{22} \end{pmatrix}, \tag{2.12}$$

where the decay rate of the ground state $\Gamma_1 = 0$ and the decay rate of the excited state $\Gamma_2 \equiv \Gamma$.

2.2.3. Optical Bloch Equations

For a two-level atomic system, the time evolution of the density matrix elements can be obtained by substituting the total Hamiltonian $\hat{\mathcal{H}}_{\text{tot}}$ in Eq. (2.9) and the phenomenological decay matrix $\hat{\mathcal{L}}$ in Eq. (2.12) into the Lindblad master equation in Eq. (2.11). The resulting first-order, coupled differential equations are known as the Optical Bloch Equations (OBE)

$$\dot{\rho}_{11} = \frac{i\Omega}{2}(\tilde{\rho}_{12} - \tilde{\rho}_{21}) + \Gamma\rho_{22}, \tag{2.13a}$$

$$\dot{\tilde{\rho}}_{12} = \frac{i\Omega}{2}(\rho_{11} - \rho_{22}) + \tilde{\rho}_{12}(-i\Delta - \Gamma/2), \tag{2.13b}$$

$$\dot{\tilde{\rho}}_{21} = \frac{i\Omega}{2}(\rho_{22} - \rho_{11}) + \tilde{\rho}_{21}(i\Delta - \Gamma/2), \tag{2.13c}$$

$$\dot{\rho}_{22} = \frac{i\Omega}{2}(\tilde{\rho}_{21} - \tilde{\rho}_{12}) - \Gamma\rho_{22}, \tag{2.13d}$$

where the dot represents the first derivative and the slow variables $\tilde{\rho}_{21} = \rho_{21}e^{i\omega_L t}$ and $\tilde{\rho}_{12} = \rho_{12}e^{-i\omega_L t}$ are used on the coherence terms [75]. When the atomic evolution has reached a steady state, the rate of change of the density matrix $d\rho/dt = 0$. Under the condition that the total population is conserved, $(\rho_{11} + \rho_{22}) = 1$, the OBE's can be reduced to a single characteristic equation for the system

$$\tilde{\rho}_{21} = \frac{i\Omega/2}{\Gamma/2 - i\Delta}(\rho_{22} - \rho_{11}), \tag{2.14}$$

where $\tilde{\rho}_{21} = \tilde{\rho}_{12}^*$ for the coherence terms.

2.2.4. Optical Response

The electric susceptibility χ describes the degree of polarisation of a dielectric medium in response to an applied electric field. For an atomic ensemble with uniform number density $\mathcal{N}$, the susceptibility is related to the density matrix by [55]

$$\chi = -\frac{2\mathcal{N}d_{21}^2}{\epsilon_0\hbar\Omega}\tilde{\rho}_{21}. \tag{2.15}$$

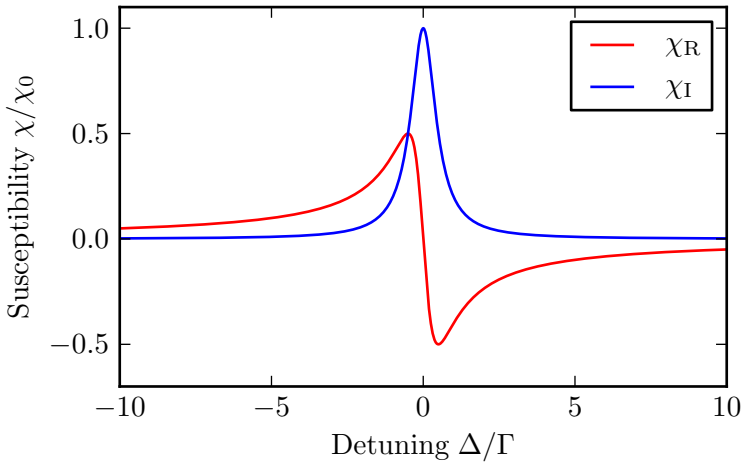

Figure 2.1.: Two-level atom susceptibility. The real part of the susceptibility χ_R (red curve) has a dispersive lineshape. The imaginary part of the susceptibility χ_I (blue curve) has a Lorentzian lineshape. The susceptibility is normalised to the resonant susceptibility $\chi_0 = 2\mathcal{N}d_{21}^2/\epsilon_0\hbar\Gamma$.

This equation relates the macroscopic property of the ensemble χ to the microscopic property of the atom $\tilde{\rho}_{21}$. When the applied field is weak $\Omega \ll \Gamma$, the population of the ground state $\rho_{11} \approx 1$ and the population of the excited state $\rho_{22} \approx 0$. Using this approximation, the characteristic equation for the coherence in Eq. (2.14) can be substituted into Eq. (2.15) to obtain the susceptibility

$$\chi = \frac{i\mathcal{N}d_{21}^2}{\epsilon_0\hbar(\Gamma/2 - i\Delta)}. \tag{2.16}$$

The susceptibility can be broken down into real and imaginary parts $\chi = \chi_R + i\chi_I$ and these components are shown in Fig. 2.1. The real part χ_R has a dispersive lineshape whilst the imaginary part χ_I has a Lorentzian lineshape. The optical properties of the atomic system are determined by the refractive index n, which can be related back to the susceptibility via

$$n = \sqrt{1+\chi} \approx 1 + \frac{\chi_R + i\chi_I}{2}, \tag{2.17}$$

where the approximation is valid for $|\chi| \ll 1$. For a monochromatic electric field passing through an isotropic medium, the output electric field $\mathcal{E}_{out}$ is given by

$$\mathcal{E}_{out} = \mathcal{E}_{in}e^{inkz} = \mathcal{E}_{in}e^{-n_I kl}e^{in_R kz} = \mathcal{E}_{in}e^{ikz}e^{i\chi_R kz/2}e^{-\chi_I kz/2}, \tag{2.18}$$

where the wavevector $k = 2\pi/\lambda$. From this expression, it is possible to identify an attenuation (proportional to the imaginary part of the susceptibility) and a phase

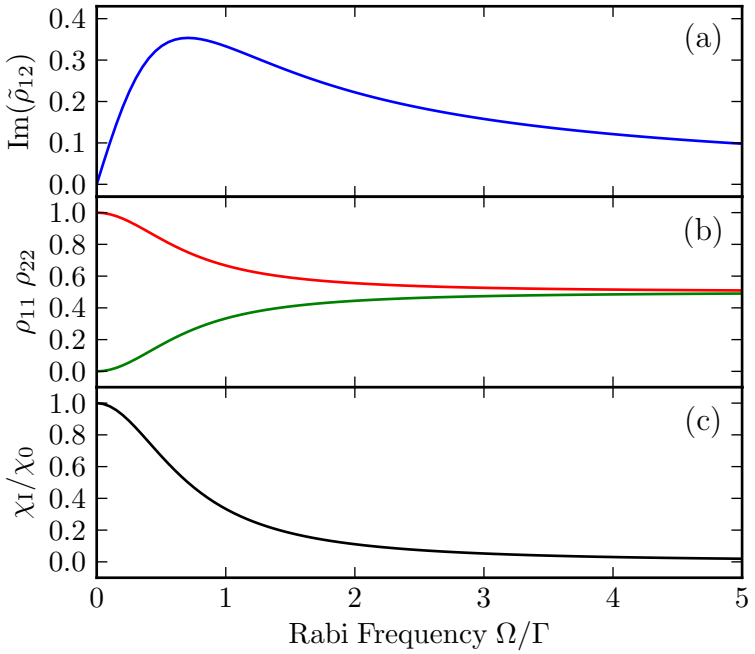

Figure 2.2.: Two-level atomic response as a function of Rabi frequency Ω. (a) Imaginary part of the coherence $\mathrm{Im}(\tilde{\rho}_{12})$. (b) Population of the ground state ρ_{11} (red) and excited state ρ_{22} (green). (c) Imaginary part of the complex susceptibility χ_I/χ_0 where $\chi_0 = 2\mathcal{N}d_{21}^2/\hbar\epsilon_0\Gamma$.

shift (proportional to the real part of the susceptibility) of the output electric field. The resulting change in intensity and phase in a medium with length L are given by

$$I = I_0 e^{-k\chi_\mathrm{I}L}, \tag{2.19}$$

$$\Delta\phi = k\chi_\mathrm{R}L/2, \tag{2.20}$$

where Eq. 2.19 is the Beer-Lambert Law with absorption coefficient $\alpha = k\chi_\mathrm{I}$.

This approximation breaks down when the laser Rabi frequency is no longer weak $\Omega > \Gamma$ as population can be transferred from the ground state into the excited state. As a result, the optical response is modified by saturation effects. The two-level atomic response is shown in Fig. 2.2 as a function of Rabi frequency Ω. Whilst the imaginary part of the coherence $\mathrm{Im}(\tilde{\rho}_{12})$ initially increases with Rabi frequency, shown in (a), it eventually turns over and decays slowly. This occurs due to saturation of the excited-state population $\rho_{22} \to 0.5$, as shown in (b). As a result of this saturation, the absorption of the atomic system, proportional to the imaginary part of the susceptibility χ_I, decreases steadily to zero, as shown in (c).

In atomic spectroscopy, the radiation field is used to "probe" the atomic system and determine its properties. The saturation of absorption is therefore a detrimental effect which can be minimised in most experimental situations by ensuring $\Omega \ll \Gamma$.

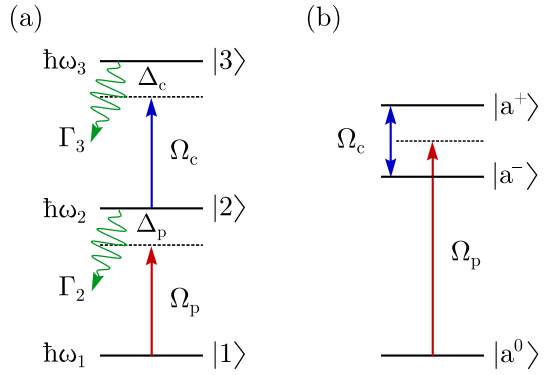

Figure 2.3.: (a) Three-level ladder system with bare ground state $|1\rangle$, intermediate state $|2\rangle$ and excited state $|3\rangle$. (b) When the probe is weak $\Omega_\mathrm{p} \ll \Omega_\mathrm{c}$ and detuning $\Delta_\mathrm{p} = \Delta_\mathrm{c} = 0$, the dressed states $|a^\pm\rangle = (|2\rangle \pm |3\rangle)/\sqrt{2}$ are split by Ω_c. The dressed state $|a^0\rangle = |1\rangle$ remains unperturbed.

The intensity I of the laser is often expressed in terms of the saturation intensity I_sat where

$$\frac{I}{I_\mathrm{sat}} = \frac{2\Omega^2}{\Gamma^2}. \tag{2.21}$$

When the intensity $I = I_\mathrm{sat}$, the Rabi frequency $\Omega/\Gamma = 1/\sqrt{2}$, corresponding to the peak of the coherence in Fig. 2.2(a) or the point at which the absorption has decreased by 50% in Fig. 2.2(c). Given that the electric field intensity $I = (1/2)c\epsilon_0\mathcal{E}_0^2$, the saturation intensity I_sat can also be written as [76]

$$I_\mathrm{sat} = \frac{c\epsilon_0\Gamma^2\hbar^2}{4d_{21}^2}. \tag{2.22}$$

2.3. Three-Level Atom-Light Interaction

In this section, the atom-light interaction is extended to an atomic system with three levels which are coupled by two lasers, as shown in Fig. 2.3(a). Consider an atomic system with ground state $|1\rangle$ with energy $\hbar\omega_1$, intermediate state $|2\rangle$ with energy $\hbar\omega_2$ and excited state $|3\rangle$ with energy $\hbar\omega_3$. The ground and intermediate state are coupled by a "probe" laser with Rabi frequency Ω_p which is detuned from resonance by $\Delta_\mathrm{p} = \omega_\mathrm{p} - \omega_{21}$. Throughout this thesis, the probe laser is defined as the laser that is detected using a photodiode and used to determine the spectroscopic properties of the atomic medium.

In addition, the intermediate and excited state are coupled by a "coupling" laser with Rabi frequency Ω_c which is detuned from resonance by $\Delta_\mathrm{c} = \omega_\mathrm{c} - \omega_{32}$. The three levels of the atomic system are arranged in a ladder such that $\hbar\omega_1 < \hbar\omega_2 < \hbar\omega_3$.

The excited state $|3\rangle$ decays at rate Γ_3 to the intermediate state $|2\rangle$. Additionally, the intermediate state $|2\rangle$ decays to the stable ground state $|1\rangle$ at rate Γ_2.

Using the semi-classical treatment discussed in Section 2.2, the total Hamiltonian in the dipole and rotating wave approximation is given by

$$\hat{\mathcal{H}}_{\text{tot}} = \hbar \begin{pmatrix} 0 & \Omega_\text{p}/2 & 0 \\ \Omega_\text{p}/2 & -\Delta_\text{p} & \Omega_\text{c}/2 \\ 0 & \Omega_\text{c}/2 & -(\Delta_\text{p}+\Delta_\text{c}) \end{pmatrix}. \tag{2.23}$$

As a result of the off-diagonal coupling provided by Ω_p and Ω_c, the bare states $\{|1\rangle, |2\rangle, |3\rangle\}$ are no longer the eigenstates of the atomic system. Diagonalising the Hamiltonian at two-photon resonance $\Delta_\text{p}+\Delta_\text{c} = 0$ results in the following eigenstates or "dressed" states [54]

$$\left|a^+\right\rangle = \sin\theta\sin\phi\,|1\rangle + \cos\phi\,|2\rangle + \cos\theta\sin\phi\,|3\rangle, \tag{2.24a}$$

$$\left|a^0\right\rangle = \cos\theta\,|1\rangle - \sin\theta\,|3\rangle, \tag{2.24b}$$

$$\left|a^-\right\rangle = \sin\theta\cos\phi\,|1\rangle - \sin\phi\,|2\rangle + \cos\theta\cos\phi\,|3\rangle, \tag{2.24c}$$

where the Stückelberg mixing angles are defined as

$$\tan\theta = \frac{\Omega_\text{p}}{\Omega_\text{c}}, \tag{2.25a}$$

$$\tan 2\phi = \frac{\sqrt{\Omega_\text{p}^2+\Omega_\text{c}^2}}{\Delta_\text{p}}. \tag{2.25b}$$

Whilst the energy of the eigenstate $\left|a^0\right\rangle$ remains zero, the eigenstates $|a^\pm\rangle$ are shifted up and down in energy by an amount [54]

$$\hbar\omega_\pm = \frac{\hbar}{2}\left(\Delta_\text{p} \pm \sqrt{\Delta_\text{p}^2+\Omega_\text{p}^2+\Omega_\text{c}^2}\right). \tag{2.26}$$

When the probe can be considered to be weak such that $\Omega_\text{p} \ll \Gamma_2$ and the detuning $\Delta_\text{p} = \Delta_\text{c} = 0$, the dressed states are given by

$$\left|a^0\right\rangle = |1\rangle, \tag{2.27a}$$

$$\left|a^\pm\right\rangle = \frac{1}{\sqrt{2}}(|2\rangle \pm |3\rangle). \tag{2.27b}$$

These dressed states are illustrated in Fig. 2.3(b). The Autler-Townes splitting [77] of the dressed states is determined by the coupling Rabi frequency Ω_c. If the system is initially prepared in the ground state $|1\rangle$ then the dressed state $\left|a^0\right\rangle$ is a decoupled or "dark" state of the system. Consequently, excitation cannot occur out of the ground state and into the excited states. This is the origin of electromagnetically induced transparency that will be discussed in the next section.

2.3.1. Electromagnetically Induced Transparency

Electromagnetically induced transparency (EIT) [56] can be understood by analysing the equations of motion for the density operator. For a three-level ladder system, the phenomenological decay matrix $\hat{\mathcal{L}}$ is given by

$$\hat{\mathcal{L}} = \frac{1}{2}\begin{pmatrix} 2\Gamma_2\rho_{22} & -\Gamma_2\tilde{\rho}_{12} & -\Gamma_3\tilde{\rho}_{13} \\ -\Gamma_2\tilde{\rho}_{21} & 2\Gamma_3\rho_{33} - 2\Gamma_2\rho_{22} & -(\Gamma_2+\Gamma_3)\tilde{\rho}_{23} \\ -\Gamma_3\tilde{\rho}_{31} & -(\Gamma_2+\Gamma_3)\tilde{\rho}_{32} & -2\Gamma_3\rho_{33} \end{pmatrix}. \tag{2.28}$$

Substituting the three-level total Hamiltonian $\hat{\mathcal{H}}_{\text{tot}}$ in Eq. (2.23) and decay matrix $\hat{\mathcal{L}}$ in Eq. (2.28) into the Lindblad master equation in Eq. (2.11), produces the time evolution of the density matrix. The coherences between the levels are of particular interest and these are given by [55]

$$\dot{\tilde{\rho}}_{21} = \frac{i\Omega_{\text{p}}}{2}(\rho_{22}-\rho_{11}) - \frac{i\Omega_{\text{c}}}{2}\tilde{\rho}_{31} + \left(i\Delta_{\text{p}} - \frac{\Gamma_2}{2}\right)\tilde{\rho}_{21}, \tag{2.29a}$$

$$\dot{\tilde{\rho}}_{31} = \frac{i\Omega_{\text{p}}}{2}\tilde{\rho}_{32} - \frac{i\Omega_{\text{c}}}{2}\tilde{\rho}_{21} + \left(i(\Delta_{\text{p}}+\Delta_{\text{c}}) - \frac{\Gamma_3}{2}\right)\tilde{\rho}_{31}, \tag{2.29b}$$

$$\dot{\tilde{\rho}}_{32} = \frac{i\Omega_{\text{c}}}{2}(\rho_{33}-\rho_{22}) + \frac{i\Omega_{\text{p}}}{2}\tilde{\rho}_{31} + \left(i\Delta_{\text{c}} - \frac{\Gamma_2+\Gamma_3}{2}\right)\tilde{\rho}_{32}, \tag{2.29c}$$

where $\tilde{\rho}_{12} = \tilde{\rho}_{21}^*$, $\tilde{\rho}_{13} = \tilde{\rho}_{31}^*$ and $\tilde{\rho}_{23} = \tilde{\rho}_{32}^*$. In the limit of a weak probe where $\Omega_{\text{p}} \simeq 0$, intermediate state population $\rho_{22} \simeq 0$ and excited-state population $\rho_{33} \simeq 0$, the steady-state coherence $\tilde{\rho}_{21}$ between the ground and intermediate state can be expressed as [55]

$$\tilde{\rho}_{21} \simeq -\frac{\frac{i\Omega_{\text{p}}}{2}}{\frac{\Gamma_2}{2} - i\Delta_{\text{p}} + \frac{\frac{\Omega_{\text{c}}^2}{4}}{\frac{\Gamma_3}{2}-i(\Delta_{\text{p}}+\Delta_{\text{c}})}}. \tag{2.30}$$

Inserting this expression into the complex susceptibility in Eq. (2.15), the weak probe susceptibility as a function of laser detuning Δ is given by

$$\chi = \frac{i\mathcal{N}d_{21}^2}{\epsilon_0\hbar\left(\frac{\Gamma_2}{2} - i\Delta_{\text{p}} + \frac{\frac{\Omega_c^2}{4}}{\frac{\Gamma_3}{2}-i(\Delta_{\text{p}}+\Delta_{\text{c}})}\right)}. \tag{2.31}$$

The real χ_{R} and imaginary χ_{I} parts of the susceptibility are shown as a function of probe detuning Δ_{p} for coupling Rabi frequency $\Omega_{\text{c}}/\Gamma_2 = \{0, 0.5, 2\}$ in Fig. 2.4. When $\Omega_{\text{c}} = 0$, the imaginary part of the susceptibility χ_{I} results in a Lorentzian absorption lineshape with width Γ_2, as expected for a two-level system. However, when $\Omega_{\text{c}} = 0.5\Gamma_2$, an electromagnetically induced transparency peak appears when $\Delta_{\text{p}} = 0$. The cancellation of absorption on resonance occurs due to Fano interference; the transition probability for $|a^0\rangle \rightarrow |a^-\rangle$ has the same magnitude but opposite sign

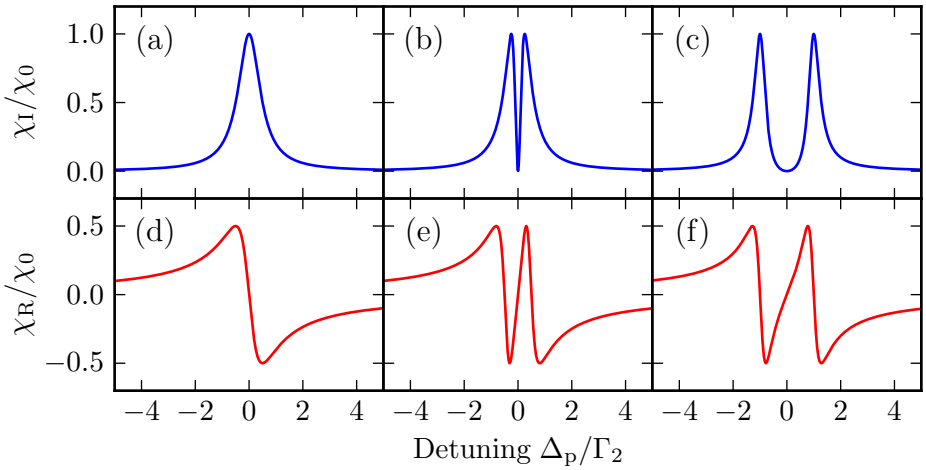

Figure 2.4.: The real χ_R and imaginary χ_I parts of the susceptibility χ are shown as a function of probe detuning Δ_p. The coupling Rabi frequency is varied from (a,d) Ω_c/Γ_2=0, (b,e) $\Omega_c/\Gamma_2 = 0.5$ and (c,f) $\Omega_c/\Gamma_2 = 2$. In all cases, the probe Rabi frequency $\Omega_p \ll \Gamma_2$, excited-state decay rate $\Gamma_3 \simeq 0$ and $\chi_0 = 2\mathcal{N}d_{21}^2/\epsilon_0\hbar\Gamma_2$.

as the $|a^0\rangle \rightarrow |a^+\rangle$ transition probability [54].

Fano interference between the transition pathways in an atomic system is a coherent process. This can be observed directly in the absorption spectrum as the linewidth of the EIT transparency is smaller than the linewidth of the absorption profile $\Gamma_{EIT} < \Gamma_2$. When $\Omega_c = 2\Gamma_2$, the absorption lineshape is a doublet formed due to Autler-Townes splitting (ATS) of the dressed states. The probe detuning of the two absorption peaks $\Delta_\pm$ originates from the dressed state energies given by Eq. (2.26). It is important to note that in the transition between EIT and ATS, the coherent Fano interference process ceases. Objectively discerning EIT and ATS has been the subject of recent interest [78].

As predicted by the Kramers-Kronig relations, the narrow EIT transparency in the imaginary part of the susceptibility χ_I is accompanied by a sharp change in the real part of the susceptibility χ_R. When $\Omega_c < \Gamma_2$, a steep positive gradient appears in the dispersion profile. This represents an extremely low group velocity v_g which is defined by

$$v_g = \frac{c}{n + \omega\frac{dn}{d\omega}}, \tag{2.32}$$

where ω is the frequency of the light propagating through the atomic ensemble and n is the refractive index. This results in the ability to observe "slow" light [79, 80] or "stopped" light which can be stored in the medium and recovered deterministically [81].

2.4. Multi-Level Atom-Light Interaction

2.4.1. Fine and Hyperfine Structure

The energy levels in Hydrogen, which has a single electron, are well described by the Bohr model in terms of the principal quantum number n where $E_n = -13.6/n^2$ eV [82]. For a given principal quantum number n, the angular momentum of the electron $\boldsymbol{L}$ with magnitude $|\boldsymbol{L}| = \sqrt{L(L+1)}\hbar$ is constrained to quantum numbers $L = 0, 1, ..., n-1$. The angular momentum quantum number is written in spectroscopic notation as $S, P, D, F, ...$ for $L = 0, 1, 2, 3, ...$ The stable isotope caesium-133 is an alkali metal with 55 electrons arranged in shells

$$1S^2\ 2S^2\ 2P^6\ 3S^2\ 3P^6\ 3D^{10}\ 4S^2\ 4P^6\ 4D^{10}\ 5S^2\ 5P^6\ 6S^1, \tag{2.33}$$

where the superscript refers to the number of electrons in the shell with given principal quantum number n and angular momentum quantum number L. The single valance electron is in the stable ground state $6S$.

Fine Structure

Fine structure results from the spin-orbit interaction between the electronic spin $\boldsymbol{S}$ and the magnetic field generated by its motion around the nucleus, described by orbital angular momentum $\boldsymbol{L}$. This effect is referred to as Russel-Saunders or LS-coupling [82]. In the fine structure basis, the total angular momentum

$$\boldsymbol{J} = \boldsymbol{L} + \boldsymbol{S}, \tag{2.34}$$

with magnitude $|\boldsymbol{J}| = \sqrt{J(J+1)}\hbar$. For a single valence electron, the total angular momentum quantum number J is constrained to values $J = |L-S|$ and $J = |L+S|$. In the fine structure basis, the atomic eigenstates can be fully described using the quantum numbers $|n, L, S, J, m_J\rangle$ where m_J is the z-component of the total angular momentum quantum number J.

Hyperfine Structure

Hyperfine structure results from the interaction between the nuclear spin $\boldsymbol{I}$ and the fields generated by the motion of the electron, described by the fine structure angular momentum $\boldsymbol{J}$ [82]. The total angular momentum in the hyperfine basis

$$\boldsymbol{F} = \boldsymbol{I} + \boldsymbol{J}, \tag{2.35}$$

where for a single valence electron, the total angular momentum quantum number $F = |J-I|, |J-I+1|, ..., J+I-1, J+I$. In the hyperfine structure basis, the

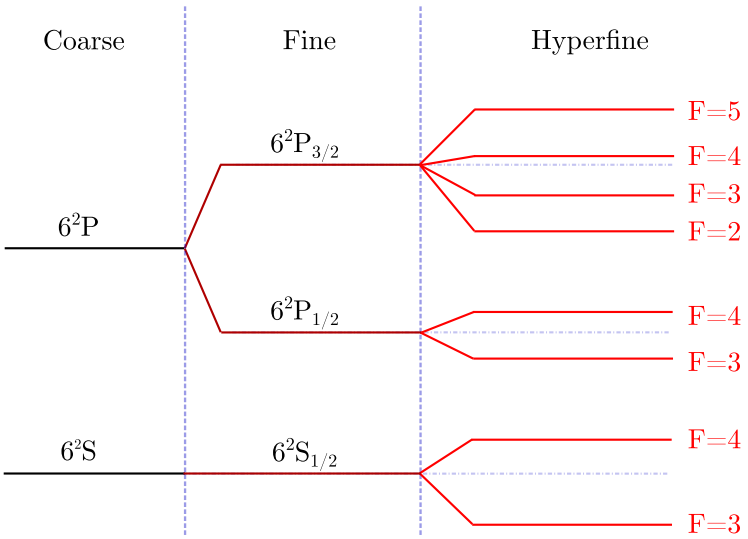

Figure 2.5.: Schematic showing the coarse, fine and hyperfine structure of the atomic energy levels in caesium for the single valence electron. The stable ground state is 6^2S and the first excited state is 6^2P.

eigenstates can be fully described by the basis $|n, L, S, J, I, F, m_F\rangle$, where m_F is the z-component of the total angular momentum quantum number F. The atomic energy level structure of caesium-133 with nuclear spin quantum number $I = 7/2$, is illustrated by the schematic in Fig. 2.5. The simple two-level picture of the ground state 6^2S and excited state 6^2P is significantly modified by the spin-orbit and spin-nucleon interaction. The subscript corresponds to the fine structure angular momentum quantum number J and the superscript corresponds to the spin quantum number $2S + 1$.

2.4.2. Optical Pumping

An optically-driven dipole transition between two states in either the coarse, fine or hyperfine basis, must obey a number of selection rules including $\Delta L = \pm 1$, $\Delta J = 0, \pm 1$ and $\Delta F = 0, \pm 1$ [82]. As a result of these angular momentum restrictions, closed transitions occur where the an atom can only decay back to the state from which it was excited. For example in caesium, as shown in Fig. 2.5, the $\left|6^2S_{1/2}, F = 4\right\rangle$ to $\left|6^2P_{3/2}, F' = 5\right\rangle$ transition is closed as atoms cannot decay from $F' = 5$ to $F = 3$.

The situation becomes even more complicated when the polarisation of the light and the magnetic sublevels are considered. Without perturbation, an ensemble of atoms are randomly distributed among the magnetic sublevels $m_F = -F, -F + 1, ..., F - 1, F$. When the propagation direction of the light and weak quantisation

magnetic field are parallel $\boldsymbol{k} \parallel \boldsymbol{B}$, circularly-polarised light drives $\sigma^{\pm}$ transitions where $\Delta m_F = \pm 1$. When the electric field of the light and weak quantisation magnetic field are parallel $\boldsymbol{E} \parallel \boldsymbol{B}$, linearly-polarised light drives π transitions where $\Delta m_F = 0$. It is important to note that the transition $\Delta F = 0$, $\Delta m_F = 0$ is not allowed according to the selection rules.

Optical pumping is a process through which the random population of the magnetic sublevels can be redistributed. For example, consider the closed transition between $\left|6^2\mathrm{S}_{1/2}, F = 4\right\rangle$ and $\left|6^2\mathrm{P}_{3/2}, F' = 5\right\rangle$. Initially, the atoms are randomly distributed in $2m_F + 1 = 9$ magnetic sublevels of the ground state. However, when light is applied which only drives σ^+ transitions, the population begins to accumulate in a single magnetic sublevel $|F = 4, m_F = 4\rangle$. This occurs because an atom which enters this state cannot leave, it can only circulate on the "stretched" transition $|F = 4, m_F = 4\rangle$ to $|F' = 5, m'_F = 5\rangle$. Alternatively, by applying light which drives π transitions between $\left|6^2\mathrm{S}_{1/2}, F = 4\right\rangle$ and $\left|6^2\mathrm{P}_{3/2}, F' = 4\right\rangle$, it is possible to optically pump all atoms into the lower hyperfine ground state $F = 3$.

2.4.3. Complex Susceptibility

Calculating the complex susceptibility χ of a multi-level atomic system follows the same analysis presented for a two-level atom in Section 2.2 and a three-level atom in Section 2.3. However, when the system is sufficiently complicated by laser couplings, decay pathways and atomic velocities, it is usually not efficient or possible to derive an analytical form of the susceptibility. Instead, the Lindblad master equation in Eq. (2.11) can be solved numerically using a programming language such as Matlab or Python. A numerical solution also allows for more complicated time-dependent excitation schemes such as modelling pulsed laser excitation to perform Stimulated Raman Adiabatic Passage [83]. A sample python script is provided in Appendix A to calculate the complex susceptibility in a four-level ladder system.

2.5. Transition Dipole Moment

The transition dipole moment between state $|1\rangle$ and $|2\rangle$ is given by [84]

$$d_{21} = e \langle 2 | \hat{\boldsymbol{\epsilon}} \cdot \boldsymbol{r} | 1 \rangle , \tag{2.36}$$

where $\boldsymbol{r}$ is the position vector and $\hat{\boldsymbol{\epsilon}}$ is the unit vector for the polarisation of the light. This interaction can be simplified by working in the spherical basis $\{r, \theta, \phi\}$ rather than the cartesian basis $\{x, y, z\}$. The position vector $\boldsymbol{r}$ is transformed according to

$$\boldsymbol{r} = \begin{pmatrix} x \\ y \\ z \end{pmatrix} \rightarrow \begin{pmatrix} r\sin\theta\cos\phi \\ r\sin\theta\sin\phi \\ r\cos\theta \end{pmatrix}, \tag{2.37}$$

and the unit vector $\hat{\boldsymbol{\epsilon}}$ is written according to the polarisation of the light [84]

$$\hat{\boldsymbol{u}}_{\pm} = \mp\frac{1}{\sqrt{2}}(\hat{\boldsymbol{x}} \pm i\hat{\boldsymbol{y}}), \tag{2.38a}$$

$$\hat{\boldsymbol{u}}_0 = \hat{\boldsymbol{z}}, \tag{2.38b}$$

where $\hat{\boldsymbol{u}}_{\pm}$ corresponds to circularly-polarised light and $\hat{\boldsymbol{u}}_0$ corresponds to linearly-polarised light. The dot product in the dipole moment $\hat{\boldsymbol{\epsilon}} \cdot \boldsymbol{r}$ can then be expanded as

$$r_q = \hat{\boldsymbol{u}}_q \cdot \boldsymbol{r} = r\sqrt{\frac{4\pi}{3}}\, Y_1^q(\theta,\phi), \tag{2.39}$$

where $Y_1^q(\theta,\phi)$ is a spherical harmonic function. The q term corresponds to the inverse of the polarisation such that $q = 0$ drives π transitions and $q = \pm 1$ drives $\sigma^{\mp}$ transitions. The important result in Eq. (2.39) is that the dipole moment d_{21} can be separated into radial and angular components.

2.5.1. Wigner-Eckart Theorem

The inclusion of fine structure or hyperfine structure significantly complicates the calculation of the dipole moment. Although the states are fully described in the J or F basis, the applied electric field only couples to the electronic orbital angular momentum L. As a result, the eigenfunctions of the fine or hyperfine basis must be reduced into the L basis. Consider a transition between initial state $|F, m_F\rangle$ and final state $|F', m'_F\rangle$ driven by a light field with polarisation q. The dipole moment, often referred to as the "matrix element" in analogy with off-diagonal coupling, is given by

$$d_{21} = \langle F, m_F | \, er_q \, | F', m'_F \rangle . \tag{2.40}$$

Using the Wigner-Eckart theorem [85] the matrix element can be separated into radial and angular components

$$\langle F, m_F | \, er_q \, | F', m'_F \rangle = \langle F || e\boldsymbol{r} || F' \rangle (-1)^{F'-1+m_F}\sqrt{2F+1} \begin{pmatrix} F' & 1 & F \\ m'_F & q & -m_F \end{pmatrix}, \tag{2.41}$$

where $\langle F||e\boldsymbol{r}||F'\rangle$ is the reduced matrix element and (:::) is a Wigner-3j symbol. The angular terms are often referred to as the Clebsch-Gordan coefficient [84]. The

radial term can be further reduced by transforming into the J basis

$$\langle F||e\boldsymbol{r}||F'\rangle = \langle J||e\boldsymbol{r}||J'\rangle(-1)^{F'+J+1+I}\sqrt{(2F'+1)(2J+1)}\begin{Bmatrix} J & J' & 1 \\ F' & F & I \end{Bmatrix}, \quad (2.42)$$

where $\{:::\}$ is a Wigner-6j symbol. Once again, the radial term can be reduced by transforming into the L basis

$$\langle J||e\boldsymbol{r}||J'\rangle = \langle L||e\boldsymbol{r}||L'\rangle(-1)^{J'+L+1+S}\sqrt{(2J'+1)(2L+1)}\begin{Bmatrix} L & L' & 1 \\ J' & J & S \end{Bmatrix}. \quad (2.43)$$

The reduced matrix element $\langle L||e\boldsymbol{r}||L'\rangle$ still contains angular terms which can be separated to give the fully decoupled expression

$$\langle L||e\boldsymbol{r}||L'\rangle = \langle R_{nl}|\, er\, |R_{n'l'}\rangle\,(-1)^{\frac{L'-L+1}{2}}\sqrt{\frac{L_{\max}}{2L+1}}, \quad (2.44)$$

where $L_{\max}$ is equal to L or L', depending on which is larger. Importantly, the radial wavefunction $R_{nl}(r)$ does not contain any angular factors. The radial matrix element $\langle R_{nl}|\, er\, |R_{n'l'}\rangle$ can be calculated from the radial overlap of the initial and final wavefunctions

$$\langle R_{nl}|\, er\, |R_{n'l'}\rangle = e\int R^*_{n'l'}r^3R_{nl}dr. \quad (2.45)$$

It is often useful to calculate the reduced matrix element between initial state J and final state J' using the Einstein-A coefficient using the expression [75]

$$A_{21} = \frac{\omega_0^3}{3\pi\epsilon_0\hbar c^3}\frac{2J+1}{2J'+1}|\langle J||e\boldsymbol{r}||J'\rangle|^2. \quad (2.46)$$

Furthermore, the transition strength can be expressed through the Rabi frequency

$$\Omega = \frac{d_{21}\mathcal{E}_0}{\hbar} = \frac{d_{21}}{\hbar}\sqrt{\frac{2I}{c\epsilon_0}}, \quad (2.47)$$

where $I = (1/2)c\epsilon_0\mathcal{E}_0^2$ is the light intensity. For a Gaussian beam, the intensity $I = 2P/(\pi w^2)$ where P is the beam power and w is the beam waist. The Rabi frequency can then be expressed as

$$\Omega = \frac{d_{21}}{\hbar}\sqrt{\frac{4P}{c\epsilon_0\pi w^2}}. \quad (2.48)$$

Reduced Matrix Element $\langle J\|\|e\boldsymbol{r}\|\|J'\rangle$	Value (ea_0)	Reduced Matrix Element $\langle J\|\|e\boldsymbol{r}\|\|J'\rangle$	Value (ea_0)
$\langle 6^2\mathrm{S}_{1/2}\|\|e\boldsymbol{r}\|\|6^2\mathrm{P}_{1/2}\rangle$	3.174	$\langle 6^2\mathrm{P}_{1/2}\|\|e\boldsymbol{r}\|\|7^2\mathrm{S}_{1/2}\rangle$	2.995
$\langle 6^2\mathrm{S}_{1/2}\|\|e\boldsymbol{r}\|\|6^2\mathrm{P}_{3/2}\rangle$	4.484	$\langle 6^2\mathrm{P}_{3/2}\|\|e\boldsymbol{r}\|\|7^2\mathrm{S}_{1/2}\rangle$	3.2365
$\langle 6^2\mathrm{S}_{1/2}\|\|e\boldsymbol{r}\|\|7^2\mathrm{P}_{1/2}\rangle$	0.195	$\langle 7^2\mathrm{S}_{1/2}\|\|e\boldsymbol{r}\|\|7^2\mathrm{P}_{1/2}\rangle$	7.289
$\langle 6^2\mathrm{S}_{1/2}\|\|e\boldsymbol{r}\|\|7^2\mathrm{P}_{3/2}\rangle$	0.414	$\langle 7^2\mathrm{S}_{1/2}\|\|e\boldsymbol{r}\|\|7^2\mathrm{P}_{3/2}\rangle$	10.126
$\langle 6^2\mathrm{S}_{1/2}\|\|e\boldsymbol{r}\|\|8^2\mathrm{P}_{1/2}\rangle$	0.057	$\langle 7^2\mathrm{S}_{1/2}\|\|e\boldsymbol{r}\|\|8^2\mathrm{P}_{1/2}\rangle$	0.647
$\langle 6^2\mathrm{S}_{1/2}\|\|e\boldsymbol{r}\|\|8^2\mathrm{P}_{3/2}\rangle$	0.154	$\langle 7^2\mathrm{S}_{1/2}\|\|e\boldsymbol{r}\|\|8^2\mathrm{P}_{3/2}\rangle$	1.147

Table 2.1.: The reduced matrix elements $\langle J||e\boldsymbol{r}||J'\rangle$ are given for various low-lying transitions in caesium. The values are derived from [86, 76].

2.5.2. Matrix elements for caesium

The reduced matrix elements $\langle J||e\boldsymbol{r}||J'\rangle$ are shown in Table 2.1 for various low-lying states in caesium. These values were derived from $(J||e\boldsymbol{r}||J')$ (an alternative system for the reduced matrix element) given in [86] and the following transformation [76] must be used

$$\langle J||e\boldsymbol{r}||J'\rangle = \frac{1}{\sqrt{J+1}}(J||e\boldsymbol{r}||J'). \tag{2.49}$$

The radial matrix elements $\langle 7^2\mathrm{S}_{1/2}|\, er\, |n^2\mathrm{P}_{3/2}\rangle$ are shown as a function of the effective principal quantum number $n^* = n - \delta_{nlj}$ in Fig. 2.6. The quantum defect parameter δ_{nlj} describes the deviation from the Hydrogen model and is discussed in Section 2.6.2. As the radial matrix element for $\langle 7S_{1/2}|\, er\, |nP_{1/2}\rangle$ is near degenerate, it is not shown. The dashed line indicates the scaling of the radial matrix element with principal quantum number $\propto n^{*-3/2}$. In this case, the constant of proportionality $C \simeq 10\ ea_0$. When the hyperfine structure is unresolvable, for example in a high-lying Rydberg state (discussed in Section 2.6), the dipole moment must instead be calculated in the J basis. This is because F is no longer a good quantum number to describe the energy levels.

2.6. Rydberg Atoms

2.6.1. Properties

Rydberg atoms are atoms with a valence electron excited to a high principal quantum number, $n > 10$ [34]. The physical significance of high n did not become clear until Bohr proposed his model of the hydrogen atom in 1913. In this model Bohr proposed an electron moving classically in a circular orbit around an ionic core. This simple model contains many of the interesting properties of Rydberg atoms. In a Rydberg

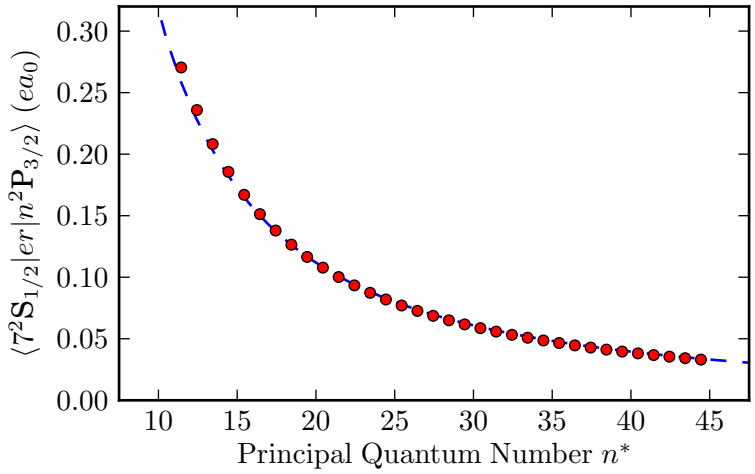

Figure 2.6.: The radial matrix elements $\langle 7^2\mathrm{S}_{1/2}|\, er\, |n^2\mathrm{P}_{3/2}\rangle$ are shown as a function of effective principal quantum number $n^* = n - \delta_{nlj}$. The data points are numerical calculations by J. Pritchard [87]. The dashed line indicates the scaling of the radial matrix element with principal quantum number $\langle 7^2S_{1/2}|er|26^2P_{3/2}\rangle = Cn^{*-3/2}$ where $C \simeq 10\ ea_0$. The radial matrix element for the transition to $nP_{1/2}$ is near degenerate and therefore not shown.

state, the valence electron has a binding energy which decreases as $1/n^2$, whilst the orbital radius increases as n^2. As the valence electron is in a large, loosely-bound orbit, Rydberg states have a wealth of fascinating properties. These properties include [34]

- *Sensitivity to external electric fields:* polarisability $\alpha \propto n^7$.
- *Long radiative lifetimes:* Einstein-A coefficient $A_{ij} \propto 1/n^3$.
- *Energy level spacing:* separation $\Delta E_{ij} \propto 1/n^3$.
- *Strong dipole-dipole interactions:* dipole moment $d \propto n^2$.

2.6.2. Binding Energies

For heavy alkali metals such as caesium, the core electrons interact with the Rydberg electron wavefunction and the effective principal quantum number $n^* = n - \delta_{nlj}$

State	δ_0	δ_2	δ_4
$n^2\mathrm{S}_{1/2}$	4.049	0.2377	0.2554
$n^2\mathrm{P}_{1/2}$	3.592	0.3609	0.4191
$n^2\mathrm{D}_{5/2}$	2.466	0.0136	-0.3746
$n^2\mathrm{F}_{5/2}$	0.03341	-0.1987	0.2895

Table 2.2.: Quantum defect parameters for calculating the effective principal quantum number in caesium [89].

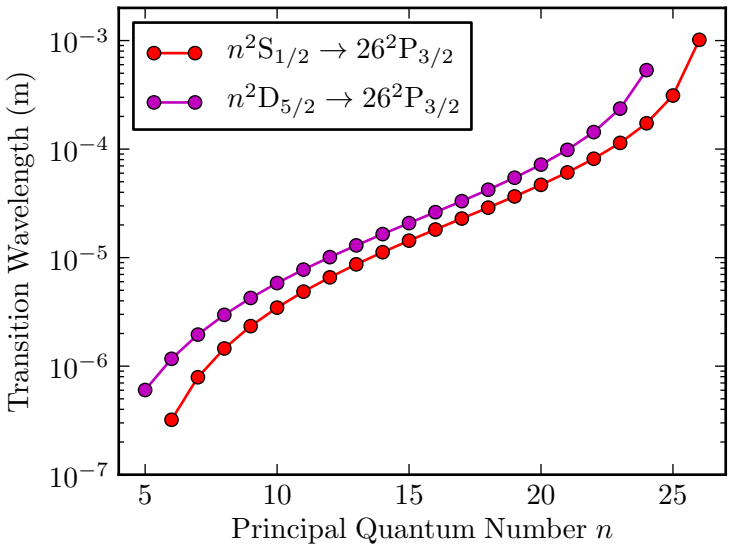

Figure 2.7.: Transition wavelengths for $n^2S_{1/2} \rightarrow 26^2P_{3/2}$ and $n^2D_{5/2} \rightarrow 26^2P_{3/2}$ calculated using measured energy levels for $n \leq 12$ [88] and quantum defect parameters for $n > 12$ [89].

must be used instead. The quantum defect can be calculated from the Rydberg-Ritz formula

$$\delta_{nlj} = \delta_0 + \frac{\delta_2}{(n-\delta_0)^2} + \frac{\delta_4}{(n-\delta_0)^4} + \frac{\delta_6}{(n-\delta_0)^6} + \ldots, \tag{2.50}$$

where the coefficients δ_i are derived from spectroscopic data from a large range of Rydberg states and shown in Table 2.2. The binding energies E_{nl} can then be expressed in analogy to the Hydrogen atom as

$$E_{nl} = -\frac{R_\infty}{(n-\delta_{n,l,j})^2}, \tag{2.51}$$

where $R_\infty = 1.097 \times 10^7$ m^{-1} is the Rydberg constant. In the case of caesium, the ground-state ionisation energy is 31406.46766 cm^{-1}. Finally, the vacuum transition wavelength between two states with energy E_{nl} and $E_{n'l'}$ is given by

$$\lambda = \frac{hc}{E_{n',l'} - E_{n,l}}, \tag{2.52}$$

where h is Planck's constant and c is the speed of light in vacuum. The transition wavelengths to the $26^2P_{3/2}$ Rydberg state are shown in Fig. 2.7. From the ground state $6^2S_{1/2}$, the transition wavelength $\lambda = 319$ nm whereas from the nearest Rydberg state $26^2S_{1/2}$, the transition wavelength is more than three orders of magnitude

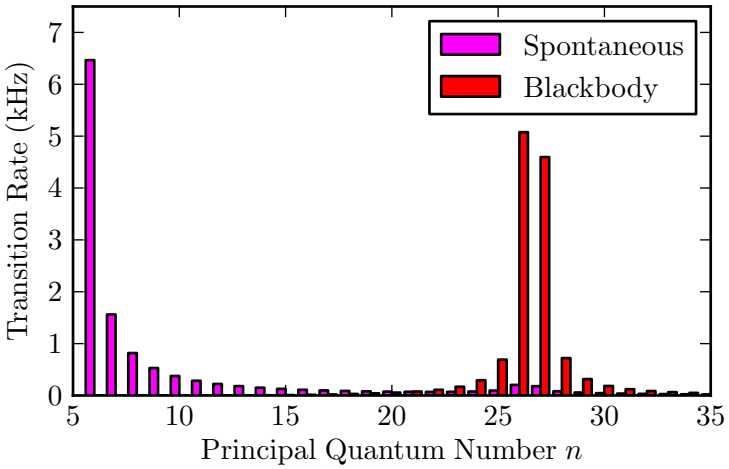

Figure 2.8.: Comparison of spontaneous (blue) and BBR-induced (red) transition rates for $26^2\mathrm{P}_{3/2} \rightarrow n^2\mathrm{S}_{1/2}$ at temperature $T = 350$ K.

larger $\lambda = 1$ mm.

2.6.3. Lifetime

The rate of spontaneous emission on a transition $|n, l\rangle \rightarrow |n', l'\rangle$ is given by the Einstein A-coefficient [90]

$$A_{n,l\rightarrow n',l'} = \frac{1}{4\pi\epsilon_0\hbar}\frac{4\omega_{nn'}^3}{3c^3}\frac{l_{\max}}{2l+1}|\langle n', l'|er|n, l\rangle|^2, \tag{2.53}$$

where $\omega_{nn'} = |E_{n,l} - E_{n',l'}|/\hbar$ is the transition frequency, $l_{\max}$ is the largest angular momentum from l and l'. The radial matrix element $\langle n', l'|er|n, l\rangle$ is discussed in Section 2.5. As there are multiple transitions from initial state $|n, l\rangle$, the radiative lifetime τ_0 of a Rydberg state is determined by the total rate of spontaneous transitions

$$\frac{1}{\tau_0} = \Gamma_0 = \sum_{E_{n,l}>E_{n',l'}} A_{n,l\rightarrow n',l'}. \tag{2.54}$$

The transition to lower-lying and higher-lying states can also be initiated by blackbody photons. The average number of photons per mode $\bar{n}_\omega$ at the transition frequency is determined by the temperature T of the blackbody using the Planck distribution

$$\bar{n}_\omega = \frac{1}{e^{\hbar\omega_{n,n'}/k_BT}}, \tag{2.55}$$

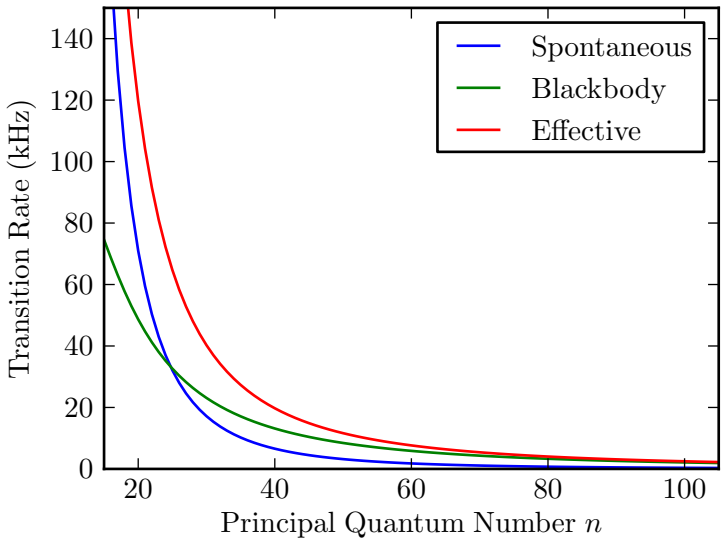

Figure 2.9.: Total spontaneous decay rate (blue), blackbody-induced decay rate (green) and effective decay rate (red) for Rydberg state $26^2P_{3/2}$ at temperature $T = 350$ K. When the principal quantum number $n > 24$, the blackbody-induced decay rate is dominant. The spontaneous decay rate is calculated using Eq. (2.59) and the blackbody-induced decay rate is calculated using Eq. (2.60).

where k_B is Boltzmann's constant. The rate of blackbody radiation (BBR) transitions can be written in terms of the Einstein A-coefficient as

$$W_{n,l\to n'l'} = \bar{n}_\omega A_{n,l\to n'l'}. \tag{2.56}$$

The total rate of BBR-induced transitions is given by

$$\Gamma_{\text{BBR}} = \sum W_{n,l\to n',l'}. \tag{2.57}$$

The effective lifetime of the Rydberg state is then given by both the spontaneous and BBR-induced transition rate

$$\frac{1}{\tau_{\text{eff}}} = \Gamma_0 + \Gamma_{\text{BBR}} = \frac{1}{\tau_0} + \frac{1}{\tau_{\text{BBR}}}. \tag{2.58}$$

A commonly used semi-empirical formula for calculating the spontaneous and BBR-induced transition rate is given by [90]

$$\tau_0 = \tau_s \bar{n}^\delta, \tag{2.59}$$

$$\Gamma_{\text{BBR}} = \frac{A}{\bar{n}^D} \frac{2.14\times 10^{10}}{\exp(\frac{315780B}{\bar{n}^C T}) - 1}, \tag{2.60}$$

State	τ_s (ns)	δ	A	B	C	D
$^2S_{1/2}$	1.2926	3.0005	0.123	0.231	2.517	4.375
$^2P_{1/2}$	2.9921	2.9892	0.041	0.072	1.693	3.607
$^2P_{3/2}$	3.2849	2.9875	0.038	0.056	1.552	3.505
$^2D_{3/2}$	0.6580	2.9944	0.038	0.076	1.790	3.656
$^2D_{5/2}$	0.6681	2.9941	0.036	0.073	1.770	3.636

Table 2.3.: Effective lifetime parameters for determining the spontaneous and BBR-induced emission rates. Adapted from Beterov et al. [90].

where $\bar{n}$ is the effective principal quantum number and the coefficients are given in Table 2.3. A comparison of the spontaneous and blackbody radiation induced transition rates from $26^2P_{3/2}$ are shown in Fig. 2.8. The dominant spontaneous emission transitions occur to the lowest-lying states. However, the dominant blackbody radiation transitions occur to nearby Rydberg states. As a result, blackbody radiation is a significant mechanism that reduces the lifetime of the Rydberg state. In the case of $n^2P_{3/2}$ Rydberg states, shown in Fig. 2.9, the BBR-induced transition rate is greater than the spontaneous emission rate for $n > 24$. For the $26^2P_{3/2}$ Rydberg state, the total spontaneous emission lifetime $\tau_0 \simeq 35$ μs, blackbody radiation induced lifetime $\tau_{\text{BBR}} \simeq 33$ μs and total effective lifetime $\tau_{\text{eff}} \simeq 17$ μs.

2.7. Thermal Vapours

There are numerous advantages of working with thermal vapours over cold atom experiments. These include, but are not limited to:

1. *Number density:* the number density can be tuned over several orders of magnitude using the atom temperature.
2. *Simplicity:* less technical components such as a vacuum chamber are required.
3. *Flexibility:* short setup times allow the experiment to be modified quickly.
4. *Cost:* inexpensive thermal vapour cells.

However, there are a number of disadvantages, some of which can be overcome in practice:

1. *Doppler effect:* the atoms are shifted out of resonance with an excitation laser according to their velocity.
2. *Collisions:* self broadening and collisional shift of resonance due to motional dipole-dipole interactions.

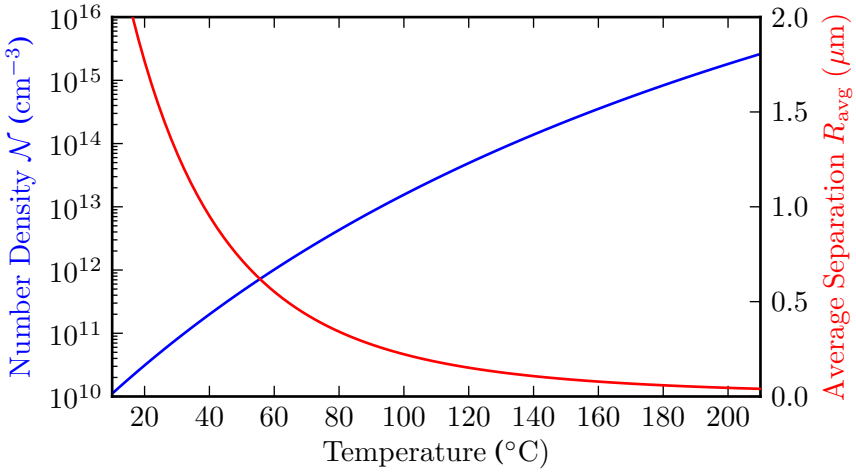

Figure 2.10.: Ground-state number density $\mathcal{N}$ and average inter-atomic separation R_{avg} as a function of temperature T.

2.7.1. Density

The vapour pressure of caesium in the liquid phase is given by [76]

$$\log_{10} P_{\mathrm{v}} = 2.881 + 4.165 - \frac{3830}{T}, \tag{2.61}$$

where P_{v} is the pressure in Torr and T is the temperature in Kelvin. The ground-state number density $\mathcal{N}$ is then given by

$$\mathcal{N} = \frac{133.323 P_{\mathrm{v}}}{k_{\mathrm{B}} T}, \tag{2.62}$$

where k_{B} is Boltzmann's constant and 133.323 converts the vapour pressure from Torr to Pascals. The average inter-atomic separation R_{avg} can be calculated from the number density by [91]

$$R_{\mathrm{avg}} \simeq \frac{5}{9} \mathcal{N}^{-1/3}. \tag{2.63}$$

The ground-state number density $\mathcal{N}$ and average inter-atomic separation R_{avg} are shown in Fig. 2.10 as a function of temperature T. By increasing the temperature of the atoms from room temperature to 200°C, it is possible to increase the number density by over five orders of magnitude.

2.7.2. Vapour Cell

Atomic spectroscopy of a thermal vapour can be achieved by confining the atoms in a glass vapour cell with a fixed optical path length between the windows. These

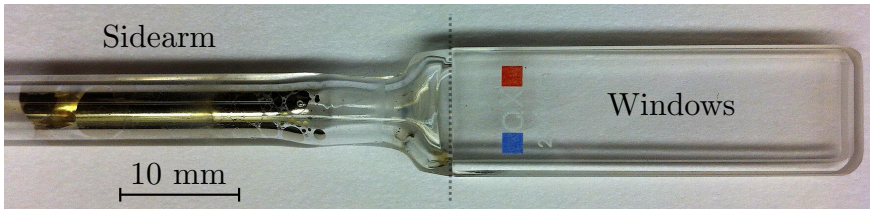

Figure 2.11.: Homemade thermal vapour cell. The borosilicate sidearm contains the reservoir of caesium and prevents condensation onto the quartz windows. The optical path length is 2 mm.

cells can be obtained commercially or manufactured in-house. Fig. 2.11 shows a thermal vapour cell that was manufactured at Durham University. The cell consists of two parts: (i) the sidearm containing the reservoir of caesium and (ii) the flat windows made of fused-silica quartz and separated by 2 mm. The sidearm is made from borosilicate glass.

A commercial thermal vapour cell from Triad is shown in Fig. 2.12. The entire cell is manufactured from quartz and the optical path length is 2 mm. This vapour cell is more expensive than those produced in house and there is often a significant lead time for production. A micro-fabricated thermal vapour cell obtained from National Institute of Standards and Technology (NIST) is shown in Fig. 2.13. This type of thermal vapour cell has applications in chip-scale atomic clocks [64] and atomic magnetometers [65]. The cell is manufactured from two 300 μm thick layers of borosilicate glass which are anodic bonded to a 2 mm thick silicon wafer. A hole etched into this wafer forms a cavity for the atoms. Inert neon and argon buffer gases are also present in the vapour cell due to the filling process [64].

The fabrication of vapour cells with micrometer [62] or nanometer [20, 92] path lengths is particularly difficult. As a result, these vapour cells are custom made by a small number of research groups. Furthermore, electrically-contacted vapour cells [63] have now been produced which allows Rydberg atoms to be detected using the ionisation current. This detection method has been shown to produce spectra with a higher signal-to-noise ratio than conventional optical techniques.

The temperature of the vapour cell can be controlled by placing it in a ceramic resistive heater. Using two separate heating regions, the temperature of the sidearm and windows of the cell can be adjusted independently. In order to prevent atoms condensing onto the windows, the sidearm region is always kept 10°C cooler than the window region.

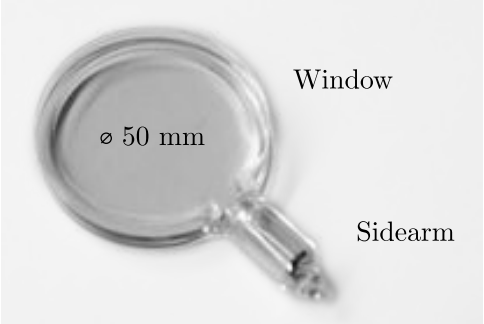

Figure 2.12.: Commercial thermal vapour cell from Triad. The quartz sidearm contains the reservoir of caesium and prevents condensation onto the quartz windows. The optical path length is 2 mm.

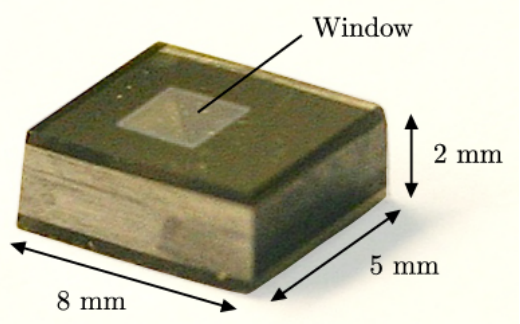

Figure 2.13.: Microfabricated thermal vapour cell from National Institute of Standards and Technology. As the cell does not contain a sidearm, caesium can condense on the windows. The optical path length is 2 mm.

2.8. Summary

In summary, this Chapter introduced a broad range of theoretical subjects which form the foundation of the thesis. The semi-classical description of the atom-light interaction was first presented for a two-level atom, before extension to a three-level and then a multi-level atom. Through the interaction with the applied light field, the atomic dynamics can evolve coherently (in the case of EIT or ATS) or incoherently (in the case of optical pumping). The strength of the light-induced coupling between two atomic states was introduced through the transition dipole moment. This was followed by a discussion of the properties of Rydberg atoms and a comparison between the radiative and blackbody-induced components of their lifetime. The chapter concluded with a discussion about thermal vapours and the various methods of confinement that exist.

3. Dipole-Dipole Interactions

3.1. Introduction

This Chapter considers the interaction between optically-induced atomic dipoles. The interaction originates from the electric field that is emitted by an oscillating dipole and can be described using the Liénard-Wiechert potential. The full potential is presented for a pair of dipoles in Section 3.2 and an approximation is derived when the dipoles have the same orientation.

The Liénard-Wiechert potential is first applied to a pair of interacting dipoles in Section 3.3. The pair-state picture is introduced and the distinction between the resonant and non-resonant dipole-dipole interaction is considered. In the case of the resonant dipole-dipole interaction, the energy and decay rate of the atomic state is modified when the pair separation is less than their transition wavelength. The non-resonant or induced van der Waals interaction is shown to occur at long range and displays resonant dipole-dipole behaviour when the pair separation is below a critical value.

The discussion is then extended to an interacting many-body ensemble of dipoles in Section 3.4. In this complex system, it is shown that the energy shift due to the dipole-dipole interaction can be sub-divided into a number of components and each of these contributions are considered in detail. Finally, the Chapter concludes with a discussion of superradiance, which arises due to inter-atomic correlations in a many-body ensemble.

3.2. Liénard-Wiechert Potential

A pair of oscillating dipoles with transition dipole moments $\boldsymbol{d}_1$ and $\boldsymbol{d}_2$ and separation $\boldsymbol{r}_{12}$ interact via the Coulomb potential and the exchange of transversely polarised photons [19]. The sum of these two components produces the Liénard-Wiechert potential $V_{\mathrm{dd}}(\boldsymbol{r}_{12})$ from classical electromagnetic field theory [93]

$$V_{\mathrm{dd}}(\boldsymbol{r}_{12}) = -\frac{1}{4\pi\epsilon_0}\Bigg[\frac{k^2}{\boldsymbol{r}_{12}}(\boldsymbol{d}_1\cdot\boldsymbol{d}_2 - \boldsymbol{d}_1\cdot\hat{\boldsymbol{r}}_{12}\boldsymbol{d}_2\cdot\hat{\boldsymbol{r}}_{12}) + \left(\frac{1}{\boldsymbol{r}_{12}^3} - \frac{ik}{\boldsymbol{r}_{12}^2}\right)(3\boldsymbol{d}_1\cdot\hat{\boldsymbol{r}}_{12}\boldsymbol{d}_2\cdot\hat{\boldsymbol{r}}_{12} - \boldsymbol{d}_1\cdot\boldsymbol{d}_2)\Bigg]e^{ik\boldsymbol{r}_{12}}, \quad (3.1)$$

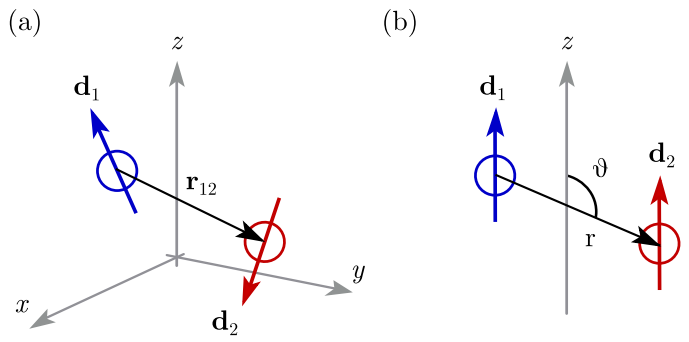

Figure 3.1.: Dipole-dipole interaction schematic for a pair of atoms with dipole moments $\boldsymbol{d}_1$ and $\boldsymbol{d}_2$. (a) The dipoles are randomly orientated and separated by distance $\boldsymbol{r}_{12}$. (b) The dipoles are aligned with the z-axis and their separation can be described by distance r and angle θ.

where the wavevector $k = 2\pi/\lambda$ and separation unit vector $\hat{\boldsymbol{r}}_{12} = \boldsymbol{r}_{12}/|\boldsymbol{r}_{12}|$. The phase factor $\exp(ikr_{12})$ results in a retarded potential due to the finite speed of light. This potential can also be derived using a second-quantised treatment of the dipole-dipole interaction [94], illustrating the overlap between classical and quantum interpretations.

The geometry of the dipole-dipole interaction $V_{\mathrm{dd}}(\boldsymbol{r}_{12})$ is shown schematically in Fig. 3.1(a). This interaction picture can be simplified by considering that the dipoles are orientated with the z-axis such that $\boldsymbol{d}_1 = d_1\hat{\boldsymbol{z}}$ and $\boldsymbol{d}_2 = d_2\hat{\boldsymbol{z}}$, as shown in Fig. 3.1(b). This situation arises in experiments where the dipoles are excited with linearly-polarised light. The interaction can now be described using the pair separation r and polar angle θ. As the potential is symmetric about the z-axis, the azimuthal angle ϕ is not required. The interaction potential V_{dd} is now given by

$$V_{\mathrm{dd}}(r,\theta) = -\frac{d_1 d_2 k^3}{4\pi\epsilon_0}\left[\frac{1}{kr}\sin^2\theta + \left(\frac{1}{(kr)^3} - \frac{i}{(kr)^2}\right)(3\cos^2\theta - 1)\right]e^{ikr}. \tag{3.2}$$

3.3. Pairwise Dipole-Dipole Interaction

3.3.1. Resonant Interaction

Consider a pair of identical two-level atoms A and B with dipole-coupled transitions between ground state $|1\rangle$ and excited state $|2\rangle$, as shown in Fig. 3.2(a). In this system, the resonant dipole-dipole interaction corresponds to the reaction processes given by

$$|1\rangle_{\mathrm{A}} + |2\rangle_{\mathrm{B}} \;\rightarrow\; |2\rangle_{\mathrm{A}} + |1\rangle_{\mathrm{B}}\,, \tag{3.3a}$$

$$|2\rangle_{\mathrm{A}} + |1\rangle_{\mathrm{B}} \;\rightarrow\; |1\rangle_{\mathrm{A}} + |2\rangle_{\mathrm{B}}\,. \tag{3.3b}$$

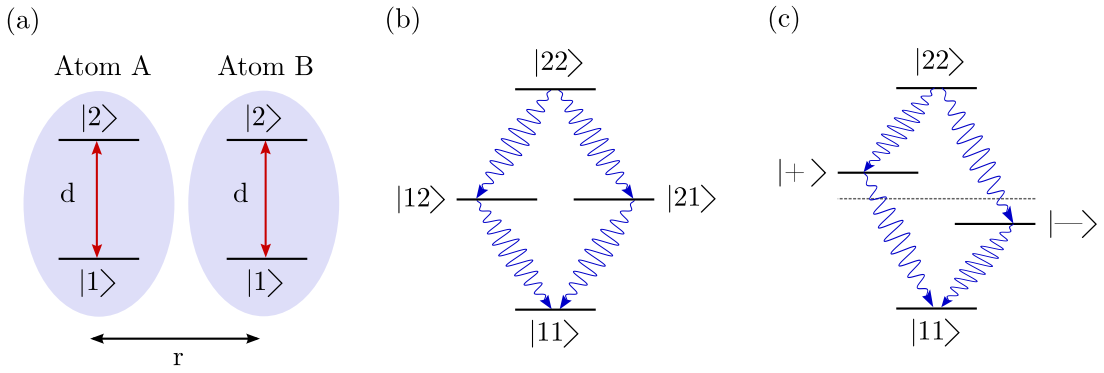

Figure 3.2.: (a) Bare-state picture for atom A and atom B interacting over separation r with dipole moment d_1 and d_2. (b) Pair-state picture for $r \to \infty$ where the singly-excited states $|12\rangle$ and $|21\rangle$ are degenerate. (c) Pair-state picture for finite separation where the Dicke superposition states $|\pm\rangle$ are non-degenerate due to the dipole-dipole interaction.

The processes are resonant because the initial and final pair state have the same energy. When the separation r between the atoms is large and the dipole-dipole interaction is negligible, the system can be written in the pair-state basis, as shown in Fig. 3.2(b). If the system is initially prepared in the doubly-excited state $|22\rangle$, the spontaneous emission of a single photon projects the system into the singly-excited state $|12\rangle$ or $|21\rangle$. After a second single photon is emitted, the system decays to the ground state $|11\rangle$.

When the separation between the atoms is less than the transition wavelength $kr \ll 1$, this description is no longer valid. Following decay from the doubly-excited state $|22\rangle$, it is not possible to determine whether the system enters state $|12\rangle$ or $|21\rangle$. Instead the system enters a superposition or Dicke state [13] given by

$$|\pm\rangle = \frac{1}{\sqrt{2}}(|21\rangle \pm |12\rangle), \tag{3.4}$$

and represented by the pair-state picture in Fig. 3.2(c). The Dicke picture is equally valid when the system starts in the ground state $|11\rangle$ and a single excitation is created.

The effect of the dipole-dipole interaction $V_{\mathrm{dd}}(r, \theta)$ between atoms in the Dicke state is to modify both their energy and decay rate [95]. Given an unperturbed energy E_0 and decay rate Γ of the bare states, the dipole-dipole interaction leads to

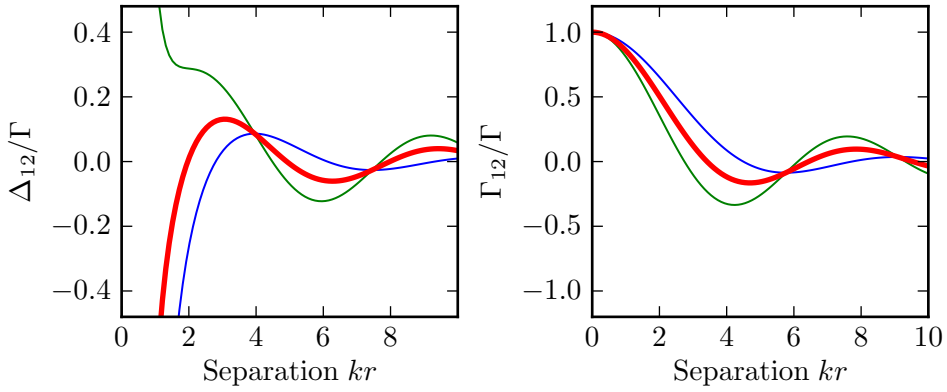

Figure 3.3.: The real and imaginary part of the dipole-dipole interaction $V_{\mathrm{dd}}(r,\theta)$ result in an energy shift Δ_{12} and broadening Γ_{12} of the Dicke states $|\pm\rangle$. The green and blue curves correspond to dipole orientation angles $\theta = 0$ and $\theta = \pi/2$ respectively. The thick red curve corresponds to an angular average over all possible dipole orientations.

the following modification

$$E_{\pm} = E_0 \pm \Delta_{12}, \tag{3.5}$$

$$\Gamma_{\pm} = \Gamma \pm \Gamma_{12}, \tag{3.6}$$

where the energy shift $\Delta_{12} = \mathrm{Re}(V_{\mathrm{dd}}(r,\theta))$ and additional broadening $\Gamma_{12} = -2\mathrm{Im}(V_{\mathrm{dd}}(r,\theta))$. The energy shift Δ_{12} and decay rate Γ_{12} are shown as a function of dipole separation kr in Fig. 3.3. Both quantities are normalised to the unperturbed decay rate $\Gamma = d^2k^3/(3\pi\epsilon_0)$. The green and blue curves show the radial dependence for orientation angle $\theta = 0$ and $\theta = \pi/2$ respectively. The red curve shows the radial dependence averaged over all orientation angles $0 \leq \theta \leq \pi$. When $kr \ll 1$, the energy shift diverges to lower frequencies and the decay rate is enhanced $\Gamma_+ \to 2\Gamma$. For this reason, the Dicke state $|+\rangle$ is referred to as a superradiant state. Similarly, the Dicke state $|-\rangle$ is referred to as a subradiant state as the decay rate $\Gamma_- \to 0$.

3.3.2. Non-Resonant Interaction

The van der Waals (vdW) interaction, or more specifically the London dispersion interaction [96], occurs between non-polar atoms without transition or permanent dipole moments. When the pair separation is small, the electron density distribution of each atom is distorted and an instantaneous dipole results. In the induced vdW interaction, the energy difference between the initial $|\phi_{\mathrm{i}}\rangle$ and final $|\phi_{\mathrm{f}}\rangle$ pair state is

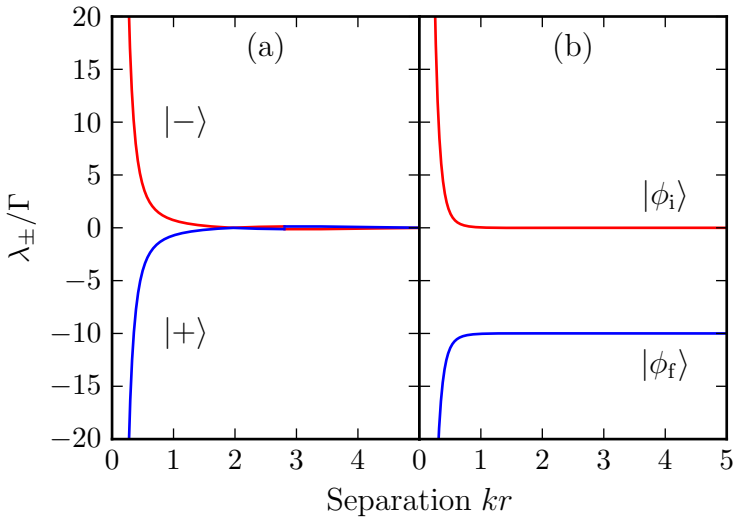

Figure 3.4.: The eigenvalues $\lambda_\pm$ are shown as a function of pair separation kr for energy defect (a) $\Delta = 0$ and (b) $\Delta = -10\Gamma$. In the resonant case, it is not possible to distinguish between the initial $|\phi_\mathrm{i}\rangle$ and final $|\phi_\mathrm{f}\rangle$ pair states, so the Dicke states $|\pm\rangle = 1/\sqrt{2}(|\phi_\mathrm{i}\rangle \pm |\phi_\mathrm{f}\rangle)$ must be used instead. The dipole-dipole interaction $V_\mathrm{dd}(r,\theta)$ has been averaged over all angular orientations.

non-zero and the energy defect Δ is given by

$$\Delta = E_\mathrm{f} - E_\mathrm{i}. \tag{3.7}$$

In the pair state picture, the atomic Hamiltonian is given by

$$\hat{\mathcal{H}}_\mathrm{atom} = \hbar \begin{pmatrix} 0 & 0 \\ 0 & \Delta \end{pmatrix}, \tag{3.8}$$

with the basis pair states $|\phi_\mathrm{i}\rangle = (1,0)^T$ and $|\phi_\mathrm{f}\rangle = (0,1)^T$. Furthermore, the pair states are coupled by the dipole-dipole interaction $V_\mathrm{dd}(r,\theta)$ through the interaction Hamiltonian

$$\hat{\mathcal{H}}_\mathrm{int} = \hbar \begin{pmatrix} 0 & V_\mathrm{dd}(r,\theta) \\ V_\mathrm{dd}(r,\theta) & 0 \end{pmatrix}. \tag{3.9}$$

The total Hamiltonian describing the two-atom system $\hat{\mathcal{H}}_\mathrm{tot} = \hat{\mathcal{H}}_\mathrm{atom} + \hat{\mathcal{H}}_\mathrm{int}$ can now be diagonalised to yield the eigenvalues $\lambda_\pm$ of the pair states

$$\lambda_\pm = \frac{\Delta}{2} \pm \frac{1}{2}\sqrt{\Delta^2 + 4V_\mathrm{dd}^2(r,\theta)}. \tag{3.10}$$

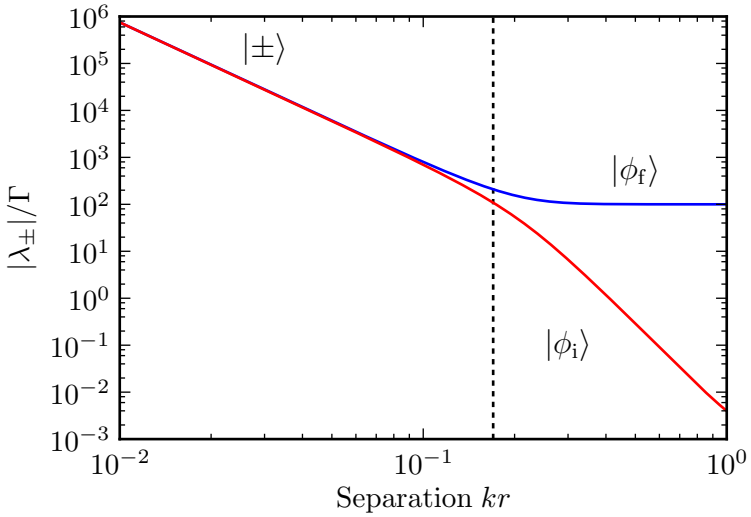

Figure 3.5.: The eigenvalues $\lambda_\pm$ are shown as a function of pair separation kr for the non-resonant dipole-dipole interaction $\Delta = -100\Gamma$. At long range, the interaction scales as van der Waals $1/r^6$, whilst at short range, the interaction scales as resonant dipole-dipole $1/r^3$. The van der Waals radius $kr_\mathrm{vdW} \simeq 0.17$ is indicated by the vertical dashed line. The dipole-dipole interaction $V_\mathrm{dd}(r,\theta)$ has been averaged over all angular orientations.

As a result of the off-diagonal coupling provided by the dipole-dipole interaction, the eigenenergies of the pair states are now dependent upon the separation and angular orientation of the two dipoles. The eigenvalues are shown in Fig. 3.4 as a function of pair separation kr for energy defect (a) $\Delta = 0$ and (b) $\Delta = -10\Gamma$. In both cases, the dipole-dipole potential $V_\mathrm{dd}(r,\theta)$ has been averaged over the angular orientation of the dipoles. When the interaction is weak $V_\mathrm{dd}(r,\theta) \ll \Delta$, the eigenvalues can be associated with the initial pair state $|\phi_\mathrm{i}\rangle$ and final pair state $|\phi_\mathrm{f}\rangle$. However, when the interaction is strong $V_\mathrm{dd}(r,\theta) \gg \Delta$, the eigenvalues cannot be associated with the initial and final pair states and must be described by the Dicke states $|\pm\rangle$.

Consequently, it is possible to identify two regimes in the non-resonant dipole-dipole interaction. When the energy defect dominates over the interaction $\Delta \gg V_\mathrm{dd}(r,\theta)$, the eigenvalues of the system are given by

$$\lambda_+ = \Delta + \frac{V_\mathrm{dd}(r,\theta)^2}{\Delta}, \tag{3.11}$$

$$\lambda_- = -\frac{V_\mathrm{dd}(r,\theta)^2}{\Delta}. \tag{3.12}$$

This is the long range van der Waals regime where the interaction energy scales as $1/r^6$. Conversely, when the interaction energy dominates over the energy defect

$\Delta \ll V_{\mathrm{dd}}(r,\theta)$, the eigenvalues are given by

$$\lambda_{\pm} = \pm V_{\mathrm{dd}}(r,\theta). \tag{3.13}$$

This is the resonant dipole-dipole regime where the interaction energy scales as $1/r^3$. The transition between these two regimes occurs at the van der Waals radius R_{vdW} where the energy defect is equivalent to the interaction energy $\Delta = V_{\mathrm{dd}}(r,\theta)$. This behaviour is illustrated in Fig. 3.5 as a function of pair separation kr for energy defect $\Delta = -100\Gamma$. The interaction potential $V_{\mathrm{dd}}(r,\theta)$ has been averaged over all possible angular orientations. In this case, the transition between the short-range and long-range behaviour occurs at the van der Waals radius $kr_{\mathrm{vdW}} \approx 0.17$.

3.4. Many-Body Dipole-Dipole Interaction

In an experimental situation, the ability to isolate two individual dipoles and observe their interaction represents a significant technical challenge [37]. An alternative approach is to work with a macroscopic ensemble of interacting dipoles, for example, an alkali metal vapour at room temperature. As the number of interacting dipoles in such an ensemble can exceed one billion, the pair analysis from the previous section must be carefully applied to this many-body system.

There are four dipole-dipole interaction contributions to the energy shift that must be combined in an extended sample:

- *Coulomb Shift:* arises from the average instantaneous interaction between the dipoles.
- *Cooperative Lamb Shift:* arises from the exchange of virtual photons between the dipoles.
- *van der Waals Shift:* arises from the exchange of real photons between the dipoles.
- *Collisional Shift:* arises from two-body scattering in the Coulomb potential.

In an ensemble with fixed or "frozen" dipole positions, the collisional shift does not occur. Furthermore, when the energy defect Δ for the non-resonant interaction is large, the van der Waals interaction can be neglected. Both the Coulomb and Cooperative Lamb shift are described by the real part of the Liénard-Wiechert potential introduced in Section 3.2. In a many-body ensemble, these shifts can be calculated by averaging over the pairwise interactions.

The dipole-dipole interaction also leads to a modification of the decay rate in a many-body system:

- *Cooperative Decay Rate* - arises from the exchange of virtual photons between the dipoles.

3.4.1. Coulomb Shift

Within a dense medium, the applied electric field $\boldsymbol{\mathcal{E}}$ is different to the local electric field $\boldsymbol{\mathcal{E}}_{\text{loc}}$ that each atom experiences. This problem was solved by Lorentz [97] by considering a spherical cavity around a typical dipole in the medium. The radius of the sphere is taken to be sufficiently large that the dipoles which lie outside the sphere can be treated as a continuous medium. The interaction with dipoles within the spherical cavity must still be calculated microscopically. The local electric field acting on the considered dipole is therefore given by a sum of components

$$\boldsymbol{\mathcal{E}}_{\text{loc}} = \boldsymbol{\mathcal{E}} + \boldsymbol{\mathcal{E}}_{\text{p}} + \boldsymbol{\mathcal{E}}_{\text{near}}, \tag{3.14}$$

where $\boldsymbol{\mathcal{E}}_{\text{p}}$ is the electric field due to dipoles outside the cavity and $\boldsymbol{\mathcal{E}}_{\text{near}}$ is the electric field due to dipoles within the cavity. As the configuration of nearby atoms in a gas can be assumed to be random, the $\boldsymbol{\mathcal{E}}_{\text{near}}$ contribution can be neglected [98]. The average electric field at the centre of a spherical cavity $\boldsymbol{\mathcal{E}}_{\text{p}}$ due to a surface charge polarisation $\boldsymbol{\mathcal{P}}$ is given by [93]

$$\boldsymbol{\mathcal{E}}_{\text{p}} = \frac{1}{3\epsilon_0}\boldsymbol{\mathcal{P}}. \tag{3.15}$$

Therefore the total local electric field can be expressed as

$$\boldsymbol{\mathcal{E}}_{\text{loc}} = \boldsymbol{\mathcal{E}} + \frac{1}{3\epsilon_0}\boldsymbol{\mathcal{P}}. \tag{3.16}$$

The polarisation response to the local field can be expressed in terms of the microscopic dipole moment $\boldsymbol{p}$ and the atomic number density $\mathcal{N}$ as

$$\boldsymbol{\mathcal{P}} = 4\pi\epsilon_0\mathcal{N}\boldsymbol{p}, \tag{3.17}$$

where the dipole moment $\boldsymbol{p} = \alpha\boldsymbol{\mathcal{E}}_{\text{loc}}$ and α is the atomic polarisability. Combining Eq. (3.16) and Eq. (3.17) with the bulk polarisation response $\boldsymbol{\mathcal{P}} = \epsilon_0\chi_e\boldsymbol{\mathcal{E}}$ and rearranging for the electric susceptibility results in the following expression

$$\chi_e = \frac{4\pi\mathcal{N}\alpha}{1 - \frac{4}{3}\pi\mathcal{N}\alpha}. \tag{3.18}$$

This is the Lorentz-Lorenz law [97] which relates the macroscopic susceptibility χ_e of a dense medium to the microscopic polarisability α of an atom. The polarisability

is related to the susceptibility of an atom in a dilute gas through the expression

$$\alpha = \frac{\chi_{\text{atom}}}{4\pi\mathcal{N}} = -\frac{1}{4\pi\epsilon_0\hbar}\,\frac{d^2}{\Delta + \frac{i\Gamma}{2}}, \tag{3.19}$$

where χ_{atom} is given by the weak probe susceptibility in Eq. (2.16). Substituting Eq. (3.19) into Eq. (3.18) results in the susceptibility for an atom in a dense medium

$$\chi_e = -\frac{\mathcal{N}d^2}{\epsilon_0\hbar}\,\frac{1}{\Delta + \frac{\mathcal{N}d^2}{3\epsilon_0\hbar} + i\frac{\Gamma}{2}}. \tag{3.20}$$

This is equivalent to the expression in Eq. (2.16) except that the dense medium has introduced a Lorentz-Lorenz frequency shift given by

$$\Delta_{\text{LL}} = -\frac{\mathcal{N}d^2}{3\epsilon_0\hbar}. \tag{3.21}$$

3.4.2. Cooperative Lamb Shift

The Lorentz-Lorenz shift discussed in the previous section arises due to the instantaneous Coulomb interaction between dipoles in a dense medium. As discussed in Section 3.2, the exchange of transversely-polarised photons also contributes to the dipole-dipole interaction. This exchange process results in a cooperative frequency shift that will be presented in this section.

The dipole-dipole interaction between a pair of dipoles $V_{\text{dd}}(r,\theta)$ given by Eq. (3.2) can be extended to a many-body system by summing over all possible pairs. When the number of dipoles is large $\mathcal{N}\lambda^3 \gg 1$, it is possible to use a continuum approximation and replace the sum over pairs of dipoles with an integral over the geometry of the sample [99]. As a result, the exact geometry of the sample determines both the magnitude and sign of the resultant energy shift.

Slab Geometry

In the slab geometry, the ensemble is confined along the axis of beam propagation and is unconfined in the transverse axes. For a beam of diameter d and wavelength λ propagating through a medium of length L, the slab geometry is satisfied when $\lambda L/d^2 \ll 1$. Due to the weak transverse confinement, the problem can be reduced to just one dimension.

The Lénard-Wiechert interaction potential in one dimension with pair separation $z = z_1 - z_2$ is given by

$$V_{\text{dd}}(z,\theta) = -\frac{3\Gamma}{8}\left[\frac{1}{k\bar{z}} + \frac{1}{(k\bar{z})^3} - \frac{i}{(k\bar{z})^2}\right] e^{ik\bar{z}}, \tag{3.22}$$

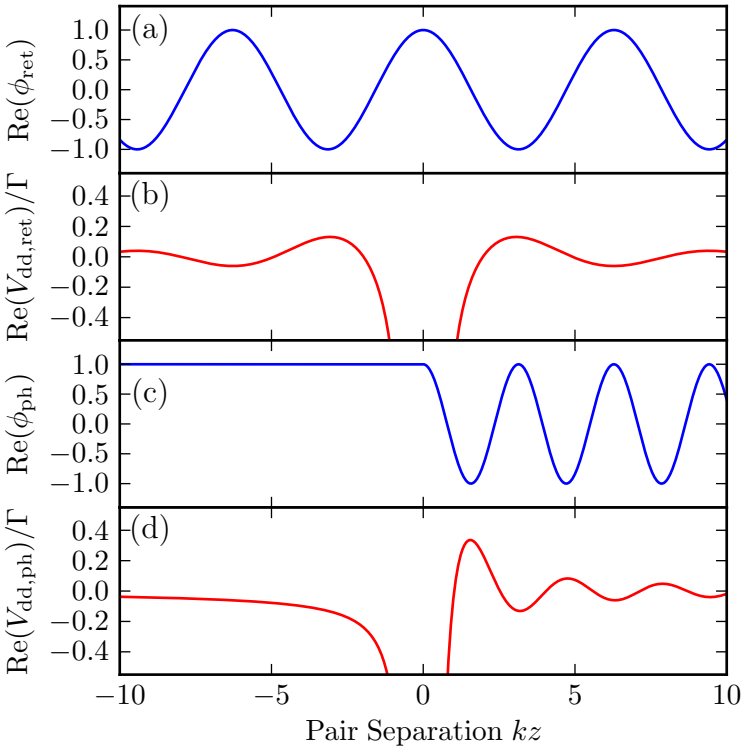

Figure 3.6.: Propagation effects in the cooperative Lamb shift. (a) The real part of the complex phase for retarded dipoles $\phi_{\rm ret} = \exp(ik\bar{z})$ and (b) the resulting real part of the dipole-dipole potential $V_{\rm dd,ret}$. (c) The real part of the complex phase for phased dipoles $\phi_{\rm ph} = \exp(ik(\bar{z}+z))$ and (d) the resulting real part of the dipole-dipole potential $V_{\rm dd,ph}$.

where $\bar{z} = |z| = |z_1 - z_2|$ and an average over angular orientation θ has been performed. The complex phase $\phi_{\rm ret} \equiv \exp(ik\bar{z})$ accounts for retardation due to the finite propagation speed between the dipoles. The real part of the complex phase $\mathrm{Re}(\phi_{\rm ret})$ and the resulting real part of the dipole-dipole interaction $V_{\rm dd,ret}$ are shown in Fig. 3.6(a) and (b) respectively. As a result of the variation in phase, the sign of the dipole-dipole interaction oscillates with pair separation.

In the preceding analysis, the initial phase of the dipoles was assumed to be homogenous throughout the medium. This is not the case for optically-induced dipoles and a second complex phase term must be included to account for this effect

$$V_{\rm dd}(z,\theta) = -\frac{3\Gamma}{8}\left[\frac{1}{k\bar{z}} + \frac{1}{(k\bar{z})^3} - \frac{i}{(k\bar{z})^2}\right] e^{ik(\bar{z}+z)}, \tag{3.23}$$

where the complex phase $\phi_{\rm ph} \equiv \exp(ik(\bar{z}+z))$ is due to the phasing and retardation of the dipoles. The real part of the complex phase $\mathrm{Re}(\phi_{\rm ph})$ and the resulting real part

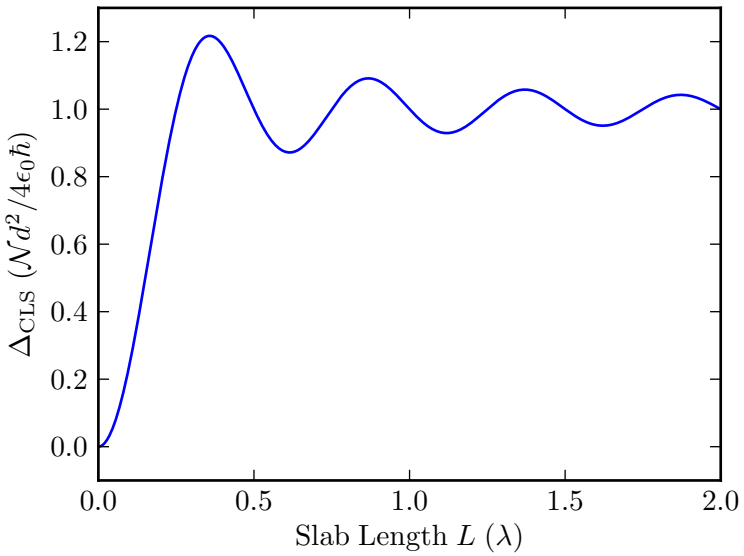

Figure 3.7.: The cooperative Lamb shift Δ_{CLS} is shown as a function of slab length L. When $L \gg \lambda$, the shift tends to a steady state value of $-3/4\Delta_{\mathrm{LL}}$.

of the dipole-dipole interaction $V_{\mathrm{dd,ph}}$ are shown in Fig. 3.6(c) and (d) respectively. In the backward direction $kz < 0$, the phase does not oscillate whilst in the forward direction $kz > 0$, the phase now oscillates at twice the frequency.

In a medium with length L, the cooperative shift due to the dipole-dipole interaction can be obtained by integrating Eq. (3.23) over the positions $0 \leq z_1 \leq L$ and $0 \leq z_2 \leq$L of the dipoles. The resulting shift, referred to as the cooperative Lamb shift due to the dependence on twice the propagation phase, is given by [19]

$$\Delta_{\mathrm{CLS}} = \frac{\mathcal{N}d^2}{4\epsilon_0\hbar}\left(1 - \frac{\sin 2kL}{2kL}\right). \tag{3.24}$$

The cooperative Lamb shift Δ_{CLS} is shown as a function of slab length L in Fig. 3.7. When the slab length $kL \gg 1$, the cooperative Lamb shift reaches a steady state value

$$\Delta_{\mathrm{CLS}} \to \frac{\mathcal{N}d^2}{4\epsilon_0\hbar} = -\frac{3}{4}\Delta_{\mathrm{LL}}. \tag{3.25}$$

As previously confirmed in an atomic vapour layer of nanometer thickness [20], the Lorentz-Lorenz shift Δ_{LL} can only be measured when the cooperative Lamb shift $\Delta_{\mathrm{CLS}} = 0$, i.e. when the slab length $L \to 0$. It is also important to note that the Lorentz-Lorenz shift is to lower frequencies (red shift) whilst the cooperative Lamb shift in a slab is to higher frequencies (blue shift).

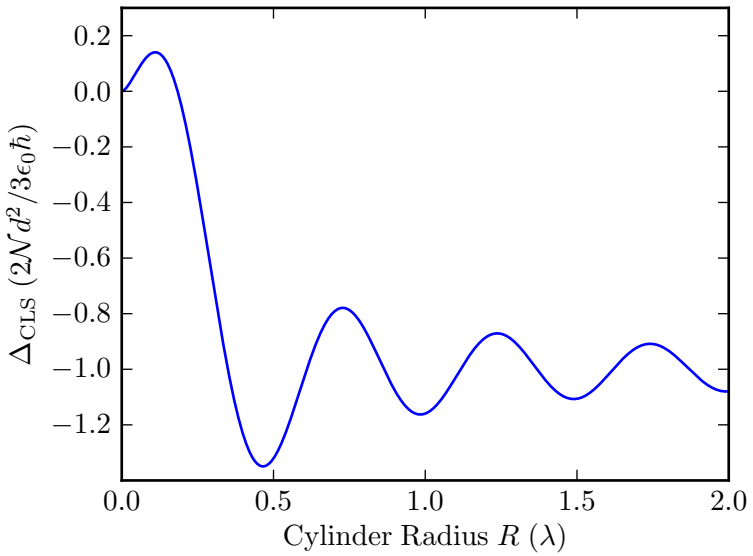

Figure 3.8.: The cooperative Lamb shift Δ_{CLS} is shown as a function of cylinder radius R. When $R \gg \lambda$, the shift tends to a steady state value of $2\Delta_{\mathrm{LL}}$. Notably, the shift changes to lower frequencies (red shift) when $R \gtrsim 0.18\lambda$.

Cylinder Geometry

In an experiment with an extended sample in the beam propagation direction $L \gg \lambda$, the slab geometry is no longer valid. Instead, when the beam diameter d is comparable to the wavelength λ, the sample can be considered as an infinite cylinder [100]. The cooperative Lamb shift is then given by [101]

$$\Delta_{\mathrm{CLS}} = -\frac{2\mathcal{N}d^2}{3\epsilon_0\hbar}\left(\pi J_1(kR)Y_1(kR) + 1\right), \tag{3.26}$$

where R is the cylinder radius, J_1 is the first-order Bessel function and Y_1 is the first-order Weber function. The cooperative Lamb shift Δ_{CLS} is shown as a function of cylinder radius R in Fig. 3.8. Notably, when the cylinder radius $R \gtrsim 0.183\lambda$, the cooperative Lamb shift changes sign. When the cylinder radius $R \gg \lambda$, the shift reaches a steady state value

$$\Delta_{\mathrm{LL}} \to -\frac{2\mathcal{N}d^2}{3\epsilon_0\hbar} = 2\Delta_{\mathrm{LL}}. \tag{3.27}$$

3.4.3. Collisional Broadening

The thermal motion of atoms in a vapour also contributes to the dipole-dipole interaction. In the impact approximation, collisions are only considered when the

interatomic separation is less than the Weisskopf radius [102]. Furthermore, the binary approximation assumes that the collisional process only involves two atoms. Under these approximations, the Weisskopf radius can be expressed as [103]

$$r_w = \sqrt{\frac{\beta}{2\pi\bar{v}}}, \tag{3.28}$$

where β is the self-broadening coefficient and $\bar{v} = \sqrt{16k_{\mathrm{B}}T/\pi m}$ is the mean relative velocity for the collision. The self-broadening coefficient is given by [103]

$$\beta = \frac{d^2}{3\hbar\epsilon_0}\frac{\sqrt{2J+1}}{\sqrt{2J'+1}}, \tag{3.29}$$

where d is the transition dipole moment from an initial state with total angular momentum J to a final state with total angular momentum J'. For the caesium D2 line, the measured self-broadening coefficient $\beta/2\pi = (1.15 \pm 0.12) \times 10^{-7}$ Hz cm^{-3} [104]. The collisional or self-broadening of the resonance is then given by $\Gamma_{\mathrm{col}} = \beta\mathcal{N}$. Furthermore, the collisional shift is given by $\Delta_{\mathrm{col}} = \alpha\mathcal{N}$ where the measured coefficient for the caesium D2 line $\alpha/2\pi = (-0.9 \pm 0.5) \times 10^{-8}$ Hz cm^{-3} [105].

3.4.4. Cooperative Decay Rate

The Dicke model can be generalised to an N-atom system by considering each atom as a spin-1/2 particle [106]. The excited state is represented by spin up $m_s = +1/2$ and the ground state by spin down $m_s = -1/2$. The total angular momentum $J = \sum s^{(i)}$ and the projection $M = \sum m_s^{(i)}$ now fully characterise the many-body state of the system. For an N-atom system, there are $(N+1)$ Dicke states which can be arranged in an excitation ladder

$$\begin{aligned}
|J, M = J\rangle &= |\uparrow\uparrow\uparrow\cdots\uparrow\uparrow\uparrow\rangle\,, && \text{(3.30a)}\\
|J, M = J-1\rangle &= \frac{1}{\sqrt{N}}(|\uparrow\uparrow\uparrow\cdots\uparrow\uparrow\downarrow\rangle + |\uparrow\uparrow\uparrow\cdots\uparrow\downarrow\uparrow\rangle + \cdots), && \text{(3.30b)}\\
&\vdots\\
|J, M = 0\rangle &= \sqrt{\frac{N/2!N/2!}{N!}}(|\uparrow\uparrow\uparrow\cdots\downarrow\downarrow\downarrow\rangle + \cdots), && \text{(3.30c)}\\
&\vdots\\
|J, M = 1-J\rangle &= \frac{1}{\sqrt{N}}(|\uparrow\downarrow\downarrow\cdots\downarrow\downarrow\downarrow\rangle + |\downarrow\uparrow\downarrow\cdots\downarrow\downarrow\downarrow\rangle + \cdots), && \text{(3.30d)}\\
|J, M = -J\rangle &= |\downarrow\downarrow\downarrow\cdots\downarrow\downarrow\downarrow\rangle\,. && \text{(3.30e)}
\end{aligned}$$

Consider that the system starts in a fully symmetric state $|N/2, N/2\rangle$, as shown in Eq. (3.30a), where all the atoms are in the spin-up state. Each photon that is emitted causes the system to fall through the ladder of Dicke states. The system

moves from $M \to M-1$ with a decay rate [106]

$$\Gamma_{M\to M-1} = (J+M)(J-M+1)\Gamma. \tag{3.31}$$

The first photon is emitted with a decay rate $N\Gamma$ as expected for N-atoms. However, the system now enters a symmetric superposition state given by Eq. (3.30b) as any of the N atoms could have decayed. As a result, this Dicke state decays with an enhanced rate $(2N-1)\Gamma$. When half of the atoms have decayed, the system is in the centre of the Dicke ladder and in the maximally correlated state $|J, M=0\rangle$. At this point, the decay rate reaches a maximum value of $(N^2/4+N/2)\Gamma$. In an intially fully-inverted system, the rise and fall of the decay rate produces a characteristic pulse of emission known as superradiance. In a multi-level atom with several cooperative transitions, it is possible to observe a superradiant cascade process [107].

Throughout this analysis, it has been assumed that the system is invariant to atom perturbation and that each dipole evolves with the same phase. In reality this may not necessarily be the case due to collisions [108], propagation effects [14] and the inhomogenous spacing of the dipoles in a gas [106]. This leads to a weakening of superradiance as the system is projected into a state where $J < N/2$.

3.5. Summary

In summary, this Chapter considered the interaction which arises between optically-induced atomic dipoles. The Liénard-Wiechert potential was presented, which describes the dipole-dipole interaction via the Coulomb potential and the exchange of photons. This potential was applied to the pairwise dipole-dipole interaction and shown to result in a modification of both the energy and decay rate of the atomic states.

In a many-body atomic ensemble, the dipole-dipole induced energy shift has several components. The Coulomb interaction between the dipoles was shown to produce a Lorentz-Lorenz shift to lower frequencies. The geometry-dependent Cooperative Lamb shift was presented for a slab and cylinder geometry. Motional effects were also considered and contribute to a frequency shift and broadening of the atomic resonance. Finally, the Dicke picture was extended to a many-body ensemble and shown to produce a superradiant pulse of emission in an initially-inverted system.

4. Ground-State Spectroscopy

4.1. Introduction

This Chapter considers ground-state spectroscopy of caesium atoms in a thermal vapour. A laser with wavelength $\lambda = 852$ nm excites the atoms from the ground state $6^2S_{1/2}$ to the excited state $6^2P_{3/2}$. In a stationary atom, the transition linewidth is homogeneously broadened by the Heisenberg uncertainty principle. This limits the ground-state spectroscopic resolution to approximately 5 MHz. However, in a thermal vapour, the atoms have a distribution of atomic velocities determined by their temperature. Consequently, the transition linewidth is inhomogeneously broadened by the Doppler effect, documented in Section 4.2. At room temperature, the ground-state linewidth is broadened to approximately 375 MHz.

Saturated absorption spectroscopy, discussed in Section 4.3, is a method of increasing the spectroscopic resolution by eliminating the Doppler effect. This can be achieved by using a counter-propagating pump and probe beam of the same frequency. The pump beam effectively selects a small range of atomic velocities that are analysed by the probe beam. This technique is extended to polarisation spectroscopy in Section 4.4, where the atomic resonances produce narrow dispersive features. The chapter concludes in Section 4.5 with a discussion of laser frequency stabilisation using polarisation spectroscopy.

4.2. Doppler Broadening

The linewidth of an atomic transition is defined as the full-width at half-maximum (FWHM). In a stationary atom, the transition linewidth is determined by natural or homogeneous broadening. As a result, photons are absorbed with a Lorentzian distribution of frequencies given by [82]

$$g_{\mathrm{N}}(\Delta) = \frac{1}{2\pi}\frac{\Gamma}{\Delta^2 + \Gamma^2/4}, \tag{4.1}$$

where Γ is the natural linewidth, $\Delta = \omega_{\mathrm{L}} - \omega_0$ is the laser detuning, ω_0 is the transition frequency and ω_{L} is the laser frequency. When atomic motion is considered, the transition linewidth is inhomogeneously broadening by the Doppler effect. Consider an atom travelling at velocity $\boldsymbol{v}$ and an excitation laser with wavevector $\boldsymbol{k}$. The

excitation laser frequency ω_{L} will appear Doppler-shifted by an amount

$$\Delta_{\mathrm{D}} = -\boldsymbol{k} \cdot \boldsymbol{v}. \tag{4.2}$$

As the Doppler shift is dependent on the atomic velocity with respect to the beam, the expression can be simplified to $\Delta_{\mathrm{D}} = -kv$. The minus sign accounts for the fact that an atom moving in the opposite direction as the source, will observe a blue (positive) frequency shift.

In an ideal gas, the one dimensional velocity distribution $f(v)$ is given by the Maxwell-Boltzmann distribution

$$f(v) = \frac{1}{\sqrt{\pi} v_{\mathrm{p}}} \exp\left(-\frac{v^2}{v_{\mathrm{p}}^2}\right), \tag{4.3}$$

where $v_{\mathrm{p}} = \sqrt{2k_{\mathrm{B}}T/m}$ is the most probable speed, T is the temperature, k_{B} is Boltzmann's constant and m is the atomic mass. This is a Gaussian distribution with mean $\bar{v} = 0$ and standard deviation $\sigma_v = v_{\mathrm{p}}/\sqrt{2}$. Due to the Doppler effect, a single atom moving with velocity v will now absorb a Lorentzian distribution of frequencies given by $g_{\mathrm{N}}(\Delta - kv)$. The full Doppler-broadened absorption lineshape for an ensemble of atoms $g_{\mathrm{D}}(\Delta)$ is given by a convolution of the Lorentzian absorption lineshape $g_{\mathrm{N}}(\Delta - kv)$ at velocity v, and the atomic velocity distribution $f(v)$. This can be written in integral form as [82]

$$g_{\mathrm{D}}(\Delta) = \int_{-\infty}^{\infty} f(v) g_{\mathrm{N}}(\Delta - kv)\, dv, \tag{4.4}$$

which can be calculated numerically to obtain a Voigt profile. When the Doppler broadening dominates over the natural broadening $kv_{\mathrm{p}} \gg \Gamma$, the Lorentzian absorption profile can be replaced by a delta function

$$g_{\mathrm{N}}(\Delta - kv) \to \frac{1}{k}\, \delta(v - \Delta/k). \tag{4.5}$$

The Doppler-broadened absorption lineshape in Eq. (4.4) can now be written as

$$g_{\mathrm{D}}(\Delta) = \frac{1}{k} \int_{-\infty}^{\infty} f(v) \delta(v - \Delta/k)\, dv \tag{4.6}$$

$$= \frac{1}{\sqrt{\pi} k v_{\mathrm{p}}} \exp\left(-\frac{\Delta^2}{(kv_{\mathrm{p}})^2}\right), \tag{4.7}$$

which is a Gaussian function with mean $\bar{\Delta} = 0$ and standard deviation $\sigma_\Delta = kv_{\mathrm{p}}/\sqrt{2}$. Converting from standard deviation to full-width at half-maximum, the Doppler-broadened transition linewidth in the absence of natural broadening is given by

$$\Gamma_{\mathrm{D}} = 2\sqrt{\ln 2}\; k v_{\mathrm{p}}. \tag{4.8}$$

Alternatively, when the contribution from the natural linewidth cannot be neglected, an approximation can be used to determine the linewidth of the Voigt profile [109]

$$\Gamma_{\mathrm{D}} \approx 0.5346\Gamma + \sqrt{0.2166\Gamma^2 + 2.773(k v_{\mathrm{p}})^2}, \tag{4.9}$$

with an accuracy of $\pm 0.02\%$. Using this approximation, the natural linewidth Γ and Doppler-broadened linewidth Γ_{D} of the ground-state transition $6^2S_{1/2} \rightarrow 6^2P_{3/2}$ in caesium are

$$\Gamma = 2\pi \times 5.234 \text{ MHz}, \tag{4.10}$$

$$\Gamma_{\mathrm{D}} \simeq 2\pi \times 376 \text{ MHz}, \tag{4.11}$$

where Γ_D is calculated for atoms at room temperature $T = 293$ K. The Doppler-broadened linewidth Γ_{D} is clearly much greater than the natural linewidth Γ. Consequently, the spectroscopic resolution in a room-temperature thermal vapour is significantly reduced. This is further illustrated in Fig. 4.1 which shows the theoretical Doppler-broadened absorption lineshape for a single transition at $\lambda = 852$ nm (red dashed curve). The Lorentzian absorption lineshapes (blue solid curves) are shown for a range of atomic velocities which are separated by 25 m/s. The separation in frequency between these Lorentzian lineshapes is determined by the Doppler shift in Eq. (4.2) whilst their relative contribution is determined by the Maxwell-Boltzmann distribution in Eq. (4.3). When the Lorentzian lineshapes are summed over all possible velocities, the Doppler-broadened Voigt profile is obtained. The loss in resolution due to the Doppler effect can be recovered with a Doppler-free technique such as saturated absorption spectroscopy. This will be the subject of the discussion in the next Section.

4.3. Saturated Absorption Spectroscopy

Saturated absorption spectroscopy (SAS) is a two-photon technique for generating Doppler-free resonances in a thermal vapour [110]. The scheme uses a weak probe and strong pump beam of the same frequency, which counter-propagate through a vapour cell. At high intensities, the pump beam reduces the population difference between the lower and upper levels of the transition [82]. This leads to a reduction in the absorption of the probe beam on resonance, as demonstrated in Section 2.2.4 and Fig. 2.2.

At an atomic transition with natural linewidth Γ, the pump beam excites atoms

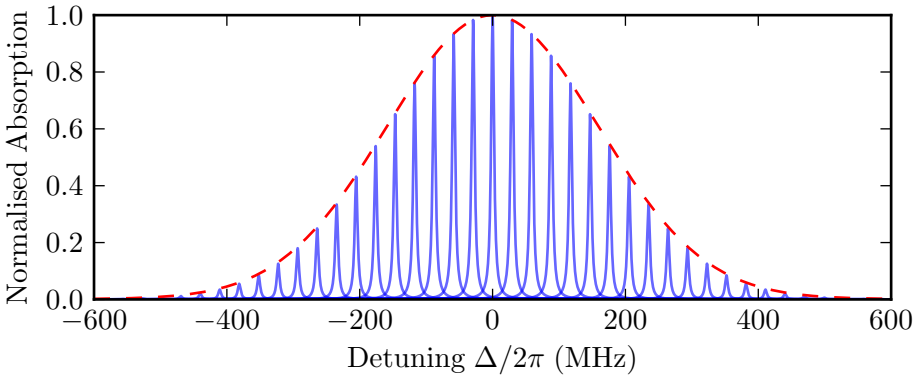

Figure 4.1.: The Doppler-broadened absorption spectrum $g_{\mathrm{D}}(\Delta)$ (red dashed line) is shown at room temperature $T = 293$ K for a single transition at wavelength $\lambda = 852$ nm. The Voigt profile is a convolution of the atomic velocity distribution $f(v)$ with the Lorentzian absorption profile $g_{\mathrm{N}}(\Delta)$ (blue solid lines - illustrated at 25 m/s intervals).

with a certain power-broadened velocity width

$$\Delta v = \frac{\Gamma}{k}\left(1 + \frac{I}{I_{\mathrm{sat}}}\right)^{1/2}, \tag{4.12}$$

where I is the pump beam intensity and I_{sat} is the saturation intensity. This leads to a phenomenon known as spectral hole burning where there is a loss of atoms in part of the atomic velocity distribution $f(v)$ given by Eq. (4.3). The hole burning which occurs on each transition can be detected in the transmission of a weak probe beam and results in a reduction in absorption with width $k\Delta v$. When the pump intensity $I \leq I_{\mathrm{sat}}$, the transmission peak has a width which is limited by the natural linewidth Γ.

The experimental setup for SAS is shown in Fig. 4.2. Using a polarising beam splitter (PBS) and half-wave plate ($\lambda/2$), the output from the 852 nm laser is split between the experiment and the SAS setup. A second PBS and $\lambda/2$ are then used to separate this beam into a weak probe and strong pump beam. The pump beam counter-propagates against the probe beam in the caesium vapour cell and is aligned using an edge mirror to maximise the beam overlap. Finally the probe beam is detected on a photodiode (PD).

Typical SAS spectra for caesium are shown in Fig. 4.3(a) and Fig. 4.3(b) for the $|6^2\mathrm{S}_{1/2}, F = 3\rangle \rightarrow |6^2\mathrm{P}_{3/2}, F' = 2, 3, 4\rangle$ and $|6^2\mathrm{S}_{1/2}, F = 4\rangle \rightarrow |6^2\mathrm{P}_{3/2}, F' = 3, 4, 5\rangle$ transitions respectively. The spectra were obtained in a room-temperature 5 cm vapour cell with pump intensity $I_{\mathrm{pump}} \approx I_{\mathrm{sat}}$ and probe intensity $I_{\mathrm{probe}} \ll I_{\mathrm{sat}}$.

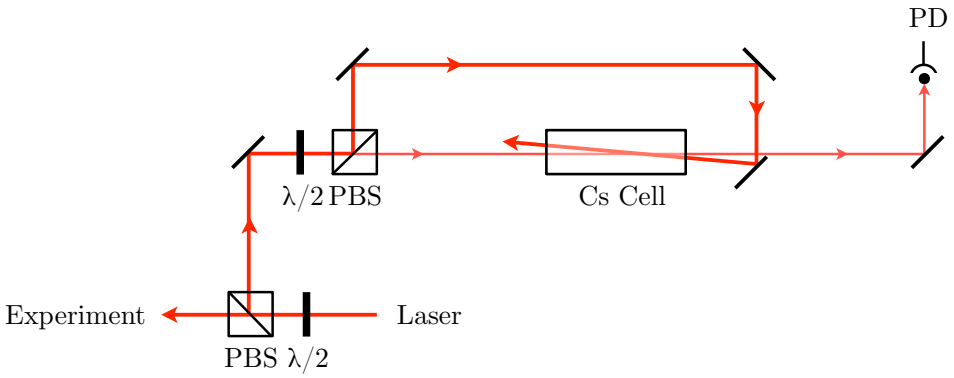

Figure 4.2.: Experimental setup diagram for saturated absorption spectroscopy. The weak probe beam counter-propagates against the strong pump beam and is detected on a photodiode (PD). A polarising beam splitter (PBS) and half-wave plate ($\lambda/2$) are used to separate the input beam into a pump and probe beam. An edge mirror is used to increase the beam overlap within the vapour cell.

There are six Doppler-free resonances in total. The three resonances corresponding to zero velocity atoms are indicated by vertical dashed lines. Notably there are also three "crossover" resonances which each lie between the three Doppler-free resonances. These resonances correspond to non-zero velocity class atoms which are pumped and probed on different transitions. For a particular hyperfine splitting Δ_{hf} between two upper levels, these atoms are excited with velocity $\pm\Delta_{\mathrm{hf}}/(2k)$.

4.4. Polarisation Spectroscopy

Polarisation spectroscopy [111] is a sub-Doppler spectroscopic technique, similar to saturated absorption spectroscopy, which utilises a counter-propagating pump and probe beam. Both the pump and probe beam have the same frequency. The strong circularly-polarised pump beam induces a birefringence in the medium which is analysed by the weak linearly-polarised probe beam. As polarisation spectroscopy produces a dispersive signal with an excellent signal-to-noise ratio, the technique is particularly suited to laser frequency stabilisation [112].

4.4.1. Polarisation Spectroscopy Setup

The experimental setup for polarisation spectroscopy is shown in Fig. 4.4. Using a polarising beam splitter (PBS) and half-wave plate ($\lambda/2$), the output from the 852 nm laser is split between the experiment and the polarisation spectroscopy setup. A second PBS and half-wave plate are then used to separate this beam into a

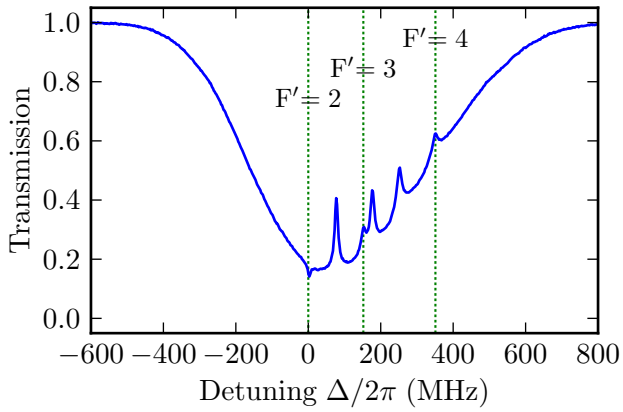

(a) $\left|6^2\mathrm{S}_{1/2}, F = 3\right\rangle \rightarrow \left|6^2\mathrm{P}_{3/2}, F' = 2, 3, 4\right\rangle$

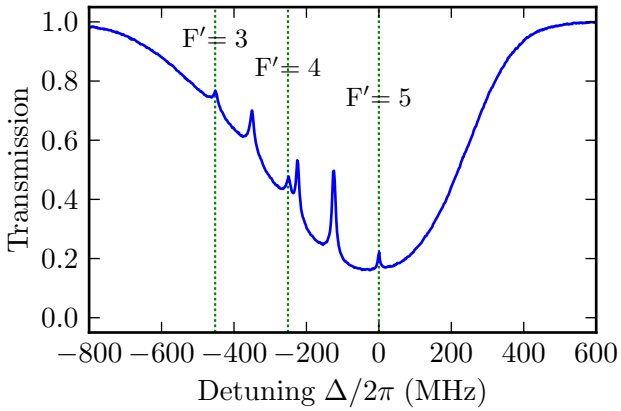

(b) $\left|6^2\mathrm{S}_{1/2}, F = 4\right\rangle \rightarrow \left|6^2\mathrm{P}_{3/2}, F' = 3, 4, 5\right\rangle$

Figure 4.3.: Typical saturated absorption spectroscopy in a room-temperature 5 cm caesium vapour cell. The peaks highlighted with vertical lines are the transitions for atoms with zero velocity. The remaining peaks are crossovers due to atoms with non-zero velocity. The pump intensity $I_{\mathrm{pump}} \approx I_{\mathrm{sat}}$ and the probe intensity $I_{\mathrm{probe}} \ll I_{\mathrm{sat}}$.

weak probe and strong pump beam. The pump beam is circularly polarised using a quarter-wave plate ($\lambda/4$) and then counter-propagates against the linearly-polarised probe beam in the caesium vapour cell. An edge mirror is used to maximise the beam overlap within the cell. The medium birefringence is analysed by decomposing the probe beam with a PBS and then detecting each component with a differencing photodiode (DPD).

4.4.2. Polarisation Spectroscopy Theory

Consider the probe beam propagating in the z-direction with the plane of linear polarisation at an angle ϕ to the x-axis. The electric field of the probe beam before

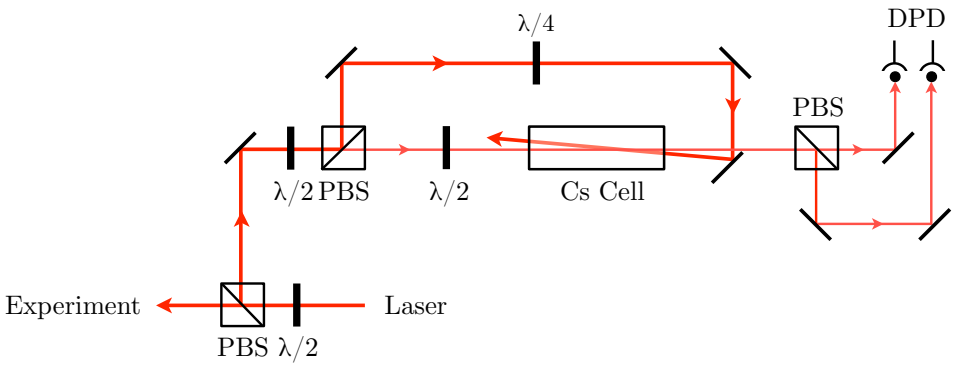

Figure 4.4.: Experimental setup diagram for polarisation spectroscopy. The linearly-polarised probe beam counter-propagates against the circularly-polarised pump beam. An edge mirror is used to increase the beam overlap within the vapour cell. The probe beam is decomposed using a polarising beam splitter (PBS) and detected on a differencing photodiode (DPD).

the medium can be decomposed into circular polarisation components [112]

$$E_{\text{inital}} = \begin{pmatrix} E_x \\ E_y \end{pmatrix} = E_0 \left[\frac{e^{-i\phi}}{2} \begin{pmatrix} 1 \\ i \end{pmatrix} + \frac{e^{i\phi}}{2} \begin{pmatrix} 1 \\ -i \end{pmatrix} \right]. \tag{4.13}$$

As the probe beam propagates through the birefringent medium of length L, each component of the electric field experiences a different level of absorption and phase shift. The electric field of the probe beam after the medium can be written

$$E_{\text{final}} = E_0 \left[\frac{e^{-i\phi}}{2} \begin{pmatrix} 1 \\ i \end{pmatrix} e^{-ik_+ L} e^{-\alpha_+/2} + \frac{e^{i\phi}}{2} \begin{pmatrix} 1 \\ -i \end{pmatrix} e^{-ik_- L} e^{-\alpha_-/2} \right], \tag{4.14}$$

where $\alpha_\pm$ and $k_\pm$ are the absorption coefficients and wavevectors for circularly-polarised light driving $\sigma^\pm$ transitions. The wavevector is directly related to the refractive index of the medium $k_\pm = (\omega/c)n_\pm$. The change in polarisation of the probe beam after the medium can be analysed using a PBS which decomposes the light into horizontal (x) and vertical (y) linear polarisation components. The signal on the differencing photodiode is given by

$$I_y - I_x = |E_y|^2 - |E_x|^2 = I_0 e^{-\alpha L} \cos\left(2\phi + \frac{\omega L}{c}\Delta n\right), \tag{4.15}$$

where $\Delta n = n_+ - n_-$ is the refractive index difference between the circular components and $\alpha = (\alpha_+ + \alpha_-)/2$ is the average absorption coefficient. From this expression, it is clear that the birefringence in the medium results in a rotation $\Phi = (\omega L \Delta n)/c$ of the plane of polarisation of the probe beam. At an atomic transi-

tion with natural linewidth Γ, the difference in absorption coefficients $\Delta\alpha = \alpha_+ - \alpha_-$ between the circular polarisation components has a Lorentzian profile given by

$$\Delta\alpha = \frac{\Delta\alpha_0}{1 + (\frac{2\Delta}{\Gamma})^2}, \tag{4.16}$$

where Δ is the laser detuning and $\Delta\alpha_0$ is the resonant difference in absorption coefficients. Using the Kramers-Kronig relation [113], it is possible to determine the corresponding difference in the refractive index as

$$\Delta n = \frac{c\Delta\alpha_0}{\omega} \frac{\frac{2\Delta}{\Gamma}}{1 + (\frac{2\Delta}{\Gamma})^2}. \tag{4.17}$$

Substituting the refractive index difference in Eq. (4.17) into the output signal in Eq. (4.15) and setting the input plane of polarisation $\phi = \pi/4$ results in the expression

$$I_y - I_x = I_0 e^{-\alpha L} L\Delta\alpha_0 \frac{\frac{2\Delta}{\Gamma}}{1 + (\frac{2\Delta}{\Gamma})^2}, \tag{4.18}$$

where the level of dispersion (angle of rotation) is assumed to be small. As a function of laser detuning, the polarisation spectroscopy signal is the derivative of a Lorentzian lineshape. In a thermal vapour, birefringence can be induced using a strong circularly-polarised pump beam. As the pump beam drives either σ^+ or σ^- transitions, an anisotropy is created in the ground-state population distribution. The largest anisotropy is created on closed transitions where the optical pumping is more effective [112].

4.4.3. Polarisation Spectroscopy in caesium

Typical polarisation spectroscopy signals are shown in Fig. 4.5 for (a) a 5 cm vapour cell and (b) a 2 mm vapour cell at room temperature $T = 293$ K. These spectra represent the best possible signals obtained by optimising all experimental parameters. Each direct and crossover transition produces a narrow dispersive resonance on a flat background of zero signal. The largest dispersive signal appears on the closed transition $|6^2\mathrm{S}_{1/2}, F = 4\rangle \rightarrow |6^2\mathrm{P}_{3/2}, F' = 5\rangle$ at $\Delta = 0$.

A common problem with polarisation spectroscopy in caesium is the high level of probe absorption that occurs in a room-temperature 5 cm vapour cell. As a result, the signal often appears on a large non-zero background. Previous work has shown this effect can be reduced using an ice bath [114] to reduce the level of probe absorption. An alternative method, as used in this experiment, is to reduce the probe absorption by using a 2 mm vapour cell.

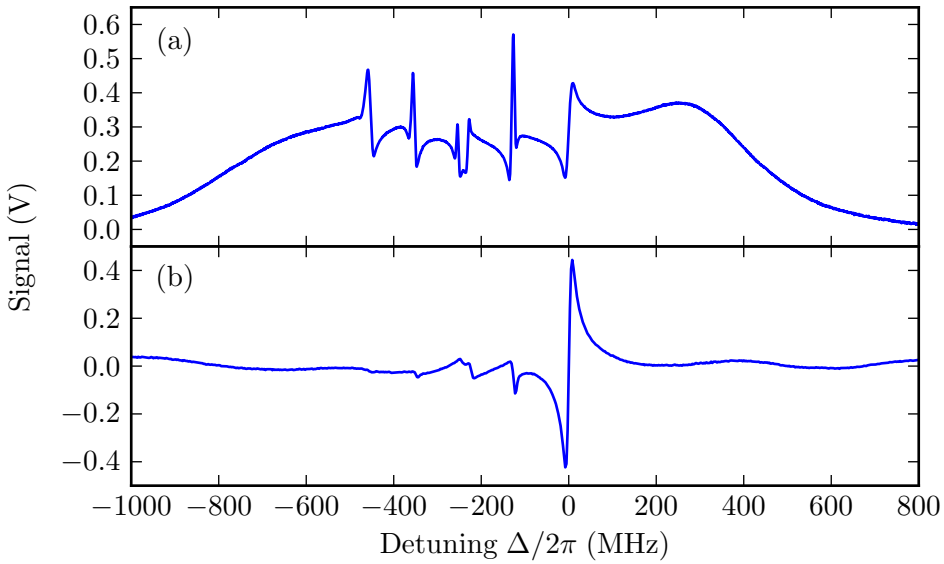

Figure 4.5.: Typical polarisation spectroscopy signals achieved in (a) 5 cm vapour cell and (b) 2 mm vapour cell. There are six dispersive resonances corresponding to three zero velocity transitions and three non-zero velocity transitions. In each case, the experimental parameters are adjusted to achieve the best possible signal.

4.5. Laser Frequency Stabilisation

The output laser frequency of an extended cavity diode laser (ECDL) is highly dependent on both its internal and external environmental conditions. Small variations in the laboratory temperature and pressure or thermal drift within the laser components can lead to a frequency drift which is significantly larger than the absorption linewidth. The free-running linewidth and short-term stability of an ECDL is therefore insufficient for the majority of experiments in atomic physics.

Active laser frequency stabilisation utilises an atomic reference signal which is converted into an electrical feedback to the laser. The narrow dispersive signal which results from polarisation spectroscopy is ideal for laser frequency stabilisation [115, 112]. Using a proportional-integral-derivative (PID) electronic feedback circuit, the laser can be stabilised to the zero crossing of the spectroscopy signal. This method allows the linewidth of the laser to be reduced to less than 1 MHz [115].

4.6. Summary

In summary, this Chapter introduced the inhomogenous broadening that results from the Doppler effect. This broadening reduces the resolution of ground-state spectroscopy of atoms in a thermal vapour. The ability to eliminate the Doppler

effect was analysed for a counter-propagating pump and probe configuration. These techniques utilise saturation or birefringence in the atomic medium to realise a Doppler-free resonance. Finally, the narrow dispersive features resulting from polarisation spectroscopy were discussed in the context of laser frequency stabilisation.

5. Excited-State Spectroscopy

5.1. Introduction

This Chapter considers excited-state spectroscopy in a three-level system where the upper transition is probed and Doppler-free spectroscopic features are observed. Spectroscopy of excited-state transitions is of growing interest for a variety of applications including the search for stable frequency references [116, 117], state lifetime measurement [118], optical filtering [119], frequency up-conversion [120] and multi-photon laser cooling [121].

A schematic of the experimental three-level system is shown in Fig. 5.1. The ground state $|1\rangle \equiv \left|6^2\mathrm{S}_{1/2}, F = 4\right\rangle$ is coupled to the intermediate state $|2\rangle \equiv \left|6^2\mathrm{P}_{3/2}, F' = 5\right\rangle$ by a coupling laser with wavelength $\lambda_\mathrm{c} = 852$ nm and Rabi frequency Ω_c. The intermediate state is coupled to the excited state $|3\rangle \equiv \left|7^2\mathrm{S}_{1/2}, F'' = 4\right\rangle$ by a probe laser with wavelength $\lambda_\mathrm{p} = 1470$ nm and Rabi frequency Ω_p. Unlike the majority of two-photon excitation schemes in alkali atoms, the wavelength of the upper transition in this system is longer than the wavelength of the lower transition.

In the experiments discussed in this Chapter, the coupling laser is ordinarily fixed on resonance $\Delta_\mathrm{c} = 0$ using ground-state polarisation spectroscopy (discussed in Section 4.4). The probe laser is scanned around resonance with detuning Δ_p and the transmission is detected on a photodiode with a germanium sensor, providing a spectral responsivity of 0.58 A/W at the probe wavelength $\lambda_\mathrm{p} = 1470$ nm. The intermediate-state decay rate $\Gamma_2 = 2\pi \times 5.32$ MHz [76] is comparable to the excited-state decay rate $\Gamma_3 = 2\pi \times 3.28$ MHz [122, 123]. Whilst the coupling transition is closed, the probe transition is open and decay can occur from the excited state $7^2\mathrm{S}_{1/2}$ into an uncoupled intermediate hyperfine level of $6^2\mathrm{P}_{1/2}$ and $6^2\mathrm{P}_{3/2}$. To avoid this population transfer, a subject of the investigation in the Chapter 6, a weak probe $\Omega_\mathrm{p} \ll \Gamma_3$ is used throughout.

The ability to conduct excited-state spectroscopy is strongly dependent on the dipole moment of the upper transition. When the coupling is small, the absorption of the applied field is weak and difficult to detect. In this system, the reduced dipole matrix element for the excited-state transition is extremely large $\langle 6^2\mathrm{P}_{3/2}||e\boldsymbol{r}||7^2\mathrm{S}_{1/2}\rangle = 3.237\ ea_0$ and comparable to that for the ground-state transition $\langle 6^2\mathrm{S}_{1/2}||e\boldsymbol{r}||6^2\mathrm{P}_{3/2}\rangle = 4.472\ ea_0$ [86].

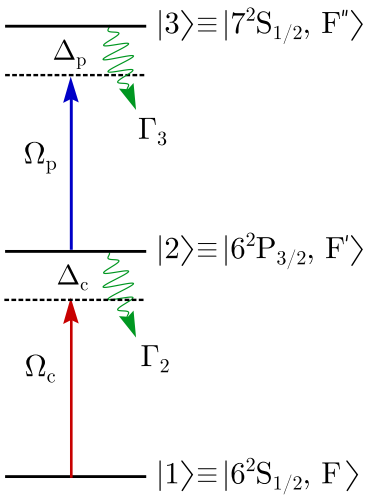

Figure 5.1.: Schematic of the three-level ladder system used for excited-state spectroscopy. The ground state $|1\rangle$ is coupled to the intermediate state $|2\rangle$ by a coupling laser with Rabi frequency Ω_c. The intermediate state $|2\rangle$ is coupled to the excited state by a probe laser with Rabi frequency Ω_p.

In Section 5.2, the transition linewidth in excited-state spectroscopy is calculated theoretically and compared to the experimentally-obtained value. Remarkably, with a weak probe and coupling laser, it is possible to obtain a sub-natural transition linewidth which is less than the combined decay rate of the intermediate and excited states $\Gamma < \Gamma_2 + \Gamma_3$. When the coupling laser is strong, a large transparency peak appears in the probe absorption spectrum. The origin of this transparency is investigated in Section 5.3 and determined to be Autler-Townes splitting. Finally, in Section 5.4, the strong circularly-polarised coupling laser is used to induce a birefringence in the atomic medium. This birefringence can be analysed through the rotation of a linearly-polarised probe laser as it propagates through the atomic ensemble. This novel excited-state polarisation spectroscopy technique produces a narrow dispersive signal with excellent signal-to-noise that is highly suitable for laser frequency stabilisation.

5.2. Excited State Absorption

The ability to observe excited-state absorption in a three-level ladder system is clearly demonstrated in Fig. 5.2. The transmission of the probe and coupling laser are shown as a function of coupling laser detuning Δ_c. The probe laser detuning is fixed on resonance $\Delta_p = 0$. As expected, the absorption profile of the coupling laser (blue curve) is Doppler-broadened with a linewidth of several hundred MHz. When the ground and excited states are in two-photon resonance $\Delta_p = \Delta_c = 0$, a narrow transmission peak appears in the broad profile. This can be confirmed as

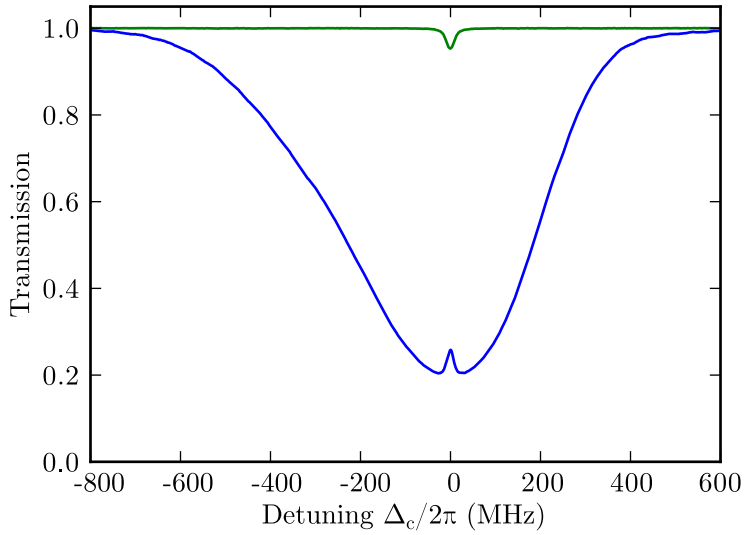

Figure 5.2.: Two-photon excitation from the ground state $6^2S_{1/2}$ to the excited state $7^2S_{1/2}$ as a function of coupling laser detuning Δ_c. The transmission of the ground-state coupling laser (blue curve) and excited-state probe laser (green curve) can be independently detected. Significant absorption is present on the excited-state transition due to the large dipole moment. Experimental parameters: vapour cell length $L = 5$ cm, atom temperature $T = 293$ K, probe laser Rabi frequency $\Omega_p/2\pi = 1$ MHz, probe laser detuning $\Delta_p = 0$ and coupling laser Rabi frequency $\Omega_c/2\pi = 8$ MHz. The coupling laser counter-propagates against the probe laser to minimise the two-photon Doppler shift.

two-photon absorption in the transmission of the probe laser (green curve). Due to the large dipole moment of the probe transition, significant absorption $> 5\%$ is observed in a 5 cm vapour cell at room temperature $T = 293$ K.

This observation also raises an interesting and deceptively difficult question: what is the linewidth Γ of the excited-state transition? Naïvely, one might expect that the linewidth is given by the sum of the decay rates of the intermediate and upper states $\Gamma = \Gamma_2 + \Gamma_3$ [124]. However this situation is only valid when the intermediate state $|2\rangle$ is incoherently prepared. When the intermediate state is coherently pumped from a lower level, the situation is quite different and the determination of the linewidth is somewhat more complicated. The aim of this section is to theoretically derive the linewidth Γ of an excited-state transition and confirm this result experimentally using the three-level ladder system shown in Fig. 5.1.

5.2.1. Complex Susceptibility

In this section, the complex susceptibility χ for an excited-state transition is derived analytically for a stationary atom and a thermal atom.

Stationary Atom

In the absence of atomic motion, the total Hamiltonian for the three-level system can be written in the dipole and rotating wave approximation (see Section 2.2.1) as

$$\hat{\mathcal{H}}_{\mathrm{tot}} = \hbar \begin{pmatrix} 0 & \Omega_{\mathrm{c}}/2 & 0 \\ \Omega_{\mathrm{c}}/2 & -\Delta_{\mathrm{c}} & \Omega_{\mathrm{p}}/2 \\ 0 & \Omega_{\mathrm{p}}/2 & -(\Delta_{\mathrm{p}} + \Delta_{\mathrm{c}}) \end{pmatrix}. \tag{5.1}$$

The phenomenological decay matrix $\hat{\mathcal{L}}$ for a three-level ladder system is given by

$$\hat{\mathcal{L}} = \begin{pmatrix} \Gamma_2\rho_{22} & -\gamma_{12}\tilde{\rho}_{12} & -\gamma_{13}\tilde{\rho}_{13} \\ -\gamma_{12}\tilde{\rho}_{21} & \Gamma_3\rho_{33} - \Gamma_2\rho_{22} & -\gamma_{23}\tilde{\rho}_{23} \\ -\gamma_{13}\tilde{\rho}_{31} & -\gamma_{23}\tilde{\rho}_{32} & -\Gamma_3\rho_{33} \end{pmatrix}. \tag{5.2}$$

The decay of the coherences can be written as

$$\gamma_{12} = \frac{\Gamma_2}{2} + \gamma_{\mathrm{c}}, \tag{5.3a}$$

$$\gamma_{23} = \frac{\Gamma_2 + \Gamma_3}{2} + \gamma_{\mathrm{p}}, \tag{5.3b}$$

$$\gamma_{13} = \frac{\Gamma_3}{2} + \gamma_{\mathrm{p}} + \gamma_{\mathrm{c}}, \tag{5.3c}$$

where γ_{p} and γ_{c} are additional dephasing terms due to the finite linewidth of the probe and coupling laser respectively. Inserting the total Hamiltonian $\hat{\mathcal{H}}_{\mathrm{tot}}$ in Eq. (5.1) and the decay matrix $\hat{\mathcal{L}}$ in Eq. (5.2) into the Lindblad master equation in Eq. (2.11), results in the following equations of motion for the density matrix elements

$$\dot{\rho}_{11} = \frac{\mathrm{i}\Omega_{\mathrm{c}}}{2}(\tilde{\rho}_{12} - \tilde{\rho}_{21}) + \Gamma_2\rho_{22}, \tag{5.4a}$$

$$\dot{\rho}_{22} = \frac{\mathrm{i}\Omega_{\mathrm{p}}}{2}(\tilde{\rho}_{23} - \tilde{\rho}_{32}) - \frac{\mathrm{i}\Omega_{\mathrm{c}}}{2}(\tilde{\rho}_{12} - \tilde{\rho}_{21}) - \Gamma_2\rho_{22} + \Gamma_3\rho_{33}, \tag{5.4b}$$

$$\dot{\rho}_{33} = -\frac{\mathrm{i}\Omega_{\mathrm{p}}}{2}(\tilde{\rho}_{23} - \tilde{\rho}_{32}) - \Gamma_3\rho_{33}, \tag{5.4c}$$

$$\dot{\tilde{\rho}}_{12} = \frac{\mathrm{i}\Omega_{\mathrm{p}}}{2}\tilde{\rho}_{13} - \frac{\mathrm{i}\Omega_{\mathrm{c}}}{2}(\rho_{22} - \rho_{11}) - (\mathrm{i}\Delta_{\mathrm{c}} + \gamma_{12})\tilde{\rho}_{12}, \tag{5.4d}$$

$$\dot{\tilde{\rho}}_{23} = -\frac{\mathrm{i}\Omega_{\mathrm{p}}}{2}(\rho_{33} - \rho_{22}) - \frac{\mathrm{i}\Omega_{\mathrm{c}}}{2}\tilde{\rho}_{13} - (\mathrm{i}\Delta_{\mathrm{p}} + \gamma_{23})\tilde{\rho}_{23}, \tag{5.4e}$$

$$\dot{\tilde{\rho}}_{13} = \frac{\mathrm{i}\Omega_{\mathrm{p}}}{2}\tilde{\rho}_{12} - \frac{\mathrm{i}\Omega_{\mathrm{c}}}{2}\tilde{\rho}_{23} - (\mathrm{i}(\Delta_{\mathrm{p}} + \Delta_{\mathrm{c}}) + \gamma_{13})\tilde{\rho}_{13}, \tag{5.4f}$$

where the tilde indicates the slowly varying coherences. An analytical steady-state solution of Eqs. (5.4) can be obtained using a perturbative technique outlined in [67]. In the limit of weak excitation $\Omega_{\mathrm{p}} \ll \gamma_{23}$ the density matrix elements can be

expressed as

$$\tilde{\rho}_{12} = \frac{\mathrm{i}\Omega_\mathrm{c}}{2}\left[\gamma_{12}+\mathrm{i}\Delta_\mathrm{c}+\frac{\frac{\Omega_\mathrm{c}^2\gamma_{12}}{\Gamma_1}}{\gamma_{12}-\mathrm{i}\Delta_\mathrm{c}}\right]^{-1}, \tag{5.5a}$$

$$\rho_{22} = \frac{\frac{\Omega_\mathrm{c}^2\gamma_{12}}{2}}{\Gamma_1\Delta_\mathrm{c}^2+\Gamma_1\gamma_{12}^2+\gamma_{12}\Omega_\mathrm{c}^2}, \tag{5.5b}$$

$$\tilde{\rho}_{13} = \frac{2\Gamma_1(\mathrm{i}\Delta_\mathrm{p}+\gamma_{23})(\mathrm{i}\Delta_\mathrm{c}-\gamma_{12})\Omega_\mathrm{c}\Omega_\mathrm{p}+\gamma_{12}\Omega_\mathrm{c}^3\Omega_\mathrm{p}}{2(\Gamma_1\Delta_\mathrm{c}^2+\Gamma_1\gamma_{12}^2+\gamma_{12}\Omega_\mathrm{c}^2)[4(\mathrm{i}\Delta_\mathrm{p}+\gamma_{23})(\mathrm{i}(\Delta_\mathrm{p}+\Delta_\mathrm{c})+\gamma_{13})+\Omega_\mathrm{c}^2]} \tag{5.5c}$$

$$\tilde{\rho}_{23} = \frac{\frac{\mathrm{i}\Omega_\mathrm{c}^2\Omega_\mathrm{p}\gamma_{12}}{4}}{\Gamma_1\Delta_\mathrm{c}^2+\Gamma_1\gamma_{12}^2+\gamma_{12}\Omega_\mathrm{c}^2}\left[1+\frac{\gamma_\mathrm{c}(1+\frac{\mathrm{i}\Delta_\mathrm{c}}{\gamma_{12}})}{\gamma_{23}+\mathrm{i}\Delta_\mathrm{p}}\right] \times \left[\gamma_{13}+\mathrm{i}(\Delta_\mathrm{p}+\Delta_\mathrm{c})+\frac{\frac{\Omega_\mathrm{c}^2}{4}}{\gamma_{23}+\mathrm{i}\Delta_\mathrm{p}}\right]^{-1}. \tag{5.5d}$$

where $\rho_{11} = (1-\rho_{22})$ and $\rho_{33} = 0$. It is clear from Eq. (5.5d) that the number of atoms pumped into the intermediate state $|2\rangle$ strongly affects the magnitude of the probe coherence $\tilde{\rho}_{23}$, manifest as the multiplication factor $(1/2)\Omega_\mathrm{p}\rho_{22}$. Furthermore, as the population of state $|2\rangle$ is resonantly pumped $\Delta_\mathrm{c} = 0$ from the ground state $|1\rangle$ by the coupling laser, the term in the first square bracket approaches unity when $\gamma_\mathrm{c} \ll \gamma_{23}$.

The interaction between the atomic system and the probe laser can be analysed through the complex susceptibility χ. Inserting the probe coherence $\tilde{\rho}_{23}$ given by Eq. (5.5d) into the general equation for the susceptibility in Eq. (2.15) results in the complex susceptibility for excited-state spectroscopy

$$\chi = \rho_{22}\frac{i\mathcal{N}d_{32}^2}{\hbar\epsilon_0}\frac{1}{\gamma_{13}-i(\Delta_\mathrm{p}+\Delta_\mathrm{c})+\frac{\Omega_\mathrm{c}^2/4}{\gamma_{23}-i\Delta_\mathrm{p}}}. \tag{5.6}$$

This expression is similar to the one obtained for EIT in Eq. (2.31), except for the strong dependence on the intermediate-state population ρ_{22} which has a Lorentzian profile as a function of coupling laser detuning Δ_c. Furthermore, when Ω_c is finite, the probe will be rendered transparent at $\Delta_\mathrm{p} = 0$ due to Autler-Townes splitting [77].

When the intermediate state $|2\rangle$ is weakly pumped, $\Omega_\mathrm{c}^2 \ll \Gamma_3(\Gamma_2+\Gamma_3)$, the complex susceptibility in Eq. (5.6) can be reduced to

$$\chi = \rho_{22}\frac{i\mathcal{N}d_{32}^2}{\hbar\epsilon_0}\frac{1}{\gamma_{13}-i(\Delta_\mathrm{p}+\Delta_\mathrm{c})}. \tag{5.7}$$

This complex susceptibility is similar to that of a two-level system obtained in Eq. (2.16) except for the multiplication factor ρ_{22}. The absorption lineshape, proportional to the imaginary part of the susceptibility χ, is simply a Lorentzian centred

at $-\Delta_c$ with linewidth $\Gamma = 2\gamma_{13}$. When the laser linewidths are sufficiently small and can be neglected, the linewidth is determined only by the excited-state decay rate $\Gamma = \Gamma_3$. This result is quite different to the case in which the intermediate state $|2\rangle$ is incoherently pumped, where the linewidth is given by the sum of the decay rates of the intermediate and excited state $\Gamma = \Gamma_2 + \Gamma_3$ [124]. Consequently, the sub-natural excited-state linewidth $\Gamma < \Gamma_2 + \Gamma_3$ indicates a coherent excitation process.

Thermal Atom

In a thermal vapour, each atomic velocity class experiences a different laser detuning Δ_p and Δ_c due to the Doppler effect. To obtain the velocity-dependent complex susceptibility $\chi(v)$, the detunings Δ_p and Δ_c, and the number density $\mathcal{N}$ are replaced with the following substitutions [55]:

$$\Delta_p \rightarrow \Delta_p - k_p v \ , \tag{5.8a}$$

$$\Delta_c \rightarrow \Delta_c + k_c v \ , \tag{5.8b}$$

$$\mathcal{N} \rightarrow \frac{\mathcal{N}}{v_p\sqrt{\pi}} \exp\left(-\frac{v^2}{v_p^2}\right) \ , \tag{5.8c}$$

where k_p is the wavevector of the probe laser, k_c is the wavevector of the counter-propagating coupling laser and v_p is the most probable speed of the atoms. By substituting Eqs. (5.8) into the analytical expression for the complex susceptibility in Eq. (5.6), the complex susceptibility of a particular velocity class $z = v/v_p$ can be expressed as

$$\begin{aligned} \chi(z)\mathrm{d}z &= -\frac{\mathcal{N} d_{32}^2 \Omega_c^2}{\hbar\epsilon_0\sqrt{\pi} k_c^2 (k_c - k_p) v_p^3} \frac{\gamma_{12}}{2\Gamma_2} \left\{ \frac{\mathrm{e}^{-z^2}}{(z+\beta)^2 + \sigma^2} \right\} \\ &\times \left[z - z_0 + \frac{\Omega_c^2/4}{(k_c - k_p) k_p v_p^2 (z - z_1)} \right]^{-1} \mathrm{d}z \ , \end{aligned} \tag{5.9}$$

where the following simplifications have been used

$$\sigma = \frac{1}{k_c v_p} \sqrt{\gamma_{12}^2 + \frac{\Omega_c^2 \gamma_{12}}{\Gamma_2}} \ , \tag{5.10a}$$

$$\xi = \frac{\Delta_p + \Delta_c}{(k_c - k_p) v_p} \ , \tag{5.10b}$$

$$\beta = \frac{\Delta_c}{k_c v_p} \ , \tag{5.10c}$$

$$z_0 = -\xi - \mathrm{i}\gamma \ , \tag{5.10d}$$

$$z_1 = \frac{\Delta_p + \mathrm{i}\gamma_{23}}{k_p v_p} \ , \tag{5.10e}$$

$$\gamma = \frac{\gamma_{13}}{(k_c - k_p) v_p} \ . \tag{5.10f}$$

The total susceptibility χ_{D} is obtained by integrating the velocity-dependent susceptibility $\chi(v)$ in Eq. (5.9) over all velocity classes. In the case where the coupling Rabi frequency Ω_{c} is sufficiently weak, the total complex susceptibility becomes

$$\chi_{\mathrm{D}}(\Delta_{\mathrm{p}}) = -\frac{\mathcal{N}d_{32}^2\Omega_{\mathrm{c}}^2}{\hbar\epsilon_0\sqrt{\pi}k_{\mathrm{c}}^2(k_{\mathrm{c}}-k_{\mathrm{p}})v_{\mathrm{p}}^3}\frac{\gamma_{12}}{2\Gamma_2}\times \int_{-\infty}^{\infty}\left\{\frac{\mathrm{e}^{-z^2}}{(z+\beta)^2+\sigma^2}\right\}\left[\frac{1}{(z+\xi)+\mathrm{i}\gamma}\right]\mathrm{d}z\ . \tag{5.11}$$

This expression shows that the total complex susceptibility χ_{D} is given by the convolution between a Lorentzian of width γ (term in square bracket describing the transition from intermediate state $|2\rangle$ to excited state $|3\rangle$) and a product of a Lorentzian of width σ and a Gaussian of width v_{p} (term in curly bracket describing the atomic velocity distribution of intermediate state $|2\rangle$).

The convolution of a Gaussian and Lorentzian in Eq. (5.11) results in the non-analytical Voigt function. This must be calculated numerically in order to obtain the full theoretical result. However, it is possible to simplify the integration by replacing the product between a Gaussian and a Lorentzian with a Lorentzian

$$\frac{\mathrm{e}^{-z^2}}{(z+\beta)^2+\sigma^2} \rightarrow \frac{\mathrm{e}^{-\beta^2}}{(z+\beta)^2+\sigma^2}. \tag{5.12}$$

This approximation is valid when the width σ of the Lorentzian absorption from the ground state $|1\rangle$ to the intermediate state $|2\rangle$ is much smaller than the width v_{p} of the Gaussian velocity distribution. The total complex susceptibility becomes

$$\chi_{\mathrm{D}}(\Delta_{\mathrm{p}}) = -\frac{\mathcal{N}d_{32}^2\Omega_{\mathrm{c}}^2\sqrt{\pi}}{\hbar\epsilon_0 k_{\mathrm{c}}^2 v_{\mathrm{p}}\sigma}\frac{\gamma_{12}}{2\Gamma_2}\frac{1}{\Delta_{\mathrm{p}}+\Delta_{\mathrm{c}}+\mathrm{i}\Gamma/2}\ , \tag{5.13}$$

where the linewidth

$$\frac{\Gamma}{2} = \gamma_{13} + \left(\frac{k_{\mathrm{c}}-k_{\mathrm{p}}}{k_{\mathrm{c}}}\right)\sqrt{\gamma_{12}^2+\frac{\Omega_{\mathrm{c}}^2\gamma_{12}}{\Gamma_2}}\ . \tag{5.14}$$

In the limit where $\Omega_{\mathrm{c}} \ll \Gamma_2$, the linewidth of the absorption is simply

$$\Gamma = \Gamma_3 + \left(\frac{k_{\mathrm{c}}-k_{\mathrm{p}}}{k_{\mathrm{c}}}\right)\Gamma_2, \tag{5.15}$$

where the laser linewidths γ_{p} and γ_{c} have been neglected. This expression contains the sum of two terms: the first term is the linewidth of the absorption lineshape in the case in which the Doppler effect is neglected and the latter is the linewidth of the intermediate state $|2\rangle$ scaled by the ratio of the wavevectors. Physically, the second term originates from the fact that the atoms are velocity-selected by

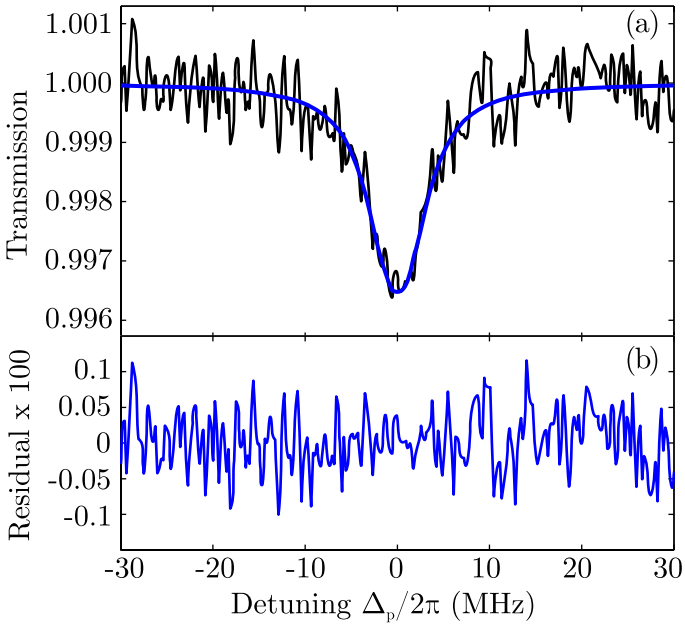

Figure 5.3.: (a) Comparison between the probe transmission spectrum (black line) and the simple theoretical model (blue line) for coupling Rabi frequency $\Omega_c/2\pi = (0.6 \pm 0.1)$ MHz. The excited-state linewidth is determined as $\Gamma/2\pi = (7.0 \pm 0.7)$ MHz. (b) Residual plot between the experimental data and the simple theoretical model.

the Doppler effect for the atom-field interaction. Only atoms whose velocities are between $-\Gamma_2/2k_c$ and $\Gamma_2/2k_c$ are coherently pumped into the intermediate state $|2\rangle$ when the coupling field is on resonance. Since Γ_2/k_c is very small compared to the width of the Doppler broadening, the atoms that are pumped into state $|2\rangle$ have approximately the same velocity distribution. Again, it is important to note that this simple model breaks down when the coupling laser is strong; in this case, the full theoretical model in Eq. (5.11) must be calculated instead.

5.2.2. Experimental Confirmation

The transition linewidth derived in Eq. (5.15) can be verified experimentally by performing excited-state spectroscopy of the three-level ladder system shown in Fig. 5.1. The transmission of a weak probe laser with Rabi frequency $\Omega_p/2\pi = 0.1$ MHz is measured as a function of detuning Δ_p in a 7.5 cm vapour cell at room temperature $T = 293$ K. The counter-propagating coupling laser is fixed on resonance $\Delta_c = 0$ and coherently pumps atoms from the ground state $|1\rangle$ into the excited state $|2\rangle$. The probe and coupling lasers are linearly-polarised with $1/e^2$ radii of 1.2 mm and 1.6 mm, respectively.

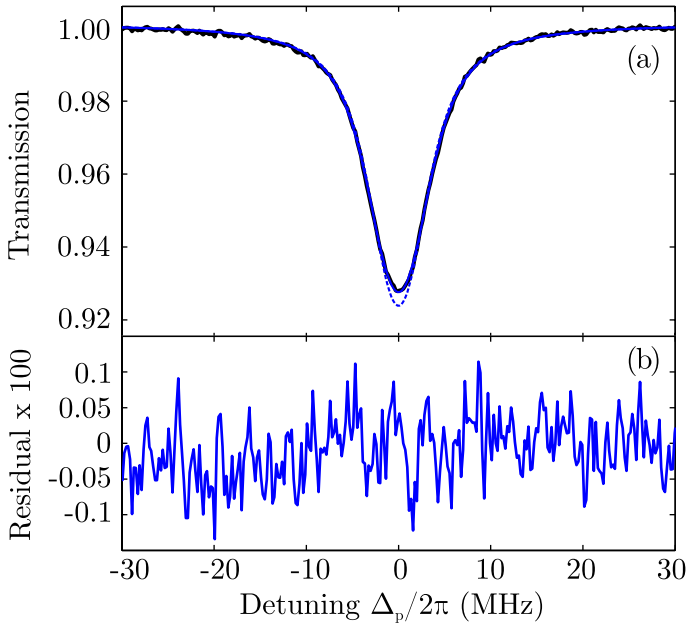

Figure 5.4.: (a) Comparison between the probe transmission spectrum (black line), simple theoretical model (dashed blue line) and full theoretical model (solid blue line) for coupling Rabi frequency $\Omega_c/2\pi = (3.0 \pm 0.1)$ MHz. The excited-state linewidth is determined as $\Gamma/2\pi = (7.5 \pm 0.1)$ MHz. (b) Residual plot between the experimental data and the full theoretical model.

In order to determine the minimum transition linewidth, the probe transmission spectra are obtained as a function of coupling laser Rabi frequency Ω_c. This data is then fit with the theoretical model presented in Section 5.2.1 to determine the transition linewidth Γ. The dephasing of the probe laser is a free fitting parameter and found to be $\gamma_p/2\pi = (0.18 \pm 0.06)$ MHz. The dephasing of the coupling laser is fixed at $\gamma_c/2\pi = 0$. The theoretical model for the complex susceptibility is calculated for each magnetic sublevel and the total complex susceptibility is the average of all complex susceptibilities over all possible magnetic sublevels. This is given by

$$\chi_{\mathrm{tot}}(\Delta_p) = \frac{1}{16} \sum_{m_F=-4}^{4} \chi_D^{m_F}(\Delta_p), \tag{5.16}$$

where $\chi_D^{m_F}(\Delta_p)$ is the complex susceptibility corresponding to the m_F magnetic sublevel of the ground state $\left|6^2S_{1/2}, F = 4\right\rangle$. The factor of 1/16 in the equation accounts for the fact that the initial population is evenly distributed among the magnetic sublevels of $\left|6^2S_{1/2}, F = 3, 4\right\rangle$. The susceptibility χ_D is calculated using the simple model in Eq. (5.13), when the coupling Rabi frequency is sufficiently weak or the full model in Eq. (5.11) when this is not the case.

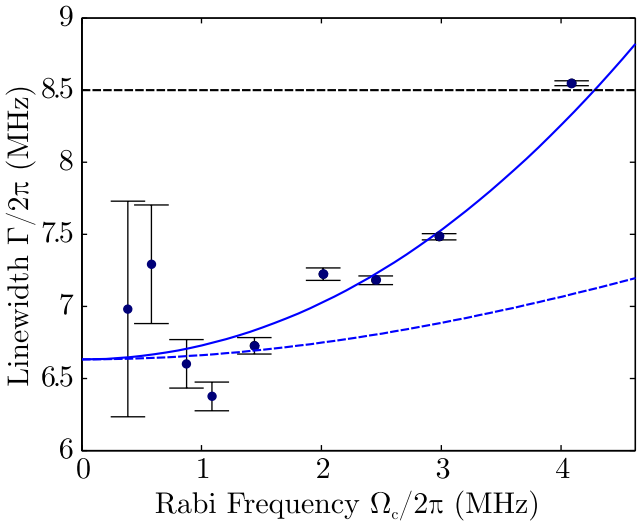

Figure 5.5.: The excited-state linewidth Γ is shown as a function of coupling Rabi frequency Ω_c. The horizontal dashed line indicates the minimum transition linewidth $\Gamma_2 + \Gamma_3$ when the intermediate state $|2\rangle$ is incoherently prepared. In the case of coherent preparation, the simple theoretical model (dashed blue line) and full theoretical model (solid blue line) converge on the minimum transition linewidth $\Gamma/2\pi \simeq 6.6$ MHz, as predicted by Eq. (5.15).

The probe transmission signal for coupling Rabi frequency $\Omega_c/2\pi = (0.6 \pm 0.1)$ MHz is shown in Fig. 5.3(a). The experimental data (black line) is fitted with the simple theoretical model (blue line) to determine the linewidth $\Gamma/2\pi = (7.0 \pm 0.7)$ MHz. This linewidth is sub-natural as it is less than the combined decay rates of the intermediate and excited states $\Gamma < \Gamma_2 + \Gamma_3$. Inspection of the residuals between experiment and theory in Fig. 5.3(b) shows there is excellent agreement. The extremely low level of probe absorption $< 0.04\%$ results in a large uncertainty in the determination of the transition linewidth Γ.

The probe transmission signal for coupling Rabi frequency $\Omega_c = (3.0 \pm 0.1)$ MHz is shown in Fig. 5.4(a). As the probe is no longer weak, the experimental data (black line) is fitted with the full theoretical model (blue line) to determine the linewidth $\Gamma/2\pi = (7.5 \pm 0.1)$ MHz. The absorption profile can no longer be described by a Lorentzian, as shown by the simple theoretical model (dashed blue line). The residuals between the experimental data and the full theoretical model in Fig. 5.4(b) demonstrate excellent agreement.

The excited-state linewidth Γ is shown as a function of coupling laser Rabi frequency Ω_c in Fig. 5.5. The horizontal dashed line indicates the minimum transition linewidth $\Gamma = \Gamma_2 + \Gamma_3$ if the intermediate state $|2\rangle$ is incoherently populated. The predictions of the simple (dashed blue line) and full (solid blue line) theoretical

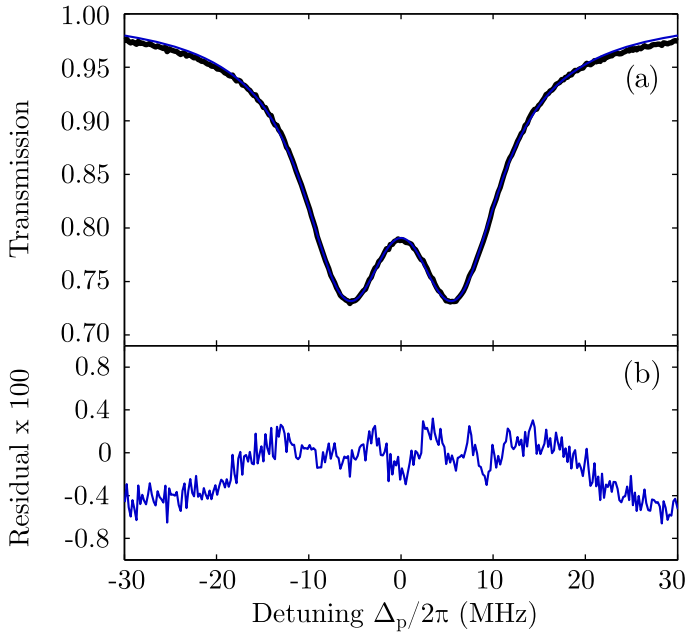

Figure 5.6.: (a) Comparison between the probe transmission spectrum (black line) and the full theoretical model (blue line) for coupling Rabi frequency $\Omega_c/2\pi = 15 \pm 0.1$ MHz. (b) The residual plot between the experimental data and the full theoretical model indicates excellent agreement.

model are also shown. Both theoretical models converge on the minimum transition linewidth $\Gamma/2\pi \simeq 6.6$ MHz as predicted by Eq. (5.15). When the coupling Rabi frequency is low, the experimental data is in excellent agreement with the simple theoretical model which predicts a Lorentzian lineshape. At higher coupling Rabi frequencies, the simple Lorentzian model is no longer a good fit to the experimental data. However, the full Voigt model which includes the distribution of atomic velocities in the intermediate state $|2\rangle$ provides excellent agreement. Importantly, the excited-state linewidths remain sub-natural, i.e. $\Gamma < \Gamma_2 + \Gamma_3$, when the coupling Rabi frequency is sufficiently weak $\Omega_c/2\pi \lesssim 4$ MHz.

5.3. Discerning EIT and ATS

The probe transmission signal for coupling Rabi frequency $\Omega_c/2\pi = (15 \pm 0.1)$ MHz is shown in Fig. 5.6. Even at high Rabi frequencies, the full theoretical model shows excellent agreement to the experimental data. This spectrum also raises the question of whether the transparency peak in the centre of the absorption profile is due to electromagnetically induced transparency (EIT) or Autler-Townes splitting (ATS). Through observation alone, it is difficult to distinguish ATS from EIT as both yield

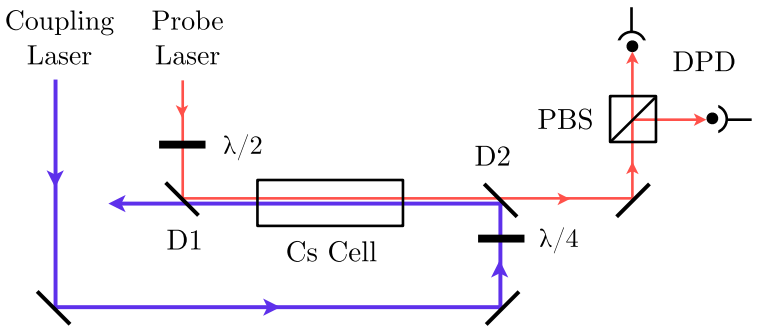

Figure 5.7.: Experimental setup diagram for excited-state polarisation spectroscopy. The linearly-polarised probe beam counter-propagates against the circularly-polarised coupling beam. The rotation of the probe beam is analysed using a polarising beam splitter (PBS) and a differencing photodiode (DPD). Dichoric mirrors (D1 and D2) are used to overlap the two beams in the caesium vapour cell.

transparency in the probe absorption profile.

In terms of the underlying mechanism, the main difference between EIT and ATS is the presence of Fano interference. This coherent phenomena arises due to interference between the transition pathways in an atomic system and results in the cancellation of resonant absorption. Furthermore, this process occurs even when the coupling laser is arbitrarily weak. On the other hand, ATS arises due to a coupling-induced absorption doublet which leads to a loss of absorption on resonance. This process does not occur when the coupling laser is weak. As the experimental data in Section 5.2.2 demonstrates, the observed transparency peak is not present when the coupling laser is weak. This indicates that it is not possible to observe EIT in the considered lower-driven ladder system [78].

5.4. Excited State Polarisation Spectroscopy

Polarisation spectroscopy [111] is a widely used Doppler-free technique that can provide a robust and modulation-free signal to which a laser can be frequency stabilised [112]. The technique has predominantly been used on strong optical transitions from the ground state of atomic vapours [114], where optical pumping induces birefringence in the medium. In this section, polarisation spectroscopy is extended to an excited-state transition. The coupling beam on the lower transition induces a birefringence which is probed on the excited-state transition.

The atomic energy levels are shown in Fig. 5.1 and a schematic of the experimental setup is shown in Fig. 5.7. The circularly-polarised 852 nm coupling beam with 1.6 mm $1/e^2$ radius is stabilised to the $\left|6^2S_{1/2}, F = 4\right\rangle \rightarrow \left|6^2P_{3/2}, F' = 5\right\rangle$ transition using ground-state polarisation spectroscopy. The linearly-polarised 1470 nm

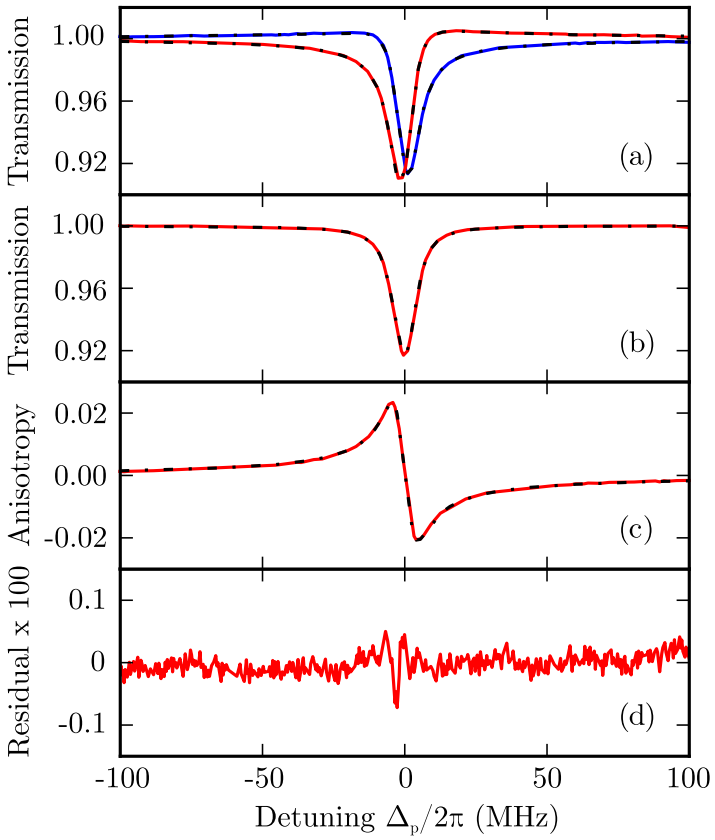

Figure 5.8.: Experimental spectra with theoretical fitting (dashed lines). (a) Individual probe transmission signals S_1 (red line) and S_2 (blue line) recorded at the each photodiode. (b) The sum $(S_1 + S_2)/2$ is a Lorentzian absorption profile and (c) the difference $(S_1 - S_2)/2$ is a dispersive profile. (d) The residual between the theoretical model and the experimental data shown in (c). Experimental parameters: probe laser Rabi frequency $\Omega_p/2\pi = 1.4$ MHz, coupling laser Rabi frequency $\Omega_c/2\pi = 12.4$ MHz and coupling laser detuning $\Delta_c = 0$.

probe beam with 1.2 mm $1/e^2$ radius is scanned across the $|6^2P_{3/2}, F' = 5\rangle \rightarrow |7^2S_{1/2}, F'' = 4\rangle$ transition and the scan position is calibrated using a wavemeter to better than 1% accuracy. Both beams counter-propagate through a 5 cm caesium vapour cell at room temperature $T = 293$ K. The beams are combined and separated using dichroic mirrors with a reflection/transmission edge between 852 nm and 1470 nm. A small magnetic field $B \simeq 2$ mT is applied along the vapour cell axis using a solenoid to provide a quantisation axis for the polarisation of the probe and coupling laser. After the vapour cell, the rotation of the probe laser is analysed using a polarising beam splitter and differencing photodiode.

The coupling beam drives σ^+ transitions between the ground and intermediate state and transfers population towards the $|6^2P_{3/2}, F' = 5, m'_F = 5\rangle$ state, inducing

an anisotropy in the medium. Within the vapour cell, the linearly-polarised probe is decomposed into equal contributions of circular polarisation and therefore drives both $\sigma^{\pm}$ transitions. The component of the probe which drives σ^{-} transitions is preferentially absorbed because there are no σ^{+} allowed transitions from the $|F' = 5, m'_F = 5\rangle$ state. This results in a rotation of the linear polarisation of the probe, as discussed in detail in Section 4.4.

A polarising beam splitter cube (PBS) oriented at angle $\phi = 45°$ to the polarisation vector of the probe resolves the probe electric field into orthogonal linear components S_1 and S_2 which are detected using two germanium photodiodes. The sum of the two signal is proportional to the difference in absorption coefficient between the circular polarisation components

$$\frac{S_1 + S_2}{2} \propto \Delta\alpha, \tag{5.17}$$

where $\Delta\alpha = \alpha^{+} - \alpha^{-}$ and $\alpha^{\pm}$ is the absorption coefficient for circular polarisation driving $\sigma^{\pm}$ transitions. Furthermore, the difference between the two signals is proportional to the difference in refractive index between the circular polarisation components

$$\frac{S_1 - S_2}{2} \propto \Delta n, \tag{5.18}$$

where $\Delta n = n^{+} - n^{-}$ and $n^{\pm}$ is the refractive index for circular polarisation driving $\sigma^{\pm}$ transitions.

The excited-state transmission spectra are shown in Fig. 5.8 as a function of probe detuning Δ_{p}. The individual signals on each photodiode, S_1 and S_2, are shown in Fig. 5.8(a). Each signal consists of a Lorentzian component (due to the difference in absorption between left and right circularly polarised light) and a dispersive component (due to the difference in dispersion between left and right circularly polarised light). Whilst the Lorentzian components have the same sign in S_1 and S_2, the dispersive components have the opposite sign. Consequently, the sum of the signals $(S_1 + S_2)/2$ shown in Fig. 5.8(b) produces a Lorentzian profile with linewidth Γ given by

$$\Delta\alpha = \frac{\Delta\alpha_0}{1 + (2\Delta_{\mathrm{p}}/\Gamma)^2}, \tag{5.19}$$

where $\Delta\alpha_0$ is the maximum difference in absorption at the line centre. Similarly, the difference between the signals $(S_1 - S_2)/2$ shown in Fig. 5.8(c) produces a dispersive signal with linewidth Γ given by

$$\Delta n = \Delta\alpha_0 \frac{2c}{\omega_0 \Gamma} \frac{\Delta_{\mathrm{p}}}{1 + (2\Delta_{\mathrm{p}}/\Gamma)^2}. \tag{5.20}$$

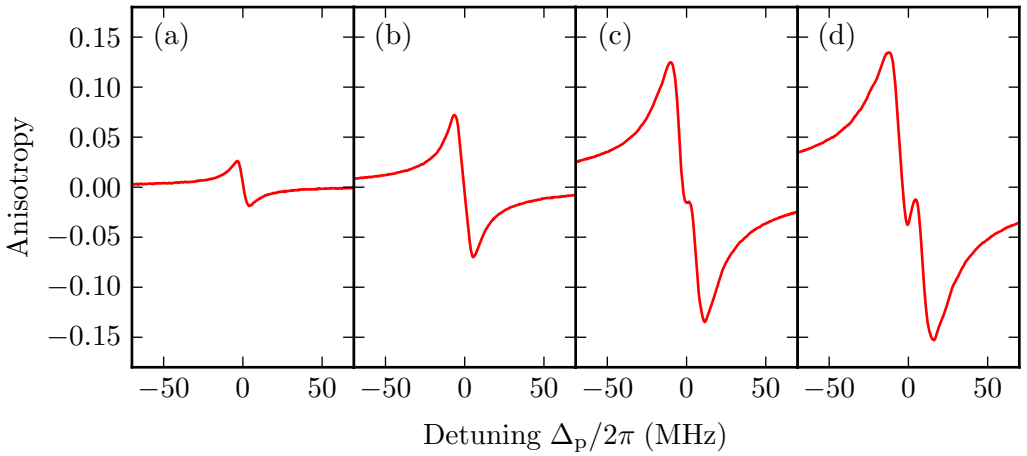

Figure 5.9.: Excited-state polarisation spectroscopy signals for coupling laser Rabi frequency $\Omega_c/2\pi$ = (a) 8.8 MHz, (b) 17.8 MHz, (c) 35.8 MHz and (d) 47.0 MHz. When the coupling laser Rabi frequency reaches a critical value, a sub-feature appears due to Autler-Townes splitting of the intermediate state $|2\rangle$. Experimental parameters: probe laser Rabi frequency $\Omega_p/2\pi = 1.4$ MHz and coupling laser detuning $\Delta_c = 0$.

The spectra in Fig. 5.8(a-c) are fitted to the functions described in Eq. (5.19) and Eq. (5.20). The residual plot in Fig. 5.8(d) shows excellent agreement between the experimental data and the theoretical model presented in Fg. 5.8(c). As with ground-state polarisation spectroscopy discussed in Section 4.4, the narrow dispersive lineshape produced by the difference in the photodiode signals is of particular interest for laser frequency stabilisation.

The development of the excited-state polarisation spectroscopy signal as a function of coupling laser Rabi frequency Ω_c is shown in Fig. 5.9. As the Rabi frequency increases, the magnitude of the feature increases until the ground-state transition is saturated. The linewidth also increases due to power broadening and the spectra eventually develops a dispersive sub-feature at Δ_p=0. This sub-feature arises due to Autler-Townes splitting (ATS) of the intermediate state. As a result, the absorption doublet produces a pair of dispersive lineshapes centred at probe laser detuning $\Delta_p = \pm\Omega_c/2$. In this regime, a single Lorentzian and its concomitant dispersion can no longer fit the data. Using a pair of displaced Lorentzians of the same width, however, allows an excellent fit to be obtained.

The evolution of the linewidth Γ and on-resonance gradient of the polarisation spectroscopy signal are shown as a function of coupling Rabi frequency Ω_c in Fig. 5.10(a) and (b) respectively. The linewidth Γ is determined by fitting the spectra with a single dispersive lineshape or a pair of dispersive lineshapes when ATS is present. These linewidth measurements are then fit to a simple theoret-

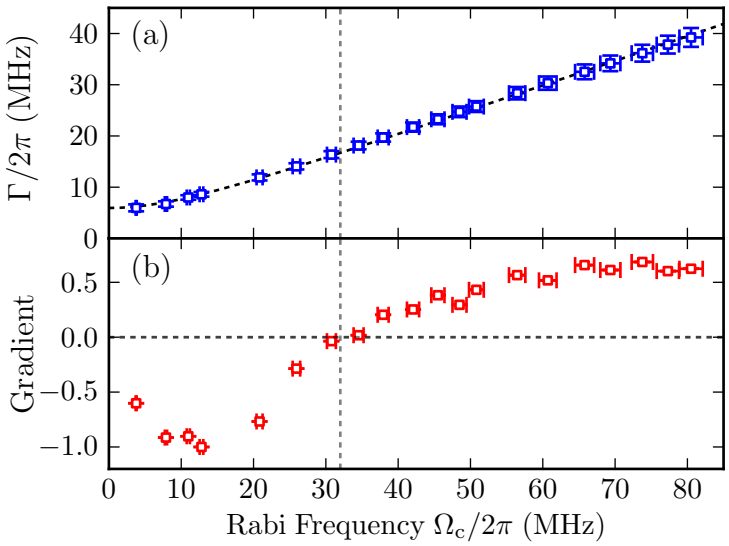

Figure 5.10.: (a) Linewidth Γ of the polarisation spectroscopy signal as a function of coupling laser Rabi frequency Ω_c. The linewidth measurements are fitted with a theoretical model (black dashed line) for power broadening and the minimum linewidth is determined as $\Gamma_0/2\pi = (5.9 \pm 0.3)$ MHz. (b) Normalised gradient of the polarisation spectroscopy signal at $\Delta_p = 0$. The grey horizontal dashed line indicates zero gradient and the vertical dashed line indicates the Rabi frequency $\Omega_c/2\pi \simeq 32$ MHz at which the sub-feature appears. The linewidth and gradient are determined by fitting the experimental data with a dispersive lineshape. Experimental parameters: probe laser Rabi frequency $\Omega_p/2\pi = 1.4$ MHz and coupling laser detuning $\Delta_c = 0$.

ical model (shown by the dashed black curve) for the power broadening of the Lorentzian lineshape $\Gamma = \sqrt{2\Omega_c^2 + \Gamma_0^2}$ and the minimum linewidth determined as $\Gamma_0/2\pi = (5.9 \pm 0.3)$ MHz. This is consistent with the sub-natural excited-state linewidth $\Gamma/2\pi \simeq 6.6$ MHz which was derived analytically in Section 5.2.1. The on-resonance gradient in Fig. 5.10(b) decreases with Rabi frequency before increasing and changing sign with the appearance of the ATS sub-feature at $\Omega_c/2\pi \simeq 32$ MHz (indicated by the vertical dashed line).

The role of Doppler averaging on the polarisation spectroscopy signal can be investigated through the steady-state probe coherence $\mathrm{Re}(\tilde{\rho}_{23})$ given in Eq. (5.4e). The real part of the coherence is considered as it is proportional to the probe dispersion and thus our experimental spectra. In order to obtain a suitable signal with ATS, the simulation uses a strong coupling field with Rabi frequency $\Omega_c/2\pi = 12.2$ MHz and a weak probe field with Rabi frequency $\Omega_p/2\pi = 3.3$ MHz. The probe coherence $\mathrm{Re}(\tilde{\rho}_{23})$ is shown as a function of probe detuning Δ_p in Fig. 5.11. The simulation is presented for an atom at rest (red line), non-zero atomic velocities (grey lines) and the Doppler-averaged signal (blue line). As a result of the Doppler averag-

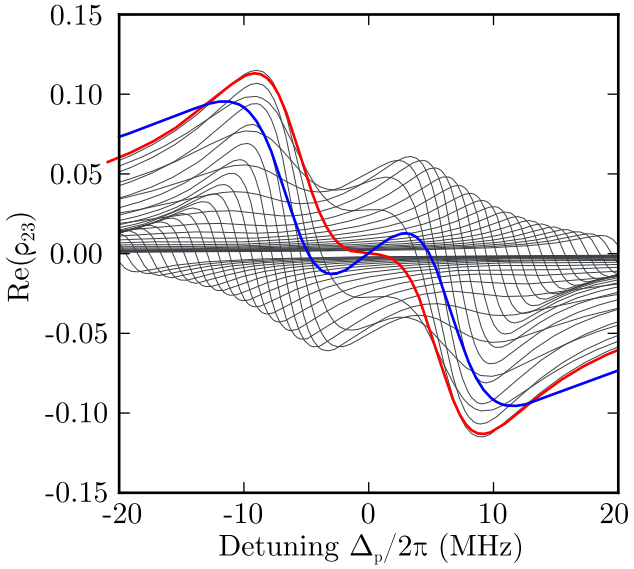

Figure 5.11.: The theoretical excited-state polarisation spectroscopy signal is shown as a function of probe laser detuning Δ_p and atomic velocity v. The red line is the lineshape for $v = 0$ and the blue line is the Doppler-averaged lineshape (multiplied by a factor of four). Each grey line represents a velocity class separated by 2 m/s. Theoretical parameters: probe laser Rabi frequency $\Omega_p/2\pi = 3.3$ MHz, coupling laser Rabi frequency $\Omega_c/2\pi = 12.2$ MHz and temperature $T = 293$ K

ing, the on-resonance gradient is enhanced enabling the ATS-induced sub-feature to be observed at lower coupling Rabi frequencies than with just zero velocity atoms. Similar narrowing effects of thermal averaging have been observed in other systems [125, 126].

5.4.1. Laser Frequency Stabilisation

Both ground-state and excited-state polarisation spectroscopy produce narrow dispersive features which are convenient for laser frequency stabilisation. In the case of excited-state polarisation spectroscopy, the signals have an extremely high signal to noise ratio and are unperturbed by other resonances. In the multi-photon experiments that are discussed in the forthcoming Chapters, both the 852 nm and 1470 nm laser are frequency stabilised on resonance using polarisation spectroscopy. A slight drawback occurs because the two lasers are not independently stabilised to atomic reference signals. As a result, sufficient care must be taken to stabilise the 852 nm laser before attempting to stabilise the 1470 nm laser.

5.5. Summary

In summary, this Chapter considered excited-state spectroscopy in a three-level ladder system in caesium. The excited-state transition at 1470 nm exhibits significant absorption due to the large transition dipole moment. The absorption linewidth of the excited-state transition was derived theoretically and the minimum linewidth found to depend on the preparation of the intermediate state. When this state is coherently prepared from the ground state, the transition linewidth can be sub-natural and this result was confirmed experimentally. Using a strong circularly-polarised coupling beam on the lower transition, it is possible to induce birefringence in the atomic medium. This birefringence can be detected in the absorption of the excited-state probe and was shown to produce narrow dispersive signals when analysed with a polarimeter. Finally, the application of excited-state polarisation spectroscopy to laser frequency stabilisation was considered.

6. Inverted-Wavelength Ladder System

6.1. Introduction

This Chapter outlines an investigation into the caesium three-level ladder system shown in Fig. 6.1. The probe laser with wavelength $\lambda_p = 852$ nm is frequency stabilised to the $\left|6^2S_{1/2}, F = 4\right\rangle \rightarrow \left|6^2P_{3/2}, F' = 5\right\rangle$ closed transition. The coupling laser with wavelength $\lambda_c = 1470$ nm is detuned by Δ_c from the $\left|6^2P_{3/2}, F' = 5\right\rangle \rightarrow \left|7^2S_{1/2}, F'' = 4\right\rangle$ transition. This configuration is referred to as an "inverted wavelength" system as the probe laser wavelength is shorter than the coupling laser wavelength $\lambda_p < \lambda_c$.

An inverted-wavelength system leads to a number of unusual and unexpected effects in a thermal vapour. Firstly, one might expect that a weak probe beam and strong coupling beam could be used to obtain a coherent EIT signal. However, due to Doppler averaging over the atomic velocities in a thermal vapour, the EIT signal is strongly suppressed when the probe and coupling wavelengths are inverted. This peculiar effect, namely the wavelength dependence of EIT, is discussed in Section 6.2.

When the probe laser is no longer weak, incoherent population transfer must be considered. When an atom is excited into the $\left|7^2S_{1/2}, F'' = 4\right\rangle$ state, it can access a large manifold of hyperfine levels through spontaneous decay. This includes the hyperfine levels of both the $\left|6^2P_{1/2}\right\rangle$ and $\left|6^2P_{3/2}\right\rangle$ states. From these intermediate states, an atom can undergo a second spontaneous decay and enter the uncoupled lower hyperfine ground state $\left|6^2S_{1/2}, F = 3\right\rangle$. This optical pumping process is measured experimentally and found to depend on the interaction time between the atom and laser. These results are presented in Section 6.3 and a theoretical model is developed which shows good quantitative agreement to the experimental data.

6.2. Wavelength Dependence of EIT

Electromagnetically induced transparency (EIT), discussed in Section 2.3.1 for a stationary atom, is a coherent process that can be obtained in a three-level ladder system with a weak probe beam on the lower transition and a strong coupling beam on the upper transition. In a thermal vapour however, the ability to observe EIT is strongly dependent on the wavelength ratio λ_p/λ_c between the probe laser wavelength λ_p and the coupling laser wavelength λ_c [127].

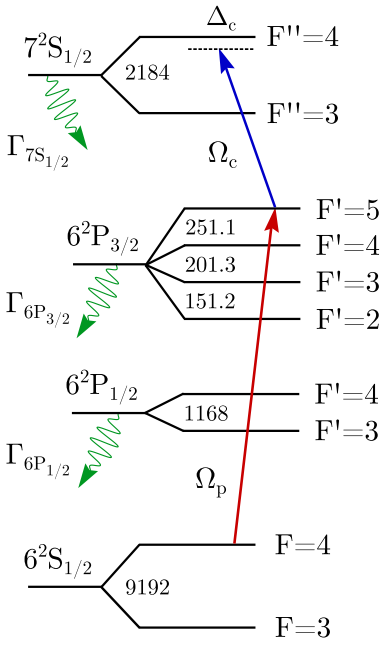

Figure 6.1.: The three-level ladder system with ground state $\left|6^2S_{1/2}\right\rangle$, intermediate state $\left|6^2P_{3/2}\right\rangle$ and final state $\left|7^2S_{1/2}\right\rangle$ becomes a ten-level system when hyperfine splitting and spontaneous emission from open transitions are considered. The splitting between the hyperfine levels are given in MHz.

The wavelength dependence of EIT can be understood theoretically by considering the three-level ladder system shown in Fig. 2.3 with ground state $|1\rangle \equiv \left|6^2S_{1/2}, F = 4\right\rangle$, intermediate state $|2\rangle \equiv \left|6^2P_{3/2}, F' = 5\right\rangle$ and excited state $|3\rangle \equiv \left|7^2S_{1/2}, F'' = 4\right\rangle$. The frequencies of the counter-propagating probe and coupling laser are Doppler-shifted by

$$\Delta_p \rightarrow \Delta_p - k_p v, \tag{6.1}$$

$$\Delta_c \rightarrow \Delta_c - (k_p - k_c)v, \tag{6.2}$$

where v is the atomic velocity perpendicular to the beam and $k_p = 2\pi/\lambda_p$ and $k_c = 2\pi/\lambda_c$ are the wavevectors of the probe and coupling beam respectively. The total Hamiltonian $\hat{\mathcal{H}}_{tot}$ for the three-level system is given by

$$\hat{\mathcal{H}}_{tot} = \hbar \begin{pmatrix} 0 & \Omega_p/2 & 0 \\ \Omega_p/2 & -\Delta_p + k_p v & \Omega_c/2 \\ 0 & \Omega_c/2 & -\Delta_p - \Delta_c + (k_p - k_c)v \end{pmatrix}. \tag{6.3}$$

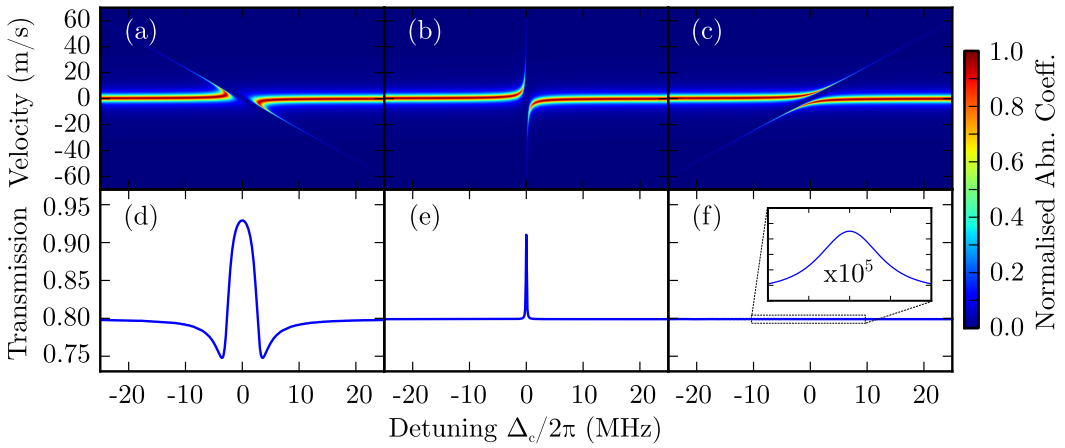

Figure 6.2.: The wavelength dependence of EIT is simulated for an upper-driven three-level ladder system as a function of coupling laser detuning Δ_c. Top panel: Normalised probe absorption coefficient per velocity class for (a) $\lambda_p/\lambda_c = 4/3$ (b) $\lambda_p/\lambda_c = 1$ and (c) $\lambda_p/\lambda_c = 2/3$. Bottom panel: Doppler-averaged probe laser transmission signal corresponding to (a)-(c). Simulation parameters: $\Delta_p = 0$, $\Omega_p/2\pi = 0.01$ MHz, $\Omega_c/2\pi = 5$ MHz, $\Gamma_2/2\pi = 5$ MHz, $\Gamma_3/2\pi = 0.1$ MHz, T = 373 K and L = 2 mm.

The phenomenological decay matrix $\hat{\mathcal{L}}$ for the three-level ladder system is given by

$$\hat{\mathcal{L}} = \frac{1}{2}\begin{pmatrix} 2\Gamma_2\rho_{22} & -\Gamma_2\tilde{\rho}_{12} & -\Gamma_3\tilde{\rho}_{13} \\ -\Gamma_2\tilde{\rho}_{21} & 2\Gamma_3\rho_{33} - 2\Gamma_2\rho_{22} & -(\Gamma_2+\Gamma_3)\tilde{\rho}_{23} \\ -\Gamma_3\tilde{\rho}_{31} & -(\Gamma_2+\Gamma_3)\tilde{\rho}_{32} & -2\Gamma_3\rho_{33} \end{pmatrix}, \tag{6.4}$$

where Γ_2 and Γ_3 are the decay rates of the intermediate $|2\rangle$ and excited $|3\rangle$ states respectively. Inserting the total Hamiltonian $\hat{\mathcal{H}}_{tot}$ in Eq. (6.3) and the decay matrix $\hat{\mathcal{L}}$ in Eq. (6.4) into the Lindblad master equation in Eq. (2.11) results in the equations of motion for the density matrix elements. The steady state can be obtained by setting $\dot{\rho} = 0$ and solving numerically (see Appendix A for more information). The absorption of the probe can be analysed as a function of coupling laser detuning Δ_c and atomic velocity v through the absorption coefficient $\alpha = k_p \mathrm{Im}(\chi)$, where χ is the complex susceptibility given in Eq. (2.15). The probe absorption coefficient is shown in Fig. 6.2 for wavelength ratio (a) $\lambda_p/\lambda_c = 4/3$ (b) $\lambda_p/\lambda_c = 1$ and (c) $\lambda_p/\lambda_c = 2/3$. The probe transmission signals, shown in Fig. 6.2(d-f), are obtained by averaging over the absorption signals from each atomic velocity weighted with the Maxwell-Boltzmann distribution in Eq. (4.3).

In the absence of the coupling laser, the absorption of the probe beam occurs over a small range of atomic velocities $\pm\Gamma_2/2k_p$, determined by the probe wavevector

k_p and the intermediate state decay rate Γ_2. This is shown by the horizontal band of absorption in Fig. 6.2(a-c) and represents the uncoupled eigenstate $|2\rangle$. When the coupling laser is off resonance and does not perturb the levels, it is possible to perform two-photon excitation from the ground state $|1\rangle$ to the excited state $|3\rangle$ using an off-resonant velocity class $v = \Delta_c/(k_p - k_c)$. This is shown by the band of absorption in Fig. 6.2(a-c) with gradient $1/(k_p - k_c)$.

When the coupling laser is near resonance, it strongly perturbs the intermediate state $|2\rangle$ and excited state $|3\rangle$ forming the dressed states $|a^{\pm}\rangle = (|2\rangle \pm |3\rangle)/\sqrt{2}$. In the probe absorption spectrum, this corresponds to an avoided crossing between the undressed eigenstates $|2\rangle$ and $|3\rangle$. The behaviour of this avoided crossing is strongly dependent on the gradient $1/(k_p - k_c)$. When the gradient is negative ($\lambda_p > \lambda_c$) as shown in Fig. 6.2(a) and (d), a large, broad EIT transparency is created. Enhanced absorption can be observed in the wings of the EIT peak due to two-photon excitation of the excited state $|3\rangle$ with non-zero velocity atoms.

When the gradient is infinite ($\lambda_p = \lambda_c$) as shown in Fig. 6.2(b) and (e), a narrow EIT peak is formed in the probe absorption profile. This occurs because the Doppler shift of the probe beam is exactly cancelled by the Doppler shift of the counter-propagating coupling beam. Finally, when the gradient is positive ($\lambda_p < \lambda_c$) as shown in Fig. 6.2(c) and (f), there is no transparency "window" in the probe absorption. As a result, the broad EIT peak is significantly suppressed. The ladder system under consideration in this Chapter is an inverted-wavelength system with $\lambda_p/\lambda_c \simeq 0.58$. As a result, EIT is difficult to observe in a thermal vapour.

6.3. Population Transfer

6.3.1. Atom-Laser Interaction Time

In a thermal vapour, it is important to consider the finite atom-laser interaction time. Although the beam size is fixed, each atom experiences a different path length through the beam and travels at a different speed. This creates a distribution of atom-laser interaction times.

Full Distribution

Consider a circular beam with radius a and uniform intensity propagating through a random distribution of thermal atoms. The probability distribution $F(l)$ for an atom passing through a length l of the beam is given by [114]

$$F(l) = \frac{l}{2a\sqrt{4a^2 - l^2}}, \tag{6.5}$$

where the length $0 \leq l \leq 2a$. The speed of an atom through the beam can be described by the Maxwell-Boltzmann distribution in Eq. (4.3). Therefore the probability distribution $G(t,l)$ for an atom taking a time t to pass through a length l of the beam is given by [114]

$$G(t,l) = \frac{ml^2}{k_\mathrm{B}Tt^3} \exp\left(-\frac{ml^2}{2k_\mathrm{B}Tt^2}\right). \tag{6.6}$$

In order to obtain the interaction time distribution $H(t)$, the length distribution $F(l)$ must be convolved with the speed distribution $G(t,l)$ by integrating over the range of path lengths

$$\begin{aligned} H(t) &= \int_{l=0}^{2a} G(t,l)\ F(l)\ \mathrm{d}l, & (6.7)\\ &= -\frac{1}{t} + \frac{\sqrt{\pi}}{2\tau}\left(1+\frac{2\tau^2}{t^2}\right)\exp\left(-\frac{\tau^2}{t^2}\right)\mathrm{erfi}\left(\frac{\tau}{t}\right), & (6.8) \end{aligned}$$

where $\tau = 2a/v_\mathrm{p}$ is the most probable interaction time and erfi is the complex error function.

Transit Time Approximation

Alternatively, one can analyse the probability $P(t)$ that an atom will remain in the beam after a time t. Assuming the loss from the beam can be considered as a relaxation process, the probability $P(t) = \exp(-\Gamma_\mathrm{t} t)$. The transit time decay constant Γ_t can be expressed as [128]

$$\Gamma_\mathrm{t} = \frac{\bar{v}}{\bar{d}} = \frac{2}{\sqrt{\pi}}\frac{v_\mathrm{p}}{D}, \tag{6.9}$$

where $\bar{v}$ is the average two-dimensional atomic speed, $\bar{d}$ is the average path length across the circular beam cross section, $v_\mathrm{p} = \sqrt{2k_\mathrm{B}T/m}$ is the most probable speed and D is the full-width at half-maximum of the beam. The average interaction time is therefore given by $\tau_\mathrm{t} = 1/\Gamma_\mathrm{t}$.

6.3.2. Long Interaction Time

Consider the effect of applying just the probe laser on resonance $\Delta_\mathrm{p} = 0$ between the ground state $\left|6^2\mathrm{S}_{1/2}, F=4\right\rangle$ and the intermediate state $\left|6^2\mathrm{P}_{3/2}, F'=5\right\rangle$. Atoms in the ground state $\left|6^2\mathrm{S}_{1/2}, F=4\right\rangle$ are excited to the hyperfine sublevels of the

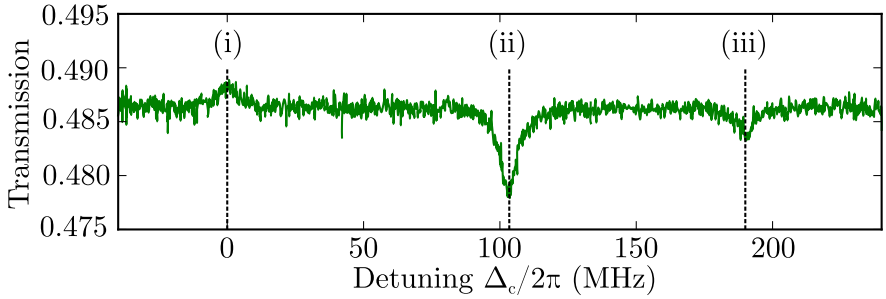

Figure 6.3.: The probe transmission spectrum is shown as a function of coupling laser detuning Δ_c. The two-photon transitions to the excited state $\left|7^2S_{1/2}, F'' = 4\right\rangle$ via the hyperfine levels of the intermediate state $\left|6^2P_{3/2}\right\rangle$ are indicated by dashed vertical lines (i) $F' = 5$ (ii) $F' = 4$ and (iii) $F' = 3$. Experimental parameters: probe laser Rabi frequency $\Omega_p/2\pi = 1.3$ MHz, probe laser waist $w_p = 730$ μm, probe laser detuning $\Delta_p = 0$, coupling laser Rabi frequency $\Omega_c/2\pi = 6.6$ MHz, coupling laser waist $w_c = 990$ μm, cell length $L = 5$ cm and temperature $T = 293$ K.

intermediate state with velocities centred around

$$\left|6^2S_{1/2}, F = 4\right\rangle \rightarrow \left|6^2P_{3/2}, F' = 5\right\rangle : \qquad v = 0 \text{ m/s} \tag{6.10a}$$

$$\left|6^2S_{1/2}, F = 4\right\rangle \rightarrow \left|6^2P_{3/2}, F' = 4\right\rangle : \qquad v = \frac{\Delta_{45}}{k_p} = 214 \text{ m/s} \tag{6.10b}$$

$$\left|6^2S_{1/2}, F = 4\right\rangle \rightarrow \left|6^2P_{3/2}, F' = 3\right\rangle : \qquad v = \frac{\Delta_{35}}{k_p} = 385 \text{ m/s} \tag{6.10c}$$

where $\Delta_{45}/2\pi = -251$ MHz is the hyperfine splitting between sublevels $F' = 4$ and $F' = 5$ and $\Delta_{35}/2\pi = -452$ MHz is the hyperfine splitting between sublevels $F' = 3$ and $F' = 5$. Whilst atoms excited to the $F' = 5$ sublevel can only decay back to the upper hyperfine ground state $F = 4$, atoms excited to the $F' = 3$ and $F' = 4$ sublevels can also decay back to the lower hyperfine ground state $F = 3$. Once an atom enters this state, it is no longer coupled by the probe laser and remains in this state until the atom decoheres, for example in a collision with another atom or the walls of the vapour cell. This time-dependent process is known as spectral hole burning [129] and continues until all atoms with velocities given by Eq. (6.10) have entered the lower hyperfine ground state $F = 3$ or the atoms leave the beam. As a result, the average level of probe absorption is determined by the atom-laser interaction time [130].

Now consider the effect of applying both the probe and coupling laser simultaneously. The probe transmission spectrum is shown in Fig. 6.3 as a function of coupling laser detuning Δ_c. The spectrum is obtained in a 5 cm vapour cell at room temperature $T = 293$ K with large collimated beams for long atom-laser interaction times. The spectrum exhibits three transitions between the intermediate state

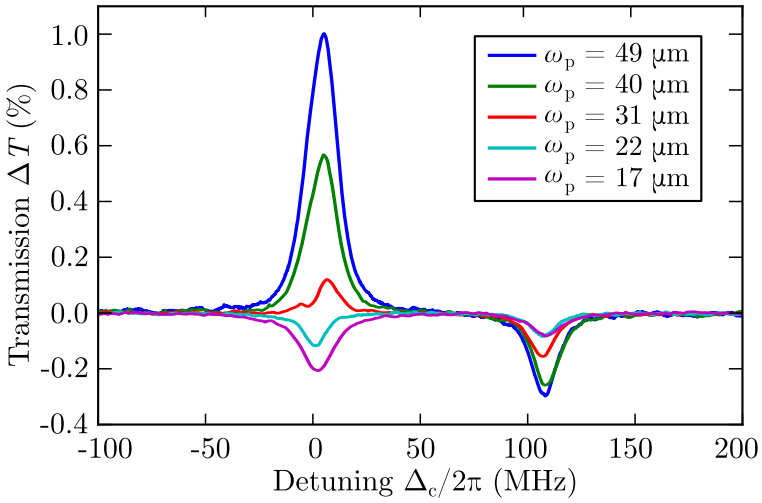

Figure 6.4.: The probe transmission spectrum is shown as a function of coupling laser detuning Δ_c and probe beam waist w_p. Experimental parameters: probe laser Rabi frequency $\Omega_p/2\pi = 8$ MHz, coupling laser Rabi frequency $\Omega_c/2\pi = 22$ MHz, coupling laser waist $w_c = 20$ μm, cell length $L = 100$ μm and temperature $T = 373$ K.

$|6^2P_{3/2}\rangle$ hyperfine levels (i) $F' = 5$ (ii) $F' = 4$ and (iii) $F' = 3$ and the excited state $|7^2S_{1/2}, F'' = 4\rangle$. The coupling laser detuning at which the features occurs is given $\Delta_c = (k_p - k_c)v$ where v is the atomic velocity given by Eqs. (6.10).

When the coupling laser is on resonance $\Delta_c = 0$, a transparency feature is observed. This occurs because atoms which are excited into the excited state $|7^2S_{1/2}, F'' = 4\rangle$ can decay via the hyperfine levels of the intermediate states $|6^2P_{3/2}\rangle$ and $|6^2P_{1/2}\rangle$ to the lower hyperfine ground state $|6^2S_{1/2}, F = 3\rangle$. Once the atoms are pumped into this state, they can no longer be absorbed by the probe laser and the average level of absorption is reduced. This process is known as Double Resonance Optical Pumping (DROP) [131] and is a time-dependent transfer of atoms between the hyperfine levels of the ground state via a two-photon excitation process.

When the coupling laser is off resonance $\Delta_c/2\pi \simeq 106$ MHz and $\Delta_c/2\pi \simeq 190$ MHz, an absorptive feature is observed. In order to understand this feature, it is important to remember that in the absence of the coupling laser, atoms in the $F' = 4$ and $F' = 3$ states can decay to the lower hyperfine ground state $F = 3$. However, when the coupling is applied, the number of routes to the lower hyperfine ground state $F = 3$ are reduced. Atoms which decay into $F' = 5$ state can only decay to the upper hyperfine ground state $F = 4$.

6.3.3. Short Interaction Time

The probe transmission spectrum is shown as a function of coupling laser detuning Δ_c and probe beam waist w_p in Fig. 6.4. The probe beam size was varied using an

iris and the exact size confirmed using a knife edge and photodiode. Unfortunately, due to experimental constraints, it was not possible to match the coupling beam size with probe beam size. Instead, the coupling beam size was fixed at the smallest possible size $w_c = 20$ μm. Whilst this does not affect the conclusions regarding the atomic dynamics, it simply reduces the feature visibility as some atoms do not interact with the coupling laser.

As the beams are tightly focused by a 5 cm lens, a 100 μm vapour cell at temperature $T = 373$ K is utilised so that the beam size does not vary appreciably over the cell length. Furthermore, the probe and coupling Rabi frequency are maintained at $\Omega_p/2\pi = 8$ MHz and $\Omega_c/2\pi = 22$ MHz for all measurements. When the probe beam size is reduced, the DROP transparency feature observed on resonance $\Delta_c = 0$ decreases in size and becomes an absorptive feature when $w_p < 31$ μm. As the coupling beam size is fixed, the excitation from the $\left|6^2P_{3/2}, F' = 5\right\rangle$ state to the $\left|7^2S_{1/2}, F'' = 4\right\rangle$ state always occurs for a fixed period of time, regardless of the probe beam size. Therefore the size of the probe beam determines how long the atomic dynamics are able to evolve before the atom leaves the beam. When the probe beam size is small and comparable to the size coupling beam, atoms which are excited into the $\left|7^2S_{1/2}, F'' = 4\right\rangle$ state almost immediately leave the probing region. As a result of the two-photon absorption process, the probe absorption is increased. However, when the probe beam size is large, atoms which are excited into the $\left|7^2S_{1/2}, F'' = 4\right\rangle$ state by the coupling laser are able to spontaneously decay to the lower hyperfine ground state $F = 4$ before they leave the probing region. As a result, the absorption of the probe decreases due to DROP.

The feature at $\Delta_c/2\pi \simeq 106$ MHz remains absorptive but decreases in size when the probe beam size is reduced. This occurs because the interaction time is sufficiently short that atoms do not decay from the $F'' = 4$ state and repopulate the upper hyperfine ground state $F = 4$. Therefore the decrease in interaction time simply weakens the closure of optical pumping.

6.3.4. Theoretical Model

The interaction time dependence of the feature at $\Delta_c = 0$ can be further investigated using a five-level theoretical model shown in Fig. 6.5. The five levels of the model represent the following hyperfine levels in the real system

$$|1\rangle \equiv \left|6^2S_{1/2}, F = 4\right\rangle, \tag{6.11a}$$

$$|2\rangle \equiv \left|6^2P_{3/2}, F' = 5\right\rangle, \tag{6.11b}$$

$$|3\rangle \equiv \left|7^2S_{1/2}, F'' = 4\right\rangle, \tag{6.11c}$$

$$|4\rangle \equiv \left|6^2P_{3/2}, F' = 3, 4\right\rangle \text{ and } \left|6^2P_{1/2}, F' = 3, 4\right\rangle, \tag{6.11d}$$

$$|5\rangle \equiv \left|6^2S_{1/2}, F = 3\right\rangle, \tag{6.11e}$$

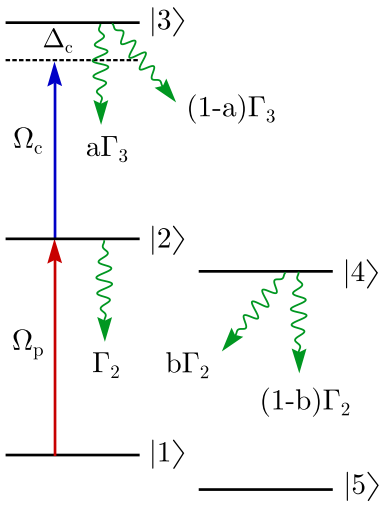

Figure 6.5.: Five-level model for the resonant atomic dynamics in an upper-driven ladder system. The ground state $|1\rangle$ is coupled to the intermediate state $|2\rangle$ by probe Rabi frequency Ω_p. The intermediate state is coupled to the excited state $|3\rangle$ by coupling Rabi frequency Ω_c. The excited state can spontaneously decay back state $|3\rangle$ or to uncoupled intermediate levels represented by state $|4\rangle$. Furthermore, the uncoupled state $|4\rangle$ can decay to the coupled ground state $|1\rangle$ or the uncoupled ground state $|5\rangle$. Once atomic population enters state $|5\rangle$, it cannot be recovered. The level of loss from the coupled system is determined by the branching ratios a and b.

where states $|1\rangle$, $|2\rangle$ and $|3\rangle$ are coupled by laser fields and states $|4\rangle$ and $|5\rangle$ serve as loss mechanisms from the three-level ladder system. The branching ratio a determines the amount of population which spontaneously decays from state $|3\rangle$ to state $|2\rangle$. Population which does not decay back to $|2\rangle$ is temporarily lost to state $|4\rangle$ and represents decay to uncoupled intermediate state hyperfine levels. There is a further branching ratio b which determines whether population decays back to the upper hyperfine ground state $|1\rangle$ or is lost into the uncoupled hyperfine ground state $|5\rangle$.

The total Hamiltonian $\hat{\mathcal{H}}_\mathrm{tot}$ for the five-level model system is given by

$$\hat{\mathcal{H}}_\mathrm{tot} = \hbar \begin{pmatrix} 0 & \Omega_\mathrm{p}/2 & 0 & 0 & 0 \\ \Omega_\mathrm{p}/2 & -\Delta_\mathrm{p} + k_\mathrm{p} v & \Omega_\mathrm{c}/2 & 0 & 0 \\ 0 & \Omega_\mathrm{c}/2 & -\Delta_\mathrm{c} + (k_\mathrm{p} - k_\mathrm{c}) v & 0 & 0 \\ 0 & 0 & 0 & 0 & 0 \\ 0 & 0 & 0 & 0 & 0 \end{pmatrix}. \tag{6.12}$$

The phenomenological decay matrix for the atom $\hat{\mathcal{L}}_{\rm a}$ is given by

$$\mathcal{L}_{\rm a}^{11} = \Gamma_2\rho_{22} + b\Gamma_2\rho_{44}, \tag{6.13a}$$
$$\mathcal{L}_{\rm a}^{22} = a\Gamma_3\rho_{33} - \Gamma_2\rho_{22}, \tag{6.13b}$$
$$\mathcal{L}_{\rm a}^{33} = -\Gamma_3\rho_{33}, \tag{6.13c}$$
$$\mathcal{L}_{\rm a}^{44} = (1-a)\Gamma_3\rho_{33} - \Gamma_2\rho_{44}, \tag{6.13d}$$
$$\mathcal{L}_{\rm a}^{55} = (1-b)\Gamma_2\rho_{44}, \tag{6.13e}$$
$$\mathcal{L}_{\rm a}^{ij} = -\frac{\Gamma_i + \Gamma_j}{2}\tilde{\rho}_{ij}. \tag{6.13f}$$

Furthermore, the finite atom-laser interaction can be included using the effective transit time decay $\Gamma_{\rm t}$ given in Eq. (6.9). The effect of the transit time is to redistribute the atomic population among the ground states $|1\rangle$ and $|5\rangle$. The phenomenological decay matrix for the transit time $\mathcal{L}_{\rm t}$ is given by

$$\mathcal{L}_{\rm t}^{11} = \frac{\Gamma_{\rm t}}{2}\left(\rho_{22} + \rho_{33} + \rho_{44} + 2\rho_{55} - 2\rho_{11}\right), \tag{6.14a}$$
$$\mathcal{L}_{\rm t}^{22} = -\Gamma_{\rm t}\rho_{22}, \tag{6.14b}$$
$$\mathcal{L}_{\rm t}^{33} = -\Gamma_{\rm t}\rho_{33}, \tag{6.14c}$$
$$\mathcal{L}_{\rm t}^{44} = -\Gamma_{\rm t}\rho_{44}, \tag{6.14d}$$
$$\mathcal{L}_{\rm t}^{55} = \frac{\Gamma_{\rm t}}{2}\left(\rho_{22} + \rho_{33} + \rho_{44} + 2\rho_{11} - 2\rho_{55}\right), \tag{6.14e}$$

where off-diagonal elements $\mathcal{L}_{\rm t}^{ij} = 0$. The total Hamiltonian $\hat{\mathcal{H}}_{\rm tot}$ in Eq. (6.12) and the total decay matrix $\hat{\mathcal{L}} = \hat{\mathcal{L}}_{\rm a} + \hat{\mathcal{L}}_{\rm t}$ given by Eq. (6.13) and Eq. (6.14) can be inserted into the Lindblad master equation in Eq. (2.11) to obtain the velocity-dependent equations of motion for the density matrix elements. The Doppler-averaged probe transmission signal can be obtained by averaging over the Maxwell-Boltzmann velocity distribution and substituting the steady state probe coherence $\tilde{\rho}_{21}$ into the expression for the complex susceptibility χ given by Eq. (2.15). The theoretical change in the probe transmission ΔT can be calculated from the difference in the probe transmission with and without the coupling laser.

The theoretical change in probe transmission is shown as a function of the combined probe and coupling beam size in Fig. 6.6. The probe and coupling laser detuning $\Delta_{\rm p} = \Delta_{\rm c} = 0$. As shown in the experimental results, the feature changes from absorption to transmission when the beam size $w_0 \simeq 30$ μm. Furthermore, the inset panel shows the probe transmission signal as a function of coupling laser detuning $\Delta_{\rm c}$ for beam size $w_0 = 17$ μm and $w_0 = 49$ μm. The lineshape profiles show good agreement to the experimental results.

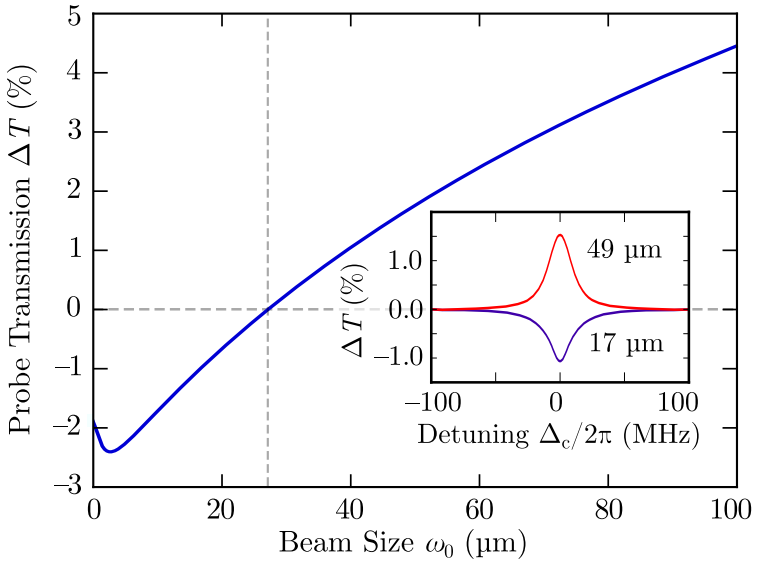

Figure 6.6.: Theoretical change in probe transmission as a function of combined beam waist w_0 with resonant probe and coupling lasers $\Delta_p = \Delta_c = 0$. Inset: Change in probe transmission as a function of coupling laser detuning for combined beam waist $w_0 = 17$ μm and $w_0 = 49$ μm. Theoretical parameters: probe Rabi frequency $\Omega_p/2\pi = 10$ MHz, coupling Rabi frequency $\Omega_c/2\pi = 27$ MHz, temperature $T = 373$ K and branching ratios $a = 0.2$ and $b = 0.3$.

6.4. Summary

This Chapter considered a three-level inverted-wavelength system where $\lambda_p < \lambda_c$. The wavelength dependence of EIT was presented using a simple three-level theoretical model. Although it is not possible to observe EIT in this system, incoherent population transfer processes arise due to the open transition between the intermediate and excited state. These processes were shown to depend strongly on the beam size and therefore the interaction time between the atom and the laser. A simple theoretical model was developed which shows good quantitative agreement to the experimental results.

7. Rydberg-State Spectroscopy

7.1. Introduction

Direct optical detection of Rydberg states is a difficult task due to the weak coupling with the ground state [59]. This has led to the development of a number of alternative methods for conducting Rydberg-state spectroscopy. A destructive, yet highly efficient technique, involves applying a large electric field to ionise the Rydberg atom [34]. The constituent ion and electron can then be detected using a sensitive micro-channel plate. Non-destructive techniques where the Rydberg state remains unperturbed during detection are particularly desirable, for example in quantum information processing applications [41, 52]. Coherent electromagnetically induced transparency (EIT) is a multi-photon non-destructive technique that transfers the weak Rydberg transition onto a strong optical transition [53]. Electron shelving (ES) is an incoherent non-destructive technique that utilises a strong probe beam to excite atomic population into the long-lived Rydberg state. As the lifetime of the Rydberg state is orders of magnitude longer than the excited states, the absorption of the probe beam is significantly modified [59].

In this Chapter, Rydberg-state spectroscopy is extended to a four-level ladder system in a thermal vapour of caesium. The three-photon excitation scheme is shown in Fig. 7.1(a-b). The ground state $|1\rangle \equiv \left|6^2\mathrm{S}_{1/2}, F = 4\right\rangle$ is coupled to the intermediate state $|2\rangle \equiv \left|6^2\mathrm{P}_{3/2}, F' = 5\right\rangle$ by a probe laser with wavelength $\lambda_\mathrm{p} = 852$ nm and Rabi frequency Ω_p. The intermediate state is coupled to the excited state $|3\rangle \equiv \left|7^2\mathrm{S}_{1/2}, F'' = 4\right\rangle$ by a coupling laser with wavelength $\lambda_\mathrm{c} = 1470$ nm and Rabi frequency Ω_c. Finally, the excited state is coupled to the Rydberg state $|4\rangle \equiv \left|26^2\mathrm{P}_{3/2}\right\rangle$ by the Rydberg laser with wavelength $\lambda_\mathrm{r} = 790$ nm and Rabi frequency Ω_r. Furthermore, it is useful to consider the semi-dressed state picture shown in Fig. 7.1(c) where the dressed states $|a^\pm\rangle = (|2\rangle \pm |3\rangle)/\sqrt{2}$ result from the application of a strong resonant coupling field Ω_c. This allows the four-level system to be reduced to two three-level ladder systems $|1\rangle \rightarrow |a^\pm\rangle \rightarrow |4\rangle$.

This multi-photon excitation scheme has a number of benefits. Traditional two-photon excitation schemes to Rydberg states in alkali metals require an upper transition laser with wavelength $\lambda_\mathrm{r} \approx 450$ nm. Due to the difficulty in obtaining a high power diode laser which operates in this wavelength range, frequency-doubled lasers are often utilised. These lasers have a number of disadvantages including cost, size,

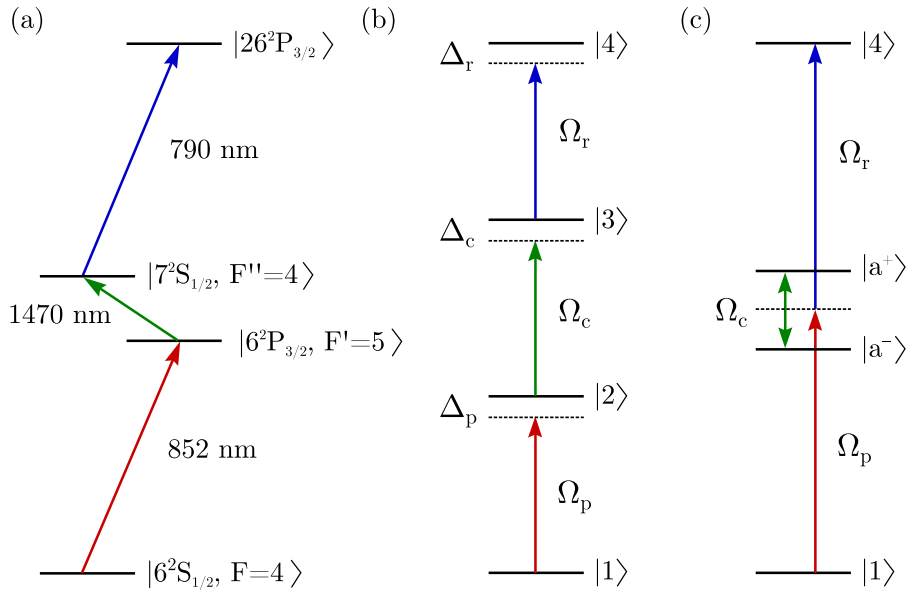

Figure 7.1.: Three-photon excitation scheme to Rydberg states in caesium. (a) Atomic energy level diagram. (b) Bare state energy level diagram. (c) Semi-dressed state energy level diagram where $|a^{\pm}\rangle = (|2\rangle \pm |3\rangle)\sqrt{2}$.

tuneability and limited power output. The three-photon excitation scheme overcomes all of these drawbacks by using infrared diode lasers on all three transitions. Furthermore, as the upper transition wavelength $780 \lesssim \lambda_r \lesssim 795$ nm, tapered amplifier systems are available with a power output in excess of 1.5 W. This is particularly important when exciting high Rydberg states as the transition dipole moment d scales as $n^{*-3/2}$.

This Chapter is divided into two parts. In Section 7.1, coherent three-photon EIT is examined and an analytical expression for the probe susceptibility is derived. In Section 7.2, incoherent electron shelving is presented and a theoretical model is employed to model the probe transmission lineshapes.

7.2. Three-Photon EIT

7.2.1. Experimental Results

The experimental results presented in this Section are acquired in a 2.4 mm vapour cell maintained at temperature $T = 323$ K. The $1/e^2$ waist of the probe, coupling and Rydberg laser is measured to be 14 μm, 30 μm and 20 μm respectively. The three-photon Doppler shift Δ_{3ph} is minimised by counter-propagating the probe laser against both the coupling and Rydberg laser such that

$$\Delta_{3ph} = \Delta_p + \Delta_c + \Delta_r - (k_p - k_c - k_r)v. \tag{7.1}$$

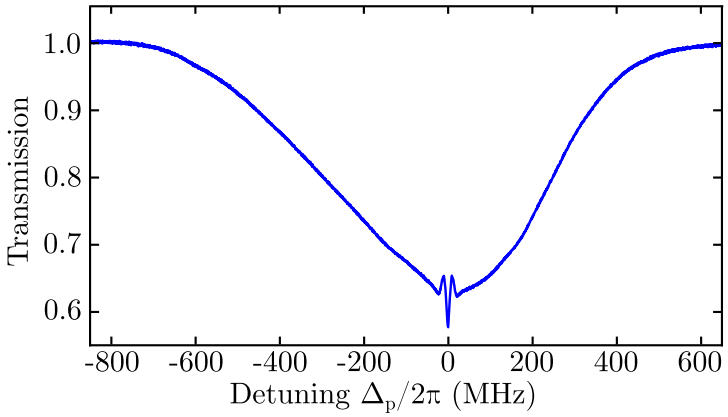

Figure 7.2.: Probe transmission spectrum as a function of probe laser detuning Δ_p. Experimental parameters: probe laser Rabi frequency $\Omega_p/2\pi = 6$ MHz, coupling laser Rabi frequency $\Omega_c/2\pi = 390$ MHz and Rydberg laser Rabi frequency $\Omega_r/2\pi = 275$ MHz.

A typical spectrum obtained when the probe detuning Δ_p is varied around resonance is shown in Fig. 7.2. Within the Doppler-broadened absorption lineshape, a narrow spectral feature is observed with enhanced absorption on resonance and enhanced transmission either side of resonance. This lineshape can be understood by considering the dressed state picture shown in Fig. 7.1(c) where the system now contains two three-level ladder EIT systems [132]. The result is two dark states which overlap in frequency space and interfere constructively to give enhanced or electromagnetically induced absorption (EIA) [133].

A typical spectrum obtained when the Rydberg detuning Δ_r is varied around resonance is shown in Fig. 7.3. The lineshape is similar to that observed in Fig. 7.2, but on a flat transmission background determined by the probe absorption. The EIA feature which appears at $\Delta_r = 0$ corresponds to $v = 0$ atoms which are in three-photon resonance between the ground state and the Rydberg state, i.e. $|1\rangle$–$|2\rangle$–$|3\rangle$–$|4\rangle$. The EIT features which appear at $\Delta_r^{\pm}/2\pi \simeq \pm 10$ MHz, correspond to non-zero velocity atoms which are in two-photon resonance between the ground state and the Rydberg state, i.e. $|1\rangle$–$|a^{\pm}\rangle$–$|4\rangle$.

The probe transmission spectrum is shown in Fig. 7.4 as a function of Rydberg laser detuning Δ_r and fixed coupling laser detuning Δ_c. When the coupling laser is detuned from resonance, the symmetry between the dressed states is broken and the EIA feature is suppressed. Instead, two EIT peaks can be observed at non-resonant Rydberg laser detunings.

The Rydberg detuning $\Delta_r^{\pm}$ of the dark states can be understood by considering the eigenstates and eigenenergies of the four-level system. In order for the probe to be absorbed, the ground state $|1\rangle$ must be in resonance with one of the dressed

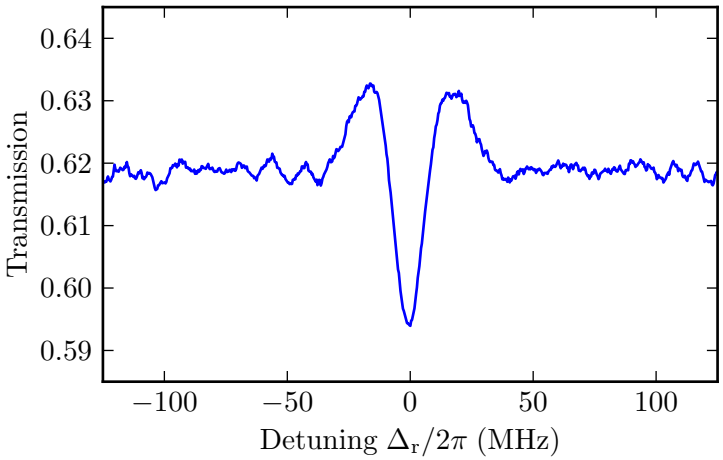

Figure 7.3.: Probe transmission spectrum as a function of Rydberg laser detuning Δ_r. Experimental parameters: probe laser Rabi frequency $\Omega_p/2\pi = 6$ MHz, coupling laser Rabi frequency $\Omega_c/2\pi = 156$ MHz and Rydberg laser Rabi frequency $\Omega_r/2\pi = 125$ MHz.

states $|a^{\pm}\rangle$, as shown in Fig. 7.1(c). The dressed state energies are dependent on the atomic velocity v and are given by

$$E^{\pm} = \hbar\omega^{\pm} = \frac{\hbar}{2}\left[(\Delta_{1ph} + \Delta_{2ph}) \pm \sqrt{(\Delta_{1ph} - \Delta_{2ph})^2 + \Omega_c^2}\right], \tag{7.2}$$

where $\Delta_{1ph} = -k_p v$ is the one-photon Doppler shift and $\Delta_{2ph} = \Delta_c - (k_p - k_c)v$ is the two-photon Doppler shift. The probe laser is assumed to be weak $\Omega_p \ll \Gamma_2$ and stabilised on resonance $\Delta_p = 0$.

The ground state $|1\rangle$ is in resonance with the dressed states $|a^{\pm}\rangle$ when $E^{\pm} = 0$. With this condition, the expression in Eq. (7.2) can be rearranged to determine the atomic velocity that is required

$$v^{\pm} = \frac{\Delta_c \pm \sqrt{\Delta_c^2 + (1 + {}^{k_c}/_{k_p})\Omega_c^2}}{2(k_p - k_c)}. \tag{7.3}$$

Finally, the three-photon Doppler shift which is given by

$$\Delta_{3ph} = \Delta_c + \Delta_r - (k_p - k_c - k_r)v^{\pm}, \tag{7.4}$$

can be used to determine the Rydberg laser detuning $\Delta_r^{\pm}$ of the dark states as a function of coupling laser detuning Δ_c. The ground state $|1\rangle$ is in resonance with the Rydberg state $|4\rangle$ when the three-photon detuning $\Delta_{3ph} = 0$ and the resulting

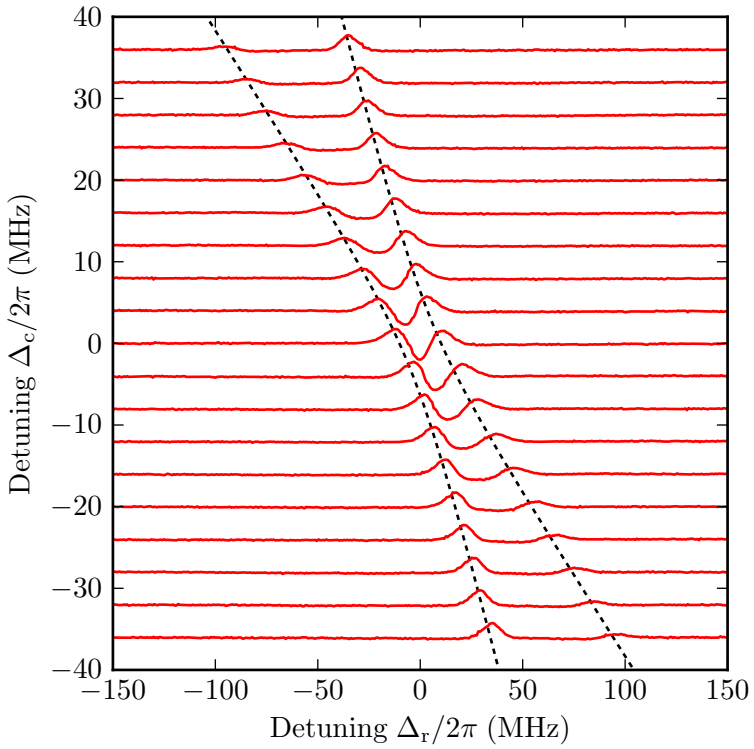

Figure 7.4.: Probe transmission spectrum as a function of Rydberg laser detuning Δ_r. As the fixed coupling laser detuning $|\Delta_c|$ is increased, the dark states $|a^{\pm}\rangle$ are separated and the enhanced absorption is suppressed. The dashed lines show the theoretical position of the dark state resonances given by Eq. (7.5). Experimental parameters: probe laser Rabi frequency $\Omega_p/2\pi = 6$ MHz, coupling laser Rabi frequency $\Omega_c/2\pi = 156$ MHz and Rydberg laser Rabi frequency $\Omega_r/2\pi = 125$ MHz.

dark state resonances are therefore located at

$$\Delta_r^{\pm} = -\Delta_c + (k_p - k_c - k_r)v^{\pm}. \tag{7.5}$$

This theoretical calculation is applied to the experimental data in Fig. 7.4 (shown by the dashes lines) and shows excellent agreement. In the limit of far detuning $\Delta_c \gg \Omega_c$, the dark state detuning $\Delta_r^{\pm}$ given in Eq. (7.5) tends to the following values

$$\Delta_r^{-} \rightarrow -\Delta_c, \tag{7.6a}$$

$$\Delta_r^{+} \rightarrow -\left(\frac{k_r}{k_p - k_c}\right)\Delta_c. \tag{7.6b}$$

7.2.2. Theoretical Model

In the weak probe approximation, the complex susceptibility per velocity class for a four-level ladder system is given by [134]

$$\chi(v)\mathrm{d}v = f(v)\mathrm{d}v\frac{\mathrm{i}d_{21}^2}{\epsilon_0\hbar}\left[\frac{\Gamma_2}{2} + ik_\mathrm{p}v + \frac{i\Omega_\mathrm{c}}{2}\frac{\tilde{\rho}_{31}}{\tilde{\rho}_{21}}\right]^{-1}, \tag{7.7}$$

where d_{21} is the probe dipole moment and $f(v)\mathrm{d}v$ is the atomic velocity distribution given in Eq. (4.3). The density matrix elements ρ_{21}, ρ_{31} and ρ_{41} represent the coherences between the ground state $|1\rangle$ and excited states $|2\rangle$, $|3\rangle$ and $|4\rangle$ respectively. The ratio $\tilde{\rho}_{31}/\tilde{\rho}_{21}$ between the coherences is given by [134]

$$\frac{\tilde{\rho}_{31}}{\rho_{21}} = -\frac{i\Omega_\mathrm{c}}{2}\left[\frac{\Gamma_3}{2} + i(k_\mathrm{p} - k_\mathrm{c})v + \frac{i\Omega_\mathrm{r}}{2}\frac{\tilde{\rho}_{41}}{\tilde{\rho}_{31}}\right]^{-1}, \tag{7.8}$$

where the coherence ratio ρ_{41}/ρ_{31} can be expressed as [134]

$$\frac{\tilde{\rho}_{41}}{\tilde{\rho}_{31}} = -\frac{i\Omega_\mathrm{r}}{2}\left[\gamma_\mathrm{r} - i\Delta_\mathrm{r} + i(k_\mathrm{p} - k_\mathrm{c} - k_\mathrm{r})v\right]^{-1}. \tag{7.9}$$

The dephasing of the Rydberg state due to transit time broadening and laser intensity variations is included through γ_r. The decay rates of states $|2\rangle$ and $|3\rangle$ are given by Γ_2 and Γ_3 respectively. The total complex susceptibility χ_tot is given by integrating Eq. (7.7) over all velocity classes. The total absorption coefficient is given by $\alpha_\mathrm{tot} = k_\mathrm{p}\mathrm{Im}(\chi_\mathrm{tot})$. Whilst this simple four-level model provides a good qualitative foundation, a full quantitive comparison can be obtained by averaging over all magnetic sublevels and the variation in Rabi frequency along the length of the cell.

7.2.3. Doppler-Compensated EIT

The normalised probe absorption coefficient is shown as a function of Rydberg laser detuning Δ_r and atomic velocity v in the top panel of Fig. 7.5. The Rabi frequency ratio $\mathcal{R} = \Omega_\mathrm{c}/\Omega_\mathrm{r}$ is varied between (a) $\mathcal{R} = 0.6$, (b) $\mathcal{R} = 1.2$ and (c) $\mathcal{R} = 2.5$. The horizontal lines of absorption occur at atomic velocities $v^\pm$ given by Eq. (7.3) and correspond to the dressed states $|a^\pm\rangle$. Due to the strong coupling with the Rydberg state $|4\rangle$, there is an avoided crossing between each of the dressed state $|a^\pm\rangle$ and this occurs at Rydberg laser detuning $\Delta_\mathrm{r}^\pm$ as given by Eq. (7.5). This can be understood as an interaction with the Rydberg state $|4\rangle$ which appears as a straight line passing through the origin with negative gradient $1/(k_\mathrm{p} - k_\mathrm{c} - k_\mathrm{r})$. As a result of this double avoided crossing, two dark states are formed off resonance whilst a bright state or enhanced absorption occurs on resonance. The exact behaviour of the bright state, particularly the resonant gradient, is determined by the Rabi frequency ratio as

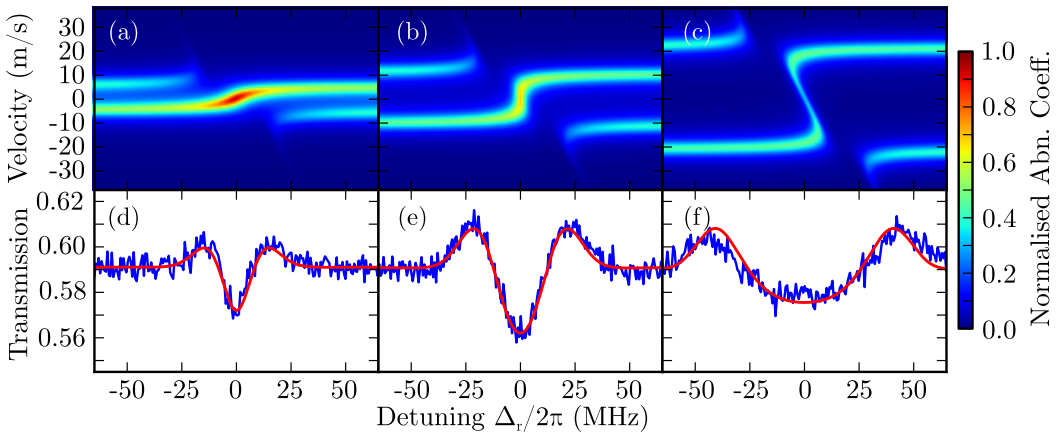

Figure 7.5.: Top panel: Normalised absorption coefficient per velocity classes from the four-level theoretical model for Rabi frequency ratio $\mathcal{R} = \Omega_c/\Omega_r$ = (a) 0.6 (b) 1.2 and (c) 2.5. At the optimum ratio of 1.2, calculated from Eq. (7.11), the bright state is insensitive to the atomic velocity. Bottom panel: Probe transmission spectra with fits from the full theoretical model for different values of coupling laser Rabi frequency $\Omega_c/2\pi$ = (d) 73 MHz, (e) 156 MHz and (f) 324 MHz. Experimental parameters: probe laser Rabi frequency $\Omega_p/2\pi = 6$ MHz, Rydberg laser Rabi frequency $\Omega_r/2\pi = 125$ MHz and laser detunings $\Delta_p = \Delta_c = 0$ MHz.

shown in Fig. 7.5(a-c). When the ratio $\mathcal{R} < 1.2$, the gradient is positive whilst for $\mathcal{R} > 1.2$, the gradient is negative. In between these two regimes at $\mathcal{R} = 1.2$, the gradient of the bright state is infinite. This corresponds to a velocity-insensitive resonance where the three-photon Doppler shift is compensated by the AC stark dressing of the coupling and Rydberg laser [135].

The experimental probe transmission spectra, fit with the full theoretical model, are shown in Fig. 7.5(d-f) as a function of coupling Rabi frequency Ω_c. As predicted by the simple four-level model, the coupling Rabi frequency determines both the visibility of the signal (defined as the change in transmission between the dark state and the bright state) and the splitting between the dark states. The feature visibility is shown in Fig. 7.6 as a function of coupling Rabi frequency Ω_c. The maximum visibility occurs at coupling laser Rabi frequency $\Omega_c/2\pi = 156$ MHz.

To understand the optimum ratio of Ω_c/Ω_r, consider the total Hamiltonian $\hat{\mathcal{H}}_{tot}$ of the four-level ladder system given by

$$\hat{\mathcal{H}}_{tot} = \hbar \begin{pmatrix} 0 & \Omega_p/2 & 0 & 0 \\ \Omega_p/2 & -\Delta_{1ph} & \Omega_c/2 & 0 \\ 0 & \Omega_c/2 & -\Delta_{2ph} & \Omega_r/2 \\ 0 & 0 & \Omega_r/2 & -\Delta_{3ph} \end{pmatrix}, \tag{7.10}$$

where the one-photon Doppler shift $\Delta_{1ph} = -k_p v$, two-photon Doppler shift

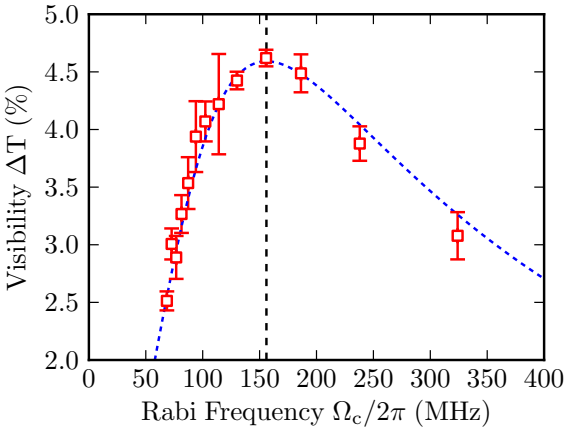

Figure 7.6.: Visibility ΔT of the three-photon EIT signal as a function of coupling laser Rabi frequency Ω_c. The dashed blue line is the theoretical calculation from the full model. The maximum visibility occurs at $\Omega_c/2\pi \simeq 156$ MHz indicated by the vertical dashed line. Experimental parameters: probe laser Rabi frequency $\Omega_p/2\pi = 6$ MHz and Rydberg laser Rabi frequency $\Omega_r/2\pi = 125$ MHz.

$\Delta_{2ph} = -(k_p - k_c)v$ and three-photon Doppler shift $\Delta_{3ph} = \Delta_r - (k_p - k_c - k_r)v$. The eigenenergies of the dressed states can be calculated by diagonalising the Hamiltonian for the three upper states when $\Delta_r = 0$. Expanding the characteristic equation in powers of v and neglecting higher-order terms, the resulting condition for a velocity-insensitive bright state is

$$\mathcal{R}_{opt} = \sqrt{\frac{k_p}{k_r + k_c - k_p}} \simeq 1.2327. \tag{7.11}$$

This prediction is in excellent agreement with the experimentally-obtained ratio $\mathcal{R}_{opt} = 1.25 \pm 0.05$.

7.3. Electron Shelving

7.3.1. Theoretical Model

Electron shelving is an incoherent spectroscopic technique that utilises the difference in atomic state lifetimes [59]. A theoretical model for the four-level ladder system in the presence of a strong probe can be obtained by solving the Lindblad master equation in Eq. (2.11) with the total Hamiltonian $\hat{\mathcal{H}}_{tot}$ given in Eq. (7.10) and the

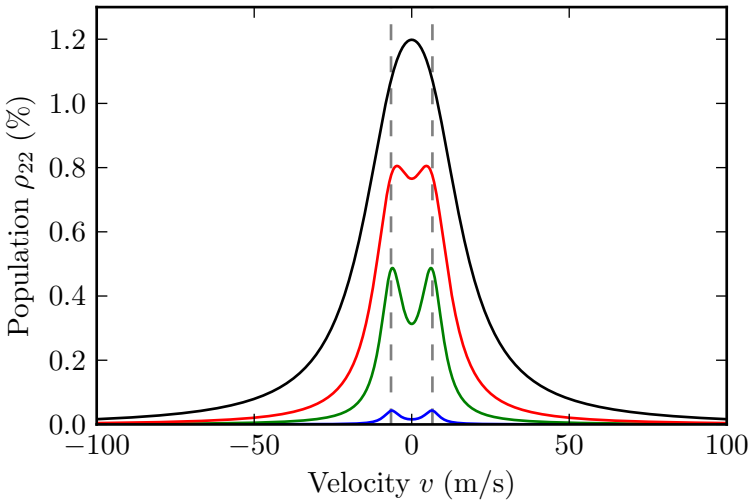

Figure 7.7.: Population ρ_{22} of the intermediate state $|2\rangle$ as a function of atomic velocity v for probe Rabi frequency $\Omega_p/2\pi = 1$ MHz (blue), 5 MHz (green), 10 MHz (red) and 20 MHz (black). The dashed lines indicate the velocities $v^{\pm}$ given in Eq. (7.3) required for resonance with the dressed states $|a^{\pm}\rangle$. Theoretical parameters: coupling laser Rabi frequency $\Omega_c/2\pi = 10$ MHz, atom temperature $T = 323$ K and laser detunings $\Delta_p = \Delta_c = 0$.

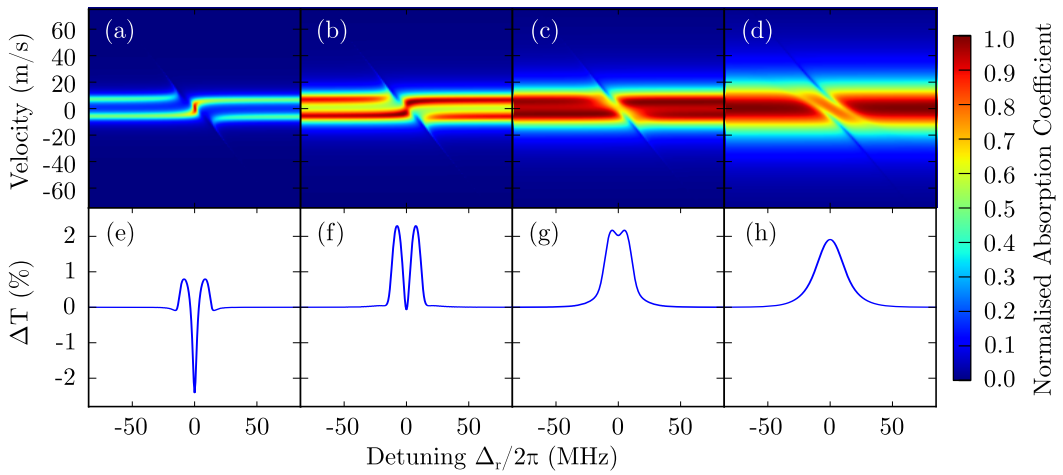

Figure 7.8.: Top panel: Normalised absorption coefficient per velocity class from the four-level theoretical model for probe Rabi frequency $\Omega_p/2\pi =$ (a) 1 MHz, (b) 5 MHz, (c) 10 MHz and (d) 20 MHz. Bottom panel: Doppler-averaged probe transmission spectra (e-h) using the same parameters in (a-d). Theoretical parameters: coupling Rabi frequency $\Omega_c/2\pi = 10$ MHz, Rydberg Rabi frequency $\Omega_r/2\pi = 8$ MHz, cell length $L = 2.4$ mm, temperature $T = 353$ K and detunings $\Delta_p = \Delta_c = 0$.

phenomenological decay matrix $\hat{\mathcal{L}}$ given by

$$\hat{\mathcal{L}} = \frac{1}{2}\begin{pmatrix} 2\Gamma_2\rho_{22} & -\Gamma_2\tilde{\rho}_{12} & -\Gamma_3\tilde{\rho}_{13} & -\Gamma_4\tilde{\rho}_{14} \\ -\Gamma_2\tilde{\rho}_{21} & 2\Gamma_3\rho_{33} - 2\Gamma_2\rho_{22} & -(\Gamma_2+\Gamma_3)\tilde{\rho}_{23} & -(\Gamma_2+\Gamma_4)\tilde{\rho}_{24} \\ -\Gamma_3\tilde{\rho}_{31} & -(\Gamma_2+\Gamma_3)\tilde{\rho}_{32} & 2\Gamma_4\rho_{44} - 2\Gamma_3\rho_{33} & -(\Gamma_3+\Gamma_4)\tilde{\rho}_{34} \\ -\Gamma_4\tilde{\rho}_{41} & -(\Gamma_2+\Gamma_4)\tilde{\rho}_{42} & -(\Gamma_3+\Gamma_4)\tilde{\rho}_{43} & -2\Gamma_4\rho_{44} \end{pmatrix}. \quad (7.12)$$

The transition between the weak probe and strong probe regime in the four-level ladder system can be elucidated by analysing the population ρ_{22} of the excited state $|2\rangle$. The population ρ_{22} is shown as a function of atomic velocity v and probe Rabi frequency Ω_p in Fig. 7.7. The Rydberg Rabi frequency $\Omega_\mathrm{r} = 0$ to simulate the probe absorption in the absence of population transfer to the Rydberg state. When the probe Rabi frequency is weak $\Omega_\mathrm{p}/2\pi = 1$ MHz (blue curve), population transfer occurs at off-resonant velocities $v^{\pm}$ given by Eq. (7.3) and indicated by vertical dashed lines. This corresponds to the Doppler shift required for the probe laser to be resonant with the dressed states $|a^{\pm}\rangle$. However, as the probe Rabi frequency is increased, the distinction between the dressed states is reduced. Eventually, when the probe Rabi frequency is strong $\Omega_\mathrm{p}/2\pi = 20$ MHz (black curve), the population distribution can be described by a broad Gaussian centred around $v = 0$.

The normalised probe absorption coefficient is shown as a function of Rydberg laser detuning Δ_r, atomic velocity v and probe Rabi frequency Ω_p in Fig. 7.8(a-d). When the Rydberg laser is far detuned, probe absorption occurs due to population transfer out of the ground state and into the intermediate states. As expected from Fig. 7.7, the probe Rabi frequency significantly changes the atomic velocities at which absorption occurs. When the probe Rabi frequency is weak $\Omega_\mathrm{p}/2\pi = 1$ MHz, the interaction between the dressed states $|a^{\pm}\rangle$ and the Rydberg state $|4\rangle$ produces a typical three-photon EIT signal, as shown in Fig. 7.8(e). However, when the probe Rabi frequency is strong $\Omega_\mathrm{p}/2\pi = 20$ MHz, the interaction between the merged dressed states $|a^{\pm}\rangle$ and the Rydberg state $|4\rangle$ produces a broad transparency peak centred at $\Delta_\mathrm{r} = 0$, as shown in Fig. 7.8(h). This transparency peak is the electron shelving signal and occurs due to atomic population being stored in the Rydberg state.

7.3.2. Experimental Results

An important consequence of increasing the probe Rabi frequency Ω_p is that the probe absorption is reduced due to saturation of the intermediate state population and optical pumping to the lower hyperfine ground state [130]. Consequently, the strong probe Rydberg experiments are conducted in a 2 mm vapour cell maintained at temperature $T = 353$ K. The three beams are weakly focused into the vapour cell in order to match the Rayleigh range to the optical path length. The $1/e^2$ waist of

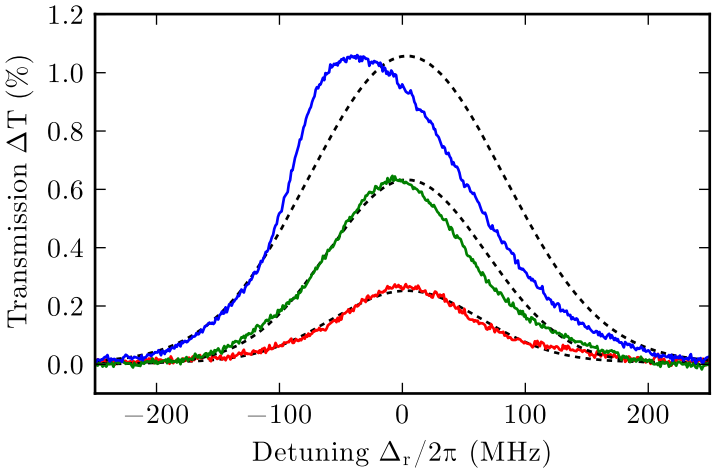

Figure 7.9.: Experimental change in probe transmission ΔT as a function of Rydberg laser detuning Δ_r and fixed Rydberg Rabi frequency $\Omega_r/2\pi = 14$ MHz (red), 25 MHz (green) and 36 MHz (blue). The dashed lines are Gaussian curves to guide the eye. Experimental parameters: probe laser Rabi frequency $\Omega_p/2\pi = 37$ MHz, coupling laser Rabi frequency $\Omega_c/2\pi = 77$ MHz, cell length $L = 2$ mm, temperature $T = 353$ K and laser detunings $\Delta_p = \Delta_c = 0$.

the probe, coupling and Rydberg laser are 150 μm, 80 μm and 80 μm respectively. Furthermore, to maximise the population transfer to the Rydberg state, all three lasers co-propagate through the vapour.

Typical electron shelving spectra are shown in Fig. 7.9 as a function of Rydberg laser detuning Δ_r and fixed Rydberg Rabi frequency Ω_r. Gaussian curves (dashed black curves) are shown to guide the eye. As predicted by the theoretical analysis, the electron shelving method produces a broad transparency in the probe absorption. When the Rydberg Rabi frequency is low $\Omega_r/2\pi = 14$ MHz (red curve), the transmission peak is symmetrical and shows excellent agreement to a Gaussian lineshape. Increasing the Rydberg Rabi frequency has the combined effect of increasing the visibility of the transparency peak (due to increased population of the Rydberg state) and also inducing an asymmetry in the lineshape. The asymmetry in the electron shelving lineshape arises due to dipole-dipole interactions between atoms in the Rydberg state $|4\rangle$. These interactions can be controlled through the Rydberg Rabi frequency Ω_r as this determines the number density $\mathcal{N}_r$ of Rydberg atoms in the thermal vapour. Cooperative Rydberg interactions in a thermal vapour will be the subject of the next Chapter.

7.4. Summary

This Chapter considered Rydberg-state spectroscopy with a three-photon excitation scheme in a thermal vapour. Experimental results on coherent electromagnetically induced transparency were presented and the ability to compensate the Doppler shift with the AC Stark shift discussed. Furthermore, incoherent electron shelving was examined and typical spectra presented. A simple four-level theoretical model was shown to reproduce the main features of the experimental results for both coherent and incoherent spectroscopy.

8. Cooperative Rydberg Interactions

8.1. Introduction

In this Chapter, the observation of strong Rydberg interactions in a thermal vapour are presented. Using an efficient three-photon excitation scheme, discussed in Section 7.3, population is transferred from the $6^2S_{1/2}$ ground state to the $26^2P_{3/2}$ Rydberg state. The three excitation lasers co-propagate through a thermal caesium vapour in order to maximise the Rydberg population. Unless otherwise specified, the experimental data presented in this Chapter is obtained in a 2 mm vapour cell maintained at temperature $T = 353$ K.

As discussed in Chapter 3, atoms in the Rydberg state experience strong resonant dipole-dipole interactions due to the millimetre wave coupling to nearby Rydberg levels. This cooperative long-range interaction results in a modification of both the energy and decay rate of the Rydberg state. The cooperative shift of the Rydberg state is investigated in Section 8.2 using probe transmission spectroscopy of the ensemble. When the number of interacting Rydberg atoms is above a critical number, the cooperative shift exceeds the width of the electron shelving resonance. This results in mirrorless or intrinsic optical bistability with hysteresis depending on the direction in which the resonance is approached. At the critical transition, the system exhibits a discontinuity between a state of high and low Rydberg population. This corresponds to a transition between cooperative many-body and independent single-body atomic behaviour. A simple theoretical model of bistability is presented which utilises a mean-field excitation-dependent shift of the Rydberg state.

The cooperative enhancement of the decay rate is investigated in Section 8.3 using fluorescence spectroscopy. Employing a high-resolution spectrometer, the fluorescence spectra are characterised in the single-body and many-body phases. Comparison of the spectra reveals strong evidence for a superradiant cascade in the many-body phase. Further evidence for a superradiant decay of the Rydberg state is observed in the ground state number density dependence of the individual emission pathways.

Finally in Section 8.4, the non-equilibrium dynamics of the ensemble are analysed at the transition between the single-body and many-body phase. A spatial first-order phase transition is observed along the length of the interaction region and appears as a sharp switch in the off-axis fluorescence. The observation of critical slowing down

in the temporal response of the ensemble, provides further evidence for a first-order phase transition. The critical exponent scaling at the phase transition is measured and found to be in excellent agreement with previous research on dynamical phase transitions.

8.2. Intrinsic Optical Bistability

Optical bistability is the result of a non-equilibrium phase transition in a driven-dissipative system with non-linear feedback. In an atomic system, the driving is provided by a resonant laser field and the dissipation is inherent to the atom-light interaction. Optical bistability was first observed in the pioneering work of Gibbs [24, 136] where the feedback upon the sodium vapour was provided by a cavity. This work was subsequently extended to semiconductor systems [137] and evidence for a non-equilibrium phase transition was observed through the temporal response of an indium antimonide etalon [138]. Optical bistability can also arise in systems where many dipoles are located within a volume which is much smaller than the optical wavelength; in this case the feedback is due to resonant dipole-dipole interactions [5]. This phenomenon is known as intrinsic optical bistability and has only been previously observed in an up-conversion process between densely-packed Yb^{3+} ions in a sold-state crystal cooled to cryogenic temperatures [21].

8.2.1. Theoretical Model

A simple theoretical model of intrinsic optical bistability can be devised by considering each atom as a two-level system with a ground state $|1\rangle$ and Rydberg state $|2\rangle$. The ground state $|1\rangle$ is coupled to the Rydberg state $|2\rangle$ by an electromagnetic field with Rabi frequency Ω and detuning Δ. Resonant dipole-dipole interactions between atoms in state $|2\rangle$ and nearby Rydberg levels results in a cooperative frequency shift Δ_{dd}, as discussed in Chapter 3. This excitation-dependent shift scales linearly with the Rydberg number density $\mathcal{N}_{\mathrm{r}}$.

Due to the long-range many-body coupling of the resonant dipole-dipole interaction $\Delta_{\mathrm{dd}} \propto 1/R^3$, simulating large atom numbers quickly becomes intractable. Mean-field theory provides a solution to this problem by replacing the quantum dynamics with a classical approximation. This approximation allows the system to be described by the response of a single atom interacting with a mean-field interaction potential. It is important to note that in making this approximation, the non-classical atom-atom correlations which give rise to phenomena such as superradiance are neglected [139, 140].

In the single-atom picture, the mean-field shift results in a renormalisation of the transition frequency $\Delta \to \Delta_{\mathrm{eff}} = \Delta - \Delta_{\mathrm{dd}}$, where Δ_{eff} is an effective detuning [141, 7]. For a two-level system, the mean-field shift can be expressed as $\Delta_{\mathrm{dd}} = V\rho_{22}$

where V is the interaction strength and ρ_{22} is the fraction of atomic population in the Rydberg state. The sign of the interaction strength V determines whether the cooperative shift of the Rydberg state $|2\rangle$ is to lower or higher energy. For generality, the mean-field interaction Δ_{dd} includes all the components of the resonant dipole-dipole interaction that were discussed in Section 3.4. Although not discussed here, an alternative method of implementing the mean-field potential involves an excitation-dependent modification of the Rabi frequency Ω [142]. As the effective Rabi frequency $\Omega_{\text{eff}} = \sqrt{\Omega^2 + \Delta^2}$ is related to both the Rabi frequency Ω and the detuning Δ, this alternative method is equivalent to the one that is followed here.

The evolution of the cooperative ensemble can now be described by the modified two-level optical Bloch equations

$$\dot{\rho}_{11} = \frac{i\Omega}{2}(\tilde{\rho}_{12} - \tilde{\rho}_{21}) + \Gamma\rho_{22}, \tag{8.1a}$$

$$\dot{\tilde{\rho}}_{12} = \frac{i\Omega}{2}(\rho_{11} - \rho_{22}) + (-i\Delta_{\text{eff}} - \Gamma/2)\tilde{\rho}_{12}, \tag{8.1b}$$

$$\dot{\tilde{\rho}}_{21} = \frac{i\Omega}{2}(\rho_{22} - \rho_{11}) + (i\Delta_{\text{eff}} - \Gamma/2)\tilde{\rho}_{21}, \tag{8.1c}$$

$$\dot{\rho}_{22} = \frac{i\Omega}{2}(\tilde{\rho}_{21} - \tilde{\rho}_{12}) - \Gamma\rho_{22}, \tag{8.1d}$$

where Γ is the decay rate from the Rydberg state $|2\rangle$ to the ground state $|1\rangle$. The tilde on the coherences indicates the slowly-varying variables approximation, as discussed in Section 2.2.1. To aid further analysis of the system, the optical Bloch equations can be simplified using the Bloch vector notation where [82]

$$u = \tilde{\rho}_{12} + \tilde{\rho}_{21}, \tag{8.2a}$$

$$v = -i(\tilde{\rho}_{12} - \tilde{\rho}_{21}), \tag{8.2b}$$

$$w = \rho_{11} - \rho_{22}. \tag{8.2c}$$

The optical Bloch equations can now be re-written in the Bloch vector components as

$$\dot{u} = \Delta_{\text{eff}} v - \frac{\Gamma}{2}u, \tag{8.3a}$$

$$\dot{v} = -\Delta_{\text{eff}} u + \Omega w - \frac{\Gamma}{2}v, \tag{8.3b}$$

$$\dot{w} = -\Omega v - \Gamma(w - 1). \tag{8.3c}$$

The steady-state solution of the optical Bloch equations can be obtained by setting $\dot{u} = \dot{v} = \dot{w} = 0$ and solving the three simultaneous equations. The resulting

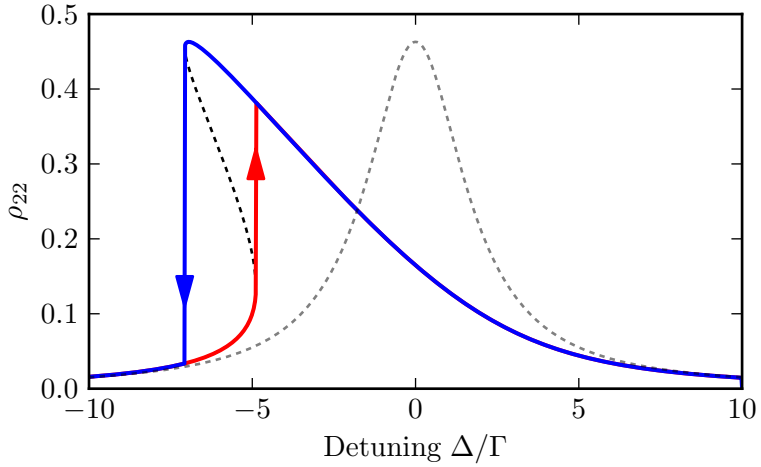

Figure 8.1.: Population of the Rydberg state ρ_{22} as a function of detuning Δ/Γ. The lineshape is shown for Rabi frequency $\Omega/\Gamma = 2.5$ and interaction strength $V = 0$ (grey dashed curve) and $V/\Gamma = -15$ (red, blue and dashed black curves). Due to the excitation-dependent cooperative shift $\Delta_{\mathrm{dd}} = V\rho_{22}$, the response is renormalised and results in bistability with hysteresis dependent upon the direction in which resonance is approached.

expressions are given by [82]

$$u_{\mathrm{ss}} = \frac{\Omega\Delta_{\mathrm{eff}}}{\Delta_{\mathrm{eff}}^2 + \Omega^2/2 + \Gamma^2/4}, \tag{8.4a}$$

$$v_{\mathrm{ss}} = \frac{\Omega\Gamma/2}{\Delta_{\mathrm{eff}}^2 + \Omega^2/2 + \Gamma^2/4}, \tag{8.4b}$$

$$w_{\mathrm{ss}} = \frac{\Delta_{\mathrm{eff}}^2 + \Gamma^2/4}{\Delta_{\mathrm{eff}}^2 + \Omega^2/2 + \Gamma^2/4}, \tag{8.4c}$$

where the renormalised detuning can be expressed as $\Delta_{\mathrm{eff}} = \Delta - V\frac{(1-w_{\mathrm{ss}})}{2}$ in Bloch vector notation. Substituting the renormalised detuning Δ_{eff} into the steady state expression for the population inversion w_{ss} in Eq. 8.4c results in a cubic equation of the form

$$w_{\mathrm{ss}}^3\left(\frac{V^2}{4}\right) + w_{\mathrm{ss}}^2\left(\Delta V - \frac{3V^2}{4}\right) + w_{\mathrm{ss}}\left(\frac{3V^2}{4} - 2\Delta V + \Delta^2 + \frac{\Gamma^2}{4} + \frac{\Omega^2}{2}\right) + \left(\Delta V - \Delta^2 - \frac{V^2}{4} - \frac{\Gamma^2}{4}\right) = 0. \tag{8.5}$$

This cubic equation can be solved numerically to obtain the steady-state Rydberg population $\rho_{22} = (1 - w_{\mathrm{ss}})/2$.

The steady-state Rydberg population ρ_{22} is shown as a function of laser detuning Δ in Fig. 8.1 for an isolated atom ($V = 0$) and a strongly-interacting atom ($V =$

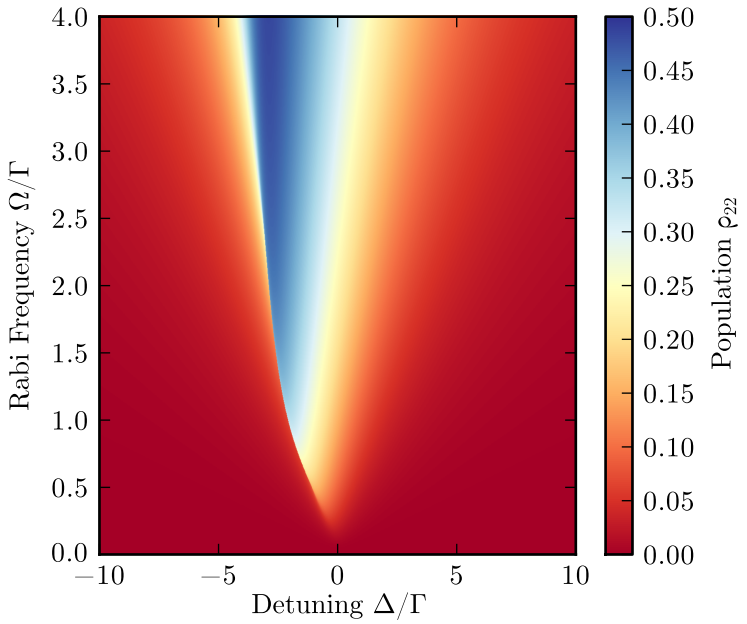

Figure 8.2.: Population of the Rydberg state ρ_{22} as a function of detuning Δ/Γ and Rabi frequency Ω/Γ. In this case, the detuning is scanned from blue to red. The interaction strength is fixed at $V/\Gamma = -6$.

-15Γ). In the case of no interactions, the atomic response can be described by a power-broadened Lorentzian lineshape. In the case of strong interactions, the atomic response is renormalised by the excitation-dependent shift. The lineshape is shifted to lower frequencies and exhibits bistability with hysteresis depending on the direction in which resonance is approached. This phenomena is referred to as intrinsic or mirrorless optical bistability as the feedback required for bistability arises from the interaction with the mean-field potential [25, 26, 27].

Within the hysteresis window, there are three steady-state solutions for the Rydberg population ρ_{22}, of which two are stable (red and blue curves) and one is unstable (dashed black curve). The blue curve represents the atomic response when the laser is scanned from the blue (higher frequencies) to the red (lower frequencies). At a critical detuning $\Delta_\downarrow$, there is a sharp transition from a state of high Rydberg population to a state of low Rydberg population. Similarly, when resonance is approached from the red, as shown by the red curve, there is a critical detuning $\Delta_\uparrow$ at which a sharp transition occurs to a state of high Rydberg population.

The steady-state Rydberg population ρ_{22} is shown as a function of laser detuning Δ and Rabi frequency Ω in Fig. 8.2. The interaction strength is fixed at $V = -6\Gamma$ and the detuning is scanned from blue to red. Increasing the Rabi frequency has a number of effects. Firstly, it increases the Rydberg state population, and therefore the mean-field shift, until it saturates $\rho_{22} \to 0.5$. The increasing Rabi frequency

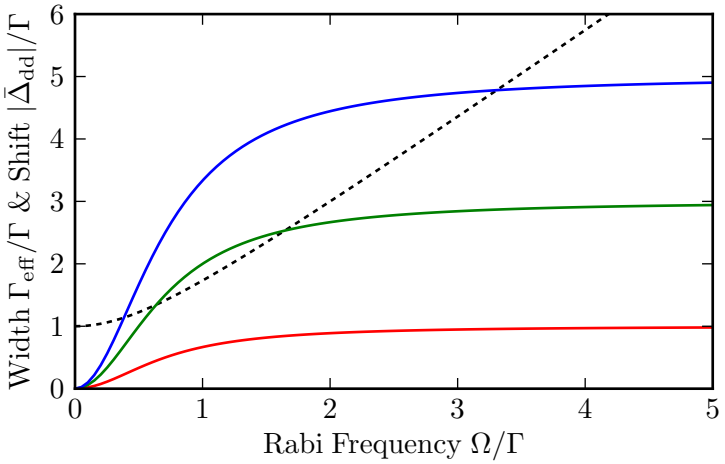

Figure 8.3.: Effective linewidth Γ_{eff} (dashed curve) and resonant mean-field shift $|\bar{\Delta}_{\text{dd}}|$ (solid curves) as a function of Rabi frequency Ω. The scaling of the mean-field shift is shown for $|V| = 2\Gamma$ (red), $|V| = 6\Gamma$ (green) and $|V| = 10\Gamma$ (blue). Due to saturation of the Rydberg state population at high Rabi frequencies, the mean-field shift $\bar{\Delta}_{\text{dd}} \to V/2$.

also leads to a broadening of the resonance. As a result, the ability to observe bistability is dependent upon the balance between the effective power-broadened linewidth $\Gamma_{\text{eff}} = \sqrt{2\Omega^2 + \Gamma^2}$ and the resonant mean-field shift $\bar{\Delta}_{\text{dd}}$. In Fig. 8.2, the lineshape exhibits bistability between Rabi frequency $0.5 \lesssim \Omega/\Gamma \lesssim 1.5$.

The scaling of the effective linewidth Γ_{eff} and the resonant mean-field shift $|\bar{\Delta}_{\text{dd}}|$ with Rabi frequency Ω are illustrated in Fig. 8.3. The interaction strength V determines the rate at which the mean-field shift increases (shown by the solid red, green and blue curves). Due to saturation of the Rydberg state population ρ_{22} at high Rabi frequencies, the mean-field shift saturates at $V/2$. The effective linewidth Γ_{eff} (shown by the dashed line) does not suffer from saturation effects and increases linearly with the Rabi frequency. Consequently, there is a finite range of parameters where the resonant mean-field shift $\bar{\Delta}_{\text{dd}}$ can dominate over the effective linewidth Γ_{eff}.

The necessary conditions to observe intrinsic optical bistability are further investigated in Fig. 8.4. The detuning $|\Delta_{\downarrow}|$ of the transition from high to low Rydberg population is shown as a function of Rabi frequency Ω and the interaction strength $|V|$. When $\Delta_{\downarrow} = 0$, shown by the dark blue region, the atomic response has a single stable solution. The theoretical prediction that the interaction strength $|V| \geq 4$ for intrinsic optical bistability has been well documented in previous work [143]. This condition arises because the mean-field shift Δ_{dd} must be greater than twice the effective linewidth Γ_{eff} [23]. Therefore the interaction strength condition $|V| \geq 4$

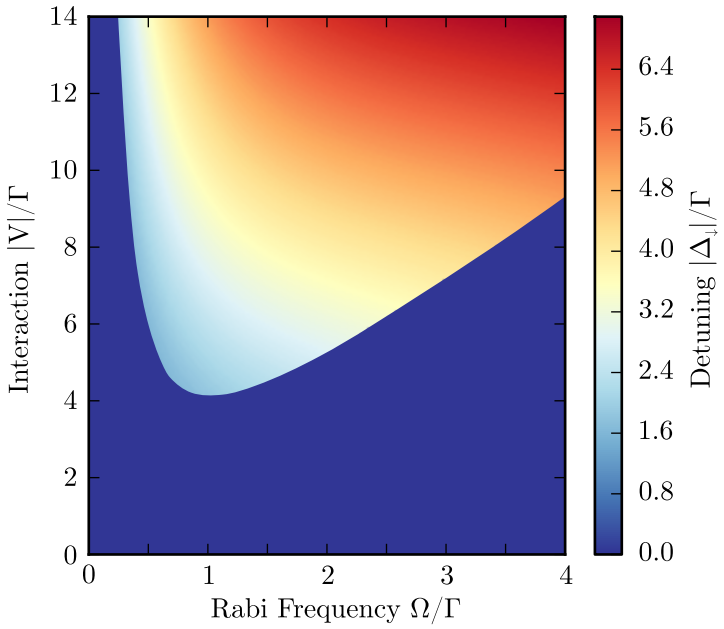

Figure 8.4.: Detuning $|\Delta_\downarrow|/\Gamma$ of the transition from high to low Rydberg population as a function of Rabi frequency Ω/Γ and interaction strength $|V|/\Gamma$. In the dark blue region, the atomic response is monostable.

can be obtained by considering that the maximum mean-field shift is constrained by the Rydberg state population $\Delta_{\mathrm{dd}} \leq V/2$ and the minimum effective linewidth is the natural linewidth $\Gamma_{\mathrm{eff}} \geq \Gamma$.

An important consequence of the condition on the interaction strength $|V| \geq 4\Gamma$, is the inability to observe intrinsic optical bistability in a two-level atomic system when the mean-field originates from the Lorentz-Lorenz local field, i.e. $\Delta_{\mathrm{dd}} = \Delta_{\mathrm{LL}}$. In this case, the interaction strength $|V| = (2/\pi)\Gamma \simeq 0.6\Gamma$ and the Lorentz-Lorenz shift is always smaller than the effective linewidth [143]. This occurs because the Lorentz-Lorenz shift and collisionally-broadened linewidth both scale with the ground state number density $\mathcal{N}$ and the transition dipole moment d^2. This restriction can be overcome in situations where the transition dipole moment for excitation is different to the dipole moment for the interaction. In the present experiment, the optical excitation to the Rydberg state has a dipole moment $d \simeq 0.01\ ea_0$ and results in a narrow spectral linewidth. However, the mean-field shift originates from the interaction with nearby Rydberg states with a large dipole moment of $d \simeq 562\ ea_0$, corresponding to the transition between $26^2\mathrm{P}_{3/2}$ and $26^2\mathrm{S}_{1/2}$.

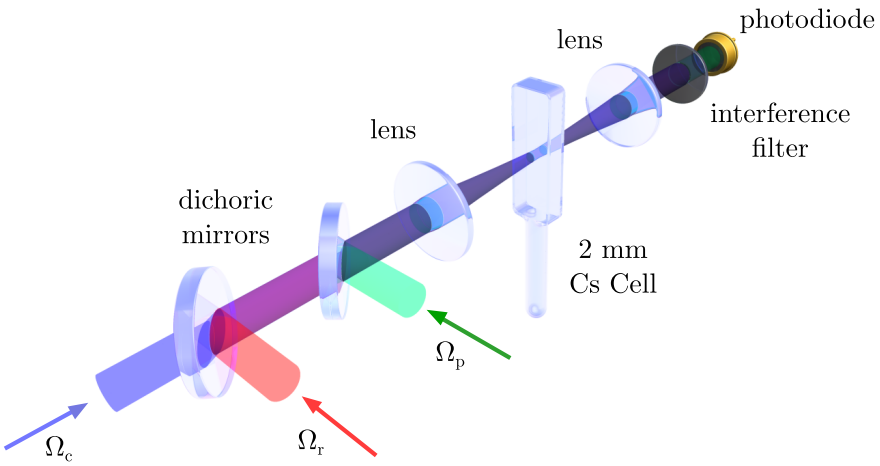

Figure 8.5.: Schematic of the experimental setup for transmission spectroscopy. The probe, coupling and Rydberg lasers are combined using dichroic mirrors and focused into the 2 mm caesium vapour cell. After the cell, a second lens re-collimates the beams and an interference filter rejects the coupling and Rydberg lasers. The transmission of the probe laser is measured at the photodiode.

8.2.2. Experimental Results

The cooperative excitation-dependent shift Δ_{dd} due to resonant dipole-dipole interactions is investigated experimentally using probe transmission spectroscopy. A schematic of the experimental setup is shown in Fig. 8.5. The probe, coupling and Rydberg lasers are combined using dichroic mirrors and focused into the 2 mm vapour cell. After the cell, an interference filter is used to separate the probe laser from the coupling and Rydberg lasers. Through electron shelving, discussed in Section 7.3, the change in transmission of the probe laser ΔT provides a direct readout of the Rydberg state population.

The probe transmission spectrum is shown as a function of Rydberg laser detuning Δ_r for increasing Rydberg Rabi frequency Ω_r in Fig. 8.6. When the Rabi frequency is low $\Omega_r/2\pi = 14$ MHz (i), the change in probe transmission ΔT is symmetrical and independent of the direction in which the laser detuning Δ_r is varied (blue and red curves). This response corresponds to a low level of population in the Rydberg state and negligible atom-atom interactions. When the Rabi frequency is increased to $\Omega_r/2\pi = 36$ MHz (ii), the optical response ΔT becomes asymmetrical and the resonance is shifted to the lower energy. Finally, when the Rabi frequency is high $\Omega_r/2\pi = 74$ MHz (iii), the optical response ΔT exhibits intrinsic optical bistability with hysteresis dependent upon the direction in which the detuning Δ_r is varied. This corresponds to a high level of population in the Rydberg state and significant interactions between the Rydberg atoms.

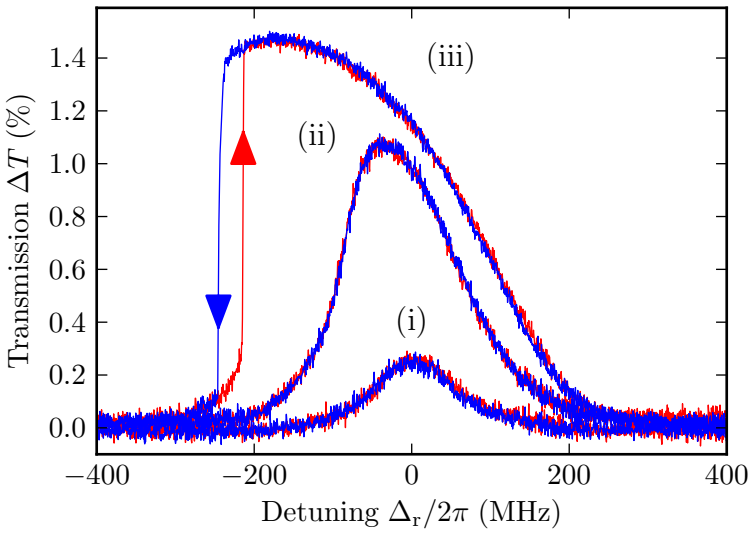

Figure 8.6.: Probe optical response ΔT as a function of Rydberg laser detuning Δ_r for Rydberg Rabi frequency Ω_r increasing from (i) to (iii). Experimental parameters: ground state density $\mathcal{N} = 4.3 \times 10^{12}$ cm^{-3}, probe Rabi frequency $\Omega_p/2\pi = 37$ MHz, coupling Rabi frequency $\Omega_c/2\pi = 77$ MHz and Rydberg Rabi frequency $\Omega_r/2\pi = (14, 36, 74)$ MHz.

It is important to note that intrinsic optical bistability is obtained when the system is in a steady state and is not a transient phenomenon. The memory of the ensemble becomes evident in the region between Rydberg laser detuning $\Delta_{r\downarrow}$ (transition from high to low Rydberg population) and $\Delta_{r\uparrow}$ (transition from low to high Rydberg population). Within the hysteresis window, the response of the ensemble is determined by the previous level of Rydberg population (blue and red curves).

The Rydberg laser detuning $\Delta_{r\downarrow}$ of the transition from high to low Rydberg population represents the resonant mean-field shift $\bar{\Delta}_{dd}$. Under the assumption that the mean-field shift is dominated by the Lorentz-Lorenz local field $\Delta_{dd} = \Delta_{LL}$, the observed shift can be used to estimate the Rydberg number density $\mathcal{N}_r$. The local field shift Δ_{LL} is given by

$$\Delta_{LL} = -\frac{d^2}{3\epsilon_0\hbar}\mathcal{N}_r = -V\mathcal{N}_r, \tag{8.6}$$

where $V/2\pi \simeq 1.3 \times 10^{-9}$ MHz cm^3 is the interaction strength calculated using the transition dipole moment $d = 562\ ea_0$ from the $26^2P_{3/2}$ state to the $26^2S_{1/2}$ state. Given a mean-field shift of $\bar{\Delta}_{dd}/2\pi \simeq -37$ MHz in Fig. 8.6(ii), the Rydberg number density can be estimated as $\mathcal{N}_r \simeq 3 \times 10^{10}$ cm^{-3}. This corresponds to a transfer efficiency between the ground and Rydberg state of approximately 0.7%.

Additionally, given a mean-field shift of $\bar{\Delta}_{\mathrm{dd}}/2\pi \simeq -238$ MHz in Fig. 8.6(iii), the Rydberg number density can be estimated as $\mathcal{N}_{\mathrm{r}} \simeq 2 \times 10^{11}$ cm^{-3} with a transfer efficiency of approximately 5%. Once again it is important to emphasise that these estimates assumes that the cooperative Lamb and collisional shift contributions to the resonant dipole-dipole interaction can be neglected.

Extreme Bistability

This section presents two short experiments that were carried out to further understand the behaviour of intrinsic optical bistability under extreme operating conditions. In the first case, the experiment is performed with tightly-focused beams in order to achieve the highest possible Rydberg Rabi frequency and therefore Rydberg number density. Due to the reduction in the Rayleigh range when the beams are tightly-focused, a 100 μm vapour cell is used to ensure that the beam size does not vary appreciably over the optical path length. The probe optical response ΔT is shown in Fig. 8.7 as a function of Rydberg laser detuning Δ_{r}. When the Rydberg laser Rabi frequency is high $\Omega_{\mathrm{r}}/2\pi = 435$ MHz, the hysteresis loop extends over 500 MHz and the maximum mean-field shift exceeds 1 GHz. Due to significant broadening, the visibility of the transition from high to low Rydberg population is degraded.

The second experiment is carried out in the 2 mm vapour cell provided by the National Institute of Standards and Technology (NIST) and shown in Fig. 2.13. The probe optical response ΔT is shown as a function of Rydberg laser detuning Δ_{r} in Fig. 8.8. Unlike previous experiments, the application of the Rydberg laser results in an increase in probe absorption when it is applied to the ensemble. Consequently the intrinsic optical bistability signal appears inverted. One possible explanation for this unusual signal is the presence of a buffer gas in the vapour cell. Gases such as argon and neon are often used in the micro-fabrication process so that the vapour cell can be sealed in an inert atmosphere [64]. As demonstrated in Section 6.3, the interaction time between the atom and laser is particularly important in determining the absorptive or transmissive properties of the ensemble. As a result, the electron shelving process could be disrupted due to collisional relaxation of the Rydberg atoms [144].

Density Dependence

In this section, the Rydberg laser detuning $|\Delta_{\mathrm{r}\downarrow}|$ of the transition from high to low Rydberg population is investigated as a function of ground state number density $\mathcal{N}$ as shown in Fig. 8.9. This detuning corresponds to the resonant mean-field shift, i.e. $|\Delta_{\mathrm{r}\downarrow}| = |\bar{\Delta}_{\mathrm{dd}}|$. The ground state number density $\mathcal{N}$ is varied by changing the temperature of the thermal vapour and calculated from the background level of

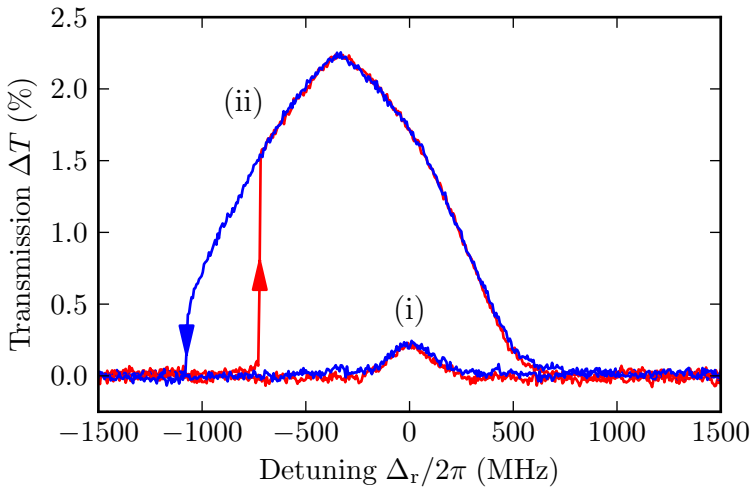

Figure 8.7.: Probe optical response ΔT as a function of Rydberg laser detuning Δ_r in the 100 μm vapour cell with Rydberg laser Rabi frequency $\Omega_r/2\pi$ = (i) 55 MHz and (ii) 435 MHz. Experimental parameters: atom temperature $T = 423$ K, probe Rabi frequency $\Omega_p/2\pi = 155$ MHz and coupling Rabi frequency $\Omega_c/2\pi = 206$ MHz.

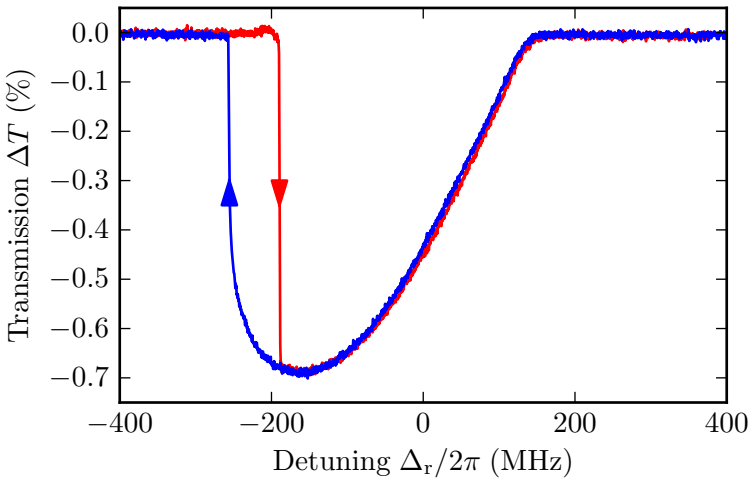

Figure 8.8.: Probe optical response ΔT as a function of Rydberg laser detuning Δ_r in the 2 mm vapour cell provided by NIST. Experimental parameters: probe Rabi frequency $\Omega_p/2\pi = 75$ MHz, coupling Rabi frequency $\Omega_c/2\pi = 107$ MHz and Rydberg Rabi frequency $\Omega_r/2\pi = 109$ MHz.

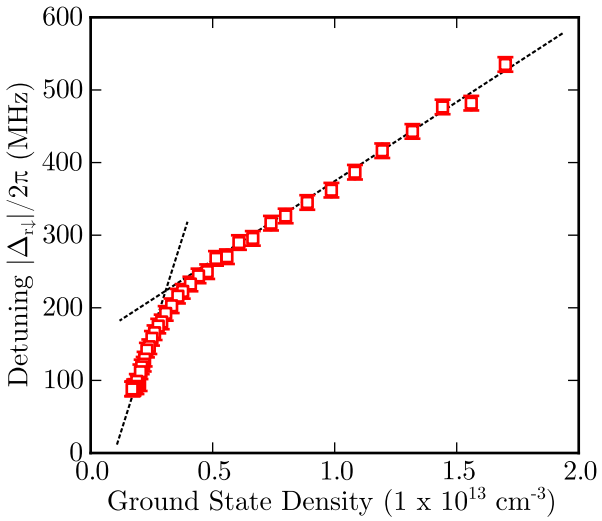

Figure 8.9.: Detuning $|\Delta_{r\downarrow}|$ of the transition from high to low Rydberg population as a function of ground state number density $\mathcal{N}$. The black dashed lines are guides to the eye. Experimental parameters: probe Rabi frequency $\Omega_\mathrm{p}/2\pi = 75$ MHz, coupling Rabi frequency $\Omega_\mathrm{c}/2\pi = 107$ MHz and Rydberg Rabi frequency $\Omega_\mathrm{r}/2\pi = 109$ MHz.

probe absorption. This calculation is based on the absorption of a two-level system in the presence of a strong probe and is discussed further in Section 2.2.4. As the ground state number density is increased, the mean-field shift increases sharply before turning over at $\mathcal{N} \simeq 5 \times 10^{12}$ cm^{-3}. When the ground state number density is increased further, the mean-field shift increases at a constant rate. Whilst the cooperative shift Δ_dd scales linearly with the Rydberg state number density $\mathcal{N}_\mathrm{r}$, as discussed in Chapter 3, this is not necessarily true for the ground state number density $\mathcal{N}$.

Increasing the ground state number density $\mathcal{N}$ results in a number of changes within the ensemble and many of these cannot be accurately quantified. Firstly, the increased vapour temperature results in an increase in the most probable speed v_p of the atoms. As a result, the velocity distribution of atoms which can be excited into the Rydberg state is broadened. This is proportional to the square root of atom temperature T which is non-linearly related to the ground state density $\mathcal{N}$ as shown in Fig. 2.10. Furthermore, the increase in velocity of atoms passing through the beams reduces the interaction time with the lasers. This reduces the efficiency of the electron shelving process. Finally, the density dependence of collisions, power-broadening of the atomic transitions and Rydberg state population along the length of the beam also require consideration. Consequently, the ground state number density dependence of the mean-field shift remains an open question which requires

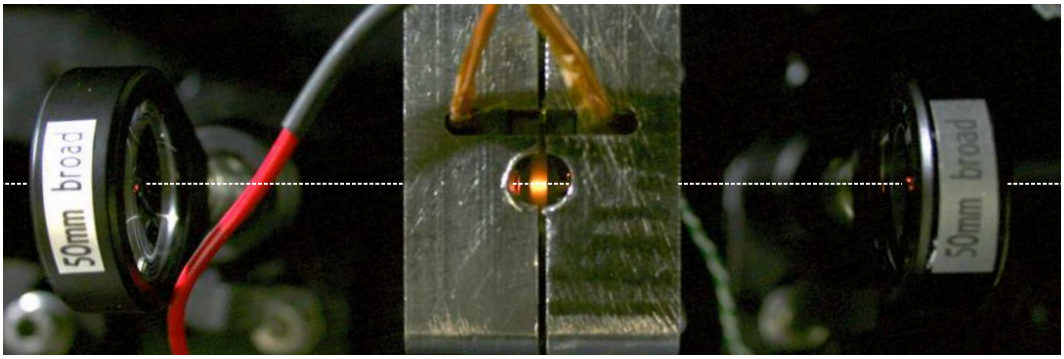

(a)

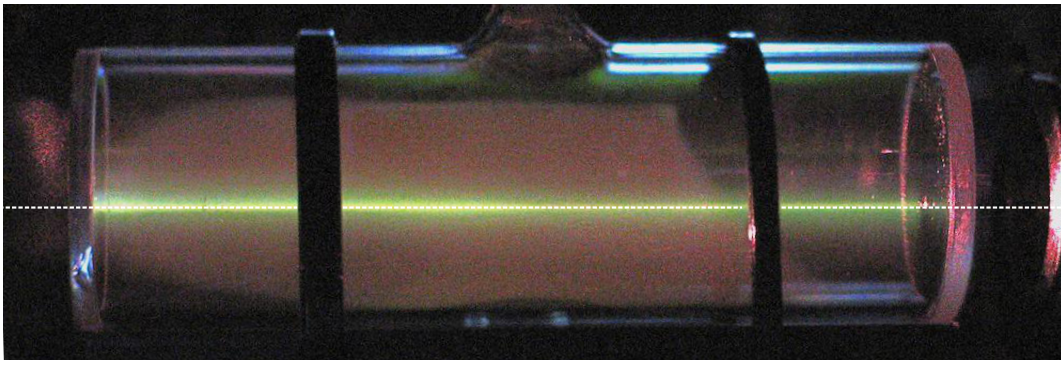

(b)

Figure 8.10.: Observations of Rydberg fluorescence with the naked eye. The three excitation lasers co-propagate from left to right (indicated by dashed white lines). (a) The beams are focused into a 2 mm vapour cell and then re-collimated using a second lens. The cell is maintained at temperature $T = 373$ K using a stainless steel oven (centre). (b) The collimated beams pass through a 5 cm vapour cell at room temperature $T = 293$ K. In both cases, the images were obtained using a standard digital camera.

further investigation.

8.3. Superradiant Rydberg Cascade

The previous section demonstrates that resonant dipole-dipole interactions in a thermal vapour can produce an excitation-dependent shift of the resonant transition frequency. This shift originates from the imaginary part of the dipole-dipole interaction, as demonstrated in Section 3.3. When the shift of the resonance is sufficiently large, intrinsic optical bistability occurs in the optical response. In this section, the atomic dynamics in the non-interacting and strongly-interacting phase will be characterised using fluorescence spectroscopy.

8.3.1. Rydberg Fluorescence

The fluorescence emitted during Rydberg excitation is remarkably strong and can be observed with the naked eye. This is demonstrated in Fig. 8.10(a) for a 2 mm vapour cell and in Fig. 8.10(b) for a 5 cm vapour cell. The fluorescence, although observed as a single colour in each image, comprises many spontaneous emission pathways between the Rydberg state and the ground state. These individual wavelengths are "mixed" together by the detector (the human eye or a digital camera) producing a strong orange glow which can be observed independent of the viewing angle. Whilst the diameter of the probe, coupling and Rydberg beam is less than 2 mm in each image, the fluorescence encompasses a much larger region. This occurs because Rydberg atoms with long radiative lifetimes can travel out of the excitation region before they spontaneously decay. Given that the $26^2\mathrm{P}_{3/2}$ Rydberg state has a blackbody-limited lifetime of $\tau \simeq 20$ μs (calculated in Section 2.6.3) and the atoms have a most probable speed $v_\mathrm{p} \simeq 200$ m/s, the width of the fluorescence distribution can be estimated to be approximately 8 mm.

A photomultiplier tube (PMT) is an extremely sensitive detector that can be used for quantitative analysis of fluorescence. PMT's consist of a vacuum tube with an input window, a photocathode, focussing electrodes, an electron multiplier and an anode [145]. The principle of its operation is outlined briefly here. Photons enter the vacuum tube through the input window and excite electrons in the photocathode which are emitted into the vacuum. Photoelectrons are accelerated and focused by the electrodes onto the first dynode where they are multiplied using the phenomena of secondary emission. This process is repeated at each dynode leading to a build up in the photoelectrons. Finally, the electrons emitted from the last dynode are collected by the anode.

The Hamamatsu H10722-110 PMT module was chosen for this particular application. The small package weighing just 100 g contains all the necessary components and has a low voltage input and output. The super bialkali photocathode is highly sensitive in the visible range, with a peak sensitivity at 400 nm and a broad spectral response from 230 nm to 700 nm. The PMT is extremely sensitive and has a typical anode radiant sensitivity of 220 V/nW. This sensitivity can be adjusted using the variable gain of the amplifier.

As an initial test of the fluorescence detection, the intrinsic optical bistability signal is observed in fluorescence using the PMT and in probe transmission using the photodiode. The fluorescence was collected by roughly aligning the PMT with the side wall of the vapour cell. A bandpass UV filter is also used which allows detection of spontaneous decay from $n^2\mathrm{P}_{1/2}$ and $n^2\mathrm{P}_{3/2}$ states with $n \geq 8$ to the ground state $6^2\mathrm{S}_{1/2}$. The results of this test are shown in Fig. 8.11 for a typical intrinsic optical bistability spectrum. The signal from the photodiode (a) and PMT

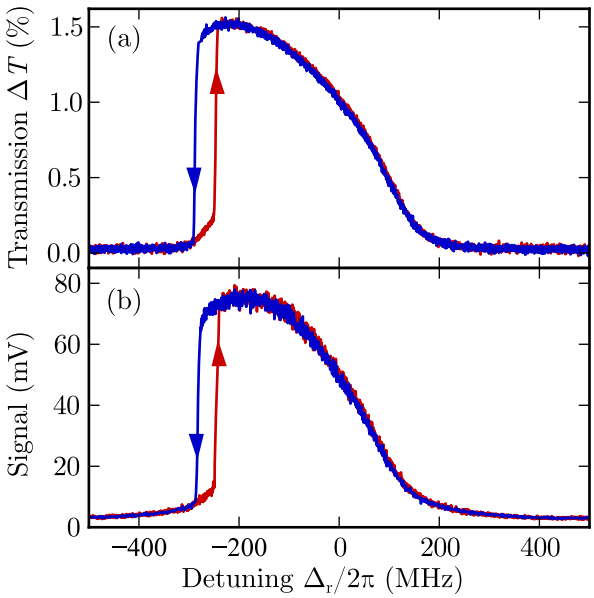

Figure 8.11.: Comparison of (a) the probe transmission signal on the photodiode and (b) the fluorescence signal on the photomultiplier tube. The fluorescence is detected using a UV bandpass filter. This corresponds to spontaneous emission from the $n^2P_{1/2}$ and $n^2P_{3/2}$ states with $n \geq 8$ to the ground state $6^2S_{1/2}$. Experimental parameters: probe laser Rabi frequency $\Omega_p/2\pi = 41$ MHz, coupling laser Rabi frequency $\Omega_c/2\pi = 109$ MHz and Rydberg laser Rabi frequency $\Omega_r/2\pi = 96$ MHz.

(b) are very similar and both produce a signal with similar levels of noise. Given the small collection area, the peak output voltage of the PMT at approximately 80 mV is particularly impressive. Another advantage of the PMT signal is that it occurs on a zero background as the probe and coupling laser do not produce UV fluorescence when the Rydberg laser is far detuned.

8.3.2. Fluorescence Spectroscopy

Whilst bandpass filters are useful for detecting particular spectral regions, wavelength selectivity is required in order to identify the emission processes that take place in the ensemble. A variety of spectrometer options were considered and these are outlined below:

- *Commercial system:* The first option considered was a commercial Ocean Optics USB4000 miniature fiber-optic spectrometer. This small unit consists of ruled diffraction grating and CCD array. Although capable of detecting wavelengths between 200 nm and 850 nm, the sensitivity of 130 photons/count and resolution of > 1 nm are unsatisfactory.

- *Pellin-Broca prism:* The second option considered was a Pellin-Broca prism in combination with the highly sensitive PMT. This type of prism is commonly used to separate wavelengths in a multi-line laser system and due to its unusual shape, the desired wavelength is deviated by 90°. Unfortunately it was not experimentally feasible to isolate a beam of collimated fluorescence which could enter the prism. As a result, the wavelength resolution of > 100 nm was extremely poor.

- *Monochromator:* The final option considered was a commercial Oriel Cornerstone 130 monochromator in combination with the PMT. This monochromator is a 1/8 m Ebert-Fastie design with an out-of-plane diffraction grating in order to reduce stray light. The ruled diffraction grating is mounted on an automated turret which allows the wavelength to be selected or scanned using computer control. The grating has a broad wavelength range of 200 nm to 1600 nm and a reciprocal dispersion of 6.6 nm/mm. In combination with the input and output slit of the monochromator, this system can achieve a wavelength resolution of 0.1 nm. As a result of the excellent specification, this spectrometer system was chosen for the presented experimental work.

The visible fluorescence spectrum of the atomic ensemble at low and high ground state number density $\mathcal{N}$ is shown in Fig. 8.12. This corresponds to a variation in the Rydberg state number density and therefore the strength of the resonant dipole-dipole interaction. The experimental data is obtained by focusing the fluorescence with a lens onto the input slit of the monochromator. The input and output slits of the monochromator are optimised for wavelength resolution and signal level. The full spectrum is obtained by slowly scanning the diffraction grating over the wavelength region of interest and detecting the PMT voltage output on an oscilloscope. The cyan vertical lines in (a) and (c) indicate the dipole-allowed spontaneous emission transitions between all states with an energy equal to or less than the $26^2\mathrm{P}_{3/2}$ Rydberg state. The thick red vertical lines indicate the ionisation limit for to $6^2\mathrm{S}_{1/2}$ at 318 nm, $6^2\mathrm{P}_{3/2}$ at 494 nm and $6^2\mathrm{P}_{1/2}$ at 508 nm. The blue shaded regions indicate the wavelengths of spontaneous emission which originates from Rydberg states with an energy greater than $26^2\mathrm{P}_{3/2}$.

In the low density phase shown in Fig. 8.12(a), the emission spectrum is dominated by spontaneous emission from high-lying Rydberg states to the ground states as illustrated in (b). The transition indicated by (i) corresponds to the 320 nm emission from the Rydberg state $26^2\mathrm{P}_{3/2}$ to the ground state $6^2\mathrm{S}_{1/2}$. The transitions indicated by (ii) correspond to 500 nm and 514 nm emission from the $26^2\mathrm{S}_{1/2}$, $24^2\mathrm{D}_{3/2}$ and $24^2\mathrm{D}_{5/2}$ Rydberg states to the $6^2\mathrm{P}_{1/2}$ and $6^2\mathrm{P}_{3/2}$ states respectively. This behaviour is consistent with spontaneous emission from non-interacting atoms where the transition rate scales with frequency cubed. Consequently, this can be

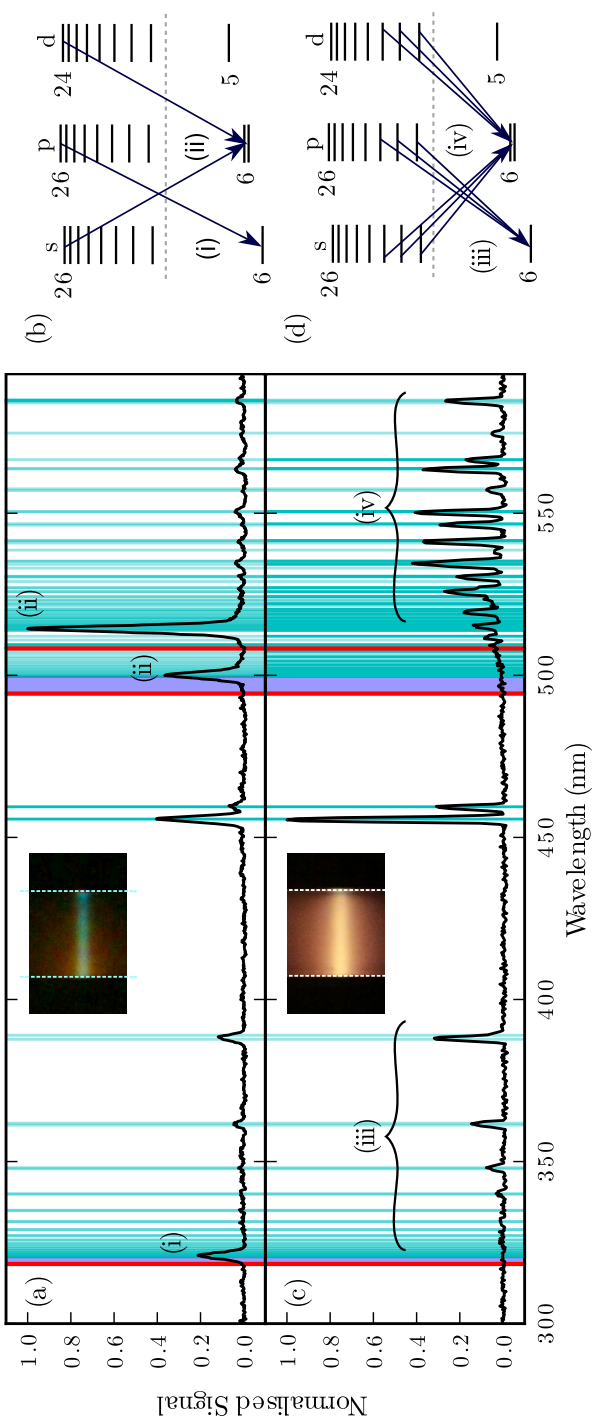

Figure 8.12.: The visible fluorescence spectrum is shown for ground state number densities (a) $\mathcal{N} = 3.1 \times 10^{11}$ cm^{-3} and (c) $\mathcal{N} = 4.3 \times 10^{12}$ cm^{-3}. In the single-body phase, the spontaneous emission originates from high-lying Rydberg states as illustrated in (b). However, in the many-body cooperative phase, the spontaneous emission originates from low-lying Rydberg states as illustrated in (d). The ionisation limits for $6S_{1/2}$, $6P_{1/2}$ and $6P_{3/2}$ are shown by red vertical lines. The blue shaded regions highlight the absence of spontaneous emission between $26P_{3/2}$ and ionisation which would occur due to a blackbody or collisional excitation process. The cyan vertical lines indicate the dipole-allowed transitions. Experimental parameters: probe laser Rabi frequency $\Omega_p/2\pi = 41$ MHz, coupling laser Rabi frequency $\Omega_c/2\pi = 74$ MHz and Rydberg laser Rabi frequency $\Omega_r/2\pi = 122$ MHz.

referred to as the single-body phase.

In the high density phase shown in Fig. 8.12(c), the emission spectrum is significantly modified due to the presence of resonant dipole-dipole interactions. The dominant spontaneous emission in the single-body phase (i) and (ii) are suppressed and rapid energy transfer occurs within the Rydberg manifold. The observed spontaneous emission now originates from a range of low-lying Rydberg states indicated by (iii) and (iv) and highlighted in (d). Importantly the absence of emission in the blue shaded regions (representing spontaneous emission from Rydberg states with higher energies than $26^2\mathrm{P}_{3/2}$) indicates that atoms are not promoted to higher-lying Rydberg states, as would occur in collisional or up-conversion processes.

These results provide strong evidence against thermal blackbody photons as the underlying mechanism. Thermal blackbody radiation, discussed in detail in Section 2.6.3, results in a significant transition rate to neighbouring Rydberg states. This transition rate is dependent upon the transition frequency and the temperature of the blackbody photons. Unlike spontaneous emission, blackbody radiation can result in transitions to both lower and higher lying Rydberg states. However, as shown in Fig. 8.12(a) and (c), there is no evidence for transfer to higher-lying Rydberg states. Furthermore, the variation in ground state number density $\mathcal{N}$ between Fig. 8.12(a) and (c) corresponds to a small change $\Delta T = 40$ K in the temperature of the blackbody radiation. For example, the blackbody transition rate between initial Rydberg state $26^2\mathrm{P}_{3/2}$ and neighbouring Rydberg state $27^2\mathrm{S}_{1/2}$ increases by just 12% between (a) and (c). It is clear that this does not provide sufficient explanation for the dramatic change in observed behaviour.

The spontaneous emission indicated by (iv) in the high density phase in Fig. 8.12(c) is decomposed into the individual atomic transitions in Fig. 8.13. These spectra show that the spontaneous emission originates from Rydberg states with principal quantum number $9 \lesssim n \lesssim 13$. At lower and higher principal quantum numbers, the level of spontaneous emission is reduced. Notably, there is little spontaneous emission from high-lying Rydberg states which would be expected from Einstein-A coefficient analysis. The lack of spontaneous emission from high-lying Rydberg states around $26^2\mathrm{P}_{3/2}$ suggests that the strong dipole-dipole interactions result in a superradiant cascade of decay to lower-lying Rydberg states. Superradiance occurs when the cooperativity on a particular transition is high and the atoms collectively emit in-phase with one another. This is discussed further in Section 3.4.4. Evidence for a superradiant cascade has been previously observed in thermal vapours [107] and ultracold atoms [146].

The superradiant cascade can be understood by first considering the single-atom picture where the transition between the $26^2\mathrm{P}_{3/2}$ and $26^2\mathrm{S}_{1/2}$ Rydberg state has a spontaneous emission lifetime $\tau \simeq 500$ μs. This is much longer than the spontaneous emission lifetime $\tau \simeq 20$ μs to the ground state $6^2\mathrm{S}_{1/2}$. As a result, the majority of

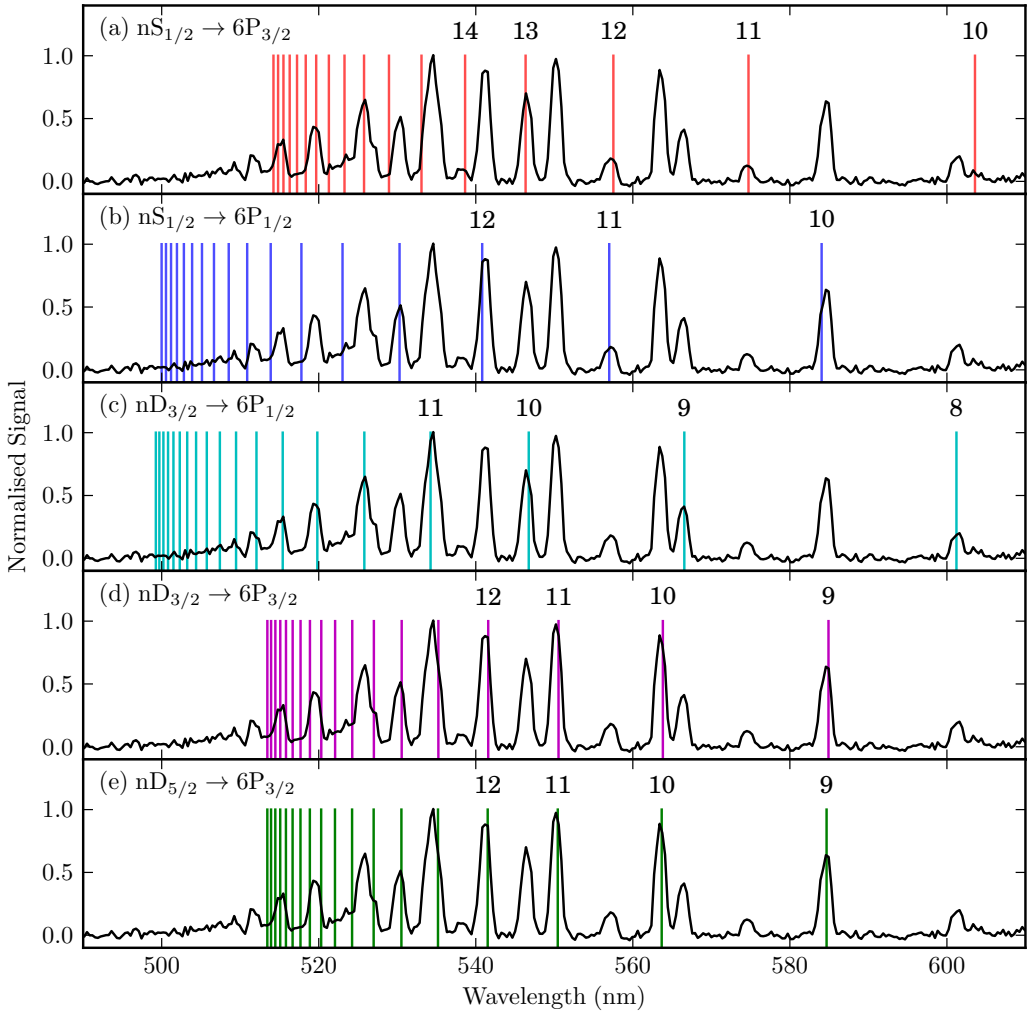

Figure 8.13.: The fluorescence spectrum is shown for ground state number density $\mathcal{N} = 4.3 \times 10^{12}$ cm^{-3}. The spectrum is separated into sets of possible transitions (a) $n^2\mathrm{S}_{1/2} \rightarrow 6^2\mathrm{P}_{3/2}$, (b) $n^2\mathrm{S}_{1/2} \rightarrow 6^2\mathrm{P}_{1/2}$, (c) $n^2\mathrm{D}_{3/2} \rightarrow 6^2\mathrm{P}_{1/2}$, (d) $n^2\mathrm{D}_{3/2} \rightarrow 6^2\mathrm{P}_{3/2}$ and (e) $n^2\mathrm{D}_{5/2} \rightarrow 6^2\mathrm{P}_{3/2}$. The dipole-allowed transitions between $n = 8$ and $n = 26$ are shown by vertical lines. Experimental parameters: probe laser Rabi frequency $\Omega_\mathrm{p}/2\pi = 41$ MHz, coupling laser Rabi frequency $\Omega_\mathrm{c}/2\pi = 74$ MHz and Rydberg laser Rabi frequency $\Omega_\mathrm{r}/2\pi = 122$ MHz.

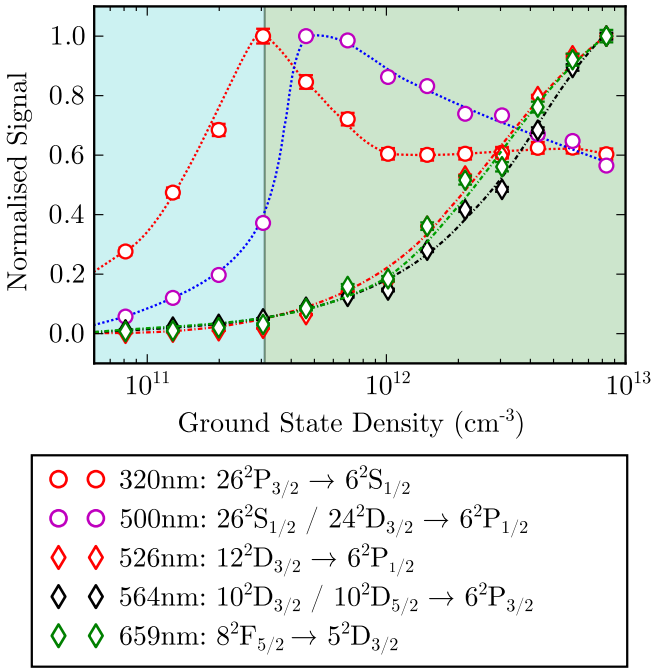

Figure 8.14.: Normalised fluorescence signal as a function of ground state number density $\mathcal{N}$. Experimental parameters: probe laser Rabi frequency $\Omega_p/2\pi = 50$ MHz, coupling laser Rabi frequency $\Omega_c/2\pi = 69$ MHz and Rydberg laser Rabi frequency $\Omega_r/2\pi = 130$ MHz.

atoms decay directly to the ground state when the density is low and the interactions can be neglected. However, due to the large transition wavelength $\lambda = 1$ mm to the $26^2S_{1/2}$ state, it is possible to have a large number of Rydberg atoms in the near field. Given the estimated Rydberg number density $N_r \approx 2 \times 10^{11}$ cm^{-3} calculated in Section 8.2, this gives a cooperativity $C = \mathcal{N}\lambda^3/4\pi^2 \simeq 5 \times 10^6$ and a cooperative enhancement of the decay rate to the $26^2S_{1/2}$ state of $\tau_{super} = \tau/C \simeq 100$ ps. Consequently, due to the cooperative many-body interaction, Rydberg atoms preferentially decay to nearby Rydberg states. This process continues between high-lying Rydberg states and the population quickly cascades to states with lower principal quantum number. As the transition wavelength to neighbouring states scales as n^3, the superradiant cascade eventually stops. This gives rise to the observed spontaneous emission, shown in Fig. 8.13, from low-lying Rydberg states.

The atomic dynamics in the single-body and many-body phase are further investigated by measuring the intensity of a number of important spontaneous emission transition pathways as a function of ground state number density $\mathcal{N}$. This investigation is shown in Fig. 8.14 for the normalised fluorescence signal. The circles indicate spontaneous emission transitions from high-lying Rydberg states which dominate in

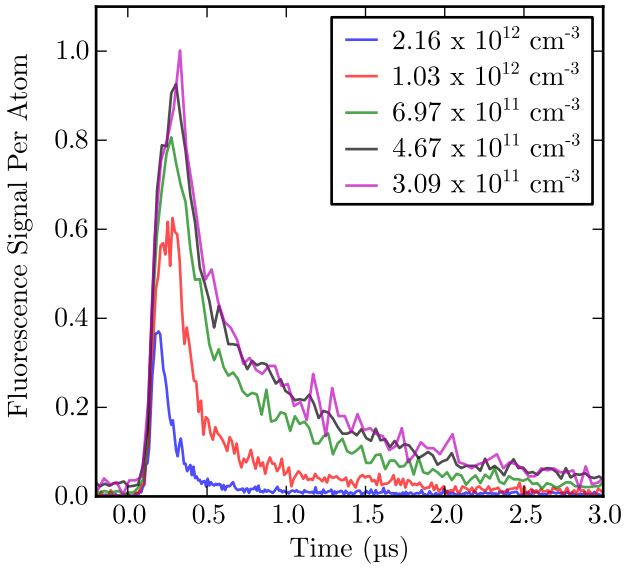

Figure 8.15.: The time-dependent fluorescence signal per atom at $\lambda = 320$ nm (corresponding to the transition between the Rydberg state $26^2P_{3/2}$ and the ground state $6^2S_{1/2}$) is shown for various ground state number densities $\mathcal{N}$. A 200 ns excitation pulse of the Rydberg laser is applied at $t = 0$. Experimental parameters: probe laser Rabi frequency $\Omega_p/2\pi = 50$ MHz, coupling laser Rabi frequency $\Omega_c/2\pi = 69$ MHz and Rydberg laser Rabi frequency $\Omega_r/2\pi = 130$ MHz.

the single-body phase. The diamonds demonstrate the behaviour of spontaneous emission transitions from low-lying Rydberg states which dominate in the many-body phase. When the ground state number density $\mathcal{N} \approx 3 \times 10^{11}$ cm^{-3} (indicated by the vertical line), there is an apparent switch in the atomic dynamics. The spontaneous emission from high-lying Rydberg states decreases whilst the emission from low-lying Rydberg states increases sharply. It is likely that at this Rydberg number density, the cooperative decay rate to neighbouring Rydberg states begins to exceed the spontaneous emission decay rate to the ground state. This behaviour could be investigated further in future work by determining the Rydberg state number density required for the medium to switch between single-body and many-body dynamics. As discussed previously, this is a particularly difficult task, but electrically-coated vapour cells for Rydberg atom detection could provide a solution [63].

Finally, the time-dependence of the 320 nm spontaneous emission from the Rydberg state $26^2P_{3/2}$ to the ground state $6^2S_{1/2}$ is investigated as a function of ground state number density $\mathcal{N}$. This transition is particularly important as atomic population can only enter $26^2P_{3/2}$ by laser excitation. The fluorescence signal per ground state atom is shown in Fig. 8.15 following the application of a 200 ns excitation pulse to the Rydberg state at $t = 0$. Each spectrum shows a sharp initial increase in

fluorescence followed by an exponential decay. However, as the ground state number density is increased, the exponential decay rate also increases. This is accompanied by a decrease in the peak fluorescence signal. These findings support the conclusion that Rydberg population is rapidly transferred to neighbouring states. As fewer atoms have the opportunity to decay on this transition pathway, the peak height decreases. Moreover, the increase in decay rate occurs because the population in the Rydberg state is rapidly transferred into neighbouring states.

It is important to note that the presented experimental results are indirect measurements of the superradiant cascade. Whilst they provide strong evidence for cooperative decay, direct observation of the superradiant wavelength would provide validation of this proposal. Nonetheless, observing emission at 250 GHz is not a simple task and further research is required to establish a suitable detection method.

8.4. Non-Equilibrium Phase Transition

A phase transition can be characterised by a discontinuity in the order parameter which describes the macroscopic state of the system. A first-order phase transition occurs when there is a discontinuity in the order parameter itself whereas a second-order phase transition occurs when there is a discontinuity in the first derivative of the order parameter. In their seminal theoretical paper in 1979, Bowden and Sung demonstrated that intrinsic optical bistability can be interpreted as a first-order phase transition in the atom-light interaction [25]. Through an examination of the resonant dipole-dipole interaction, they were able to derive the non-linear relationship between the externally applied field and the internal field within the volume. When the number of atoms within an interaction wavelength is small, there is a monotonic relationship between the applied field and the internal field. However, when the number of atoms within an interaction wavelength is large, the resonant dipole-dipole interactions act to suppress the internal field. This suppression breaks down at high external fields and results in a non-linear, multivalued response of the internal field. Consequently, at a critical value of the external field, there is a discontinuity in the internal field and the system undergoes a first-order phase transition. In the case of an atomic system, this appears as a discontinuity in the macroscopic atomic polarisation.

As demonstrated in the previous Section, the optical response and atomic dynamics of the ensemble can be separated into two distinct phases. When the number of Rydberg atoms is small and the interactions are negligible, the behaviour of the system can be described by the behaviour of a single atom. However, when the number of Rydberg atoms is large, resonant dipole-dipole interactions result in a significant modification of the ensemble properties. This cooperative many-body phase cannot be described by the behaviour of a single atom. In the frequency domain, the

interactions lead to an excitation-dependent cooperative energy shift. In the time domain, the interactions result in a cooperative enhancement of the atomic decay rate. In this section, a first-order non-equilibrium phase transition is observed in both the temporal and spatial dynamics of the ensemble.

8.4.1. Temporal Phase Transition

Critical slowing down is a phenomena that occurs when a system is approaching a critical threshold and becomes increasingly slow at recovering from perturbations [147, 148]. At the phase transition, the recovery time diverges to infinity with a power law scaling [149]. The exponent, often referred to as the critical exponent, describes the non-analytical behaviour of the order parameter near the critical point. Previous experimental measurements and theoretical considerations have shown that the critical exponent $\alpha = -0.5$ in optical bistability [138, 149, 150].

The observation of critical slowing down in the Rydberg ensemble is outlined in Fig. 8.16. The detuning of the Rydberg laser is fixed at the phase transition $\Delta_\mathrm{r}/2\pi = -220$ MHz and the Rydberg laser intensity I_r is varied. In Fig. 8.16(a), the Rydberg laser intensity is scanned continuously and the optical response ΔT exhibits bistablity with hysteresis dependent upon the direction in which the laser intensity is varied. In Fig. 8.16(b), the optical response ΔT is shown when the Rydberg laser intensity is varied discretely. Each measurement is separated by a 150 μs period where the Rydberg laser is turned off in order to reset the system to the ground state. Consequently, the hysteresis no longer exists because the system memory has been lost and the upper branch shown in Fig. 8.16(a) (blue curve) cannot be measured. At a critical intensity $I_\mathrm{r,crit} \simeq 17.5$ W/mm^2, there is a sharp switch between the single-body and many-body phase.

In Fig. 8.16(c), the switching time τ of the ensemble is shown as a function of Rydberg laser intensity. The switching time, defined in the inset, is the time τ required for the system to switch to the steady state probe transmission level. At the critical transition, the switching time diverges according to the power law $\tau \propto (I_\mathrm{r} - I_\mathrm{r,crit})^\alpha$ shown by the dashed line. The critical exponent $\alpha = -0.53 \pm 0.10$ is consistent with previous work on phase transitions in optical bistability [149, 151]. Further theoretical work is required in this area to determine the overlap with Landau theory where the critical exponent $\alpha = -0.5$ due to a mean field interaction potential [152].

The time-dependence of the optical response ΔT is shown in Fig. 8.17 for decreasing Rydberg laser intensity from (i) to (vi). This is a sample of the data that was used to calculate the switching times shown in Fig. 8.16(c). When the system is in the many-body phase and far from the phase transition, shown by (i), the system quickly switches into a high level of Rydberg population. However, as the phase transition is approached, shown by (ii), (iii) and (iv), the system becomes increas-

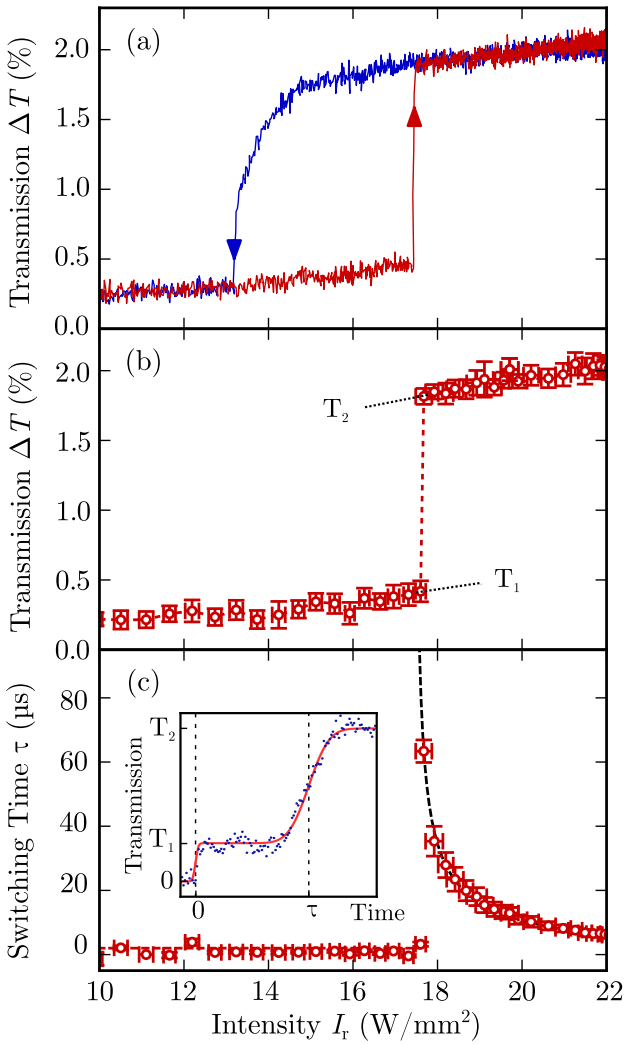

Figure 8.16.: Critical slowing down as the temporal signature of a phase transition. (a) Continuous Rydberg laser intensity I_r scan showing bistability and hysteresis in the optical response ΔT. (b) Discrete Rydberg laser intensity I_r scan showing bistability without hysteresis in the optical response ΔT. (c) At critical intensity $I_r = 17.5 \pm 0.1$ W/mm^2, the switching time to steady state τ (defined in the inset figure) diverges as $(I_r - I_{r,crit})^\alpha$ with critical exponent $\alpha = -0.53 \pm 0.10$ shown by the dashed line of best fit. Experimental parameters: ground state number density $\mathcal{N} = 4.3 \times 10^{12}$ cm^{-3}, probe Rabi frequency $\Omega_p/2\pi = 57$ MHz, coupling Rabi frequency $\Omega_c/2\pi = 116$ MHz and Rydberg detuning $\Delta_r/2\pi = -220$ MHz. The error bars represent the standard deviation error on the determination of the laser intensity, probe transmission and switching time.

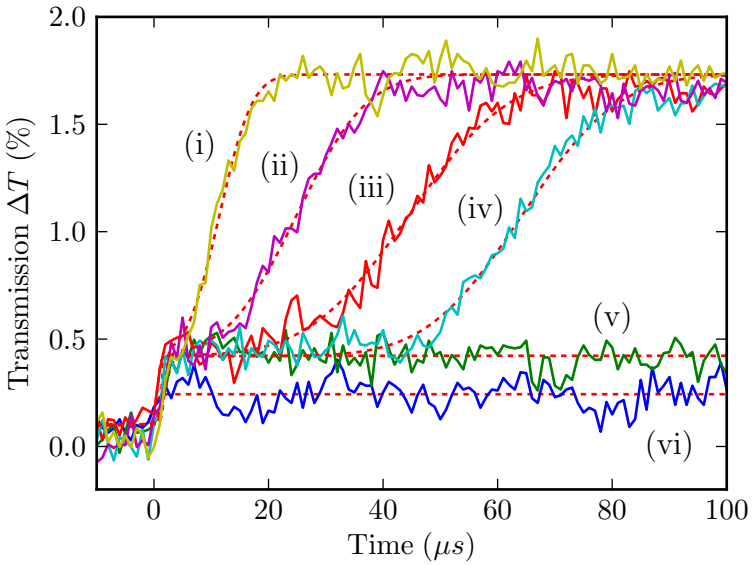

Figure 8.17.: Time dependence of the optical response ΔT for Rydberg laser intensity I_r = (i) 19.91 ± 0.21, (ii) 18.41 ± 0.20, (iii) 17.88 ± 0.14, (iv) 17.67 ± 0.19, (v) 17.02 ± 0.23 and (vi) 9.32 ± 0.17 W/mm^2. The dashed lines indicate the fitted theoretical model used to determine the switching time to steady state. Experimental parameters: probe Rabi frequency $\Omega_p/2\pi = 57$ MHz and coupling Rabi frequency $\Omega_c/2\pi = 116$ MHz.

ingly slowly at reaching the steady state. Once the system is in the single-body phase, shown by (v) and (vi), the system quickly switches to the steady state low level of Rydberg population.

The ability to observe critical slowing down in a thermal vapour is particularly remarkable when one considers the transit time of the atom crossing the laser. Although each atom interacts with the laser for less than 500 ns, it is possible to measure switching times to steady state in excess of 60 μs. This demonstrates that the entire ensemble behaves as a many-body system whose properties are determined by the mean-field interaction potential. The invariance to atom loss provides the system with the ability to retain information, even in the presence of strong decoherence. This is in agreement with recent research which documented dissipation-induced correlation in a cold molecular gas [3].

8.4.2. Spatial Phase Transition

The first-order phase transition can also be observed in the spatial dynamics of the ensemble as shown in Fig. 8.18. The fluorescence images are obtained using a digital SLR camera with a macro lens. The dashed white lines indicate the 2 mm vapour cell and the three lasers co-propagate from left to right in these images.

The Rydberg laser detuning Δ_r is varied across the phase transition, starting in the many-body phase (i) and then switching into the single-body phase (iv). As shown in previous measurements, this transition is extremely sharp and this sequence of images is obtained by varying the Rydberg laser detuning by less than 100 kHz.

As the system switches between the many-body and single-body phase, a first-order phase transition appears along the length of the excitation region as shown in (ii) and (iii). The phase transition moves gradually across the length of the beam until the entire ensemble has switched into the same phase. The spatial phase transition results from a gradual decrease in the probe, coupling and Rydberg laser Rabi frequencies as they propagate through the vapour. When the critical switching intensity occurs in the middle of the vapour cell (iii), it is possible for atoms in the first half of the interaction region to be in the many-body phase. Similarly, those in the second, less intense half of the cell are in the single-body phase. Although predicted theoretically [153, 154], this is the first experimental demonstration of a cooperative spatial phase transition.

8.5. Summary

In this chapter, the observation of a non-equilibrium phase transition in a dilute thermal atomic gas was presented. The phase transition is induced by dipole-dipole interactions between Rydberg atoms which are separated by less than the transition wavelength to neighbouring states. Using probe transmission spectroscopy, a cooperative shift of the Rydberg state is observed which results in intrinsic optical bistability above a critical number of excited atoms. The fluorescence spectrum is characterised and provides strong evidence for a superradiant cascade of decay.

Two phases in the atomic dynamics have been identified. When the population of the Rydberg state is low and interactions can be neglected, the system exists in a single-body phase. However, when the population of the Rydberg state is high, the system exists in a cooperative many-body phase. The non-equilibrium phase transition between single-body and many-body behaviour is observed in the temporal dynamics of the system and critical slowing down measurements confirm the critical exponent $\alpha = 0.53 \pm 0.10$. This exponent is found to be in excellent agreement with previous work. Furthermore, the phase transition is observed spatially as a sharp switch in the fluorescence emitted along the interaction length. This represents the first experimental demonstration of a cooperative spatial phase transition.

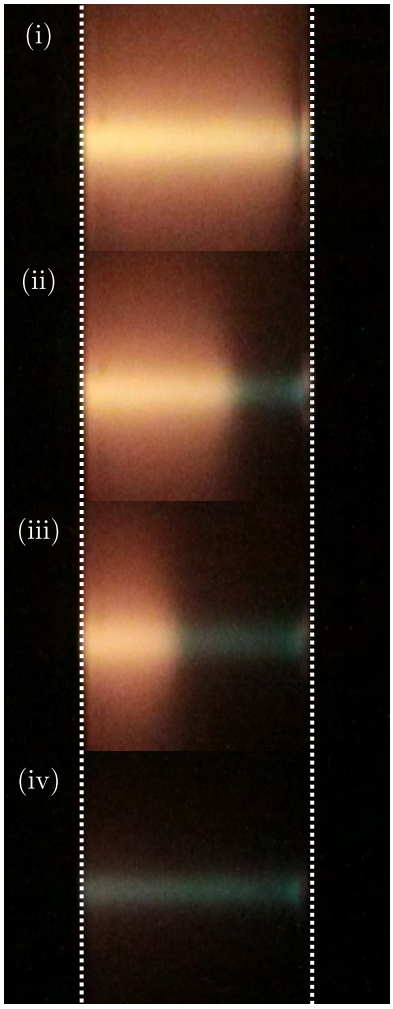

Figure 8.18.: Observation of a spatial first-order phase transition. The detuning of the Rydberg laser is varied across the critical transition $\Delta_{r\downarrow}/2\pi \simeq -220$ MHz and the fluorescence images are shown by (i) to (iv). The phase transition appears as a sharp switch in the emitted fluorescence. The ensemble switches between the many-body phase (orange fluorescence) in (i) to the single-body phase (green fluorescence) in (iv). In these images, the excitation lasers propagate from left to right. The 2 mm vapour cell is indicated by the white dashed lines. Experimental parameters: probe laser Rabi frequency $\Omega_\mathrm{p}/2\pi = 41$ MHz, coupling laser Rabi frequency $\Omega_\mathrm{c}/2\pi = 70$ MHz and Rydberg laser Rabi frequency $\Omega_\mathrm{r}/2\pi = 154$ MHz.

9. Conclusion & Outlook

9.1. Thesis Summary

In this thesis, the non-equilibrium dynamics of a cooperative Rydberg ensemble were investigated. The steady state of the system is a dynamical equilibrium between external driving and dissipative processes [2]. Cooperative behaviour arises due to resonant dipole-dipole interactions [13] between highly-excited Rydberg atoms. In order to transfer atomic population from the ground state to the Rydberg state in a thermal caesium vapour, a three-photon excitation scheme was developed. This scheme has a number of benefits over traditional two-photon Rydberg excitation as each transition utilises inexpensive high-power diode lasers operating at convenient wavelengths.

The ground state $6^2S_{1/2}$ and first excited state $6^2P_{3/2}$ are coupled by an 852 nm diode laser. Due to the distribution of atomic velocities in the vapour, the absorption of the laser is broadened by the Doppler shift. Doppler-free resonances are obtained using a counter-propagating pump laser with the same frequency. This technique is known as saturated absorption spectroscopy [110]. Furthermore, using a technique known as polarisation spectroscopy [111], a circularly-polarised pump beam is used to induce birefringence in the medium. The rotation of the linearly-polarised probe beam is then analysed using a polarimeter. The resulting narrow dispersive signals on a zero background level are used for laser frequency stabilisation of the 852 nm laser [112].

The first excited state $6^2P_{3/2}$ is coupled to the second excited state $7^2S_{1/2}$ using a 1470 nm diode laser. Due to the large transition dipole moment, it is possible to observe excited-state absorption in a room temperature vapour cell. The excited-state linewidth is derived theoretically [67] and found to be sub-natural (less than the combined decay rate of the upper and lower states) when the $6^2P_{3/2}$ state is coherently prepared. This is distinct from the well known case of incoherent preparation where the excited-state linewidth is given by the sum of the decay rates of the upper and lower states [124]. Following this, an excited-state polarisation spectroscopy technique was developed [66], where the 852 nm laser induces a birefringence that is probed by the 1470 nm laser. This technique produces narrow dispersive signals with excellent signal to noise. As with ground-state polarisation spectroscopy, this technique can be used to perform frequency stabilisation of lasers coupling excited

states, such as the 1470 nm laser that is used in this work.

When the 852 nm transition is probed and the 1470 nm transition is strongly coupled, an inverted wavelength system is created. Inverted refers to the unusual case that the probe laser wavelength is shorter than the coupling laser wavelength. In a thermal vapour, this is shown to result in the inability to observe coherent EIT as the one and two photon Doppler shift have the same sign [127]. Although coherent effects cannot be observed, the strong 1470 nm transition transfers a significant proportion of population into the $7^2S_{1/2}$ state. Unlike the ground-state transition, the excited-state transition is open and spontaneous decay can occur to uncoupled states. Consequently, it is possible to observe transmissive and absorptive features in the absorption of the probe laser [69]. An increase in transmission corresponds to the loss of population into the uncoupled hyperfine ground state whilst an increase in absorption corresponds to a re-population of the coupled hyperfine ground state. Further investigation reveals that the sign and magnitude of the transmission feature is strongly dependent on the interaction time between the atoms and the laser. By varying the beam size, it is possible to reduce the interaction time such that the $7^2S_{1/2}$ state does not decay before the atom leaves the beam. Accordingly, a transition between resonant transmission and absorption is observed [69].

The final transition from the excited state $7^2S_{1/2}$ to the Rydberg state $26^2P_{3/2}$ is driven by a 790 nm diode laser. Using a tapered amplifier system, originally designed for the 780 nm ground-state transition in Rubidium, laser powers in excess of 1.5 W are achieved. Firstly, the four-level scheme is used to observe coherent three-photon electromagnetically induced transparency (EIT) [68]. Due to the AC stark shift from the 1470 nm laser, the probe transmission spectrum has two EIT peaks on either side of resonance which correspond to the dressed states. At three-photon resonance, electromagnetically induced absorption (EIA) is observed [133]. Through manipulation of the ratio of the coupling and Rydberg laser Rabi frequencies, it is possible to maximise the visibility of the three-photon EIT signal. This occurs because the AC stark shift can partially compensate the Doppler shift [135].

In order to transfer significant population into the Rydberg state and induce strong interactions, an incoherent transfer process is used. All three lasers co-propagate through the vapour cell with high intensity. In the frequency domain, the cooperative interactions produce an excitation-dependent shift of the energy of the Rydberg state [7]. This is observed using an electron shelving technique [59], where the transmission of the strong probe laser through the ensemble is proportional to the population of the Rydberg state. When the Rydberg number density is above a critical value, the cooperative shift results in intrinsic optical bistability [21] with hysteresis dependent upon the direction in which resonance is approached. Consequently, a sharp phase transition occurs between a state of low Rydberg number density and negligible interactions and a state of high Rydberg number density and strong interactions.

In the time domain, the cooperative interactions result in an enhanced decay rate which scales strongly with the transition wavelength to neighbouring states [13]. Using fluorescence spectroscopy with sub-nanometer resolution, the atomic dynamics are characterised by identifying the transition pathways which result in spontaneous emission. When the Rydberg number density is low, the observed fluorescence originates from spontaneous emission between high-lying Rydberg states and the ground state. This corresponds to the behaviour of a non-interacting atom where the transition rate is dependent on the frequency cubed. However, when the Rydberg number density is high and strong interactions are present, the observed fluorescence originates from spontaneous emission between low-lying Rydberg states and the ground state. This provides strong evidence for a superradiant cascade of decay between high-lying Rydberg states due to cooperative enhancement of their decay rate [107]. Through the interaction-induced correlation, the system now exists in a phase-locked many-body state and cannot be described by the response of a single atom. As the transition wavelength between Rydberg states depends on the principal quantum number, the cooperative enhancement of Rydberg-Rydberg transitions in the cascade eventually weakens leading to the observed spontaneous emission from low-lying Rydberg states. The lack of spontaneous emission from Rydberg states above the initially-populated state rules out the possibility of collisional or blackbody-induced processes.

At the critical transition between the single-body and many-body phase, a first-order non-equilibrium phase transition occurs [70]. This can be observed spatially along the length of the excitation region as a sharp switch in the emitted fluorescence [154, 153]. As a result of the hierarchy of length scales between optical excitation $\lambda_{\text{ex}} \simeq 1$ μm and dipole coupling $\lambda_{\text{dd}} \simeq 1$ mm, the cooperative dipole-dipole interaction is revealed on macroscopic optically-resolvable length scales. The first-order phase transition can also be observed temporally through critical slowing down [147, 148]. Critical slowing down is a phenomenon that occurs when a system approaches a critical threshold and becomes increasingly slow at recovering from perturbations. In this work, critical slowing down emerges as a divergence in the switching time required to reach a dynamical equilibrium when the Rydberg laser is applied. This divergence follows a universal scaling law for phase transitions $(I - I_{\text{crit}})^{\alpha}$ where I is the intensity, I_{crit} is the critical intensity to switch between phases and α is the critical exponent. The critical exponent is determined as $\alpha = -0.53 \pm 0.10$ and is in excellent agreement with previous work on non-equilibrium phase transitions [149].

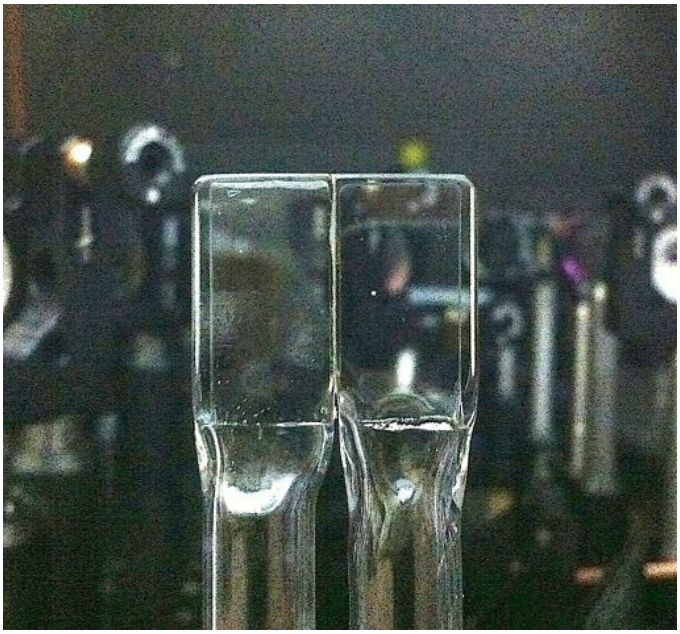

Figure 9.1.: Multi-region 2 mm vapour cell developed in collaboration with the Chemistry Department at Durham University. The separation between the chambers is approximately 800 μm.

9.2. Future Work

The demonstration of a cooperative non-equilibrium phase transition in a thermal vapour raises many interesting possibilities for future research. Some of these are outlined below:

- The three-photon excitation scheme developed in this thesis will be used to prepare single ions using the dipole blockade effect [45].
- The long-range resonant dipole-dipole interaction offers the possibility to study non-local propagation [155]. One potential scheme could involve a multi-region vapour cell such as the one that has been recently developed shown in Fig. 9.1. The vapour cell consists of two chambers which each have an optical path length of 2 mm. Using three excitation lasers in each cell, Rydberg atoms located in the first region can be detected through the cooperative shift of the Rydberg state in the second region. Preliminary results have proved inconclusive and potential issues include the transmission of the interaction wavelength through quartz glass and the directionality of the emission.
- The intrinsic optical bistability signal could be used for precision sensing applications. By biasing the system at the phase transition and utilising the

sensitivity of Rydberg atoms to external electric fields, the device could be used as an extremely sensitive detector.

- The photon statistics at the phase transition could be further investigated. At the sharp transition between a many-body and single-body phase, there is a rapid avalanche of decay out of the Rydberg state. This could result in the ability to observe non-classical photon statistics [5].

- Using a fast CCD camera capable of detecting the visible Rydberg fluorescence, the atomic dynamics could be imaged to investigate the possibility of spatial structures [39]. By biasing the system just below the phase transition, an additional localised Rydberg excitation can be used to induce the transition into the many-body phase. This would allow the diffusion of the phase transition to be observed as it moves throughout the interaction region.

- The geometry dependence of the cooperative Lamb shift could be further investigated. As discussed in Section 3.4, the cooperative Lamb shift is predicted to depend on the radius of a cylindrical excitation region [100].

Appendix

A. Four-Level Optical Bloch Simulation

In this Appendix, the complex susceptibility χ given in Eq. (2.15) is calculated for a four-level atomic system. The ground state $|1\rangle$ and first excited state $|2\rangle$ are coupled by a probe laser with Rabi frequency Ω_{12}, detuning Δ_{12} and wavevector k_{12}. The first excited state $|2\rangle$ and second excited state $|3\rangle$ are coupled by a coupling laser with Rabi frequency Ω_{23}, detuning Δ_{23} and wavevector k_{23}. Finally, the second excited state $|3\rangle$ and third excited state $|4\rangle$ are coupled by a Rydberg laser with Rabi frequency Ω_{34}, detuning Δ_{34} and wavevector k_{34}.

The total Hamiltonian for the four-level ladder system including the Doppler effect is given by

$$\hat{\mathcal{H}}_{\text{tot}} = \hbar \begin{pmatrix} 0 & \Omega_{12}/2 & 0 & 0 \\ \Omega_{12}/2 & -\Delta_{1\text{ph}} & \Omega_{23}/2 & 0 \\ 0 & \Omega_{23}/2 & -\Delta_{2\text{ph}} & \Omega_{34}/2 \\ 0 & 0 & \Omega_{34}/2 & -\Delta_{3\text{ph}} \end{pmatrix} \tag{A.1}$$

where the Doppler shifts are given by

$$\Delta_{1\text{ph}} = \Delta_{12} - k_{12}v \tag{A.2a}$$

$$\Delta_{2\text{ph}} = \Delta_{12} + \Delta_{23} - (k_{12} - k_{23})v \tag{A.2b}$$

$$\Delta_{3\text{ph}} = \Delta_{12} + \Delta_{23} + \Delta_{34} - (k_{12} - k_{23} - k_{34})v \tag{A.2c}$$

and v is the atomic velocity. The three lasers are configured such that the probe laser counter-propagates against both the coupling and Rydberg lasers. In the ladder configuration, state $|4\rangle$ spontaneously decays at rate Γ_4 to state $|3\rangle$. State $|3\rangle$ spontaneously decays at rate Γ_3 to state $|2\rangle$. Furthermore, state $|2\rangle$ spontaneously decays at rate Γ_2 to the stable ground state $|1\rangle$. The phenomenological decay matrix $\hat{\mathcal{L}}$ is given by

$$\hat{\mathcal{L}} = \frac{1}{2} \begin{pmatrix} 2\Gamma_2\rho_{22} & -\Gamma_2\tilde{\rho}_{12} & -\Gamma_3\tilde{\rho}_{13} & -\Gamma_4\tilde{\rho}_{14} \\ -\Gamma_2\tilde{\rho}_{21} & 2\Gamma_3\rho_{33} - 2\Gamma_2\rho_{22} & -(\Gamma_2+\Gamma_3)\tilde{\rho}_{23} & -(\Gamma_2+\Gamma_4)\tilde{\rho}_{24} \\ -\Gamma_3\tilde{\rho}_{31} & -(\Gamma_2+\Gamma_3)\tilde{\rho}_{32} & 2\Gamma_4\rho_{44} - 2\Gamma_3\rho_{33} & -(\Gamma_3+\Gamma_4)\tilde{\rho}_{34} \\ -\Gamma_4\tilde{\rho}_{41} & -(\Gamma_2+\Gamma_4)\tilde{\rho}_{42} & -(\Gamma_3+\Gamma_4)\tilde{\rho}_{43} & -2\Gamma_4\rho_{44} \end{pmatrix} \tag{A.3}$$

The Lindblad master equation in Eq. (2.10) can be used to obtain the time evolution of the density matrix. The time evolution can be formulated as a system of linear

equations such that

$$\dot{\boldsymbol{\rho}} = \hat{A}\boldsymbol{\rho} \tag{A.4}$$

where vectors $\dot{\boldsymbol{\rho}} = (\dot{\rho}_{11}, \dot{\rho}_{22}, \ldots, \dot{\rho}_{44})^{\mathrm{T}}$, $\boldsymbol{\rho} = (\rho_{11}, \rho_{22}, \ldots, \rho_{44})^{\mathrm{T}}$ and T indicates the transpose. The Lindblad matrix $\hat{A}$ can be calculated using the total Hamiltonian $\hat{\mathcal{H}}_{\mathrm{tot}}$ in Eq. (A.1) and decay matrix $\hat{\mathcal{L}}$ in Eq. (A.3) to give

$$\hat{\mathcal{A}} = -\frac{i}{\hbar}\left(\hat{\mathcal{H}}_{\mathrm{tot}} \otimes \hat{I}_4 - \hat{I}_4 \otimes \hat{\mathcal{H}}_{\mathrm{tot}}^{T}\right) + \hat{\mathcal{L}} \tag{A.5}$$

where $\hat{I}_4$ is the identity matrix in four dimensions and $\otimes$ indicates the Kronecker product. With an initial state $\boldsymbol{\rho}_0$, the time evolution of the density matrix elements is given by

$$\boldsymbol{\rho}(t) = \hat{P}\ \mathrm{diag}(e^{\boldsymbol{\lambda} t})\ \hat{P}^{-1}\ \boldsymbol{\rho}_0 \tag{A.6}$$

where $\hat{P}$ is the matrix of eigenvectors, $\boldsymbol{\lambda}$ is a vector of eigenvalues and diag represents a vector as the diagonals of a matrix. This calculation can be implemented in Python using linear algebra and a sample solution for the probe susceptibility in a four-level ladder system is shown below.

```
from __future__ import division
from numpy import *
from scipy import *
from pylab import *

### Maxwell-Boltzmann Velocity Distribution

def maxwell(v,vp):
        return (1/(sqrt(pi)*vp))*exp(-v**2 / vp**2)

### Constants

e = 1.60217657e-19
a0 = 5.2917721092e-11
hbar = 1.05457173e-34
e_0 = 8.854187817e-12

### Atom Parameters

vp = 230
```

```
G1 = 0
G2 = 1*2*pi*1e6
G3 = 3.3*2*pi*1e6
G4 = 1*2*pi*1e6
d_21 = 2.024*e*a0
N = 2e17
l = 0.002

### Laser Parameters

Omega_12 = 0.01*2*pi*1e6
Delta_12 = 0
k_12 = 2*pi/852e-9

Omega_23 = 4*2*pi*1e6
Delta_23 = 0
k_23 = 2*pi/1470e-9

Omega_34 = 5*2*pi*1e6
Delta_34 = 0
k_34 = 2*pi/790e-9

### Simulation Parameters

delta_max = 30*2*pi*1e6
delta_min = -delta_max
delta_points = 100
dscan = linspace(delta_min,delta_max,delta_points)

v_max = 100
v_min = -v_max
v_points = 200
vscan = linspace(v_min,v_max,v_points)
stepsize = vscan[1]-vscan[0]

time = 1

### Simulation Setup

rho_0 = zeros((16,1))
```

```
rho_0[0] = 1
vpick21 = zeros((1,16)); vpick21[0,4] = 1
vpick32 = zeros((1,16)); vpick32[0,9] = 1
rho21imag = zeros(((vscan.shape[0]),(dscan.shape[0])))

### Run Simulation

dloop = 0
for Delta_12 in dscan:
        print dloop
        vloop=0
        for v in vscan:

                Delta_1ph = Delta_12-k_12*v
                Delta_2ph = Delta_12+Delta_23-(k_12-k_23)*v
                Delta_3ph = Delta_12+Delta_23+Delta_34-(k_12-k_23-k_34)*v

                H = array([\
                [0, Omega_12/2, 0, 0],\
                [Omega_12/2, -Delta_1ph, Omega_23/2, 0],\
                [0, Omega_23/2, -Delta_2ph, Omega_34/2],\
                [0, 0, Omega_34/2, -Delta_3ph]])

                Hrho = kron(H,eye(4))
                rhoH = kron(eye(4),transpose(H))

                L = zeros((16,16))
                L[0,5] = G2
                L[1,1] = -G2/2
                L[2,2] = -G3/2
                L[3,3] = -G4/2
                L[4,4] = -G2/2
                L[5,5] = -G2
                L[5,10] = G3
                L[6,6] = -(G3 + G2)/2
                L[7,7] = -(G2 + G4)/2
                L[8,8] = -G3/2
                L[9,9] = -(G2 + G3)/2
                L[10,10] = -G3
                L[10,15] = G4
```

```
                L[11,11] = -(G3 + G4)/2
                L[12,12] = -G4/2
                L[13,13] = -(G2 + G4)/2
                L[14,14] = -(G3 + G4)/2
                L[15,15] = -G4

                eval,evec = eig(-1j*(Hrho-rhoH)+L)
                evec = mat(evec)
                rho_0 = mat(rho_0)
                solT = evec*mat(diag(exp(eval*time)))*inv(evec)*rho_0
                w = maxwell(v,vp)
                rho21imag[vloop,dloop] = w*stepsize*(vpick21*solT).imag

                vloop+=1

        dloop+=1

### Calculate Doppler-Averaged Result

rho21_averaged = add.reduce(rho21imag,axis=0)
chi_I = -(2*N*d_21**2*rho21_averaged)/(hbar*e_0*Omega_12)
T = exp(-k_12*chi_I*l)

### Plotting

fig1 = figure(1, figsize=(4,3.5), facecolor='white')
clf()
ax1 = subplot(111)
ax1.plot(dscan/(2*pi*1e6),T)
ax1.set_xlabel(r'Detuning $\Delta/2\pi$ (MHz)')
ax1.set_ylabel(r'Transmission')
fig1.savefig('file.pdf')
show()
```

B. Rydberg Transition Wavelengths

Principal Quantum n	Wavelength $n^2P_{1/2}$ (nm)	Wavelength $n^2P_{3/2}$ (nm)
21	799.4366	799.3505
22	796.9976	796.9251
23	794.9374	794.8759
24	793.1811	793.1285
25	791.6714	791.626
26	790.364	790.3245
27	789.224	789.1895
28	788.224	788.1936
29	787.3419	787.315
30	786.5597	786.5358
31	785.8628	785.8415
32	785.2393	785.2202
33	784.6792	784.662
34	784.1741	784.1586
35	783.7171	783.703
36	783.3021	783.2893
37	782.9243	782.9126
38	782.5792	782.5685
39	782.2632	782.2534
40	781.9731	781.9641
41	781.7062	781.6979
42	781.46	781.4523
43	781.2324	781.2253
44	781.0217	781.0151
45	780.8261	780.82
46	780.6443	780.6386
47	780.475	780.4697
48	780.317	780.3121
49	780.1695	780.1648
50	780.0314	780.0271

Principal Quantum n	Wavelength $n^2P_{1/2}$ (nm)	Wavelength $n^2P_{3/2}$ (nm)
51	779.902	779.898
52	779.7806	779.7768
53	779.6665	779.6629
54	779.5592	779.5558
55	779.4581	779.4549
56	779.3628	779.3598
57	779.2727	779.2699
58	779.1877	779.185
59	779.1072	779.1046
60	779.0309	779.0285
61	778.9587	778.9564
62	778.8901	778.8879
63	778.8249	778.8229
64	778.763	778.7611
65	778.7041	778.7022
66	778.648	778.6462
67	778.5946	778.5929
68	778.5436	778.542
69	778.4949	778.4934
70	778.4485	778.447
71	778.4041	778.4027
72	778.3616	778.3603
73	778.321	778.3197
74	778.282	778.2808
75	778.2448	778.2436
76	778.209	778.2079
77	778.1747	778.1736
78	778.1418	778.1407
79	778.1102	778.1092
80	778.0798	778.0788

Figure B.1.: Transition wavelengths from excited state $7^2S_{1/2}$ to Rydberg states $n^2P_{1/2}$ and $n^2P_{3/2}$. Data derived from quantum defect theory [89, 34].

C. Caesium Level Structure

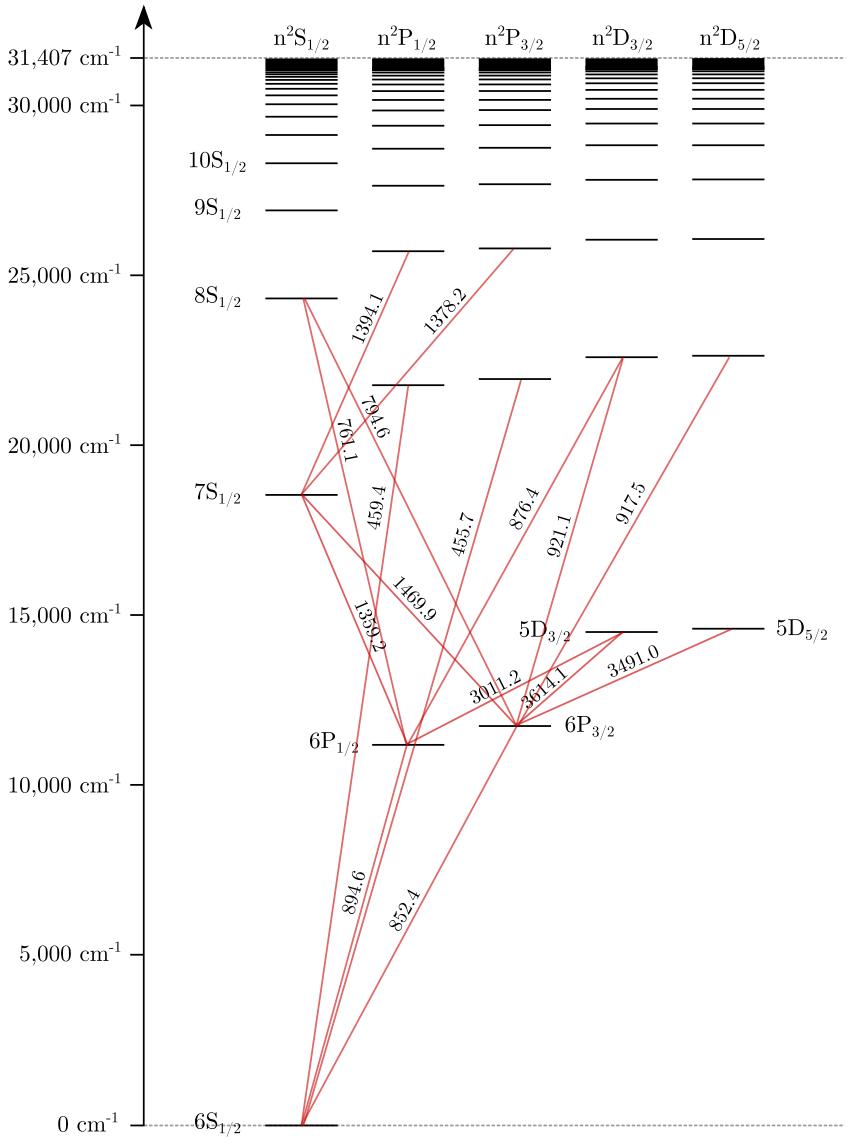

Figure C.1.: Caesium energy level structure for the nS, nP and nD states. The energy is given in wavenumber cm^{-1} and the transition wavelength in nanometres. Data adapted from [88].

D. Rydberg-Rydberg Transition Data

The radial matrix elements [87] together with the transition wavelengths and energy defects calculated using quantum defect theory are shown in the table below. The initial Rydberg state is $26^2P_{3/2}$.

Atomic Transition	Radial Matrix Element (ea_0)	Wavelength (mm)	Energy Defect (GHz)
$26^2P_{3/2} \rightarrow 27^2S_{1/2}$	551	1.04	-287
$26^2P_{3/2} \rightarrow 26^2S_{1/2}$	562	1.02	295
$26^2P_{3/2} \rightarrow 25^2D_{5/2}$	753	5.54	-54
$26^2P_{3/2} \rightarrow 25^2D_{3/2}$	754	6.14	-49
$26^2P_{3/2} \rightarrow 24^2D_{5/2}$	203	0.53	562
$26^2P_{3/2} \rightarrow 24^2D_{3/2}$	197	0.53	568

Bibliography

The last numbers of each reference denote the numbers of the pages on which the references are used.

[1] H. Haken, *Synergetics*, Naturwissenschaften **67**, 121 (1980).

[2] H. Hinrichsen, *Non-equilibrium critical phenomena and phase transitions into absorbing states*, Adv. Phys. **49**, 815 (2000).

[3] N. Syassen, D. M. Bauer, M. Lettner, T. Volz, D. Dietze, J. J. Garcia-Ripoll, J. I. Cirac, G. Rempe and S. Durr, *Strong Dissipation Inhibits Losses and Induces Correlations in Cold Molecular Gases*, Science **320**, 1329 (2008).

[4] S. Diehl, A. Tomadin, A. Micheli, R. Fazio and P. Zoller, *Dynamical Phase Transitions and Instabilities in Open Atomic Many-Body Systems*, Phys. Rev. Lett. **105**, 015702 (2010).

[5] D. F. Walls, P. D. Drummond, S. S. Hassain and H. J. Carmichael, *Non-Equilibrium Phase Transitions in Cooperative Atomic Systems*, Prog. Theor. Phys. Supplement **64**, 307 (1978).

[6] T. E. Lee and M. C. Cross, *Spatiotemporal dynamics of quantum jumps with Rydberg atoms*, Phys. Rev. A **85**, 063822 (2012).

[7] T. E. Lee, H. Häffner and M. C. Cross, *Collective Quantum Jumps of Rydberg Atoms*, Phys. Rev. Lett. **108**, 023602 (2012).

[8] E. M. Kessler, G. Giedke, A. Imamoglu, S. Yelin, M. D. Lukin and J. I. Cirac, *Dissipative phase transition in a central spin system*, Phys. Rev. A **86**, 012116 (2012).

[9] T. E. Lee, H. Häffner and M. C. Cross, *Antiferromagnetic phase transition in a nonequilibrium lattice of Rydberg atoms*, Phys. Rev. A **84**, 031402 (2011).

[10] C. Ates, B. Olmos, J. P. Garrahan and I. Lesanovsky, *Dynamical phases and intermittency of the dissipative quantum Ising model*, Phys. Rev. A **85**, 043620 (2012).

[11] J. D. Pritchard, D. Maxwell, A. Gauguet, K. J. Weatherill, M. P. A. Jones and C. S. Adams, *Cooperative Atom-Light Interaction in a Blockaded Rydberg Ensemble*, Phys. Rev. Lett. **105**, 193603 (2010).

[12] H. Haken, *Cooperative phenomena in systems far from thermal equilibrium and in nonphysical systems*, Rev. Mod. Phys. **47**, 67 (1975).

[13] R. H. Dicke, *Coherence in Spontaneous Radiation Processes*, Phys. Rev. **93**, 99 (1954).

[14] N. E. Rehler and J. H. Eberly, *Superradiance*, Phys. Rev. A **3**, 1735 (1971).

[15] J. M. Raimond, P. Goy, M. Gross, C. Fabre and S. Haroche, *Statistics of Millimeter-Wave Photons Emitted by a Rydberg-Atom Maser: An Experimental Study of Fluctuations in Single-Mode Superradiance*, Phys. Rev. Lett. **49**, 1924 (1982).

[16] R. Rohlsberger, K. Schlage, B. Sahoo, S. Couet and R. Ruffer, *Collective Lamb Shift in Single-Photon Superradiance*, Science **328**, 1248 (2010).

[17] R. G. DeVoe and R. G. Brewer, *Observation of Superradiant and Subradiant Spontaneous Emission of Two Trapped Ions*, Phys. Rev. Lett. **76**, 2049 (1996).

[18] C. Hettich, C. Schmitt, J. Zitzmann, S. Kuhn, I. Gerhardt and V. Sandoghdar, *Nanometer Resolution and Coherent Optical Dipole Coupling of Two Individual Molecules*, Science **298**, 385 (2002).

[19] R. Friedberg, S. R. Hartmann and J. T. Manassah, *Frequency shifts in emission and absorption by resonant systems ot two-level atoms*, Phys. Rep. **7**, 101 (1973).

[20] J. Keaveney, A. Sargsyan, U. Krohn, I. G. Hughes, D. Sarkisyan and C. S. Adams, *Cooperative Lamb Shift in an Atomic Vapor Layer of Nanometer Thickness*, Phys. Rev. Lett. **108**, 173601 (2012).

[21] M. P. Hehlen, H. U. Gudel, Q. Shu, J. Rai, S. Rai and S. C. Rand, *Cooperative Bistability in Dense, Excited Atomic Systems*, Phys. Rev. Lett. **73**, 1103 (1994).

[22] G. Duffing, Erzwungene Schwingungen bei Veränderlicher Eigenfrequenz (F. Vieweg u. Sohn, Braunschweig, 1918).

[23] O. Guillot-Noël, L. Binet and D. Gourier, *General conditions for intrinsic optical bistability at the atomic and molecular scale: An effective spin-Hamiltonian approach*, Phys. Rev. B **65**, 245101 (2002).

[24] H. M. Gibbs, S. L. McCall and T. N. C. Venkatesan, *Differential Gain and Bistability Using a Sodium-Filled Fabry-Perot-Interferometer*, Phys. Rev. Lett. **36**, 1135 (1976).

[25] C. M. Bowden and C. C. Sung, *First- and second-order phase transitions in the Dicke model: Relation to optical bistability*, Phys. Rev. A **19**, 2392 (1979).

[26] C. M. Bowden, M. Ciftan and H. R. Robl, *Optical Bistability* (Plenum Press, 1981).

[27] O. Guillot-Noël, P. Goldner and D. Gourier, *Dynamics of intrinsic optical bistability in two weakly interacting quantum systems*, Phys. Rev. A **66**, 063813 (2002).

[28] H. Walther, B. T. H. Varcoe, B. Englert and T. Becker, *Cavity quantum electrodynamics*, Rep. Prog. Phys. **69**, 1325 (2006).

[29] H. Morawitz, *Self-coupling of a two-level system by a mirror*, Phys. Rev. **187**, 1792 (1969).

[30] P. Goy, J. M. Raimond, M. Gross and S. Haroche, *Observation of Cavity-Enhanced Single-Atom Spontaneous Emission*, Phys. Rev. Lett. **50**, 1903 (1983).

[31] D. Meschede, H. Walther and G. Müller, *One-Atom Maser*, Phys. Rev. Lett. **54**, 551 (1985).

[32] M. Keller, B. Lange, K. Hayasaka, W. Lange and H. Walther, *Continuous generation of single photons with controlled waveform in an ion-trap cavity system*, Nature **431**, 1075 (2004).

[33] J. R. Rydberg, *On the structure of the line-spectra of the chemical elements*, Phil. Mag. 5th Ser. **29**, 331 (1890).

[34] T. F. Gallagher, *Rydberg Atoms* (Cambridge University Press, 2005).

[35] I. Mourachko, D. Comparat, F. de Tomasi, A. Fioretti, P. Nosbaum, V. M. Akulin and P. Pillet, *Many-Body Effects in a Frozen Rydberg Gas*, Phys. Rev. Lett. **80**, 253 (1998).

[36] J. D. Pritchard, K. J. Weatherill and C. S. Adams, *Non-linear optics using cold Rydberg atoms*, in *Annual Review of Cold Atoms and Molecules* (World Scientific Publishing Company, 2013).

[37] C. S. E. van Ditzhuijzen, A. F. Koenderink, J. V. Hernandez, F. Robicheaux, L. D. Noordam and H. B. van Linden van den Heuvell, *Spatially Resolved Observation of Dipole-Dipole Interaction between Rydberg Atoms*, Phys. Rev. Lett. **100**, 243201 (2008).

[38] A. Tauschinsky, C. S. E. van Ditzhuijzen, L. D. Noordam and H. B. van den Heuvell, *Radio-frequency-driven dipole-dipole interactions in spatially separated volumes*, Phys. Rev. A **78**, 063409 (2008).

[39] P. Schauß, M. Cheneau, M. Endres, T. Fukuhara, S. Hild, A. Omran, T. Pohl, C. Gross, S. Kuhr and I. Bloch, *Observation of spatially ordered structures in a two-dimensional Rydberg gas*, Nature **491**, 87 (2012).

[40] E. Urban, T. A. Johnson, T. Henage, L. Isenhower, D. D. Yavuz, T. G. Walker and M. Saffman, *Observation of Rydberg blockade between two atoms*, Nature Phys **5**, 110 (2009).

[41] D. Jaksch, J. I. Cirac, P. Zoller, S. L. Rolston, R. Cote and M. D. Lukin, *Fast Quantum Gates for Neutral Atoms*, Phys. Rev. Lett. **85**, 2208 (2000).

[42] M. D. Lukin, M. Fleischhauer, R. Cote, L. M. Dunan, D. Jaksch, J. I. Cirac and P. Zoller, *Dipole Blockade and Quantum Information Processing in Mesoscopic Atomic Ensembles*, Phys. Rev. Lett. **87**, 037901 (2001).

[43] M. Saffman, T. G. Walker and K. Mølmer, *Quantum information with Rydberg atoms*, Rev. Mod. Phys. **82**, 2313 (2010).

[44] M. Saffman and T. G. Walker, *Creating single-atom and single-photon sources from entangled atomic ensembles*, Phys. Rev. A **66**, 065403 (2002).

[45] C. Ates, I. Lesanovsky, C. S. Adams and K. J. Weatherill, *Fast and quasi-deterministic single ion source from a dipole-blockaded atomic ensemble*, Phys. Rev. Lett. **110**, 213003 (2013).

[46] M. Tanasittikosol, J. D. Pritchard, D. Maxwell, A. Gauguet, K. J. Weatherill, R. M. Potvliege and C. S. Adams, *Microwave dressing of Rydberg dark states*, J. Phys. B: At. Mol. Opt. Phys. **44**, 184020 (2011).

[47] J. A. Sedlacek, A. Schwettmann, H. Kübler, R. Löw, T. Pfau and J. P. Shaffer, *Microwave electrometry with Rydberg atoms in a vapour cell using bright atomic resonances*, Nature Phys **8**, 819 (2012).

[48] A. Tauschinsky, R. M. T. Thijssen, S. Whitlock, H. B. van Linden van den Heuvell and R. J. C. Spreeuw, *Spatially resolved excitation of Rydberg atoms and surface effects on an atom chip*, Phys. Rev. A **81**, 063411 (2010).

[49] A. Osterwalder and F. Merkt, *Using High Rydberg States as Electric Field Sensors*, Phys. Rev. Lett. **82**, 1831 (1999).

[50] R. P. Abel, C. Carr, U. Krohn and C. S. Adams, *Electrometry near a dielectric surface using Rydberg electromagnetically induced transparency*, Phys. Rev. A **84**, 023408 (2011).

[51] Y. O. Dudin, L. Li, F. Bariani and A. Kuzmich, *Observation of coherent many-body Rabi oscillations*, Nature Phys **8**, 790 (2012).

[52] I. Friedler, D. Petrosyan, M. Fleischhauer and G. Kurizki, *Long-range interactions and entanglement of slow single-photon pulses*, Phys. Rev. A **72**, 043803 (2005).

[53] A. K. Mohapatra, T. R. Jackson and C. S. Adams, *Coherent Optical Detection of Highly Excited Rydberg States Using Electromagnetically Induced Transparency*, Phys. Rev. Lett. **98**, 113003 (2007).

[54] M. Fleischhauer, A. Imamoglu and J. P. Marangos, *Electromagnetically induced transparency: Optics in coherent media*, Rev. Mod. Phys. **77**, 633 (2005).

[55] J. Gea-Banacloche, Y. Li, S. Jin and M. Xiao, *Electromagnetically induced transparency in ladder-type inhomogeneously broadened media: Theory and experiment*, Phys. Rev. A **51**, 576 (1995).

[56] K. J. Boller, A. Imamoglu and S. E. Harris, *Observation of electromagnetically induced transparency*, Phys. Rev. Lett. **66**, 2593 (1991).

[57] D. Petrosyan, J. Otterbach and M. Fleischhauer, *Electromagnetically Induced Transparency with Rydberg Atoms*, Phys. Rev. Lett. **107**, 213601 (2011).

[58] K. J. Weatherill, J. D. Pritchard, R. P. Abel, M. G. Bason, A. K. Mohapatra and C. S. Adams, *Electromagnetically induced transparency of an interacting cold Rydberg ensemble*, J. Phys. B: At. Mol. Opt. Phys. **41**, 201002 (2008).

[59] P. Thoumany, T. Germann, T. Hänsch, G. Stania, L. Urbonas and T. Becker, *Spectroscopy of rubidium Rydberg states with three diode lasers*, J. Mod. Opt. **56**, 2055 (2009).

[60] J. M. Raimond, G. Vitrant and S. Haroche, *Spectral line broadening due to the interaction between very excited atoms: 'the dense Rydberg gas'*, J. Phys. B: At. Mol. Phys. **14**, L655 (1981).

[61] T. Baluktsian, B. Huber, R. Low and T. Pfau, *Evidence for Strong van der Waals Type Rydberg-Rydberg Interaction in a Thermal Vapor*, Phys. Rev. Lett. **110**, 123001 (2013).

[62] H. Kübler, J. P. Shaffer, T. Baluktsian, R. Low and T. Pfau, *Coherent excitation of Rydberg atoms in micrometre-sized atomic vapour cells*, Nature Photon **4**, 112 (2010).

[63] D. Barredo, H. Kübler, R. Daschner, R. Low and T. Pfau, *Electrical Readout for Coherent Phenomena Involving Rydberg Atoms in Thermal Vapor Cells*, Phys. Rev. Lett. **110**, 123002 (2013).

[64] S. Knappe, V. Gerginov, P. D. D. Schwindt, V. Shah, H. G. Robinson, L. Hollberg and J. Kitching, *Atomic vapor cells for chip-scale atomic clocks with improved long-term frequency stability*, Opt. Lett. **30**, 2351 (2005).

[65] V. Shah, S. Knappe, P. D. D. Schwindt and J. Kitching, *Subpicotesla atomic magnetometry with a microfabricated vapour cell*, Nature Photon **1**, 649 (2007).

[66] C. Carr, C. S. Adams and K. J. Weatherill, *Polarization spectroscopy of an excited state transition*, Opt. Lett. **37**, 118 (2012).

[67] M. Tanasittikosol, C. Carr, C. S. Adams and K. J. Weatherill, *Subnatural linewidths in two-photon excited-state spectroscopy*, Phys. Rev. A **85**, 033830 (2012).

[68] C. Carr, M. Tanasittikosol, A. Sargsyan, D. Sarkisyan, C. S. Adams and K. J. Weatherill, *Three-photon electromagnetically induced transparency using Rydberg states*, Opt. Lett. **37**, 3858 (2012).

[69] A. Urvoy, C. Carr, R. Ritter, R. Löw, C. S. Adams and K. J. Weatherill, *Optical coherences and wavelength mismatch in ladder systems*, in preparation (2013).

[70] C. Carr, R. Ritter, C. G. Wade, C. S. Adams and K. J. Weatherill, *Nonequilibrium phase transition in a dilute Rydberg ensemble*, Phys. Rev. Lett. **111**, 113901 (2013).

[71] C. S. Adams and I. G. Hughes, *Handbook of Laser Technology and Applications*, volume 3 (Taylor & Francis Group, 2003).

[72] B. Shore, *The Theory of Atomic Coherent Excitation: Simple Atoms and Fields*, volume 1 (Wiley-Interscience, London, England, 1990).

[73] C. Cohen-Tannoudji, J. Dupont-Roc and G. Grynberg, *Atom-Photon Interaction: Basic Processes and Applications* (John Wiley and Sons, New York, USA, 1992).

[74] D. Suter, *The Physics of Laser-Atom Interactions* (Cambridge University Press, Cambridge, England, 1997).

[75] R. Loudon, *The Quantum Theory of Light* (Oxford University Press, 2000).

[76] D. A. Steck, *Cesium D Line Data*, URL `http://steck.us/alkalidata/cesiumnumbers.pdf`.

[77] S. H. Autler and C. H. Townes, *Stark Effect in Rapidly Varying Fields*, Phys. Rev. **100**, 703 (1955).

[78] P. M. Anisimov, J. P. Dowling and B. C. Sanders, *Objectively Discerning Autler-Townes Splitting from Electromagnetically Induced Transparency*, Phys. Rev. Lett. **107**, 163604 (2011).

[79] L. V. Hau, S. E. Harris, Z. Dutton and C. H. Behroozi, *Light speed reduction to 17 metres per second in an ultracold atomic gas*, Nature **397**, 594 (1999).

[80] M. Kash, V. Sautenkov, A. Zibrov, L. Hollberg, G. Welch, M. Lukin, Y. Rostovtsev, E. Fry and M. Scully, *Ultraslow Group Velocity and Enhanced Nonlinear Optical Effects in a Coherently Driven Hot Atomic Gas*, Phys. Rev. Lett. **82**, 5229 (1999).

[81] D. F. Phillips, A. Fleischhauer, A. Mair, R. Walsworth and M. D. Lukin, *Storage of Light in Atomic Vapor*, Phys. Rev. Lett. **86**, 783 (2001).

[82] C. J. Foot, *Atomic Physics* (Oxford University Press, Oxford, 2004).

[83] C. Carr, *Quantum entanglement via Rydberg excitation of atoms in an optical lattice*, Master's thesis, Durham University (2009).

[84] H. J. Metcalf and P. Van der Straten, *Laser Cooling and Trapping* (Springer, 1999).

[85] D. M. Brink and G. R. Satchler, *Angular Momentum* (Oxford University Press, 1968).

[86] A. A. Vasilyev, I. M. Savukov, M. S. Safronova and H. G. Berry, *Measurement of the 6s-7p transition probabilities in atomic cesium and a revised value for the weak charge Q(W)*, Phys. Rev. A **66**, 020101 (2002).

[87] J. D. Pritchard, *Private Communication, Radial matrix elements for caesium.*

[88] A. Kramida, Y. Ralchenko, J. Reader and N. Team, *NIST Atomic Spectra Database*, URL `http://physics.nist.gov/cgi-bin/ASD/energy1.pl`.

[89] P. Goy, J. M. Raimond, G. Vitrant and S. Haroche, *Millimeter-wave spectroscopy in cesium Rydberg states. Quantum defects, fine- and hyperfine-structure measurements*, Phys. Rev. A **26**, 2733 (1982).

[90] I. I. Beterov, I. I. Ryabtsev, D. B. Tretyakov and V. M. Entin, *Quasiclassical calculations of blackbody-radiation-induced depopulation rates and effective lifetimes of Rydberg nS, nP, and nD alkali-metal atoms with n=80*, Phys. Rev. A **79**, 052504 (2009).

[91] P. Hertz, *Über den gegenseitigen durchschnittlichen Abstand von Punkten, die mit bekannter mittlerer Dichte im Raume angeordnet sind*, Math Ann **67**, 387 (1909).

[92] A. Sargsyan, G. Hakhumyan, C. Leroy, Y. Pashayan-Leroy, A. Papoyan and D. Sarkisyan, *Hyperfine Paschen–Back regime realized in Rb nanocell*, Opt. Lett. **37**, 1379 (2012).

[93] J. D. Jackson, *Classical Electrodynamics* (J Wiley & Sons, 1998), 3rd edition.

[94] M. J. Stephen, *First-Order Dispersion Forces*, J. Chem. Phys. **40**, 669 (1964).

[95] I. E. Protsenko, *Superradiance of trapped atoms*, J Russ Laser Res **27**, 414 (2006).

[96] H.-J. Butt and M. Kappl, *Surface and Interfacial Forces* (Wiley-VCH Verlag, Weinheim, Germany, 2010).

[97] H. A. Lorentz, *The theory of electrons and its applications to the phenomena of light and radiant heat* (B G Teubner, Leipzig, 1916).

[98] T. C. Choy, *Effective Medium Theory: Principles and Applications* (Oxford University Press, 1999).

[99] J. T. Manassah, *Giant Cooperative Lamb Shift in a density-modulated slab of two-level atoms*, Phys. Lett. **374**, 1985 (2010).

[100] R. Friedberg and J. T. Manassah, *Initial cooperative decay rate and cooperative Lamb shift of resonant atoms in an infinite cylindrical geometry*, Phys. Rev. A **84**, 023839 (2011).

[101] J. T. Manassah, *Cooperative radiation from atoms in different geometries: decay rate and frequency shift*, Adv. Opt. Photon. **4**, 108 (2012).

[102] V. Sautenkov, H. van Kampen, E. R. Eliel and J. P. Woerdman, *Dipole-Dipole Broadened Line Shape in a Partially Excited Dense Atomic Gas*, Phys. Rev. Lett. **77**, 3327 (1996).

[103] A. Corney, *Atomic and Laser Spectroscopy* (Oxford University Press, Oxford, 2006).

[104] V. A. Sautenkov, V. L. Velichanskiĭ, A. S. Zibrov, V. N. Luk'yanov, V. V. Nikitin and D. A. Tyurikov, *Intra-Doppler resonances of the cesium D 2line in a selective specular reflection profile*, Sov. J. Quantum Electron. **11**, 1131 (1981).

[105] V. Vuletić, V. A. Sautenkov, C. Zimmermann and T. W. Hänsch, *Measurement of cesium resonance line self-broadening and shift with doppler-free selective reflection spectroscopy*, Opt. Commun. **99**, 185 (1993).

[106] M. Gross and S. Haroche, *Superradiance: an essay on the theory of collective spontaneous emission*, Phys. Rep. **93**, 301 (1982).

[107] F. Gounand, H. Hugon, P. R. Fournier and J. Berlande, *Superradiant cascading effects in rubidium Rydberg levels*, J. Phys. B: At. Mol. Opt. Phys. **12**, 547 (1979).

[108] L. Weller, R. J. Bettles, P. Siddons, C. S. Adams and I. G. Hughes, *Absolute absorption on the rubidium D1 line including resonant dipole–dipole interactions*, J. Phys. B: At. Mol. Opt. Phys. **44**, 195006 (2011).

[109] J. J. Olivero and R. L. Longbothum, *Empirical fits to the Voigt line width: A brief review*, J. Quant. Spectros. and Radiat. Transfer **17**, 233 (1977).

[110] P. W. Smith and R. Hänsch, *Cross-Relaxation Effects in the Saturation of the 6328-Å Neon-Laser Line*, Phys. Rev. Lett. **26**, 740 (1971).

[111] C. Wieman and T. W. Hänsch, *Doppler-Free Laser Polarization Spectroscopy*, Phys. Rev. Lett. **36**, 1170 (1976).

[112] C. P. Pearman, C. S. Adams, S. G. Cox, P. F. Griffin, D. A. Smith and I. G. Hughes, *Polarization spectroscopy of a closed atomic transition: applications to laser frequency locking*, J. Phys. B: At. Mol. Opt. Phys. **35**, 5141 (2002).

[113] R. Boyd, *Nonlinear Optics* (Academic Press Inc, 2008), 3rd edition.

[114] M. L. Harris, C. S. Adams, S. L. Cornish, I. C. McLeod, E. Tarleton and I. G. Hughes, *Polarization spectroscopy in rubidium and cesium*, Phys. Rev. A **73**, 062509 (2006).

[115] G. P. T. Lancaster, R. S. Conroy, M. A. Clifford, J. Arlt and K. Dholakia, *A polarisation spectrometer locked diode laser for trapping cold atoms*, Opt Commun **170**, 79 (1999).

[116] M. Breton, N. Cyr, P. Tremblay, M. Tetu and R. Boucher, *Frequency locking of a 1324 nm DFB laser to an optically pumped rubidium vapor*, IEEE Trans. Instrum. Meas. **42**, 162 (1993).

[117] R. P. Abel, A. K. Mohapatra, M. G. Bason, J. D. Pritchard, K. J. Weatherill, U. Raitzsch and C. S. Adams, *Laser frequency stabilization to excited state transitions using electromagnetically induced transparency in a cascade system*, Appl. Phys. Lett. **94**, 071107 (2009).

[118] D. Sheng, A. Pérez Galván and L. Orozco, *Lifetime measurements of the 5d states of rubidium*, Phys. Rev. A **78**, 062506 (2008).

[119] R. I. Billmers, S. K. Gayen, M. F. Squicciarini, V. M. Contarino, W. J. Scharpf and D. M. Allocca, *Experimental demonstration of an excited-state Faraday filter operating at 532 nm*, Opt. Lett. **20**, 106 (1995).

[120] T. Meijer, J. D. White, B. Smeets, M. Jeppesen and R. E. Scholten, *Blue five-level frequency-upconversion system in rubidium*, Opt. Lett. **31**, 1002 (2006).

[121] S. Wu, T. Plisson, R. Brown, W. Phillips and J. Porto, *Multiphoton Magnetooptical Trap*, Phys. Rev. Lett. **103**, 173003 (2009).

[122] M. A. Bouchiat, J. Guena and L. Pottier, *Absolute polarization measurements and natural lifetime in the 7s1/2 state of Cs*, J. Physique Lett. **45**, 523 (1984).

[123] C. E. Theodosiou, *Lifetimes of alkali-metal—atom Rydberg states*, Phys. Rev. A **30**, 2881 (1984).

[124] B. H. Bransden and C. J. Joachain, *Physics of Atoms and Molecules* (Prentice Hall, Essex, England, 2003).

[125] C. Y. Ye, A. S. Zibrov, Y. V. Rostovtsev and M. O. Scully, *Unexpected Doppler-free resonance in generalized double dark states*, Phys. Rev. A **65**, 043805 (2002).

[126] M. G. Bason, A. K. Mohapatra, K. J. Weatherill and C. S. Adams, *Narrow absorptive resonances in a four-level atomic system*, J. Phys. B: At. Mol. Opt. Phys. **42**, 075503 (2009).

[127] S. Shepherd, D. J. Fulton and M. H. Dunn, *Wavelength dependence of coherently induced transparency in a Doppler-broadened cascade medium*, Phys. Rev. A **54**, 5394 (1996).

[128] J. Sagle, R. K. Namiotka and J. Huennekens, *Measurement and modelling of intensity dependent absorption and transit relaxation on the cesium line*, J. Phys. B: At. Mol. Opt. Phys. **29**, 2629 (1996).

[129] D. A. Smith and I. G. Hughes, *The role of hyperfine pumping in multilevel systems exhibiting saturated absorption*, Am. J. Phys. **72**, 631 (2004).

[130] B. E. Sherlock and I. G. Hughes, *How weak is a weak probe in laser spectroscopy?*, Am. J. Phys. **77**, 111 (2009).

[131] H. S. Moon, W. K. Lee, L. Lee and J. B. Kim, *Double resonance optical pumping spectrum and its application for frequency stabilization of a laser diode*, Appl. Phys. Lett. **85**, 3965 (2004).

[132] A. Sargsyan, M. G. Bason, D. Sarkisyan, A. K. Mohapatra and C. S. Adams, *Electromagnetically induced transparency and two-photon absorption in the ladder system in thin columns of atomic vapors*, Opt. Spectrosc. **109**, 529 (2010).

[133] D. McGloin, D. J. Fulton and M. H. Dunn, *Electromagnetically induced transparency in N-level cascade schemes*, Opt. Commun. **190**, 221 (2001).

[134] M. Tanasittikosol, *Rydberg dark states in external fields*, Ph.D. thesis, Durham University (2011).

[135] S. Reynaud, M. Himbert, J. Dupont-Roc, H. H. Stroke and C. Cohen-Tannoudji, *Experimental Evidence for Compensation of Doppler Broadening by Light Shifts*, Phys. Rev. Lett. **42**, 756 (1979).

[136] H. M. Gibbs, *Optical Bistability: Controlling Light with Light* (Academic Press Inc, 1985).

[137] H. M. Gibbs, S. L. McCall, T. N. C. Venkatesan, A. C. Gossard, A. Passner and W. Wiegmann, *Optical bistability in semiconductors*, Appl. Phys. Lett. **35**, 451 (1979).

[138] H. A. Al-Attar, H. A. MacKenzie and W. J. Firth, *Critical slowing-down phenomena in an InSb optically bistable etalon*, J. Opt. Soc. Am. B **3**, 1157 (1986).

[139] S. F. Yelin, M. Kostrun, T. Wang and M. Fleischhauer, *Correlation in superradiance: A closed-form approach to cooperative effects*, arXiv:quant-ph/0509184 (2005).

[140] S. Yelin and M. Fleischhauer, *Modification of local field effects in two level systems due to quantum corrections*, Opt. Express **1**, 160 (1997).

[141] J. Qian, L. Zhou and W. Zhang, *Quantum phases of strongly interacting Rydberg atoms in triangular lattices*, arXiv:1305.6687 (2013).

[142] M. Fleischhauer and S. F. Yelin, *Radiative atom-atom interactions in optically dense media: Quantum corrections to the Lorentz-Lorenz formula*, Phys. Rev. A **59**, 2427 (1999).

[143] R. Friedberg, S. R. Hartmann and J. Manassah, *Mirrorless optical bistability condition*, Phys. Rev. A **39**, 3444 (1989).

[144] A. Flusberg, R. Kachru, T. Mossberg and S. R. Hartmann, *Foreign-gas-induced relaxation of Rydberg S and D states in atomic sodium*, Phys. Rev. A **19**, 1607 (1979).

[145] *Hamamatsu PMT Handbook*, URL `http://www.hamamatsu.com/resources/pdf/etd/PMT_handbook_v3aE.pdf`.

[146] T. Wang, S. F. Yelin, R. Cote, E. E. Eyler, S. M. Farooqi, P. L. Gould, M. Kostrun, D. Tong and D. Vrinceanu, *Superradiance in ultracold Rydberg gases*, Phys. Rev. A **75**, 033802 (2007).

[147] R. Bonifacio and P. Meystre, *Critical slowing down in optical bistability*, Opt. Commun. **29**, 131 (1979).

[148] M. Scheffer, J. Bascompte, W. A. Brock, V. Brovkin, S. R. Carpenter, V. Dakos, H. Held, E. H. van Nes, M. Rietkerk and G. Sugihara, *Early-warning signals for critical transitions*, Nature **461**, 53 (2009).

[149] G. Grynberg and S. Cribier, *Critical exponents in dispersive optical bistability*, J. Physique Lett. **44**, 449 (1983).

[150] S. Cribier, E. Giacobino and G. Grynberg, *Quantitative investigation of critical slowing down in all-optical bistability*, Opt. Comm. **47**, 170 (1983).

[151] P. C. Hohenberg and B. I. Halperin, *Theory of dynamic critical phenomena*, Rev. Mod. Phys. **49**, 435 (1977).

[152] L. Landau, *The theory of phase transitions*, Nature **138**, 840 (1936).

[153] Y. Ben-Aryeh, C. Bowden and J. Englund, *Longitudinal spacial first-order phase transition in a system of coherently-driven, two-level atoms*, Opt. Commun. **61**, 147 (1987).

[154] R. Inguva and C. Bowden, *Spatial and temporal evolution of the first-order phase transition in intrinsic optical bistability*, Phys. Rev. A **41**, 1670 (1990).

[155] S. Sevinçli, N. Henkel, C. Ates and T. Pohl, *Nonlocal Nonlinear Optics in Cold Rydberg Gases*, Phys. Rev. Lett. **107**, 153001 (2011).